UNIVERSITY OF SOUTHAMPTON

FACULTY OF NATURAL AND ENVIRONMENTAL SCIENCES

Department of Chemistry

Oxychalcogenides for Transparent p-Type Conductors

by

Gregory James Limburn, MSci

ORCID iD: 0000-0003-4275-2211

Thesis for the degree of Doctor of Philosophy

For my dear grandad, Maurice

UNIVERSITY OF SOUTHAMPTON

ABSTRACT

FACULTY OF NATURAL AND ENVRONMENTAL SCIENCES

Chemistry

Thesis for the degree of Doctor of Philosophy

OXYCHALCOGENIDES FOR TRANSPARENT P-TYPE CONDUCTORS

Gregory James Limburn, MSci

The quinary layered oxychalcogenide, $Sr_3Sc_2O_5Cu_2S_2$, was used as a prototype to investigate the effect of composition and structure, on transparency and conductivity of analogous materials. A selection of analogues was computationally screened for predicted stability and optical transparency. The compounds $Ba_3Sc_2O_5Cu_2S_2$ and $Ca_3Al_2O_5Cu_2S_2$ were both expected to show band gap energies higher than 3.1 eV and conductivities higher than that of the prototype. The compound $Ba_3Sc_2O_5Cu_2S_2$ was successfully synthesised here by solid-state reaction at 800 ^oC for 12 h, apparently for the first time. Its measured band-gap energy was 3.24 eV. Synthesis of $Ca_3Al_2O_5Cu_2S_2$ was not achieved. It was concluded that a high-pressure synthetic route would be required to realise this compound.

The compounds intermediate between the prototype and new member $Ba_xSr_{3-x}Sc_2O_5Cu_2S_2$ where x = 1 and 2, were also successfully synthesised. Refinement of their crystal structures showed a preference of barium for the 'intra-layer' site in the perovskite layer, as rationalised by the Goldschmidt tolerance factor. The perovskite *A* site mixing yielded extreme bond distances and angles in the conductive copper sulfide layer of x = 2, beyond the range spanned by the end-members. Williamson-Hall analysis revealed increased strain and reduced crystallite size for the intermediates and general anisotropic growth of these compounds favouring the direction of conduction, as confirmed by scanning-electron microscopy.

The successful syntheses of the analogous compounds $Ba_3In_2O_5Cu_2S_2$, $Ba_3Sc_2O_5Cu_2Se_2$, $Ba_3Y_2O_5Cu_2Se_2$, $Ba_3In_2O_5Cu_2Se_2$, $Ba_3Sc_2O_5Ag_2Se_2$ and $Ba_3In_2O_5Ag_2Se_2$ were also reported here, for the first time to the authors knowledge. It was found that the increased radius of the perovskite *M* cation, increased the basal lattice parameter and linked coinage metal-metal distance, expected to benefit transparency. However, observed reductions in band-gap energy for both the indium and yttrium analogues, relative to those of the scandium compounds, were rationalised by electronegativity and (n-1)*d*-orbital occupancy, respectively. The coinage metal-chalcogenide distance increased, and angle deviated from the ideal tetrahedral, with increasing *M* cation radius, in all cases. Barium and scandium proved to be the optimal candidate perovskite layer cations. Substitution of selenium and silver into the conductive layer was expected to increase conductivity at the expense of an observed decrease in band gap for the scandium analogues.

The compounds $Ba_3Sc_2O_5Cu_2S_2$ and $Ba_3Sc_2O_5Cu_2Se_2$ showed promise as improved transparent p-type conductors. Their compositions and structures suggested improved conductivity compared to that of $Sr_3Sc_2O_5Cu_2S_2$. The 3.05 eV band gap of $Ba_3Sc_2O_5Cu_2Se_2$ may be increased above the visible light threshold by p-type doping. A preliminary investigation saw the prototype successfully doped by 5 at. % sodium with an accompanied Moss-Burstein shift in band gap energy of + 0.5 eV to 3.2 eV.

Table of Contents

List of Tables i
List of Figures v
DECLARATION OF AUTHORSHIP xiii
Acknowledgements xv
List of Abbreviations xvii
Chapter 1 Introduction 1
1.1 Transparent Conductors | Development and Applications 1
1.2 Applications 2
1.3 Design Considerations for Transparent Conductor Development 3
1.3.1 Absorption 4
1.3.2 Reflection 4
1.3.3 Electrical Conductivity 5
1.3.4 Band Theory 5
1.3.5 Summary 10
1.4 Potential Applications and Development of Transparent p-Type Conductors 11
1.5 Layered Perovskite Oxychalcogenides 18
1.6 Project Aim 21
Chapter 2 Employed Analytical Methods 25
2.1 X-ray Diffraction 25
2.1.1 The Phenomenon of Diffraction 25
2.1.2 A Brief History of X-Ray Discovery, Generation and Diffraction 26
2.1.3 The Powder Diffraction Experiment 27
2.1.4 Data Analysis 28
2.2 Optical Properties 34
2.2.1 The Tauc Equation and Band-Gap Energy Derivation 34
2.2.2 The Kubelka-Munk Theory of Diffuse Reflectance 35
2.3 Scanning Electron Microscopy (SEM) 35
Chapter 3 Attempted Syntheses of 325-type Layered Oxychalcogenides Computationally Predicted to Show Promise as Improved Transparent p-Type Conductors 37
3.1 Introduction 37

3.2 Experimental 41
3.3 Results and Discussion 42
3.3.1 Repeated Synthesis of Literature Prototype $Sr_3Sc_2O_5Cu_2S_2$ 42
3.3.2 Attempted Synthesis of Predicted Transparent p-Type Conductor $Ca_3Al_2O_5Cu_2S_2$ 43
3.3.3 Synthesis of Predicted Transparent p-Type Conductor $Ba_3Sc_2O_5Cu_2S_2$ 45
3.3.4 $Sr_3Ga_2O_5Cu_2S_2$ 49
3.3.5 Attempted Synthesis of Remaining Analogous Compounds 52
3.4 Conclusions and Outlook 56

Chapter 4 Conductive Layer Geometry Modification by Isovalent Mixing of Perovskite *A* Cations 59
4.1 Introduction 59
4.2 Experimental 60
4.3 Results and Discussion 61
4.3.1 Evidence for the Successful Single-Phase Mixing of Perovskite *A* Site Cations 61
4.3.2 Effect of Perovskite *A*-Site Cation Mixing on the Geometry of the Copper Sulfide Layer 68
4.3.3 Effect of Copper Sulfide Layer Geometry on Optical Properties 71
4.3.4 Prediction of the Effect of Copper Sulfide Layer Geometry on Electronic Properties 73
4.3.5 Williamson-Hall Line Profile Analysis 74
4.3.6 Scanning-Electron Microscopic Analysis 86
4.4 Conclusions and Outlook 89

Chapter 5 Effect of Isovalent Substitution of Elements on Crystal Structure and Optoelectronic Properties in 325-Type Layered Oxychalcogenides 91
5.1 Introduction 91
5.2 Experimental 92
5.3 Results and Discussion 93
5.3.1 Isovalent Substitution at the Perovskite Metal, *M*, Site 93
5.3.2 Isovalent Substitution at the Chalcogen Site, *Ch* 99
5.3.3 Isovalent Substitution at the Perovskite Metal, *M*, Site | Revisited 105
5.3.4 Isovalent Substitution at the Coinage Metal, *M'*, Site 112

5.4 Conclusions 122
5.4.1 Perovskite Metal Site *(M)* 122
5.4.2 Conductive Chalcogen Site *(Ch)* 125
5.4.3 Coinage Metal Site *(M')* 127
5.4.4 Summary 129

Chapter 6 Final Conclusions and Outlook 131
6.1 Conclusions 131
6.2 Outlook 133
6.2.1 Conductivity and Hall Effect Measurements 133
6.2.2 Extrinsic p-Type Acceptor Doping 134
6.2.3 Further Layered Perovskite Mixed-Anion Oxide Structure Types 136
6.3 Summary 139

Appendices 141
A Derivation of the Plasma Frequency 141
B Derivation of the Conductivity Equation 143
C Selected Lattice Parameters for Quinary Layered Mixed Anion Oxides 144
D Precursor Syntheses 146
D.1 Alkali Earth Oxides 146
D.2 Alkali Earth Sulfides 147
D.3 Barium Selenide by Selenate Reduction 148
D.4 Sodium Sulfide 149
E $Ba_3Sc_2O_5Cu_2S_2$ Refined Crystal Structure Parameters 150
F Chapter 4 Supplementary Data 151
F.1 Refined Unit Cell Parameters 151
F.2 Refined Fractional Atomic Coordinates 151
F.3 Crystal Structure Geometry (Distances and Angles) 152
F.4 Instrumental Broadening Calibration Data 153
F.5 Williamson-Hall Analysis Raw Data 154
G Derivation of the Goldschmidt Tolerance Factor 163
H Chapter 5 Fractional Atomic Coordinates of Rietveld Refined Crystallographic Models 165
H.1 $Ba_3In_2O_5Cu_2S_2$ 165

H.2 $Ba_3Sc_2O_5Cu_2Se_2$ 165
H.3 $Ba_3Y_2O_5Cu_2Se_2$ 166
H.4 $Ba_3In_2O_5Cu_2Se_2$ 166
H.5 $Ba_3Sc_2O_5Ag_2Se_2$ 167
H.6 $Ba_3In_2O_5Ag_2Se_2$ 167

I Summary of Distances and Angles 168
List of References 169

List of Tables

1.1 Summary of reported properties of delafossite transparent p-type conducting thin films. 14

1.2 Summary of the properties of LaCuOS-based thin films investigated for transparent p-type conductivity. 16

1.3 Summary of the optoelectronic properties of bulk polycrystalline powder samples of layered oxychalcogenides investigated by Liu *et al.* for potential application as p-type transparent conductors. 17

3.1 Stabilities of compounds with general composition $A_3M_2O_5Cu_2S_2$, predicted by Williamson and Scanlon. 38

3.2 Computationally predicted optical band gap energies (E_g^{opt}) for the compositions ($A_3M_2O_5Cu_2S_2$) investigated. 40

3.3 Summary of the lattice parameters and key distances and angles, in terms of the electronic structure, for the prototype compound $Sr_3Sc_2O_5Cu_2S_2$, as determined by various methods. 43

3.4 Summary of the lattice parameters and key distances and angles, in terms of the electronic structure, for the prototype and newly synthesised compounds $A_3Sc_2O_5Cu_2S_2$, where A = Sr and Ba, respectively, as determined by various methods. 46

3.5 Comparison of the lattice parameters and key distances and angles, in terms of the electronic structure, for the compounds $Sr_3Sc_2O_5Cu_2S_2$ and $Sr_4Ga_2O_6Cu_2S_2$, respectively. 52

3.6 Summary of the crystalline product phases observed after attempted solid-state synthesis of targeted oxychalcogenides $A_3M_2O_5Cu_2S_2$ where A = Ca, Sr and Ba and M = Al, Sc and Ga. 57

4.1 Summary of the freely refined fractional occupancies of the A site cations in the series of compounds $Ba_xSr_{3-x}Sc_2O_5Cu_2S_2$, where x = 0, 1, 2 and 3. 63

4.2 Summary of refined fractional occupancies of cations barium and strontium across the A perovskite-like layer crystallographic sites in the compounds $Ba_xSr_{3-x}Sc_2O_5Cu_2S_2$, where x = 1 and 2. 65

4.3 Summary of selected interatomic distances and angles describing the geometry of the conductive copper sulfide layer in the mixed perovskite *A* cation compounds $Ba_xSr_{3-x}Sc_2O_5Cu_2S_2$, where x = 0, 1, 2 and 3. 70

4.4 Summary of the lattice strain and crystallite sizes calculated from the gradients and *y*-intercepts of the linear fits to the data in the Williamson-Hall plots in *figure 4.12*, from which *figure 4.13* was constructed. 80

4.5 Summary of the inhomogeneous lattice strain and crystallite domain sizes calculated independently for lattice planes with vector oriented primarily in the *ab* and *c* unit cell directions by separate linear fits to the corresponding sets in the Williamson-Halls plots in *figure 4.15*. 84

5.1 Summary of the ionic radii and tolerance factors in a barium oxide perovskite lattice, of the candidate replacement *M* site elements. 93

5.2 Summary of the ionic radii of the *M* cations being substituted and the resultant lattice parameters and interatomic distances/angles of the observed phases. 97

5.3 Extension of *table 5.1* including the electronegativity and (n-1)*d* sub-shell electronic occupany for the candidate replacement *M* site elements for the discussion of observed band-gap energy. 99

5.4 Summary of ionic radii of the chalcogen ions being substituted in $BaM_2O_5Cu_2Se_2$ and the lattice parameters of the resultant crystalline phases. 103

5.5 Summary of ionic radii of the *M* site cations being substituted and the corresponding lattice parameters describing the crystalline phases formed. 106

5.6 Summary of ionic radii of the *M* site cations being substituted in $Ba_3M_2O_5Cu_2Se_2$ and the corresponding lattice parameters describing the crystalline phases formed. 109

5.7 Summary of the composition of crystalline phases identified by PXRD for the attempted syntheses at 900 ^oC for 72 h of the family of compounds $Ba_3M_2O_5Ag_2S_2$, where *M* = Sc, Y, In and La. 113

5.8 Summary of ionic radii of the M' site cations, Cu and Ag, being substituted in the compounds $Ba_3M_2O_5M'_2Se_2$ where M = Sc and In, and the corresponding lattice parameters describing the crystalline phases formed. 118

Appendices

A 1 Selected lattice parameters of analogous quinary layered mixed anion oxides extracted from the literature. 144

A 2 Summary of the Rietveld refined crystal structure parameters of the compound with composition $Ba_3Sc_2O_5Cu_2S_2$. 150

A 3 Summary of lattice parameters, as determined by refined powder x-ray diffraction data, of the intermediate mixed *A* perovskite cation compounds $Ba_xSr_{3-x}Sc_2O_5Cu_2S_2$, where x = 1 and 2. 151

A 4 Fractional atomic coordinates extracted from the Rietveld refined model describing the crystal structures of mixed *A* site compounds of composition $Ba_xSr_{3-x}Sc_2O_2Cu_2S_2$, where x = 1 and 2. 151

A 5 Summary of distances, bond lengths and angles calculated from the Rietveld refined model for the crystal; structures of the mixed *A* compounds with compositions $Ba_xSr_{3-x}Sc_2O_5Cu_2S_2$. 152

A 6 Summary of peak parameters in collected powder x-ray diffraction profile for the LaB_6 instrumental broadening standard. 153

A 7 Raw data used in the construction of the Williamson-Hall plots. 154

A 8 Summary of the fractional atomic coordinates of the atomic sites within the $Ba_3In_2O_5Cu_2S_2$ *I4/mmm* crystal structure. 165

A 9 Summary of the fractional atomic coordinates of the atomic sites within the $Ba_3Sc_2O_5Cu_2Se_2$ *I4/mmm* crystal structure. 165

A 10 Summary of the fractional atomic coordinates of the atomic sites within the $Ba_3Y_2O_5Cu_2Se_2$ *I4/mmm* crystal structure. 166

A 11 Summary of the fractional atomic coordinates of the atomic sites within the $Ba_3In_2O_5Cu_2Se_2$ *I4/mmm* crystal structure 166

A 12 Summary of the fractional atomic coordinates of the atomic sites within the $Ba_3Sc_2O_5Ag_2Se_2$ *I4/mmm* crystal structure. 167

A 13 Summary of the fractional atomic coordinates of the atomic sites within the $Ba_3In_2O_5Ag_2Se_2$ *I4/mmm* crystal structure 167

A 14 Summary of interatomic distances and angles for compounds successfully synthesised and reported in *Chapter 5*. 168

List of Figures

1.1 Sketch of idealised absorption (green), reflection (red) and transmission (blue) spectra for a visibly transparent material. 3

1.2 Extended unit cell (grey lines) crystal structure of a generic delafossite oxide mineral AMO_2. 12

1.3 Extended unit cell (grey lines) structure of the layered oxychalcogenide compound LaCuOS 15

1.4 Extended unit cell crystal structures of perovskite and litharge 'building blocks' of a layered perovskite oxychalcogenide. 19

1.5 Plot illustrating the effect of the mean weighted ionic radius of the perovskite ions on the basal lattice parameter, *a*, for a series of layered perovskite oxychalcogenide and oxypnictide compounds with the general formulae $A_4M_2O_6M'_2Ch/Pn_2$, reported in the literature. 21

1.6 Plot to illustrate the linear relationship between the basal lattice parameter and the *Ch/Pn-M'-Ch/Pn* angle in the tetrahedral litharge-like layer of the compounds $A_xM_yO_zCu_2S_2$ (top left), $A_xM_yO_zCu_2Se_2$ (top right), $A_xM_yO_zAg_2Se_2$ (bottom left) and $A_xM_yO_zFe_2As_2$ (bottom right), where xyz = 212, 213 and 325. 22

2.1 Illustration of the diffraction and resulting observed intensity of the interference pattern of a wave by a double-slit. 25

2.2 A schematic depiction of a typical powder diffractometer in θ/2θ Bragg-Brentano geometry showing divergent/convergent x-ray beam path. 27

3.1 Graphical summary of the stabilities of compounds with general composition $A_3M_2O_5Cu_2S_2$. predicted by Williamson and Scanlon. 38

3.2 Graphical summary of the computationally predicted optical band gap energies (E_g^{opt}) for the compositions ($A_3M_2O_5Cu_2S_2$) investigated. 40

3.3 Powder x-ray diffractogram for the observed prototype compound $Sr_3Sc_2O_5Cu_2S_2$. 42

3.4 Tauc plot for the prototype compound $Sr_3Sc_2O_5Cu_2S_2$ constructed from the collected raw diffuse reflectance data (inset). 43

3.5 Observed PXRD pattern for products from attempted synthesis of target compound with composition $Ca_3Al_2O_5Cu_2S_2$. 44

3.6 Polycrystalline powder synchrotron x-ray diffraction pattern of the sample with composition $Ba_3Sc_2O_5Cu_2S_2$. 46

3.7 Graphical representation of the data in *table 3.4* summarising the lattice parameters and key distances and angles, in terms of the electronic structure; and band-gap energies (see headings) for the prototype and newly synthesised compounds $A_3Sc_2O_5Cu_2S_2$, where A = Sr and Ba, respectively, as determined by various methods 47

3.8 Tauc plot for the compound $Ba_3Sc_2O_5Cu_2S_2$ constructed from the collected raw diffuse reflectance data (inset). 48

3.9 Observed PXRD pattern for products from attempted synthesis of target compound with composition $Sr_3Ga_2O_5Cu_2S_2$. 50

3.10 Observed PXRD patterns for products from reduced temperature (600 °C) attempted syntheses of target compound with composition $Sr_3Ga_2O_5Cu_2S_2$ for differing times (12 h, bottom; 100 h, top). 50

3.11 Observed PXRD pattern for products from attempted synthesis of target compound with composition $Sr_4Ga_2O_6Cu_2S_2$ previously reported in the literature 51

3.12 Tauc plot for the literature reported compound with composition $Sr_4Ga_2O_6Cu_2S_2$ constructed from the diffuse reflectance spectrum (inset) indicating the experimentally calculated band gap energy of 2.42 eV, as given by the point at which the linear fit (red) intercepts the abscissa. 51

3.13 Observed PXRD pattern for products from attempted synthesis of target compound with composition $Ca_3Sc_2O_5Cu_2S_2$. 53

3.14 Observed PXRD pattern for products from attempted synthesis of target compound with composition $Ca_3Ga_2O_5Cu_2S_2$. 53

3.15 Observed PXRD pattern for products from attempted synthesis of target compound with composition $Sr_3Al_2O_5Cu_2S_2$. 54

3.16 Observed PXRD pattern for products from attempted synthesis of target compound with composition $Ba_3Al_2O_5Cu_2S_2$. 54

3.17 Observed PXRD pattern for products from attempted synthesis of target compound with composition $Ba_3Ga_2O_5Cu_2S_2$. 55

4.1 Rietveld refined powder x-ray diffraction patterns for the compounds in the homologous series $Ba_xSr_{3-x}Sc_2O_5Cu_2S_2$, where x = 1 and 2 61

4.2 Summary of the trend in unit cell parameters $a=b$ (blue squares), c (red circles) and V (crossed squares), for the series of compounds $Ba_xSr_{3-x}Sc_2O_5Cu_2S_2$, where x = 0, 1, 2 and 3. 62

4.3 Representation of the initial crystallographic model used in the refinement of the mixed *A* compounds $Ba_xSr_{3-x}Sc_2O_5Cu_2S_2$ where x = 1 (left) and 2 (right) showing the expected even distribution of strontium (light green) and barium (dark green) across the *A* perovskite cation sites (green) and constraint of the elements to both occupy crystallographic site with the same coordinates. 64

4.4 Visual summary of refined fractional occupancies of *A* site cations barium (dark green) and strontium (light green) in the compounds $Ba_xSr_{3-x}Sc_2O_5Cu_2S_2$, where x = 1 and 2. Those of the end-members are shown for comparison. 65

4.5 Unit cell representation, shown mainly along *a*, of the crystal structure of the $A_3M_2O_5M'_2Ch_2$ family of quinary oxychalcogenide compounds crystallising into a lattice described by the tetragonal *I4/mmm* space group. 67

4.6 Graphical representation of the unit cell, viewed mainly along *a*, illustrating the idealised most stable distribution of strontium (light green) and barium (dark green) mixing across the *A* cation sites in the layered oxysulfide compounds $Ba_xSr_{3-x}Sc_2O_5Cu_2S_2$ where x = 1 (left) and 2 (right) as predicted by the Goldschmidt tolerance factor. 67

4.7 Illustration of the geometric parameters (lengths and angles) investigated in the conductive copper sulfide layers in the layered oxysulfide compounds studied here. 68

4.8 Graphical summary of selected interatomic distances and angles describing the geometry of the conductive copper sulfide layer in the mixed perovskite *A* cation compounds $Ba_xSr_{3-x}Sc_2O_5Cu_2S_2$, where x = 0, 1, 2 and 3. 69

4.9 Tauc plots calculated from the diffuse reflectance spectra (inset) for the mixed *A* homologous series of composition $Ba_xSr_{3-x}Sc_2O_5Cu_2S_2$, where x = 1 and 2. 72

4.10 Graphical plot of the observed band gap energies, as calculated from raw diffuse reflectance data via Tauc plots *(figure 4.9)*, for the mixed *A* cation compounds $Ba_xSr_{3-x}Sc_2O_5Cu_2S_2$, where x = 0, 1, 2 and 3. 72

4.11 Plot of peak width assigned to the instrument ($\beta_{Tot, Ins}$) as a function of detector angle (2θ) for the LaB_6 instrumental broadening standard. 75

4.12 Linearly-fitted Williamson-Hall plots made from the instrument-corrected, pseudo-Voigt-modelled observed diffraction profile peaks for the series of compounds $Ba_xSr_{3-x}Sc_2O_5Cu_2S_2$, where x = 0, 1, 2 and 3. 78

4.13 Graphical summary of the lattice strain and crystallite size values calculated from the gradients and *y*-intercepts of the linear fits to the data in the Williamson-Hall plots in *figure 4.12* 79

4.14 Repeat of the graphical representation of the unit cell viewed mainly along *a,* illustrating the idealised most stable distribution of strontium (light green) and barium (dark green) mixing across the *A* cation sites in the layered oxysulfide compounds $Ba_xSr_{3-x}Sc_2O_5Cu_2S_2$ where x = 1 (left) and 2 (right), as predicted by the Goldschmidt tolerance factor. 80

4.15 Williamson-Hall plots derived from powder x-ray diffraction profile peak widths of mixed *A* cation samples $Ba_xSr_{3-x}Sc_2O_5Cu_2S_2$, where x = 0, 1, 2, and 3. 82

4.16 Graphical summary of the inhomogeneous lattice strain and crystallite domain sizes calculated independently for lattice planes with vector oriented primarily in the *ab* and *c* unit cell directions, by separate linear fits to the corresponding sets in the Williamson-Halls plots in *figure 4.15,* and derived from the raw data provided in *table 4.5*..... 83

4.17 Scanning electron microscopy images taken of the compound $Sr_3Sc_2O_5Cu_2S_2$ at magnifications 12000 x (a), 8000 x (b), 15000 x (c) and 50000 x (d)..... 87

4.18 Scanning electron microscopy images taken of the compound $BaSr_2Sc_2O_5Cu_2S_2$ at magnifications 8000 x (a), 25000 x (b), 50000 x (c) and 15000 x (d)..... 87

4.19 Scanning electron microscopy images taken of the compound $Ba_2SrSc_2O_5Cu_2S_2$ at magnifications 10000 x (a), 10000 x (b), 25000 x (c) and 10000 x (d)..... 88

4.20 Scanning electron microscopy images taken of the compound $Ba_3Sc_2O_5Cu_2S_2$ at magnifications 10000 x (a), 25000 x (b), 12000 x (c) and 8000 x (d)..... 88

5.1 Observed PXRD pattern for products of the attempted synthesis of target compound $Ba_3Y_2O_5Cu_2S_2$. 95

5.2 Observed PXRD pattern for products of the attempted synthesis of target compound $Ba_3La_2O_5Cu_2S_2$. 95

5.3 Powder x-ray diffractogram for the observed compound $Ba_3In_2O_5Cu_2S_2$..... 96

5.4 Illustration of the geometric parameters (lengths and angles) investigated in the conductive copper sulfide layers in the 325-type layered oxysulfide compounds studied here. 96

5.5 Tauc plot for the compound $Ba_3In_2O_5Cu_2S_2$ constructed from the collected raw diffuse reflectance data (inset). 98

5.6 Powder x-ray diffractograms of samples with intended composition $Ba_3Sc_2O_5Cu_2Se_2$. 101

5.7 Powder x-ray diffractogram of phase-pure $Ba_3Sc_2O_5Cu_2Se_2$. 101

5.8 Graphical summary of the effect on the lattice parameters and distances and angles, of ionic substitution of sulfur for selenium on the chalcogen (*Ch*) site, in the two sets of analogous compounds with general formulae $Ba_3Sc_2O_5Cu_2Ch_2$ synthesised here (green squares) and the analogous $Sr_3Fe_2O_5Cu_2Ch_2$ reported in the literature....102

5.9 Tauc plot for the compound $Ba_3Sc_2O_5Cu_2Se_2$ constructed from the collected raw diffuse reflectance data (shown plotted inset). 105

5.10 Powder x-ray diffractogram of $Ba_3Y_2O_5Cu_2Se_2$. 106

5.11 Tauc plot constructed from raw diffuse reflectance data (inset) for the compound $Ba_3Y_2O_5Cu_2Se_2$, the solid red line shows a linear fit to the region of steepest gradient – its *x*-intercept marking the band gap energy at 2.67 eV. 107

5.12 Observed PXRD pattern for products of the attempted synthesis of target compound $Ba_3La_2O_5Cu_2Se_2$. 108

5.13 Powder x-ray diffractogram of $Ba_3In_2O_5Cu_2Se_2$. 110

5.14 Tauc plot of the compound $Ba_3In_2O_5Cu_2Se_2$ constructed from the raw diffuse reflectance spectrum (inset) collected from the sample. The solid red line shows a linear fit to the region of steepest gradient – its *x*-intercept marking the band gap energy at 1.31 eV. 110

5.15 Graphical summary of the lattice parameters and key distances and angles, in terms of the electronic structure, for the compounds $Ba_3M_2O_5Cu_2Se_2$, where *M* = Sc, In and Y. 111

5.16 Observed PXRD pattern for products from attempted syntheses at 800 °C for 12 h and 900 °C for 72 h of the target compound with composition $Ba_3Sc_2O_5Ag_2S_2$.114

5.17 Observed PXRD pattern for products from attempted synthesis at 800 °C for 12 h and 900 °C for 72 h of target compound with composition $Ba_3Y_2O_5Ag_2S_2$. 114

5.18 Observed PXRD pattern for products from attempted synthesis at 800 °C for 12 h and 900 °C for 72 h of target compound with composition $Ba_3In_2O_5Ag_2S_2$..... 115

5.19 Observed PXRD pattern for products from attempted synthesis at 800 °C for 12 h and 900 °C for 72 h of target compound with composition $Ba_3La_2O_5Ag_2S_2$. 115

5.20 Powder x-ray diffractogram of the compound $Ba_3Sc_2O_5Ag_2Se_2$ which crystallised into a structure with the tetragonal *I4/mmm* space group..... 116

5.21 Powder x-ray diffractogram of the compound $Ba_3In_2O_5Ag_2Se_2$ which crystallised into a structure with the tetragonal *I4/mmm* space group..... 117

5.22 Observed PXRD pattern for products from attempted synthesis of the target compound with composition $Ba_3La_2O_5Ag_2Se_2$..... 117

5.23 Graphical summary of the effect on the lattice parameters and distances and angles, of ionic substitution of copper for silver on the coinage metal (M') site, in the two sets of analogous compounds with general formulae $Ba_3Sc_2O_5M'_2Se_2$ (red squares) and $Ba_3In_2O_5M'_2Se_2$ (green circles), where M' = Cu and Ag synthesised here... 119

5.24 Tauc plot constructed from the raw diffuse reflectance data (inset) of the compound $Ba_3Sc_2O_5Ag_2Se_2$..... 120

5.25 Tauc plot constructed from the raw diffuse reflectance data (inset) of the compound $Ba_3In_2O_5Ag_2Se_2$..... 120

5.26 Summary of the geometric properties of the crystalline lattice and band gap energy 124

5.27 Summary of the geometric properties of the crystalline lattice and band gap energy for the compounds where *Ch* = S and Se in the conductive layer $[Cu_2Ch_2]^{2-}$ within the series of compounds $Ba_3M_2O_5Cu_2Ch_2$ each with a different perovskite layer in common, namely $[Ba_3Sc_2O_5]^{2+}$(red squares) and $[Ba_3In_2O_5]^{2+}$(green circles)..... 126

5.28 Summary of the geometric properties of the crystalline lattice and band gap energy for the compounds where *M'* = Cu and Ag in the conductive layer $[M'_2Se_2]^{2-}$ within the series of compounds $Ba_3M_2O_5M'_2Se_2$ with a different perovskite layer in common, namely $[Ba_3Sc_2O_5]^{2+}$ (red squares) and $[Ba_3In_2O_5]^{2+}$ (green circles)... 128

6.1 Powder x-ray diffractogram and Tauc plot (inset) of the newly observed doped compound $Na_{0.15}Sr_{2.85}Sc_2O_5Cu_2S_2$..... 135

6.2 Summary of the crystal structures of quinary layered perovskite oxychalcogenides. 137

Appendices

A 1 Powder x-ray diffraction patterns indicating the successful syntheses of the phase-pure alkali earth oxide precursors CaO (top), SrO (centre) and BaO (bottom). 146

A 2 Powder x-ray diffraction patterns indicating the successful syntheses of the phase-pure alkali earth sulfide precursors SrS (top) and BaS (bottom). 147

A 3 Powder x-ray diffraction patterns indicating the successful synthesis of the phase-pure precursor BaSe (top) and $BaSeO_4$ (bottom) from which it was synthesised.148

A 4 Powder x-ray diffraction pattern indicating the successful synthesis of the phase-pure precursor Na_2S.....149

A 5 'Ball-and-stick' (I) and 'space-filling' (II) representations of the generic perovskite, AMO_3, unit cell and the $[A_4O]^x$ square plane on the unit cell face (III) and at 0.5a (IV), as viewed along the cubic crystallographic axis. 163

DECLARATION OF AUTHORSHIP

I, Mr Gregory J Limburn, declare that this thesis and the work presented in it are my own and has been generated by me as the result of my own original research.

OXYCHALCOGENIDES FOR TRANSPARENT P-TYPE CONDUCTORS

I confirm that:

1. **This work was done wholly or mainly while in candidature for a research degree at this University;**
2. **Where any part of this thesis has previously been submitted for a degree or any other qualification at this University or any other institution, this has been clearly stated;**
3. **Where I have consulted the published work of others, this is always clearly attributed;**
4. **Where I have quoted from the work of others, the source is always given. With the exception of such quotations, this thesis is entirely my own work;**
5. **I have acknowledged all main sources of help;**
6. **Where the thesis is based on work done by myself jointly with others, I have made clear exactly what was done by others and what I have contributed myself;**
7. **Parts of this work have been published as:**

B. A. D. Williamson, G. J. Limburn, G. W. Watson, G. Hyett and D. O. Scanlon, *ChemRXiv*.

Signed:.....

Date: .....

Acknowledgements

The author would like to thank the undergraduate project students David Salazar-Marcano, Peter Bayliss, Nathaniel Davies and Mathew Stephens for conducting related projects and contributing to useful conversations and confirming the understanding of the behaviour and characteristics of these layered perovskite oxychalcogenides.

Grateful thanks are also extended to Chui Tang, Principal Beamline Scientist for I11, Diamond Light Source, and Dr Alexander Kulak, Materials Characterisation Specialist, University of Leeds, for collecting, on behalf of the author, synchrotron x-ray diffraction data and scanning-electron microscopy images, respectively. Gratitude is also expressed towards Dr Gavin Stenning, Materials Characterisation Laboratory Manager, ISIS Neutron and Muon Source, for access to the laboratory and to Dr Robert Palgrave, XPS Facility Manager, UCL, for collection of preliminary VB-XPS data.

Discussions during progression and *viva voce* examinations with Profs Gillian Reid, Andrew Hector and Richard Walton, and Dr Darren Bradshaw were greatly appreciated. A special thanks is given to Dr Benjamin Williamson and Prof David Scanlon for their computational analysis which underpinned the project and in particular to Dr Geoffrey Hyett for the PhD opportunity, project proposal, advice and support, both personal and technical, given during this candidature.

The personal and professional support of Prof David Read and Dr Simon Gerrard in providing teaching and outreach opportunities and experience critical to the desired career path of the author is gratefully acknowledged. Personal thanks are also given to the members of the Hyett group, past and present; Drs Samuel Cosham and Karl Kaye, Antonio Iborra Torres and Iona Doig, for their support, company and friendship.

Finally, gratitude is shown to the Limburn, Young and Peterson families and, in particular, Hilary Peterson, without all of whom the author would not have been able to undertake, nor have been in a position to complete, this PhD project.

List of Abbreviations

AZO	Aluminium zinc oxide
CBM	Conduction band minimum
CMVB	Chemical modulation of the valence band
DFT	Density functional theory
EXPGUI	Experimental Graphical User Interface
FTO	Fluorine tin oxide
FWHM	Full-width at half-maximum height
GSAS	General Structure Analysis Software
HSAB	Hard-soft acid-base theory
IBM	International Business Machines
ICSD	Inorganic Crystal Structure Database
IR	Infra-red
ITO	Indium tin oxide
LCAO	Linear combination of atomic orbitals
LCD	Liquid crystal display
LOF	Libbey-Owens-Ford Glass Co
MO	Molecular orbital
NFE	Nearly-free electron
NIST	National Institute of Standards and Technology
PPG	Pittsburgh Plate Glass Co
PTFE	Polytetrafluoroethene
PV	Photovoltaic
PXRD	Polycrystalline/powder x-ray diffraction
SEM	Scanning-electron microscopy

SI	Supplementary/supporting information
TCO	Transparent conducting oxide
UCL	University College London
UV	Ultra-violet
VBM	Valence band maximum
VB-XPS	Valence band x-ray photoelectron spectroscopy
VESTA	Visualization for Electronic and Structural Analysis

Chapter 1 Introduction

1.1 Transparent Conductors | Development and Applications

Transparent conductors (TCs) are materials which simultaneously possess optical transparency and electrical conductivity. Early transparent conductors were made by depositing thin films of high-conductivity metals such as silver and platinum.[1] The earliest example of a transparent conducting oxide (TCO) is CdO.[2] The compound was produced upon oxidation of pure cadmium films being investigated for the same purpose. The films were of relatively low transparency (40 %) with the intrinsic n-type conductivity observed, resulting from the presence of compensating cadmium interstitial point defects, which increased the free electron carrier concentration to 10^{21} cm^{-3}. However, the toxicity of the carcinogenic cadmium compound was a major barrier to commercialisation – it was already banned from some applications at the time.[3] Dopant elements such as tin and indium, were employed to improve the properties of these films. However, it was later realised that the oxides of the dopant metals were better structural prototypes for effective TCs.

For example, tin oxide, SnO_2, proved less toxic, cheaper and showed greater chemical stability than its predecessor, CdO, and, as such, was the first transparent conducting oxide to find commercial application.[4] Known to be a TCO since 1942, a patent was taken out on chlorine-doped SnO_2 thin films by McMaster of the Libbey-Owens-Ford (LOF) Glass Company in 1947.[5,6] Today's widely used fluorine-doped tin oxide (FTO), $F:SnO_2$, was later developed and protected by the competing Pittsburgh Plate Glass (PPG) Company with continued commercial interest in the development of doped forms of the metal oxide shown by Bell Telephone Laboratories and IBM.[7–9]

Indium oxide, In_2O_3, was also being commercially developed as a candidate TCO at the same time.[10] Its use in high-performance applications eclipsed that of doped SnO_2, owing to its improved conductivity. In 1972 Fraser *et al.* of the Bell Labs reported an observed conductivity of 5.65 kS cm^{-1} for a 9 at. % tin-doped thin film sample, with simultaneous 83 % light transmission at 500 nm.[11] High-quality films with these conductivities were routinely produced until the early nineties. Technological developments in flat-panel display screens required the use of thinner electrodes which in turn, demanded higher conductivity from the material. It was known that the resistivity of such films was proportional to the sputtering voltage used during the deposition procedure.[12] Shigesato *et al.* used a low-voltage DC magnetron sputter-coating technique to synthesise films of 10 at. % indium tin oxide (ITO), $Sn:In_2O_3$, with conductivity as high as 7.40 kS cm^{-1}. Today, the conductivity of indium oxide-based films has reached 14.9 kS cm^{-1} with reported mobility as high as 250 cm^2 V^{-1} s^{-1} for 100 nm thick films of 2 at. % $Mo:In_2O_3$.[13] Its average visible transmittance of 87 % accompanied by the highest known mobility, makes doped indium oxide a widely used TC today, and the benchmark for future development.[14]

Subsequent work on n-type TCs included the alloying of combinations of the established materials in an effort to improve their conductivity and transparency, while reducing the content of the rare and costly indium.[15] ZnO-based materials were also investigated. Their potential came not from their conductivity, which could not compete with that of the doped indium oxide compounds, but from their high transparency, a feature that resulted in their widespread use in current photovoltaics, and above all, their ability to be doped p-type.[16,17]

1.2 Applications

Materials which were developed to exhibit electrical conductivity and visible-light transparency were first applied in a militarian context as anti-frosting coatings on aircraft windows.[1] Their partial conductivity allowed resistive heating, preventing condensation and ice formation, while their transparency was crucial in maintaining visibility. This combination of properties also enabled application in the same aircraft as anti-static coatings for cockpit instruments and dials.

Transparent conductors are still used as anti-frosting coatings today in the transport, and food and drink sectors, for example on the windscreens of large vehicles, such as aircraft and trains, and drinks refrigerators in the hospitality industry. A subsidiary of the Ford motor company owns a patent for similar coatings designed for automobile windows, however, these have not been commercialised, partially owing to the high energy needed to supply the required voltages.[18]

Some transparent conducting materials are doped to such an extent that the plasma frequency *(section 1.3.2)* borders on the low-energy end of the visible spectrum, causing high reflectivity in the infra-red (IR) region. This IR reflectivity makes transparent conductors applicable as thermally efficient materials where visible transparency is required, for example, as coatings for glazing in the built environment or on food oven doors. In the case of vending refrigerators, these materials serve two purposes: frost prevention and energy conservation.

In addition to coatings, the other area of application for transparent conducting materials is as transparent electrodes in optoelectronic devices, such as, photovoltaic (PV) cells, touchscreens and displays.[19] Currently, n-type inorganic oxide transparent conductors, ITO in particular, act as windows in PV cells which allow the transmission of visible light onto the absorber layer, and collection and conduction of the charge carriers produced by the photoexcitation.[20] In liquid-crystal displays (LCDs), the TC acts again as a transparent window; allowing light to be emitted from the device, whilst applying the required voltage across the liquid-crystal cell.

In touchscreens the transparent conductors form the plates of the capacitors, the voltage gradient across which is registered by the device as a touch input. The capacitive layers are overlaid across a conventional display, wherein their visible transparency is imperative.

1.3 Design Considerations for Transparent Conductor Development

In designing novel TC materials, it is of obvious importance to determine the effects of the composition and structure of a compound, on its optoelectronic properties; namely its transmittance of light in the visible range, *T*, and electrical conductivity, *σ*. All light incident on a sample must be accounted for by one or more of the phenomena of absorption, reflection and transmission, as is summarised in *equation 1.1*. It follows, therefore, that in order to maximise transparency (determined by the transmission), the contributions from absorption and reflection must be minimised. An idealised qualitative spectrum for a visibly transparent material is shown in *figure 1.1*. It can be seen that it is necessary for a desirably transparent material, to exhibit an absorption *(green)* onset at energies above those of visible light and for the reflectance *(red)* to have subsided at lower energies; thus, yielding high transmittance *(blue)* throughout the visible region.

$$A + R + T = 1 \qquad 1.1$$

A – Absorption
R – Reflection
T – Transmission

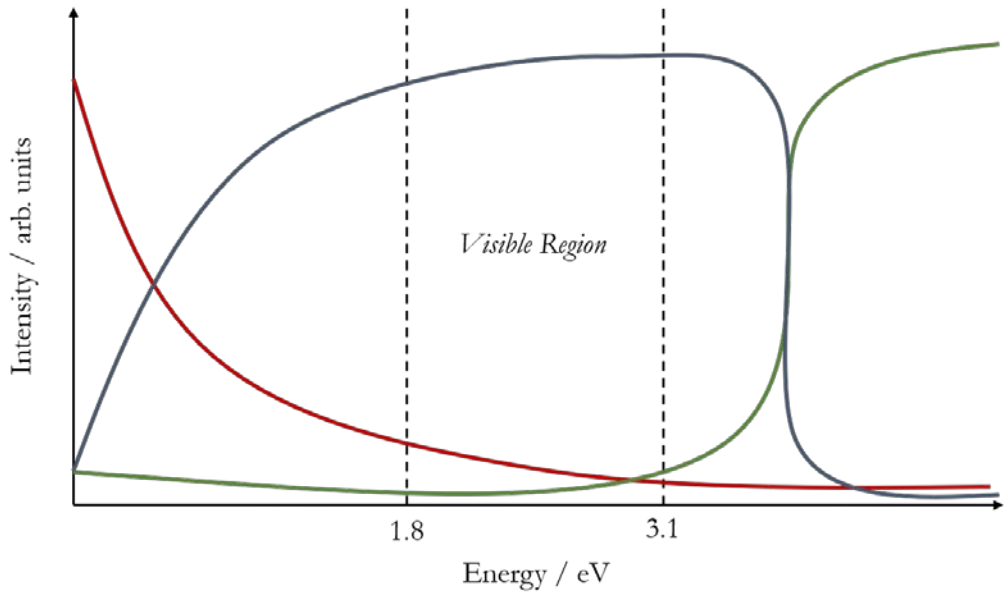

Figure 1.1 *Sketch of idealised absorption (green), reflection (red) and transmission (blue) spectra for a visibly transparent material. The region enclosed by the black dashed lines represents the energy range of visible light photons.*

1.3.1 Absorption

Absorption of photons by a sample, occurs at energies corresponding to allowed electronic transitions between states described by its electronic structure. In a simple semiconductor, electronic states in the valence band are fully occupied and those in the conduction band unoccupied. The lowest possible energy of electronic transition, disregarding any selection rules, is given by the energy separation between the bands, known as the band gap. The onset of absorption occurs as the energy exceeds this value and rises sharply beyond. In order to support the visible transparency of a sample, its crystal structure, and therefore electronic band structure, is engineered in such a way as to ensure the band gap is at a greater energy than the maximum energy of visible light photons, 3.1 eV (corresponding to a wavelength of 400 nm). This ensures that the absorption edge, the point in the spectrum where the absorption rises rapidly, lies beyond the energy region spanned by visible light photons *(black dashed lines)*, as illustrated in *figure 1.1*.

1.3.2 Reflection

Reflection of incident electromagnetic radiation by a material occurs when photons arriving at the surface are effectively 'screened' by the conduction electrons present and prevented from penetrating the sample. This occurs more readily at low incident frequency (energy) when the displacement of conduction electrons in a sample by the incoming electromagnetic wave, results in coordinated oscillations of the conduction electrons and reemission of radiation out of the surface, that is detected as reflected light. This occurs when the incident frequency is below the plasma frequency and the reemission/reflection is possible within the period of the incident radiation. Above the plasma frequency, the displacement of the conduction electrons does not occur within the period of the incident wave and it passes through unscreened. In assessing and designing candidate TCs, the plasma frequency is required to be lower than that of the minimum frequency of visible light radiation. The plasma frequency can be calculated as shown in *equation 1.2*. A derivation of this equation is given in *appendix A*. It can be seen that the greater the charge carrier number density, the higher the plasma frequency. For metals, with high electron densities, this explains why reflection occurs throughout the visible region. The plasma frequency lies in the high-frequency UV range, resulting in the screening of all lower frequency visible light radiation. For example, silver, from which many mirrors are made, has a plasma energy of $\hbar\omega_p$ = 8.9 eV.[21]

$$\omega_p = \sqrt{\frac{n\, e^2}{\varepsilon_0\, m}} \qquad 1.2$$

ω_p – plasma frequency
n – charge carrier number density
e – fundamental charge
ε_0 – vacuum permittivity
m – mass of charge carrier

1.3.3 Electrical Conductivity

The observed macroscopic electrical conductivity, σ, of a medium is defined as the degree to which it permits the flow of electric charge (given by the current density, *j*) in response to an applied electric field, *E*. It can be described as the proportionality constant between the two, as shown in *equation 1.3*.

It is shown in *appendix B*, that *equation 1.3* can be used to derive a more telling expression for the conductivity: *equation 1.4*. From this, it can be seen that the bulk conductivity, σ, depends on the number of charge carriers, *n*, the mean free time between their collisions or scattering events, τ, and their mass, *m*. The charge carrier density is primarily controlled in semiconductors by extrinsic doping. Similarly, the mean free time was expected be majorly affected by the microstructure of the crystallites in solid materials and was therefore, deemed important, along with the charge carrier mass. In order to predict the conductivity in these materials and to design new candidates, it was important to understand how the composition and crystalline structures affected the mass of the charge carriers. In order to do this, it was necessary to consider the electronic structure of solid-state crystalline materials. This is the subject of the following section.

$$j = \sigma E \tag{1.3}$$

j - current density
σ - conductivity
E - electric field strength

$$\sigma = \frac{n e^2 \tau}{m} \tag{1.4}$$

σ - conductivity
n - volumetric number density of charge carriers
e - fundamental charge
τ - mean free time
m - mass of charge carrier

1.3.4 Band Theory

Band Theory is a method used for describing and interpreting the fundamental electronic structures of the crystalline solid candidate materials studied in this project. The band theory of electronic structure in solids is commonly introduced to chemists with respect to its molecular analogue, molecular orbital (MO) theory. Taking the diatomic hydrogen molecule as an example, the formation of the two observed electronic energy levels can be understood by the overlap of the contributing *s* orbitals from each constituent hydrogen atom. The interaction of the component atomic orbitals upon spatial overlap, results in the formation of molecular orbitals with a difference in energy. The loss of degeneracy in combining molecular orbitals is described by the Pauli exclusion principle.

The qualitative idea of combining constituent atomic orbitals to form larger, 'delocalised' molecular orbitals can be extended to solids. These can be thought of as very large, periodically repeating arrays of atoms, each with their own atomic orbitals. These atomic orbitals interact with the same loss of degeneracy, resulting in the formation of crystal orbitals, analogous to lower energy bonding and higher energy antibonding molecular orbitals. The result for very large numbers of constituent atoms, as are found in macroscopic solid samples, is the formation of a series of orbitals separated, yet very closely spaced in energy. These are approximated to continua, referred to as bands, and give the basis for the band structure interpretation.

In the ground state, electrons occupy the orbitals in order of increasing energy, as described by the Aufbau principle. The equilibrium energy between the occupied and unoccupied states, or chemical potential of the system, is given by the Fermi energy, E_F. The separation between the highest energy bands occupied in the ground state and the lowest energy unoccupied bands, if distinct as is the case in semiconductors and insulators, is known as the band gap, E_g.

The size of the band gap, if present, and therefore the thermal accessibility of these states, is what dictates the conductivities of materials. For example, metals show no band gap. In the ground state the Fermi level lies within the energy range of a partially occupied band. Thermal population of electrons into delocalised states is easily possible at room temperature and electrical conductivity readily observed. On the other hand, semiconductors and insulators possess a band gap. Their Fermi energy is positioned below the minimum energy of the conduction band (CBM). In their ground states, these materials do not conduct electricity. The broad division between the two depends on the size of the band gap. Semiconductors have band gaps typically less than 4 eV whereas those of insulators are usually larger. The relatively small band gaps in semiconductors mean that it is possible that electrons can be excited thermally or by absorption of electromagnetic radiation, to energies of partially occupied states above the CBM and, hence, carry charge and conduct electricity.

At room temperature, metals and semiconductors will both have electrons in thermally excited states which may allow observable electrical conductivity. Semiconductors typically possess charge carrier concentrations several orders of magnitude lower than those of metals, in addition to lower mobilities. Therefore, their conductivities are also lower. Semiconductors can be extrinsically doped to increase their charge carrier concentration. When this occurs to such a degree that the Fermi energy lies within the conduction band, the semiconductor is said to be 'degenerately' doped and shows metallic conductive behaviour.

1.3.4.1 Linear Combination of Atomic Orbitals

In building a picture of the electronic band structure for a particular atomic arrangement, the linear combination of atomic orbitals (LCAO) is used. This is an approximation used to combine the individual atomic orbitals described by wavefunctions, to derive a quantitative picture of the band structure. It produces an expression for the energy as a function of the wave number, E_k, in terms of α and β, representing the energy of the constituent atomic orbitals and the extent of overlap between neighbouring orbitals, respectively *(eqn. 1.5)*.[22] In order to directly relate the 'sub-microscopic' properties of orbital energy and overlap extent to the macroscopic property of conductivity, required to evaluate the expected electronic performance, an extension to this approach was required.

$$E_{k,\,LCAO} \cong (\alpha + 2\beta) - \beta(ka)^2 \qquad 1.5$$

$E_{k,\,LCAO}$ - energy as a function of wave number
α - self-overlap integral/ energy of atomic orbitals
β - overlap integral of neighbouring atomic orbitals
k - wave number
a - lattice spacing

1.3.4.2 Nearly-Free Electron Model

The nearly-free electron (NFE) model is used to link to the band structure produced by the LCAO to the conductivity.[22] It is a method wherein the wave function for free particles (electrons) is used and the effect of a periodic potential, described by the host lattice structure, is applied to generate a band structure model. The advantage of modelling the band structure in this way is that the energy is described, not in terms of the individual orbitals, but in terms of the mass of the particles in the free gas, which is more easily related to the conductivity.

The nearly-free model of electron dynamics models the behaviour of electrons in crystalline solids by considering the effect of a periodic electrostatic potential, *i.e.* the cationic lattice, on electrons modelled as a free electron or 'Fermi gas'. Electrons considered to be unbound in a free electron gas can be represented by the wave function in *equation 1.6* overleaf. This is written in terms of the wave number which, as *equation 1.7* shows, is inversely related to the wavelength. Using *de Broglie's* relation *(eqn. 1.8)*, it is shown in *equation 1.9*, that the wave number is proportional to the momentum of the charge carrier.

The energies of the electrons in a solid are of prime importance when considering conductivity. The total energy, of the electron in this case, can be decomposed into contributions from kinetic energy and potential energy. Substituting *equation 1.9* for momentum into the *equation 1.10* for kinetic energy gives an expression *(eqn. 1.11)* for the total energy within a constant potential, V_0, in terms of the wave number, k. The band structure is described by this energy dispersion in reciprocal space and adopts a parabolic form owing to the energy dependence on the square of the wave number.

$$\psi_x = \exp(i\,\mathrm{k}x) = \cos(\mathrm{k}x) + i\sin(\mathrm{k}x) \quad (1.6)$$

ψ_x - wave function
i - square root of negative one
k - wave number
x - position along one dimensional axis

$$\mathrm{k} = \frac{2\pi}{\lambda} \quad (1.7)$$

λ - wavelength of electron

$$\mathrm{p} = \frac{\mathrm{h}}{\lambda} \quad (1.8)$$

p - momentum
h - the Planck constant

$$\mathrm{p} = \hbar\mathrm{k} \quad (1.9)$$

ħ - the reduced Planck constant

$$\mathrm{T} = \frac{\mathrm{p}^2}{2\,\mathrm{m}} \quad (1.10)$$

T - kinetic energy
m - mass

$$\mathrm{E}_{\mathbf{k},\,\mathrm{NFE}} = \frac{(\hbar\mathrm{k})^2}{2\mathrm{m}} + \mathrm{V}_0 \quad (1.11)$$

E - energy as a function of wavenumber

1.3.4.3 Combination of Models and the Concept of Effective Mass

It has been shown that the energy function in *k*-space or band structure can be modelled using two different approaches, namely from the LCAO or the NFE model. The first is known as a 'bottom up' approach as the energy function is calculated from the wavefunctions of the constituent atomic orbitals. The 'top down' approach of the nearly-free electron model, derives the energy distribution in terms of the wavenumber of a free electron in constant potential.

In order to relate these differing models, the electron mass constant in the NFE model is treated as a variable, the effective mass, *m**, and permitted to vary to achieve a fit between the functions calculated by the two different routes. Once equivalence is achieved, the two functions can be equated and the integrals from the LCAO related to the effective mass and, therefore, the optoelectronic properties.

The expressions from *equations 1.5 and 1.11* for the energy distribution in *k*-space from the LCAO and the NFE model are repeated in *equations 1.12 and 1.13,* respectively. The two kinetic energy terms can be equated, if the mass is treated as a variable, as in *equation 1.14*, and rearranged to yield an expression for the variable, 'effective' mass *(eqn. 1.15)*.

$$E_{k,\,LCAO} \cong (\alpha + 2\beta) - \beta(ka)^2 \tag{1.12}$$

E_k - energy as a function of wave number
α - self-overlap integral/ energy of atomic orbitals
β - neighbouring atomic orbital overlap integral
k - wave number
a - lattice spacing

$$E_{k,\,NFE} = \frac{(\hbar k)^2}{2m} + V_0 \tag{1.13}$$

E_k - energy as a function of wavenumber
$\hbar$ - the reduced Planck constant
m* - effective mass variable

$$\frac{(\hbar k)^2}{2m^*} = -\beta(ka)^2 \tag{1.14}$$

$$m^* = -\frac{\hbar^2}{2\beta a^2} \tag{1.15}$$

1.3.5 Summary

By combining these two band structure models, the effective charge carrier mass can be derived from the wavefunctions of the constituent atoms. This can then be related to the optoelectronic properties via the conductivity and plasma frequency, as shown in *equations 1.16 and 1.17*, respectively. It can be seen that the properties desirable for conductivity, including high charge carrier density and orbital overlap of atoms contributing to the relevant band edge state, also increase the plasma frequency which must be kept below the visible region to prevent reflectivity. Understanding these factors, which determine the properties affecting the often-competing optoelectronic behaviours, enables appreciation of the rarity of, and difficulty in, making materials of this type but, most importantly, can guide the investigation into compounds which exhibit the delicate balance of attributes required.

$$\sigma \propto n \tau \beta a^2 \qquad 1.16$$

σ - conductivity
n - charge carrier density
τ - mean free time
β - overlap integral
a - lattice parameter

$$\omega_p \propto \sqrt{n \beta a^2} \qquad 1.17$$

ω_p - plasma frequency

1.4 Potential Applications and Development of Transparent p-Type Conductors

The realisation of a transparent p-type conductor with electrical conductivity and visible light transmission comparable to that of the currently commercialised n-type counterparts, could increase the performance of current devices and allow the fabrication of novel architectures and apparatus. The use of wide-gap p-type hole transport layers in photovoltaic cells could alleviate traditional design rules, allow for a wider range of absorber materials to be used and permit the construction of more efficient devices.[23,24] The presence of a p-type transparent electrode could also pave the way to visibly transparent solar cells, that would harvest the energy of UV and IR light. This could result in the manufacture of energy harvesting windows which, by enabling utilisation of the side of high-rise buildings, could significantly increase the urban area over which solar energy could be collected.[25] Transparent p-type conductors could also be applied to the fabrication of fully transparent p-n junctions that are fundamental to diodes and transistors, the vital components in modern electronic devices. These could lead to 'invisible' circuitry or to transparent 'smart glass' displays being made: apparatus with application in the security of valuable display items, or in glasses and windscreens, in which images are overlaid upon the natural visual field.[26,27]

The first step in trying to synthesise these desirable high-performance p-type analogues, was to introduce p-type dopants into the existing intrinsically n-type TCs. One of the earliest 'transparent' p-type semiconductors to be synthesised in thin film form was ZnO:N.[28] Monovalent cation doping of copper and silver into zinc oxide, ZnO, was also attempted with little success. The solid-solubility of the dopants in the host lattice was low, and defect compensation resulted in low charge carrier concentration of $\approx 10^{8}$ cm^{-3}, *c.f.* $\approx 10^{21}$ cm^{-3} in ITO.[29,30]

Zinc oxide has since been doped with arsenic and shown to exhibit significantly higher carrier concentrations ($\approx 10^{20}$ cm^{-3}) and, therefore, conductivities of up to 3.45 $x10^{2}$ S cm^{-1}.[31] The benefit of p-type doping current n-type TCs is that, by having the same host crystal structure, the two oppositely doped semiconductors can be grown in a single chemically bonded layered structure, on top of one another, enabling the fabrication of p-n junction components. This was first demonstrated by Ryu *et al.* whereby p-type arsenic-doped zinc oxide films were deposited on top of the n-type material Al:ZnO (AZO), to form the first transparent p-n junction that demonstrated non-ohmic, current rectifying behaviour.[17] While this proof-of-concept demonstration of a transparent p-n homojunction was a milestone in the field, its development was still fundamentally limited.

The main issue with 'reverse' doping known n-type TCs lies in their band structure. For n-type semiconductors, as are all of the commercial TCs, conduction occurs in the conduction band by donor-doped electrons. The CBM of the current n-types comprise bands formed primarily by the overlap of empty metal ns^{0} orbitals.[32] These are high in energy and diffuse, promoting good overlap, hybridisation, mobility and, therefore, n-type conductivity.

On the other hand, synthesis of high-conductivity p-type analogues required the introduction of acceptor defects that create positive hole charge carriers at the VBM, and facilitation of their mobility within. The VBs of current n-type oxides consist of overlapping 2*p* orbitals of the highly electronegative oxygen atoms. As a result, the orbitals are compact and highly localised. The poor orbital hybridisation and high electrostatic potential of the lattice, results in low mobility of p-type charge carriers and poor conductivity. Without alteration of the fundamental band structure by an overhaul of material design, including composition and crystal structure, p-type conductivity in the current compounds is inherently limited.

In a letter to Nature published in 1997, Kawazoe *et al.* of the Hosono group, reported on the synthesis of thin films of the compound $AlCuO_2$ with p-type conductivity of 1 S cm^{-1} and high mobility of 10 cm^2 V^{-1} s^{-1}, previously unsurpassed for a transparent sample.[33] This compound possessed $3d^{10}$ Cu(I) ions hybridising with oxygen 2*p* orbitals with tetrahedral coordination at the VBM, interspersed with aluminium oxide layers. The compound $AlCuO_2$ possessed the general delafossite crystal structure of the eponymous mineral, $CaFeO_2$, discovered in Ekaterinburg, Russia by Charles Friedel in 1873.[34] The mineral was named in honour of Gabriel Delafosse, the then Professor of Minerology at the Sorbonne, Paris.[35] Its structure is represented in *figure 1.2*. The compound consisted of O-*M*-O linear dumbbell-like moieties *(shown with 'sticks')*, with the oxygen atoms being tetrahedrally coordinated with the *M* atom and three *A* atoms. The intervening *A*O layers were formed of corner-shared, tilted [AO_6] octahedra *(shown shaded in grey)*.

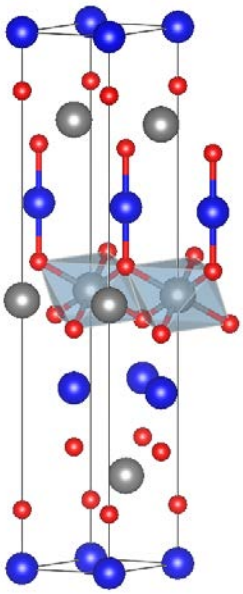

Figure 1.2 *Extended unit cell (grey lines) crystal structure of a generic delafossite oxide mineral AMO_2. Colour key: grey - A, blue - M and red - O. Crystallographic representations, such as this, included throughout this thesis were created with the Visualization for Electronic and Structural Analysis (VESTA) software programme.*[36]

The success in achieving increased p-type mobility and conductivity in a transparent sample was rationalised by a series of structural and compositional features of $CuAlO_2$. These were summarised by Kawazoe *et al.* as steps in a procedure called "chemical modulation of the valance band" (CMVB). These were reported as 'design rules' to guide the further development of materials with these desirable optoelectronic properties and are summarised here:

1. Occupancy of *d*-orbitals of transition metals used.

The energies of intra-band *d-d* transitions frequently coincide with those of visible light photons, giving the wide range of observed colours of transition metal compounds. The use of the fully occupied $3d^{10}$ copper (I) ions in $CuAlO_2$ precluded this.

2. Energy of *d*-orbitals of transition metals used.

The energy of the copper 3*d* orbitals were similar to those of the oxygen 2*p* orbitals. This increased the hybridisation, dispersion and charge carrier mobility within the VB, to which these electronic states contributed.

3. Coordination geometry in target crystal structure.

The tetrahedral geometry of the oxide ions was shown to be preferable. Their crystal-field splitting produced no non-bonding orbitals which reduced the localisation of the charge carriers and promoted their conductivity.

4. Dimensionality of target crystal structure.

As a result of the layers of intervening aluminium, the crystal structure of $CuAlO_2$ served to reduce the hybridisation between the copper and oxygen in the *c* direction, and therefore limited the curvature of the VB and maintained a wide band gap.

The groundwork laid by Kawazoe provoked investigations into the p-type doping and thin film fabrication of this and related compounds. The conductivities were improved by alteration of the host oxide composition and subvalent doping at the *M* sites. These are summarised in *table 1.1* overleaf.

Table 1.1 *Summary of reported properties of delafossite transparent p-type conducting thin films. The rows are arranged in order of decreasing conductivity. *n/a = data not applicable. *n/r = data not reported.*

Composition *M* ($CuMO_2$)	Dopant	Dopant Conc. / at. %	Conductivity / S cm^{-1}	Carrier Conc. / cm^{-3}	Mobility / $cm^2 V^{-1} s^{-1}$	Band Gap / eV	Ref/s
Cr	Mg	5	2.2×10^2	*n/r**	10^{-1}	3.1	37
Cr	Undoped	*n/a**	1×10^1	*n/r*	*n/r*	*n/r*	37
Sc	Undoped	*n/a*	3×10^1	*n/r*	*n/r*	3.3	38
B	Undoped	*n/a*	1.65×10^0	10^{17}	100	4.5	39
Al	Undoped	*n/a*	1×10^0	1.3×10^{17}	10	3.5	33
Y	Ca	2	1×10^0	*n/r*	<1	3.5	40
Y	undoped	*n/a*	2×10^{-2}	*n/r*	<1	3.5	40

In 2000, Ueda *et al.*, again of the Hosono group, first reported on the use of the known oxychalcogenide compound LaCuOS for transparent optoelectronic applications.[41] In its solid crystalline form, it exhibited a structure layered at the unit cell level consisting of [LaO] and [CuS] moieties of the litharge and anti-litharge structures, respectively *(fig. 1.3)*. The two-dimensional layers consisted of $[CuS_4]$ and $[La_4O]$ tetrahedra, shown as the *blue* and *red polyhedra*, respectively. The natural segregation into these layers can be rationalised by the relative so-called litho- and chalcophilicity of the lanthanum and copper, respectively.

A computational review of the electronic structure of the compound showed that it was indeed a wide-gap material with a band-gap energy of 3.1 eV, and that the CBM and VBM consisted of copper 4*s*, and hybridised copper 3*d* and sulfur 3*p* states, respectively.[42] This study confirmed that LaCuOS was a promising candidate for a wide-gap high-mobility p-type conductor. The tetrahedral copper sulfide layer showed good orbital overlap, large extent of hybridisation, high dispersion and good mobility. The layered structure served to reduce overlap between neighbouring copper atoms and, therefore their vacant 4*s* orbitals. As these composed the CBM, the layering had the effect of reducing the width of the CB and increasing the band gap, relative to an analogous three-dimensional structure, *e.g.* Cu_2S.

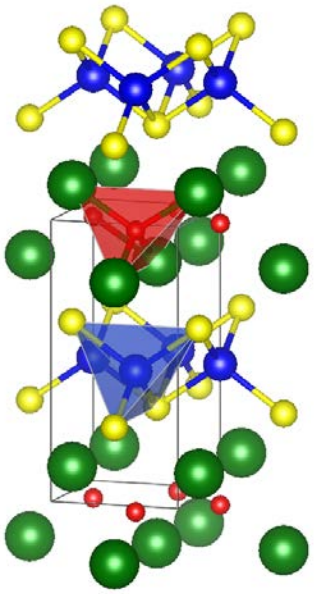

Figure 1.3 *Extended unit cell (grey lines) structure of the layered oxychalcogenide compound LaCuOS Colour key: green – La, red – O, blue – Cu and yellow – S.*

The report on this material in the context of transparent p-type conductivity, sparked increased research activity in this area over the following years. Dopants were incorporated into the material, as in the original study, and their concentration varied, along with the synthetic conditions. Post-annealing of the thin film samples, synthesised by radio-frequency sputtering, improved the observed conductivity by two orders of magnitude.[43] The substitution of sulfur for selenium showed an increase in conductivity for magnesium-doped samples of nearly a further two orders of magnitude to 910 S cm^{-1}, for epitaxial thin films.[44] However, a decrease in the band gap was also observed as a result of increased hybridisation and widening of the VBM. A summary of the properties of the LaCuOS-based thin films, developed as a result of the early work by Hiramatsu, is given in *table 1.2*.

*Table 1.2 Summary of the properties of LaCuOS-based thin films investigated for transparent p-type conductivity. The rows are arranged in order of decreasing conductivity. *n/a = data not applicable. *n/r = data not reported.*

Composition *Ch* (LaOCu*Ch*)	**Dopant**	**Dopant Conc. / at. %**	**Conductivity / S cm^{-1}**	**Carrier Conc. / cm^{-3}**	**Mobility / cm^2 V^{-1} s^{-1}**	**Band Gap / eV**	**Form**	**Thickness / nm**	**Ref./s**
Se	Mg	20	9.1 x10^2	1.7 x10^{21}	3.4	≈ 2.8	Epitaxial	40	[44]
Se	Mg	20	1.4 x10^2	2.2 x10^{20}	4	2.8	Epitaxial	40	[45]
Se	Undoped	*n/a*	2.4 x10^1	≈ 10^{19}	8	*n/r*	Polycrystalline	≈ 150	[45]
S	Sr	3	2 x10^1	2.7 x10^{20}	0.47	≈ 3.1	Polycrystalline	≈ 150	[43,46]
S	Sr	5	2.6 x10^{-1}	*n/r*	*n/r*	3.1	Polycrystalline	130	[41]
S	Undoped	*n/a*	1.2 x10^{-2}	*n/r*	*n/r*	3.1	Polycrystalline	200	[41]
S	Undoped	*n/a*	6.4 x10^{-5}	≈ 10^{15}	0.2	≈ 3.1	Polycrystalline	≈ 150	[43,46]

Liu *et al.* extended the chalcogen substitution of sulfur in LaCuOS to include tellurium. LaCuOTe was synthesised in polycrystalline powder form, along with the original LaCuOS for comparison.[47] The optoelectronic properties of the samples are summarised in *table 1.3*. The telluride, as with the selenide analogue, exhibited an expected decrease in band gap energy compared to that of the sulfide. The chalcogen n*p* orbitals increased in energy and hybridised with the copper to a greater extent. This had the effect of increasing the energy and width of the VB at the expense of the band gap. However, the telluride analogue exhibited a high mobility of ≈ 80 $cm^2\ V^{-1}\ s^{-1}$, an increase in intrinsic carrier concentration by two orders of magnitude, and a resultant 10^3 increase in conductivity.

Table 1.3 *Summary of the optoelectronic properties of bulk polycrystalline powder samples of layered oxychalcogenides investigated by Liu et al. for potential application as p-type transparent conductors. *n/r = data not reported.*

Composition *Ch* (LaOCu*Ch*)	**Conductivity / S cm^{-1}**	**Carrier Conc. / cm^{-3}**	**Mobility / $cm^2\ V^{-1}\ s^{-1}$**	**Band Gap / eV**	**Ref.**
LaCuOSe	2.4	10^{19}	8	2.8	[45]
LaCuOTe	1.65	1.3×10^{17}	80.6	2.31	[47]
LaCuOS	4.5×10^{-3}	3×10^{15}	*n/r*	3.1	[47]

1.5 Layered Perovskite Oxychalcogenides

The inclusion of tellurium proved promising in increasing the conductivity of the LaCuO*Ch* p-type semiconductors, however, this came at the expense of transparency. In an attempt to maintain the wide band gap, later that year, Liu *et al.* investigated the more complex layered oxysulfide, "$[Cu_2S_2][Sr_3Sc_2O_5]$" .*, already reported regarding its potential superconductivity.[48,49]

This compound was an example of a quinary layered perovskite oxychalcogenide. It consisted of perovskite- and litharge-like building blocks alternating in the *c* unit cell direction, the direction of asymmetry in the tetragonal litharge structural building block. As a result, an overall tetragonal symmetry was exhibited. The 'composite' layered structure is illustrated in *figure 1.4*. The structure of the compound $Sr_3Sc_2O_5Cu_2S_2$ contained a double-perovskite layer with two cubic perovskite units face sharing and stacked in the *c*-direction. The *M* environment, as a result of the alternate layering of the building-blocks, was described as square-pyramidal with the axial oxygen shared across the double perovskite layer.

The original perovskite mineral was discovered in 1839 in the Ural Mountains of Russia by mineralogist Gustavus Rose and named in honour of fellow professional Lev Perovski. The elemental composition of perovskite was later found to be $CaTiO_3$. However, the term perovskite now applies more generally to a wide range of typically cubic materials of general composition $^{XII}A^{VI}MX_3$, where the preceding roman numeral superscript describes the coordination environment of the ions. Its structure can be described by twelve-coordinate *A* cations residing in the volume between corner-shared [MX_6] octahedra *(grey, figure 1.4, left)*.

Litharge, from λιθάργυρος/'lithargyos', describes the lead oxide mineral, PbO, and derives from the Greek for stone (λιθος/'lithos') and silver (άργυρος/ 'argyos') referring to the remnant mineral residue from the silver smelting process.[50] Its crystal structure was characterised in 1924 by Levi and can be described as a three-dimensional network of edge shared lead tetrahedra *(red, figure 1.4, right)* with oxygen ions at the centre of alternate tetrahedra in the *c*-direction of the tetragonal structure.[51]

* *The compound will be referred to here as $Sr_3Sc_2O_5Cu_2S_2$. This deviates from conventional nomenclature in an effort to make clear the layered structure. The formula of the cationic perovskite layer, $[Sr_3Sc_2O_5]^{2+}$, is written prior to that of the anionic litharge-like layer, $[Cu_2S_2]^{2-}$, and the square brackets and charges omitted for clarity.*

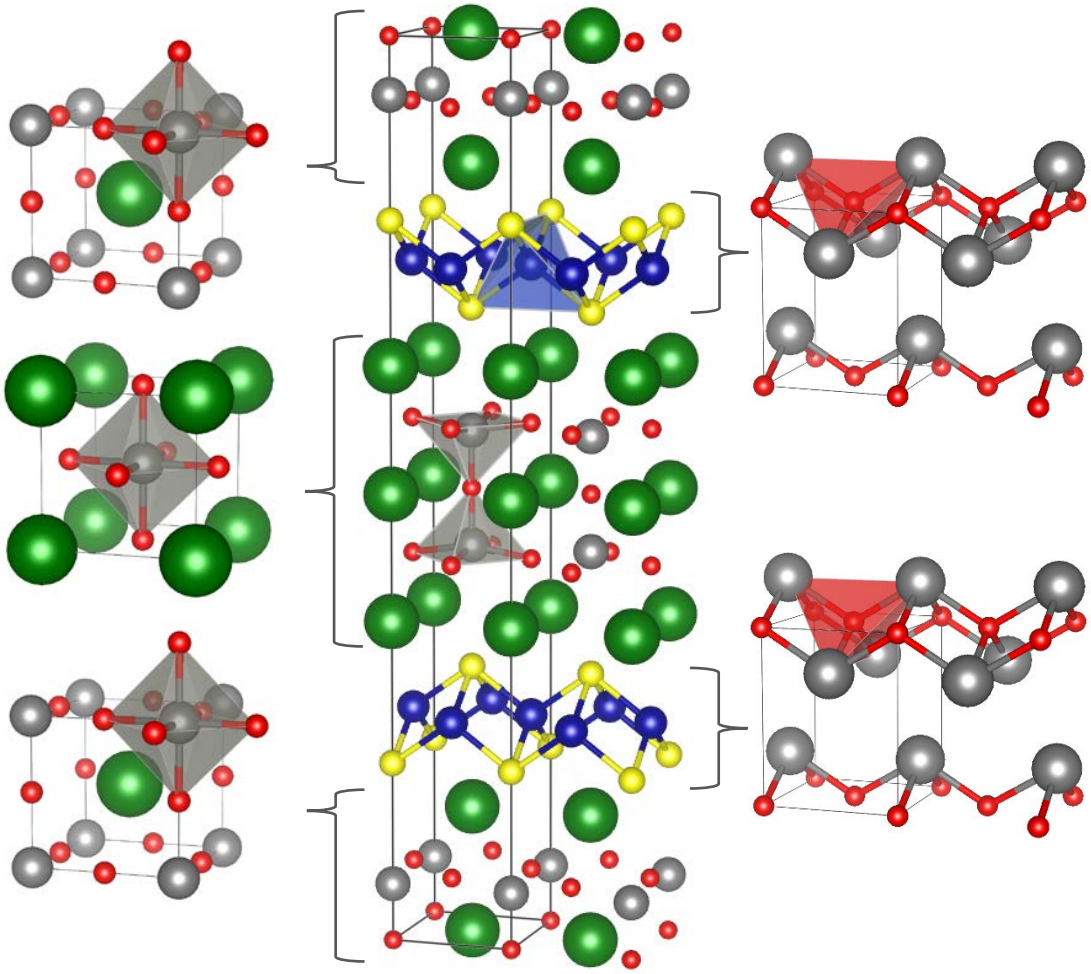

		Layered Perovskite	
	Perovskite	**Oxychalcogenide**	**Litharge**
			PbO
	AMO_3	$A_xM_yO_zM'_2Ch_2$	*M'Ch*
	Pm-3m	*I4/mmm*	*I4/mmm*

Figure 1.4 *Extended unit cell crystal structures of the perovskite and litharge 'building blocks' and a layered perovskite oxychalcogenide. The parent mineral formulae (of the building blocks), general formulae (parentheses) and space groups (italicised) of the structures are given below. Key: green – A, grey – M (perovskite) lead (litharge), red – oxygen, blue – copper and yellow – sulfur.*

The natural layering in the crystal structure of $Sr_3Sc_2O_5Cu_2S_2$ was a result of interactions between particular elements that can be rationalised by simple ionic radii arguments and the Hard-Soft Acid-Base (HSAB) theory. An idea introduced by Ralph Pearson to describe the relative stability of various acid-base pairs.[52] The cations in these structures were considered as Lewis acids and the counter anions as Lewis bases. Empirical observations have shown that bonding preferentially occurs between like acid/base pairs, *i.e.* hard bonds to hard and soft with soft. The harder alkali earth metal cations and oxide anions aggregate in the perovskite-like layer and the softer copper and sulfide ions in the litharge-like block.

The compound $Sr_3Sc_2O_5Cu_2S_2$ was reported to possess a hole mobility of 150 $cm^2\ V^{-1}\ s^{-1}$, higher than that reported for any other potential p-type transparent conductor, and higher too than reported for its n-type counterparts at the time [*]. Coupled with high mobility, a conductivity of the same order of magnitude as the LaCuOTe (around 500 times greater than for LaCuOS) was observed with maintenance of a wide band gap energy of 3.1 eV.

The compound $Sr_3Sc_2O_5Cu_2S_2$ conformed to the design rules devised by Kawazoe *et al.* rationalising the promising optoelectronic properties of the compound $AlCuO_2$.[33] The $3d^{10}$ copper (I) ions possessed fully-occupied *d*-orbitals; the copper and sulfur, and their tetrahedral coordination in the litharge-like layer, resulted in significant hybridisation of their 3*d* and 3*p* states; and the dimensionality of the layered structure, reduced copper-copper hybridisation in the *c*-direction. This reduced broadening of the band edges and maintained the desirably high transparency.

[*] *A year later a mobility of 250 $cm^2\ V^{-1}\ s^{-1}$ was reported for thin films of n-type Mo:In_2O_3 synthesised by Gupta et al.*[13]

1.6 Project Aim

The electronic band structure and, therefore optoelectronic properties of materials such as $Sr_3Sc_2O_5Cu_2S_2$, are directly linked to the geometry of the litharge-like layer. It can be seen by inspection of *figure 1.5* that the rigidity of the perovskite-like layer in these compounds results in a linear correlation between the weighted mean ionic radius of the ions within, and the basal lattice parameter, as determined experimentally for oxychalcogenide/-pnictide compounds reported in the literature.

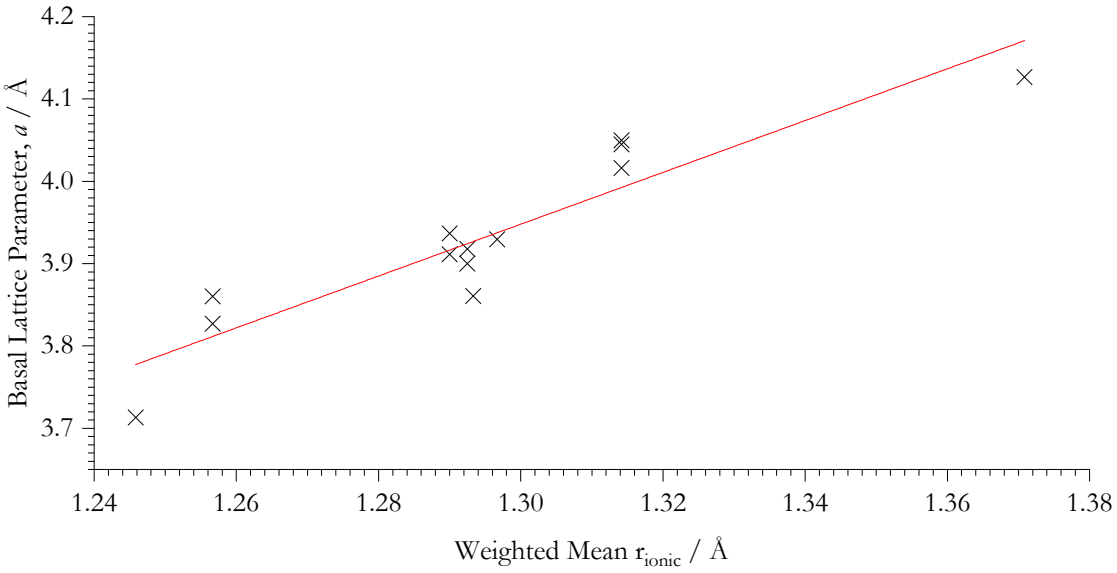

Figure 1.5 *Plot illustrating the effect of the mean weighted ionic radius of the perovskite ions on the basal lattice parameter, a, for a series of layered perovskite oxychalcogenide and oxypnictide compounds with the general formulae $A_4M_2O_6M'_2Ch/Pn_2$, reported in the literature.*

On the other hand, the litharge-like layer has shown geometric flexibility. Single composition litharge-like layers, namely $[Cu_2S_2]^{2-}$, $[Cu_2Se_2]^{2-}$, $[Ag_2Se_2]^{2-}$ and $[Fe_2As_2]^{2-}$, exhibit a range of *Ch/Pn-M'-Ch/Pn* angles, which vary linearly with basal lattice parameter, as illustrated by *figure 1.6*. The effect of the ionic radii in the perovskite-like layer on the basal lattice parameter and, in turn, on the geometry of the tetrahedral layer, through which conductivity was proven to occur, makes these layered perovskite mixed anion oxides ideal candidates for investigation of the effect of compositional modification on their optoelectronic properties.

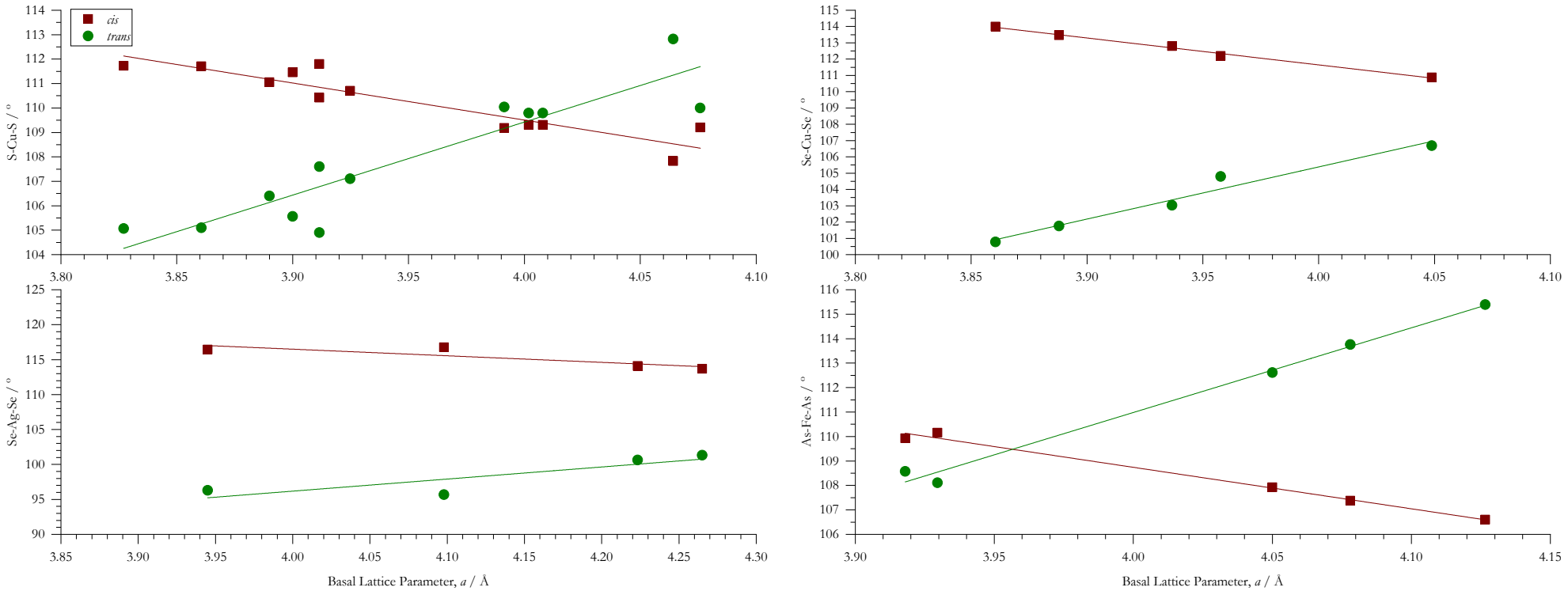

Figure 1.6 *Plot to illustrate the linear relationship between the basal lattice parameter and the Ch/Pn-M'-Ch/Pn angle in the tetrahedral litharge-like layer of the compounds $A_xM_yO_zCu_2S_2$ (top left), $A_xM_yO_zCu_2Se_2$ (top right), $A_xM_yO_zAg_2Se_2$ (bottom left) and $A_xM_yO_zFe_2As_2$ (bottom right), where xyz = 212, 213 and 325. The data from which this plot was constructed and information of the composition of the respective compounds is tabulated in appendix C.*

After the report of the compound $Sr_3Sc_2O_5Cu_2S_2$, the only example of its structure investigated to the end of transparent p-type conductivity, the field has seemingly stagnated. None of the twenty-one citations of the paper in which this compound is reported, report on any novel analogous quinary oxychalcogenide structures, with only one reporting a new material for application as a p-type transparent conductor.[53] The authors themselves apparently neglected the compound and moved on to investigate other candidate materials of alternative structures.[53,54]

The compound $Sr_3Sc_2O_5Cu_2S_2$ was found to show high p-type mobility and its structure, by investigation of analogous layered compounds, exhibited rigidity in the perovskite-like layer and flexibility in the litharge-like layer that was found to dictate its electronic structure. In this project the compound was therefore used as a structural prototype for compositional modification in search of novel optoelectronic properties with the aim of realising a transparent p-type conductor with increased conductivity, closer to that of the commercialised n-type counterparts.

"Thus [$Sr_3Sc_2O_5Cu_2S_2$], which was originally synthesized as a candidate superconductor, could possibly represent the ideal structural motif for designing high figure of merit p-type transparent conducting materials"

Scanlon, 2009[27]

Initially, modification of the composition of the perovskite-like layer was to be attempted with any success monitored by powder x-ray diffraction. The effect of successful substitution in the perovskite layer on the optoelectronic properties of the compound was to be investigated. The electronic properties were to be predicted by using an understanding developed by empirical observations and computational calculation from any observed crystal structure. The optical properties were to be determined by diffuse reflectance measurements using a spectrophotometer.

Any results obtained were expected to improve understanding of the relationship in these compounds between structure and composition, and optoelectronic properties, with any new knowledge gained employed to improve the transparency and conductivity in these candidate transparent p-type conductors.

Chapter 2 Employed Analytical Methods

2.1 X-ray Diffraction

2.1.1 The Phenomenon of Diffraction

Diffraction is a physical phenomenon of waves. When waves propagating through space encounter an obstacle, such as a slit or isolated obstruction, some of the waves are attenuated. This gives a region of the field beyond that remains initially unperturbed. Waves passing through or around the obstacle propagate into regions of the field originally shielded from the waves in the initial direction of propagation, spreading and increasing their directional range. If two or more emergent wave-fronts are generated they will spread towards each other. Upon meeting, these wave-fronts interact. The two waves will continue to propagate through each other; the total 'observed' perturbation in the field is given by the sum of the two waves. Waves of a given wavelength can be described using a complex function of amplitude (the magnitude of maximum displacement) and phase (the relative position of nodes and displacement minima/maxima). When two waves propagate through the same space their amplitudes may reinforce each other by constructive interference if the phases are aligned, or cancel each other by destructive interference if the phases are anti-aligned. The interference of two initially parallel waves emergent from a double slit and the subsequently observed combined intensity at a distance from the obstacle is represented in *figure 2.1*.

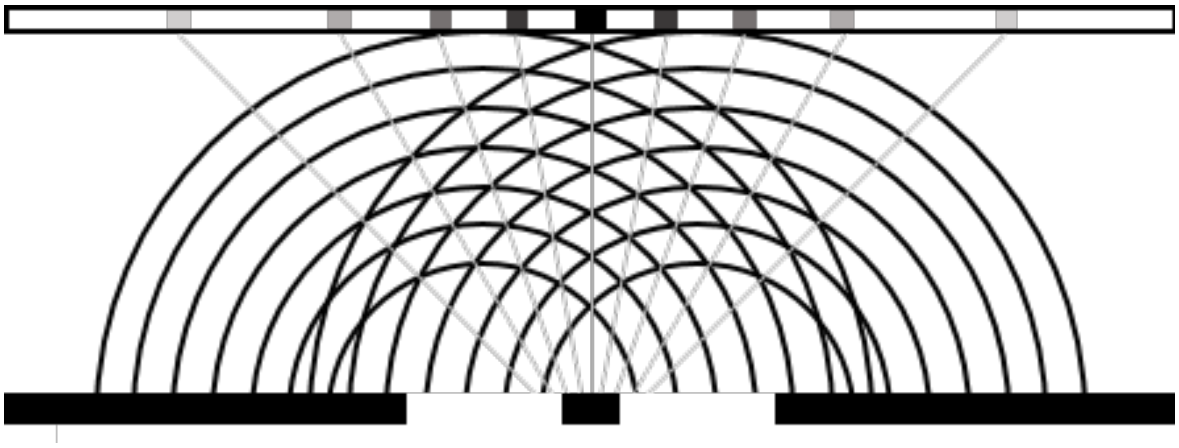

Figure 2.1 Illustration of the diffraction of a wave by a double-slit and resulting observed intensity of the interference pattern.

2.1.2 A Brief History of X-Ray Discovery, Generation and Diffraction

X-rays were discovered in 1895 by the first Nobel Prize winning physicist, Wilhelm Röntgen, when investigating the cathode-ray tube; a device that accelerated electrons through a vacuum between two electrodes.[55] By chance, it was found that during the operation of the device an unrelated (fluorescent) material in the laboratory began to glow. This phenomenon persisted even when the tube was covered with visually opaque material and objects were placed in its path. The penetrating waves emanating from the cathode-ray tube were termed 'Röntgen rays' (now x-rays) in honour of the discoverer. Another revelation occurred when Anna Ludwig placed her hand between the cathode-ray tube and the fluorescent material. The produced shadow showed her skeletal structure, owing to the contrasting attenuation of the x-rays by the soft tissue and bone in her hand. This was the first demonstration of the principles behind the now routine medical imaging technique.

While the contrasting attenuation of x-rays by various components of matter has proved useful in x-ray imaging, it is the diffraction of x-rays that is concerned here. In work that would earn the Nobel Prize of 1914, physicist Max von Laue first reported on the ability of crystalline solids to diffract x-ray radiation in a paper entitled Röntgenstrahlinterferenzen or 'interference of Röntgen rays/x-rays'.[56] In this document, the now-called Laue equations were published, which first described a mathematical basis for the observed diffraction patterns in terms of physical sub-microscopic dimensions of the crystals, within which the planes of atoms were providing slits and obstacles and acting as a diffraction grating.

Rapid progress was made, as the following year the Nobel Prize in Physics was once again awarded to researchers in the field; this time the father-and-son team of William Henry and William Lawrence Bragg.[57] The father William Henry, made instrumentation to produce higher-quality more consistent diffraction patterns while his son William Lawrence, simplified and generalised von Laue's mathematics[58]. The equation of William Lawrence, known as 'Bragg's law', is given in *equation 2.1* and shows the relationship between the interplanar spacing, *d*, between the sets of parallel lattice planes and the angle of observed diffraction peaks, θ. Between them, the Braggs essentially founded the process of analysis of crystalline solids by x-ray diffraction by both mass-production of the diffractometer and the development of the underlying mathematical basis which allowed reliable collection, and meaningful physical interpretation of diffraction data.

$$n\lambda = 2d_{hkl} \sin(\theta) \qquad 2.1$$

n - integer value
λ - wavelength of (X-ray) radiation
d - interplanar spacing
θ - observed diffraction angle *(see figure 2.2)*

2.1.3 The Powder Diffraction Experiment

The modern process of the collection of diffraction data employed during this project is fundamentally the same as that developed by William Henry Bragg. In the Bruker D2 Phaser and Rigaku SmartLab diffractometers used, the sample was placed on a stationary holder while the x-ray source and detector scanned a range of angles, typically $20 \leq 2\theta \leq 80^{o}$, measuring the intensity of 'observed' x-rays as a function of the diffraction angle, 2θ. The source and detector both operated in a plane perpendicular to that of the sample surface. The incident angle spanned between both the source and detector, and the sample surface, was equal in so-called 'theta/two-theta' ($\theta/2\theta$) or Bragg-Brentano geometry. A divergent beam was also used by default in the Bruker D2 Phaser to increase crystallite sampling at each angle. See *figure 2.2* for a schematic of the geometry of this diffraction experiment. The I11 beamline at Diamond Light Source was also utilised during this project. In this diffractometer the sample was mounted in a capillary and rotated in θ during the experiment. In this set-up the source remained stationary while a bank of 45 multi-analyser crystals (MAC) detectors rotated 40^{o} giving a total range of $3 \leq 2\theta \leq 150^{o}$.

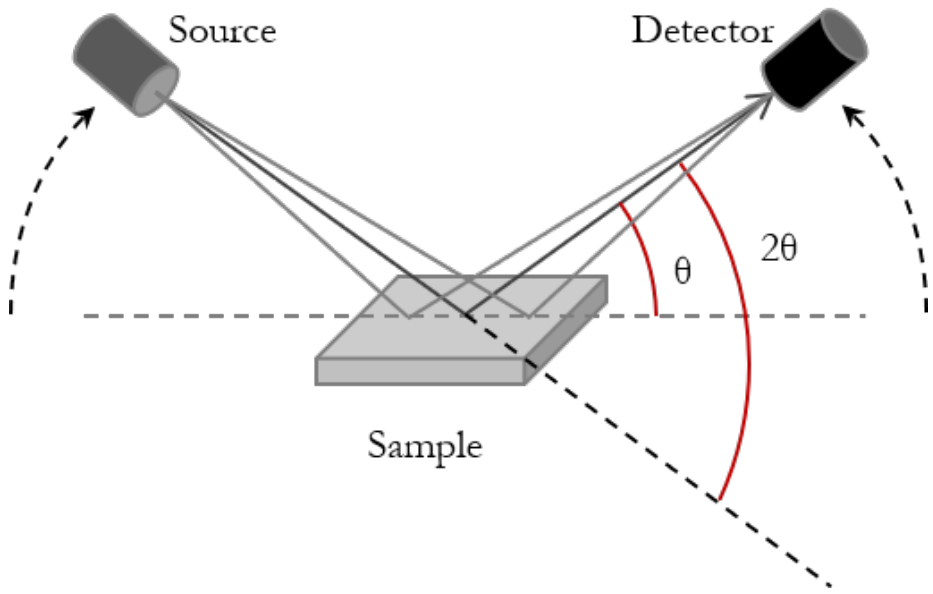

Figure 2.2 *A schematic depiction of a typical powder diffractometer in $\theta/2\theta$ Bragg-Brentano geometry showing a divergent/convergent x-ray beam path.*

The laboratory x-rays were generated in the same manner as in the original cathode ray tubes. Electrons were released by thermionic emission at the cathode and accelerated through a vacuum across a potential difference of 30 kV causing collision with the copper anode. Upon collision, the electrons excited those within the cathodic atoms. Electrons from higher energy orbitals relaxed to fill the vacancies created, emitting excess energy in the form of x-ray photons. The x-rays emitted formed emission peaks of precise wavelengths owing to the energy level separation in the metallic atoms from which they were emitted. Here, the Cu Kα emission peaks were used. Emitted x-rays accompanying electronic transitions between $2p_{3/2}$ and $2p_{1/2}$ to $1s$ states (Kα1 and Kα2 with λ = 1.54056 and 1.54439 Å, respectively) were selected by use of a filter for the Bruker D2 Phaser and Rigaku SmartLab. Synchrotron x-ray radiation of wavelength λ = 0.826027(10) Å was also used on the I11 beamline at Diamond Light Source, as discussed further in *section 3.3.3*.

Polycrystalline powder samples were regularly produced during this project containing many randomly orientated grains, which in turn may have comprised a single crystal or many crystalline domains. Different planes within these crystal domains scattered the x-rays in different directions. When the angle of the detector was equal to the angle of diffracted x-ray beam for a given set of parallel lattice planes, x-ray photons were diffracted towards the detector.

When x-rays were incident on the solid-state detector, the energy caused excitation of electrons from their equilibrium positions generating electron-hole pairs. The pairs were separated with an applied potential across the photoconducting layer and the resulting current was used as a direct indicator of observed x-ray intensity. The observed current with detector angle was interpreted by the commanding computer running Bruker DiffracSuite software to yield the x-ray diffraction patterns or diffractograms of observed x-ray intensity versus the diffraction angle, 2θ, which are reported throughout this thesis.

2.1.4 Data Analysis

2.1.4.1 X-Ray Diffraction by the Crystalline Lattice

It was found that the internal structure of a diffraction grating was related to the diffraction pattern observed at a distance by a Fourier Transform.[59] In the case of x-ray diffraction, it is the atoms, or more precisely their surrounding electrons, that diffract the x-ray electromagnetic radiation.

The Fourier Transform that yielded the structure factor, $\boldsymbol{F}_{hkl}$, describing the emanant x-rays that caused the diffraction patterns observed here, is given by *equation 2.2*. The structure factor is a complex number encoding information of both the amplitude, $|\boldsymbol{F}_{hkl}|$, and phase, φ, as shown in *equation 2.3*. The observed intensity of the diffracted x-rays is proportional to the square of the structure factor amplitude as shown in *equation 2.4*. The aim of the analysis of the diffraction data is therefore to deduce the structure of the diffracting crystal lattice (given by its electron density function) from the recorded intensities of the diffracted x-rays.

This cannot be directly performed by reversing the Fourier Transform, as it is not the structure factor itself that is calculated from measurement of x-ray diffraction, but rather only its amplitude. In the analysis of x-ray diffraction data, one is blind to the phase of the detected waves. This is known as the phase problem and it is a fundamental limitation in crystallography, prohibiting the direct transformation between observed diffracted x-ray intensity and the underlying crystal structure.

$$\mathbf{F}_{hkl} = \int_{\text{Cell Vol}} \varrho_{xyx}\, e^{2\pi i(hx+ky+lz)}\, dV \qquad 2.2$$

$\mathbf{F}_{hkl}$ - structure factor of diffracted x-rays
ϱ - electron density
xyz - Cartesian coordinates of real space
hkl - Miller indices describing sets of lattice planes in reciprocal space
V - volume of real space

$$\mathbf{F_{hkl}} = |\mathbf{F}_{hkl}|\, e^{i\varphi} \qquad 2.3$$

$|\mathbf{F}_{hkl}|$ - structure factor amplitude
φ - phase of x-ray wave

$$I_{hkl} \propto |\mathbf{F}_{hkl}|^2 \qquad 2.4$$

I - intensity of diffracted x-ray diffracted from the crystalline lattice

2.1.4.2 Structure Solution

Instead, the solution of the crystal structure is performed by taking a starting/'trial' crystal structure, modelling the diffracted x-ray intensity and comparing it to the observed data, modifying the model as appropriate to achieve the best fit. To model the observed diffraction data, the forward Fourier Transform (*eqn. 2.2*) in the direction of the diffraction experiment was calculated using the expected crystal structure containing the known constituent atoms by the General Structure Analysis System (GSAS) software suite.* The software calculated the structure factor of the diffracted x-rays from the trial crystal structure. To simplify the mathematical calculations, the software approximated the electron density, continuous throughout space, to discrete regions of electron density localised on each of the atoms in the structure. This allowed summation of these contributions for each atom, as shown in *equation 2.5* overleaf. The contribution that each atom makes to the overall diffraction of x-rays is quantified by its fundamental atomic scattering factor, $f(\theta)$. This is a function of incident angle, θ, and unique for each element. The scattering factor increases with the atomic number of the element.

* *Written by Larson and von Dreele of the Los Alamos National Laboratory, New Mexico, USA.*

It can be seen that the structure factor is modelled as a function of diffraction angle, consistent with that recorded from the experiment, instead of Miller indices, as per the Rietveld method. Formerly, the observed diffraction data would have been 'reduced'. Each diffraction peak in the observed profile assigned Miller indices and an intensity, equivalent to its area, then compared to the predicted intensity as a function of Miller indices. In one-dimensional polycrystalline diffraction patterns, peaks typically overlap in the angular range spanned. The crystallographer Hugo Rietveld was part of a group at the central neutron source in the Netherlands which attempted to overcome this issue. The group used long-wavelength neutron diffraction which increased the angular separation of diffraction peaks resulting from planes with larger *d*-spacing.[60] However, neutron diffraction yielded poor atomic resolution and proved time consuming.

Rietveld's main contribution to crystallography was the notion of refining the diffraction pattern profile as a whole.[60] To deal with the increased data load required, Rietveld identified that the process required automating. He used his experience in the computerisation of diffraction data analysis developed a few years earlier to develop a programme for such purpose.[61] The whole-profile refinement method of diffraction data fitting employed here is widely used in crystallography today and still bears his name.

The amplitude of the calculated structure factor, now a function of diffraction angle, was used to describe the intensity with diffraction angle, $I_{2\theta}$, to model the pattern as a whole, as pioneered by Rietveld. The proportionality constant between this and the structure factor amplitude, included corrections accounting for the relative multiplicity of the lattice planes in the crystal structure, the polarisation of the diffracted x-ray radiation, the anisotropy of the crystals and the partial absorption of the incident x-rays by the sample *(eqn.* 2.6*)*. In the diffraction experiments undertaken throughout this project the x-ray source was non-polarised (and assumed to remain so after diffraction), the crystallites assumed initially to be isotropic *(see section 4.3.5)* and the x-ray scattering events assumed to be perfectly elastic, *i.e.* no absorption accompanied the diffraction. The multiplicity of the lattice planes was fixed by the expected trial crystal structure and calculated by the software.

$$\mathbf{F}_{2\theta} = \sum_{j} f_j(2\theta)\, e^{2\pi i(hx+ky+lz)}\, dV \qquad 2.5$$

$f_j(2\theta)$ - fundamental atomic scattering factor

$$I_{2\theta} = m_{2\theta}\, L_{2\theta}\, P_{2\theta}\, A_{2\theta}\, |F_{2\theta}|^2 \qquad 2.6$$

$m_{2\theta}$ - multiplicity
$L_{2\theta}$ - Lorentz polarisation correction
$P_{2\theta}$ - preferred orientation correction
$A_{2\theta}$ - absorption correction

In calculating the expected diffraction profile, $I_{calc,\ 2\theta,}$ instrumental corrections were also made to the observed intensity expected from the diffracting lattice alone as in *equation 2.7*. These included the background intensity, I_{bkg}, generated by the diffractometer, a scaling factor, *s*, relating to the intensity of the source, a zero-point error correction, $2\theta_{zero}$, to account for detector alignment, and a profile-shape parameter, Σ, describing the peak geometry dependent on the instrument and crystallite size and strain in the sample. The peak profiles were modelled by the software using *Pseudo-Voigt*, V_P, functions that are linear combinations of *Gaussian*, *G*, and *Lorentzian (Cauchy), L*, distributions as described in *equation 2.8*, where η is a mixing parameter.

$$I_{2\theta,\,calc} = I_{2\theta,\,bkg} + s \sum_{2\theta} 2\theta_{zero}\ \Sigma\ I_{2\theta} \qquad 2.7$$

I_{calc} - calculated detected x-ray intensity
I_{bkg} - background detected x-ray intensity
s - global scale factor
$2\theta_{zero}$ - sample displacement parameter
Σ - peak profile shape
$I_{2\theta}$ - intensity of diffraction

$$\Sigma = V_{P\,\theta,\Gamma} = \eta\, L_{\theta,\,\gamma} + (1 - \eta)\, G_{\theta,\,\sigma} \qquad 2.8$$

$V_{P\,\theta,\Gamma}$ - Pseudo-Voigt function of diffraction angle, θ, and total full-width at half-maximum, Γ
η - mixing parameter
$L_{\theta,\,\gamma}$ - Lorentzian (Cauchy) distribution of diffraction angle, θ, and width parameter, γ
$G_{\theta,\sigma}$ - Gaussian distribution of the diffraction angle, θ, and width parameter, σ

The modelled observed x-ray intensity profile required starting values for all of the parameters contributing to the calculated intensity which were determined by user input. The details of the crystallographic model were read, in this case, from standard Crystallographic Information Files ('CIFs') derived from previously determined experimental results for samples expected to exhibit crystal structures analogous to that of the target compounds. These were loaded to the GSAS software via the EXPGUI graphical user interface and the constituent elements modified to match the intended composition. Instrumental parameters were stored in '.ins' computer files for access by the refinement software and described the contribution to observed profile by the Bruker D2 Phaser diffractometer.

2.1.4.3 The Refinement Process and Quality of Fit

The refinement method used was a least-squares procedure, in which the aforementioned user-selected parameters contributing to the observed x-ray intensity were systematically varied, the predicted diffraction pattern generated and subsequently compared to the observed diffractogram. If the new calculated profile deviated further from the original it was discarded and if it showed improvement it was retained by the algorithm and the cycle repeated.

The 'least-squares' referred to the statistical analysis used to quantify the quality of fit between the calculated and observed whole-profile diffraction patterns. The algorithm controlling the Rietveld refinement process ultimately strived to minimise the value of the sum of squared differences between the calculated and observed diffracted x-ray intensity *(eqn. 2.9)*. Intuitively, this meant that the smaller the resulting sum of squared differences, the smaller the difference between the model and experimental data and the 'better' the fit. Various other statistical parameters which are all commonly reported in the literature, were used to quantify the value judgement of a 'good' fit, namely the weighted profile reliability factor, R_{wp}, and the 'reduced chi squared', χ^2_{red}, and are reported from Rietveld least-squares refinements of x-ray diffraction data throughout this project.

$$s = \sum_{I} \left(I_{2\theta,\,obs} - I_{2\theta,\,calc} \right)^2 \qquad 2.9$$

s - sum of squared differences
$I_{2\theta,\,obs}$ - observed intensity of detected x-rays
$I_{2\theta,\,calc}$ - calculated or predicted intensity of detected x-rays

The (unweighted) profile reliability factor, R_P *(eqn. 2.10)* took the root of the sum of squared differences between the observed data and the calculated model divided by the total squared intensity of observed x-rays. The larger the observed intensity compared to the differences, the less significant the deviation between the two, the smaller the reliability factor and the more reliable the refined model was concluded to be. However, the more accurate weighted-profile reliability factor was reported for refined x-ray diffraction data throughout this thesis *(eqn. 2.11)*. This lent greater weight to the fit of lower intensity peaks owing to the inclusion of a weighting factor inversely proportional to the peak intensity *(eqn. 2.12)*. The smaller the peaks, the greater the relative error on their values and the more they increased the weighted reliability factor.

$$R_p = \sqrt{\frac{\sum_I (I_{obs} - I_{calc})^2}{\sum_I (I_{obs})^2}} \quad 2.10$$

R_p - profile reliability factor

$$R_{wp} = \sqrt{\frac{\sum_I (I_{obs} - I_{calc})^2}{\sum_I w_I (I_{obs})^2}} \quad 2.11$$

R_{wp} - weighted profile reliability factor
w_I - weight factor, where…

$$w_I = \frac{1}{|I_{obs}|} \quad 2.12$$

The reduced chi squared, χ^2_{red}, values which were used to monitor the refinement process, compared the weighted profile reliability factor with that expected from the data given by the 'expected profile reliability factor', R_{exp}. The number of observed data points collected, *N*, the number of parameters which were refined, *P*, and constraints used, *C*, (none in this case) were taken into account to give a 'maximum expected reliability', given the quality of the data collected *(eqn. 2.13)*. The weighted profile and expected reliability factors were combined in a ratio to yield the reduced chi squared *(eqn. 2.14)*, a more generic reliability factor which enabled a fairer comparison of the reliability of crystallographic models refined to a wider range of diffraction data collected with different parameters across different instruments.

$$R_{exp} = \sqrt{\frac{N - P + C}{\sum_I w_I (I_{obs})^2}} \quad 2.13$$

R_{exp} - expected reliability factor
N - number of observations
P - number of refined parameters
C - number of constraints

$$\chi^2_{red} = \frac{R_{wp}}{R_{exp}} = \sqrt{\frac{\sum_I (I_{obs} - I_{calc})^2}{N + P - C}} \quad 2.14$$

χ^2_{red} - reduced chi squared value

Once a satisfactory quality of fit was achieved by the refinement process, the crystallographic information was extracted from the trial model generating the well-fitting calculated intensity. This 'best' theoretical model, as defined using the fit statistics; the one which most closely matched the observed data, was then taken to represent the underlying 'true' crystal structures which are reported throughout this thesis.

2.2 Optical Properties

2.2.1 The Tauc Equation and Band-Gap Energy Derivation

The attenuation coefficient, α, can be related to the optical band-gap energy by the Tauc relation *(eqn. 2.15)*, where the absorbed energy is proportional to the energy difference between the incident light and the optical band-gap raised to a power.[62,63] The proportionality constant, *A*, depends on the probability of electronic excitation across the band gap and the order depends on the nature of the transition process: *n = 2* for direct allowed transitions was used here. A thorough derivation of the Tauc equation can be found in *Appendix A* of the thesis of Huxter.[64] It can be seen that the absorbed energy is proportional to the incident energy for a given material (with constant band-gap energy). The Tauc equation *(eqn. 2.15)* shows that in order to reduce absorption of visible light, desirable for the transparent conducting materials targeted here, the band-gap energy must be greater than that of the maximum energy of visible light photons, 3.1 eV.

In assessing the potential of candidate transparent p-type conductors, the band gap is calculated using the Tauc equation. The absorption coefficient is measured across a range of incident light intensity and the resulting data used to construct a Tauc plot of the square root ($n = 2$) of the energy absorbed versus the incident energy, as described by *equation 2.16*. The absorption onset, across which *A* is constant, is fitted by a linear function which gives the band-gap energy, E_g, as the *x*-intercept.

$$\alpha h\nu = A\left(h\nu - E_g\right)^n \qquad 2.15$$

α - attenuation (absorption) coefficient
h - Planck's constant
ν - frequency of incident light radiation
A - constant
E_g - optical band-gap energy
n – order (= 2 for a direct allowed electronic transition)

$$(\alpha h\nu)^{\frac{1}{n}} = A\left(h\nu - E_g\right) \qquad 2.16$$

2.2.2 The Kubelka-Munk Theory of Diffuse Reflectance

However, the absorption coefficient could not be directly measured owing to the inhomogeneity of solid powder samples, such as those which were investigated here, and the significant contribution to their reflectance by scattering process from the particle surfaces. The ratio of attenuation (absorption) coefficient to that of scattering, is described by the Kubelka-Munk function of diffuse reflectance *(eqn. 2.17)*.[65,66] A more recent derivation and discussion of the Kubelka-Munk function is given by Džimbeg *et al.*[67] The scattering coefficient is dependent on particle size, however, is proposed not to vary significantly with incident light energy, particularly over the visible region.[68] The Kubelka-Munk function of diffuse reflectance, $f(R)$, is therefore assumed to be proportional to the absorption coefficient and can be used in its place in the construction of a Tauc plot. The proportionality constant affected the gradient of the plot but not the *x*-intercept required to calculate the band gap energy.

In practice during this project, the diffuse reflectance, R_∞, was measured as a function of incident light wavelength (250 – 2000 nm at intervals of 5 nm) using a Perkin Elmer Lambda 750 S spectrophotometer equipped with deuterium and tungsten lamps and a 100 mm integrating sphere. Data was processed and exported using the Perkin Elmer UVWinLab software package. The resulting diffuse reflectance data was used to calculate the Kubelka-Munk function. The function was assumed proportional to the absorption coefficient and used along with the varied wavelength, to construct a Tauc plot. The band gap energy was calculated as the *x*-intercept of the linear fit of the absorption edge. The linear fits were made in Microsoft Excel using the two data points in the Tauc plot between which the gradient was at its greatest.

$$\frac{\alpha}{s} = f_R = \frac{(1 - R_\infty)^2}{2 R_\infty} \qquad 2.17$$

α - attenuation (absorption) coefficient
s - scattering coefficient
f_R - Kubelka-Munk function of reflectance
R_∞ - measured diffuse reflectance for 'infinitely thick'/opaque sample

2.3 Scanning Electron Microscopy (SEM)

Images of the microstructure of the samples investigated in *chapter 4* were produced on behalf of the author by Alexander Kulak of the University of Leeds using a Nova Nano scanning-electron microscope. Images on the scale of 1-5 μm were produced under magnifications of 8000 to 50000 times, indicated on each of the images presented in *section 4.3.6*.

Chapter 3 Attempted Syntheses of 325-type Layered Oxychalcogenides Computationally Predicted to Show Promise as Improved Transparent p-Type Conductors

3.1 Introduction

The compound $Sr_3Sc_2O_5Cu_2S_2$ was found to be a promising candidate high-performance p-type conductor.[48] Liu *et al.* demonstrated the high mobility (150 $cm^2\ V^{-1}\ s^{-1}$) of the sample, the origin of which was verified by a subsequent computational study by Scanlon *et al.*[27] The phase space of these quinary oxysulfides, $A_3M_2O_5Cu_2S_2$, remains relatively unexplored: only twelve examples of oxychalcogenides with the same '325'-type crystal structure were found to have been reported in the literature. Only one of these, $Sr_3Fe_2O_5Cu_2S_2$, shared the copper sulfide layer but was unsuitable for transparent applications as a result of the partially-filed *d*-orbitals of the iron (II).[49,69–75] This prompted the computational investigation by Williamson and Scanlon of the Scanlon Materials Theory Group, UCL, with whom the work in this chapter was in collaboration. The stability and optoelectronic properties were investigated of compositional variants of the strontium scandium prototype, $A_3M_2O_5Cu_2S_2$, where A = Mg, Ca, Sr and Ba, and M = Al, Sc, Ga, Y, In and La. These elements were chosen as they are isovalent with the cations in the perovskite block of the prototype and do not possess partially filled *d*-states, electronic transitions between which could result in optical absorption and loss of transparency of the resultant compounds.

Density functional theory (DFT) was used to evaluate the thermodynamic stability (at 0 K), dynamical stability (at 800 ^oC) and electronic structure of the twenty-four compositions.[76] For details of the computation, please see 'Computational Methodology' in the cited literature. All compositions were found to 'geometry relax' into the predicted tetragonal *I4/mmm* space group, isostructural with the prototype. Evaluation of the thermodynamic stability of the candidate compounds, indicated that eight new compositions analogous to $Sr_3Sc_2O_5Cu_2S_2$, were expected to be stable in the tetragonal *I4/mmm* crystalline structure. These were each determined by calculation of their 'E above Hull', the calculated enthalpy change of decomposition of the candidate compound into the relevant competing products. Values of 0 – 0.09 eV $atom^{-1}$ were considered to be stable.[77] The calculated stabilities for the twenty-four compounds investigated are provided in *table 3.1* and summarised graphically in *figure 3.1*. It can be seen that eight of these were predicted to be stable, in addition to the $Sr_3Sc_2O_5Cu_2S_2$ already reported: $Ca_3Al_2O_5Cu_2S_2$, $Ca_3Sc_2O_5Cu_2S_2$, $Ca_3Ga_2O_5Cu_2S_2$, $Sr_3Al_2O_5Cu_2S_2$, $Sr_3Ga_2O_5Cu_2S_2$, $Ba_3Al_2O_5Cu_2S_2$, $Ba_3Sc_2O_5Cu_2S_2$ and $Ba_3Ga_2O_5Cu_2S_2$. No compositions containing magnesium on the A site nor yttrium, indium nor lanthanum on M, were calculated to be stable. The small atomic radius of magnesium (II) precluded it from hypothetical crystallisation in high-coordination sites, such as, the twelve-coordinate $^{XII}A^{2+}$ site in the perovskite oxysulfide prototype.

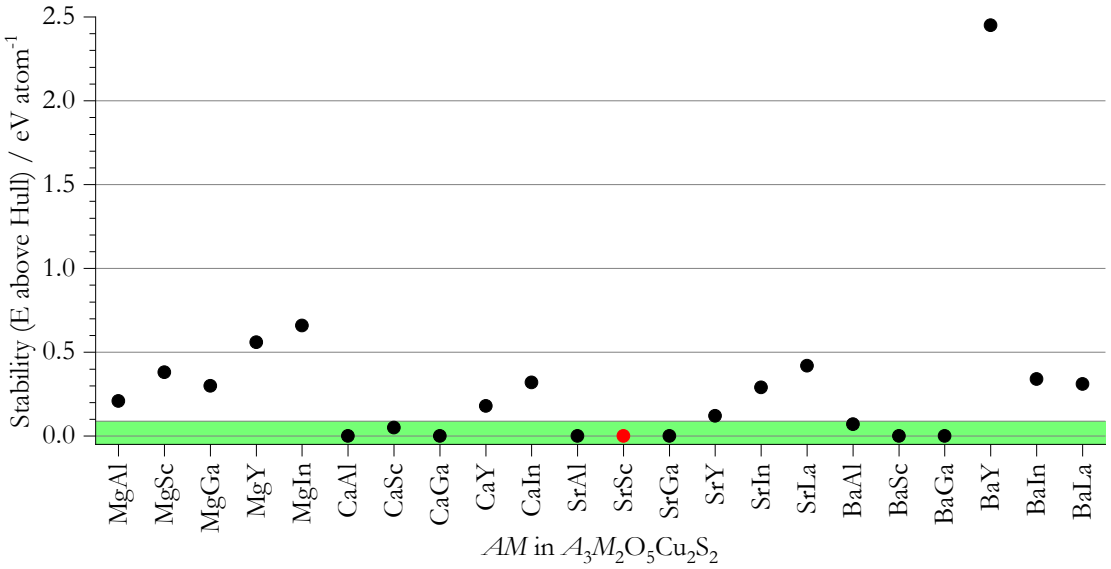

Figure 3.1 *Graphical summary of the stabilities of compounds with general composition $A_3M_2O_5Cu_2S_2$ predicted by Williamson and Scanlon.[76] Data from which the plot was constructed are provided in table 3.1.Compounds with predicted stability in the region 0 – 0.09 eV atom^{-1}(shaded) are expected to be thermodynamically stable at room temperature. The point in red corresponds to the AM = SrSc compound already reported to have been synthesised in the literature.*

Table 3.1 *Stabilities of compounds with general composition $A_3M_2O_5Cu_2S_2$ predicted by Williamson and Scanlon.[76] Compounds with predicted stability in the region 0 – 0.09 eV atom^{-1}(shaded) are expected to be thermodynamically stable at room temperature. The entry in bold font corresponds to the AM = SrSc compound already reported to have been synthesised in the literature. The compounds where AM = MgLa and CaLa were not amenable to geometric relaxation and, therefore, their stabilities not reported.*

		M					
		Al	**Sc**	**Ga**	**Y**	**In**	**La**
A	**Mg**	*0.21*	*0.38*	*0.30*	*0.56*	*0.66*	*n/a*
	Ca	*0.00*	*0.05*	*0.00*	*0.18*	*0.32*	*n/a*
	Sr	*0.00*	***0.0005***	*0.00*	*0.12*	*0.29*	*0.42*
	Ba	*0.07*	*0.00*	*0.00*	*2.45*	*0.34*	*0.31*

The electronic band structures and band gap energies *(figure 3.2* and *table 3.2)* for the compounds predicted to be stable were calculated. This was done by calculating the absorption coefficient for all possible allowed electronic transitions, taking the square of the coefficient to yield predicted absorption spectra provided in the SI in the literature.[76] Of those predicted stable, the compounds *AM* = CaAl and BaSc were predicted to possess band gap energies above the 3.1 eV threshold (3.17 and 3.24 eV, respectively), in addition to the prototype where *AM* = SrSc.[76] The predicted intrinsic conductivity of the compound $Sr_3Sc_2O_5Cu_2S_2$ was calculated to be 1673 S cm^{-1}, for a charge carrier concentration of 10^{21} cm^{-3}, *c.f.* 1.49 x10^4 S cm^{-1} for ITO.[13] In order to achieve a predicted conductivity close to the 2.8 S cm^{-1} measured in the literature at a charge carrier concentration of around 10^{17} cm^{-3}, a carrier concentration of 10^{18} cm^{-3} was required.[48] This indicated that the predicted conductivity at 10^{21} cm^{-3} would be an underestimate.

However, in addition to the effective mass and charge carrier concentration, the bulk conductivity of a sample depends on the mean free time between scattering events, as is illustrated in *equation 1.4, page 5*. This is neglected in the theoretical calculation, suggesting that the predicted conductivities are actually overestimates, and it is only the 'intrinsic' conductivity that is calculated (ignoring microstructural variables). It is more likely the case as is suggested by Williamson, that overall the charge carrier concentrations calculated and reported in the literature are actually over-estimates.[48,76]

Nonetheless, the predicted 'intrinsic' conductivity of the compounds $Ca_3Al_2O_5Cu_2S_2$ and $Ba_3Sc_2O_5Cu_2S_2$ were both expected to be higher than that of the strontium scandium prototype, 1767 and 2058 S cm^{-1}, respectively, *c.f.* 1673 S cm^{-1}. It was, therefore, deemed worthwhile to attempt the syntheses of the predicted compounds in pursuit of novel high-performance transparent p-type conductors.

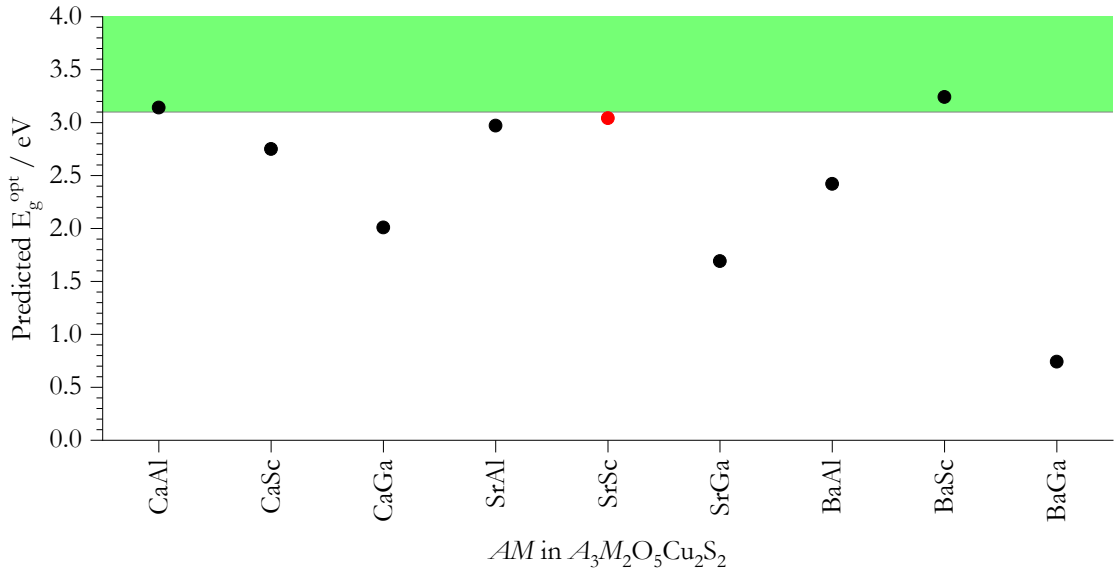

Figure 3.2 *Graphical summary of the computationally predicted optical band gap energies (E_g^{opt}) for the compositions ($A_3M_2O_5Cu_2S_2$) investigated. Compounds with predicted optical band gaps > 3.1 eV (shaded) are expected to be visibly transparent. The point in red corresponds to the AM = SrSc compound already reported in the literature. Its band gap was reported as 3.1 eV on the cusp of the cut-off criterion for transparency. The data from which this plot was constructed is provided in table 3.2.*

Table 3.2 *Computationally predicted optical band gap energies (E_g^{opt}) for the compositions ($A_3M_2O_5Cu_2S_2$) investigated. Compounds with predicted optical band gaps > 3.1 eV (shaded) are expected to be visibly transparent. The entry in bold font corresponds to the AM = SrSc compound already reported in the literature. Its band gap was reported as 3.1 eV on the cusp of the cut-off criterion for transparency.*

		M		
		Al	**Sc**	**Ga**
A	**Ca**	3.14	2.75	2.01
	Sr	2.97	**3.04**	1.69
	Ba	2.42	3.24	0.74

3.2 Experimental

The compounds investigated were targeted by the conventional solid-state synthesis of 0.5 g-scale polycrystalline bulk powder samples according to the general *equation 3.1*. The powder precursors in the appropriate stoichiometric ratio were ground, pressed into pellets (≈ 0.75 GPa) and placed in alumina crucibles. The alkali earth oxides and sulfides were synthesised in-house *(appendices D.1 and D.2)*. (It is noted that it was necessary to fracture the pellet into several pieces in order to fit it into the crucible). The crucible was placed inside a quartz tube sealed at one end. A quartz spacer, made from a narrower tube, was placed in the bottom of the main tube to avoid the thermal expansion of the alumina crucible from applying pressure on the inner walls of tube at the weaker tapered end. The entire process thus far was conducted under the inert atmosphere (< 10 ppm O_2) of a nitrogen-filled glovebox. Once the sample-containing crucibles were loaded, the tube was sealed at the open end by use of a Swagelok union, linking the tube to a side arm adapter fitted with a Youngs' tap. The tap was closed and the ensemble removed from the glovebox. The tube was clamped in place and the side arm adapter connected to a vacuum pump. The tap was opened, and the tube kept under dynamic vacuum for > 15 mins. An oxypropane blowtorch (O_2/C_3H_8 = 2.5/0.25 bar) was used to seal the quartz tube, creating an ampoule sealed under static vacuum. The ampoule was then heated in a box furnace at a rate of 10 °C min^{-1} to 800 °C at which point the temperature was held for 12 h before cooling naturally to room temperature. The ampoules were opened under inert atmosphere and the contents analysed by air-sensitive powder x-ray diffraction. The samples were subjected to further heating cycles until consistent product(s) were observed by x-ray diffraction.

$$2\,A\mathrm{O} + A\mathrm{S} + M_2\mathrm{O}_3 + \mathrm{Cu}_2\mathrm{S} \rightarrow A_3M_2\mathrm{O}_5\mathrm{Cu}_2\mathrm{S}_2 \qquad 3.1$$

3.3 Results and Discussion

3.3.1 Repeated Synthesis of Literature Prototype $Sr_3Sc_2O_5Cu_2S_2$

In order to verify the repeatability of the synthesis described in the literature and to confirm the reliability of the experimental set-up and procedure used, the synthesis of the prototype compound was initially attempted. The synthesis of the compound $Sr_3Sc_2O_5Cu_2S_2$ was successfully completed from the precursors SrO, SrS, Sc_2O_3 and Cu_2S, after two 12 h cycles at 800 ^oC, using the experimental procedure described in the previous section. The Rietveld refined powder x-ray diffraction pattern is shown in *figure 3.3*. The band gap of 3.1 eV was confirmed by linear fitting of a Tauc plot constructed from the raw diffuse reflectance data *(inset)* shown in *figure 3.4*. The synthesised compound was beige/ light brown in colour, consistent with the "brownish white" reported by Liu.[48] It can be seen from inspection of the Tauc plot in *figure 3.4*, that there is considerable absorption (consistent with that observed in the literature) at the high-energy (blue) end of the visible spectrum, possibly due to copper (II) defects causing the red/ brown colouration.[27,48] It can be seen in *table 3.3* that the observed band-gap energy of 3.1 eV was consistent with that reported by Liu *et al.* and slightly higher than the 3.04-3.06 eV, predicted by Williamson and Scanlon.[76] The lattice parameters and, distances and angles showed good agreement with both of those previously reported by Liu *et al.* and predicted by Williamson *et al.*, apart from the sulfur-copper-sulfur angle. It was found here to be 114^o, as predicted by Williamson, which was considerably larger than that previously experimentally determined and reported.

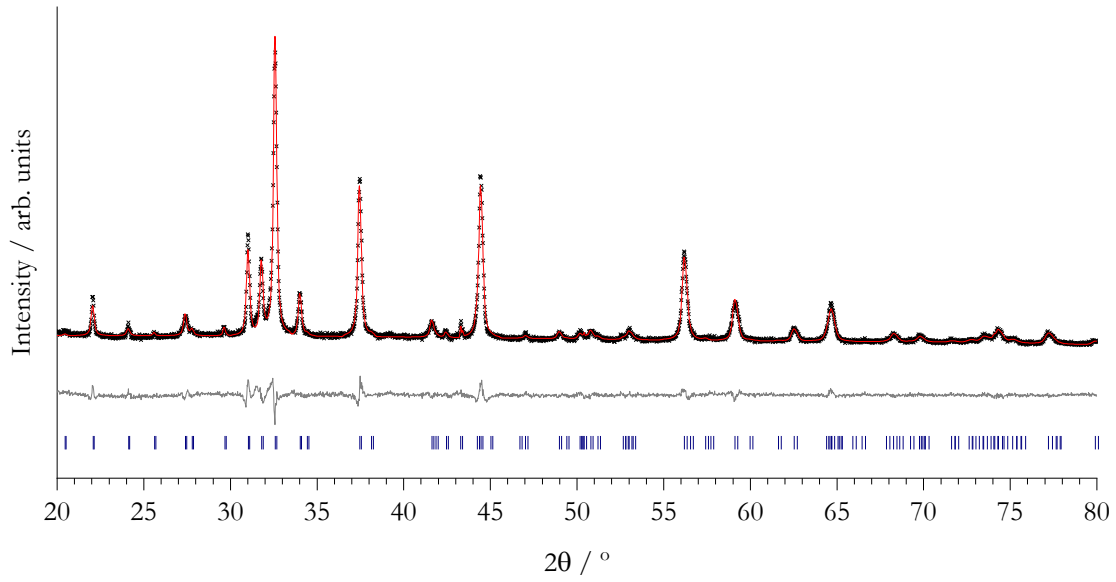

Figure 3.3 *Powder x-ray diffractogram for the observed prototype compound $Sr_3Sc_2O_5Cu_2S_2$. The observed data is represented by black crosses, the calculated diffraction pattern by a solid red line and the difference profile as a solid grey line below. The blue tick marks show the expected peak positions from the Rietveld refined model. The compound crystallised into a structure with the tetragonal I4/mmm space group. R_{wp} = 6.26 % and χ^2_{red} = 2.396.*

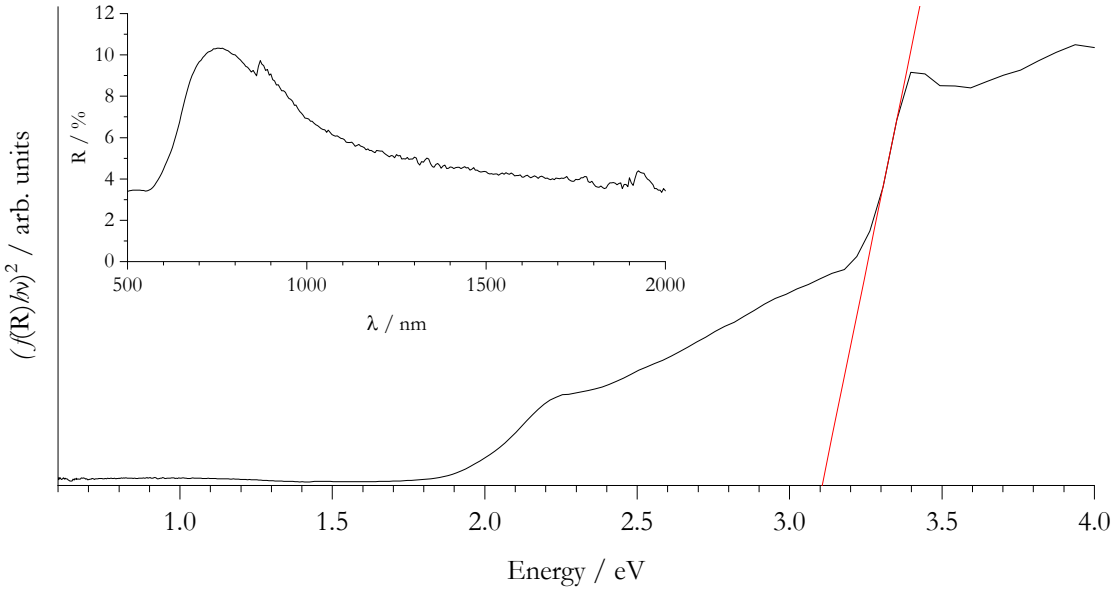

Figure 3.4 *Tauc plot for the prototype compound $Sr_3Sc_2O_5Cu_2S_2$ constructed from the collected raw diffuse reflectance data (inset). The solid red line shows a linear fit to the region of steepest gradient; its x-intercept marking the band gap energy at 3.1 eV.*

Table 3.3 *Summary of the lattice parameters and key distances and angles, in terms of the electronic structure, for the prototype compound $Sr_3Sc_2O_5Cu_2S_2$, as determined by various methods (column 1).*

Method	*a* / Å	*c* / Å	Cu-Cu / Å	Cu-S / Å	S-Cu-S / °	E_g / eV
Predicted[76]	4.08	26.07	2.89	2.45	114.55	3.04
Literature Observed[48]	4.08	25.99	2.88	2.49	110.00	3.1
Observed Here	4.07	26.02	2.88	2.43	114.14	3.1

3.3.2 Attempted Synthesis of Predicted Transparent p-Type Conductor $Ca_3Al_2O_5Cu_2S_2$

The compound $Ca_3Al_2O_5Cu_2S_2$ structurally analogous to the strontium/scandium prototype, was predicted by Williamson to be thermodynamically stable (E above Hull = 0.00 eV atom^{-1}) and to show increased transparency (E_g^{opt} = 3.14 eV) and conductivity (1767 S cm^{-1}), compared to the 3.04 eV and 1673 S cm^{-1} calculated for the strontium/scandium analogue, at a charge carrier concentration of 10^{21} cm^{-3}.[76] The synthesis of this compound was attempted using the relevant precursors in the generic reaction scheme in *equation 3.1*, namely CaO, CaS, Al_2O_3 and Cu_2S, for heating cycles of 12 h at 800 °C. The x-ray diffraction pattern for the powder sample observed after the second synthetic cycle showed no clear evolution in phase composition from the product obtained after a single cycle and is shown in *figure 3.5*. It was refined against the crystal structures of the identified phases present. The predicted diffraction pattern *(black line)* is shown for reference. This was calculated for each of the structurally relaxed compositions.

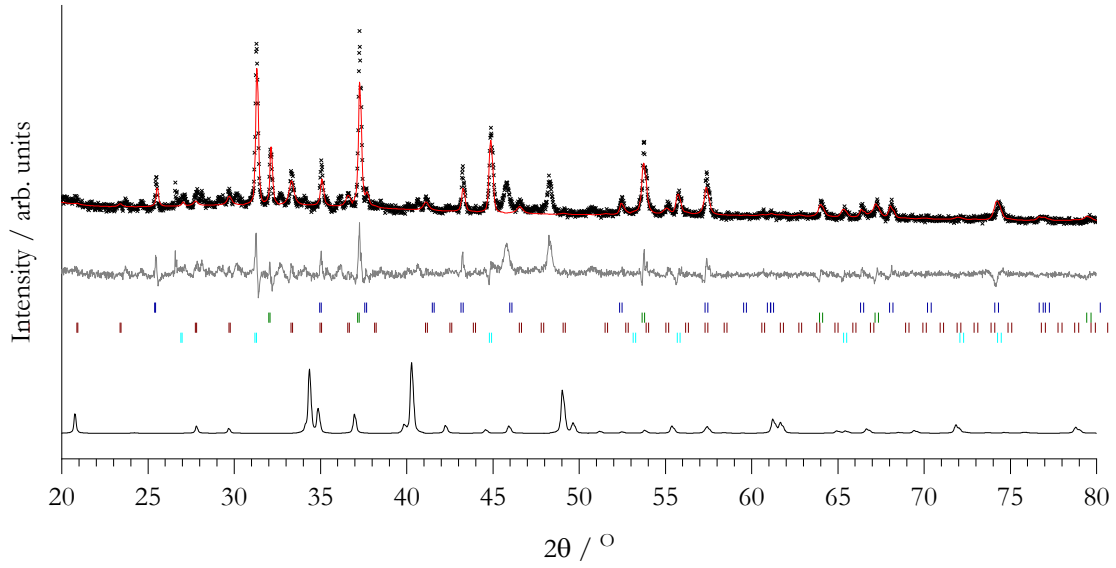

Figure 3.5 *Observed PXRD pattern for products from attempted synthesis of target compound with composition $Ca_3Al_2O_5Cu_2S_2$. The black crosses illustrate the observed data points, the red line shows the calculated profile from the Rietveld refined model and the grey line is the difference profile between the two. The black profile (bottom) shows a predicted pattern calculated from the predicted crystal structure of the target. Observed phases included Al_2O_3 (blue, 28 wt. %), CaO (green, 27 wt.%), $Al_{14}Ca_{12}O_{33}$ (red, 25 wt.%) and CaS (cyan, 20 wt.%). R_{wp} = 11.77 % and χ^2_{red} = 5.042.*

It was found that the resultant powder sample consisted of the precursors calcium oxide, calcium sulfide and alumina, in addition to the seemingly competing phase $Al_{14}Ca_{12}O_{33}$. This was considered by Williamson as one of the 313 potential competing phases, yet the target compound was still predicted to be stable and observed experimentally in its place. This was not found to be the case experimentally here.

It was found that in the literature the synthesis had been reported of layered oxypnictides that possessed the same perovskite-like layer in the same 325-type structure as in the targeted compound, *i.e.* $Ca_3Al_2O_5Fe_2Pn_2$, where *Pn* = P and As.[73] However, the synthesis of these compounds was carried out under high pressure (4.5 GPa). It may be that while the compound $Ca_3Al_2O_5Cu_2S_2$ is stable, high pressures are required to force the constituent atoms into the high-density configuration required. It is noted that the predicted unit cell volume of 353.84 Å^3 is larger than that of the reported iron pnictide analogues yet smaller than that of $Sr_3Fe_2O_5Cu_2S_2$, the analogous compound with the smallest unit cell volume synthesised without application of mechanical pressure.[71] Therefore, it was anticipated that the synthesis of the potential p-type transparent conductor $Ca_3Al_2O_5Cu_2S_2$ would benefit from the application of high-pressure, requiring facilities not available to this project.

3.3.3 Synthesis of Predicted Transparent p-Type Conductor $Ba_3Sc_2O_5Cu_2S_2$

The barium analogue of the prototype compound, $Ba_3Sc_2O_5Cu_2S_2$, was also predicted by Williamson to be stable, with an Energy above Hull of 0.00 eV atom^{-1}; shows the greatest transparency of the compounds investigated (E_g^{opt} = 3.24 eV); and possess an intrinsic conductivity of 2058 S cm^{-1}, higher than any other composition calculated, and only an order of magnitude below those measured experimentally for the current commercialised n-type TCs.

The target compound of composition $Ba_3Sc_2O_5Cu_2S_2$ was successfully synthesised, apparently for the first time, after a single cycle at 800 °C for 12 h. The compound is isostructural (*I4/mmm*) with the analogous strontium prototype, as confirmed by laboratory and synchrotron powder x-ray diffraction. The diffractogram resultant from the synchrotron analysis is shown in *figure 3.6*. Laboratory PXRD showed the compound to be phase pure, yet small contributing peaks corresponding to the barium sulfide precursor were observed in the synchrotron data.

The geometric parameters relevant to the electronic structure in these compounds, were extracted from the Rietveld refined crystallographic model *(appendix E)* and are presented in *table 3.4* and summarised graphically in *figure 3.7*. It can be seen from inspection of the data in *table 3.4* that the effective substitution of strontium (II) ($^{XII}r_{ionic}$ = 1.44 Å) by barium (1.61 Å) had the predicted effect of expanding the lattice as indicated by the increase in unit cell parameters *a*(=*b*), from 4.08 to 4.14 Å, and *c*, from 25.99 to 27.44 Å. A similar increase from *a* = 4.07 to 4.13 Å and from *c* = 26.88 to 28.63 Å was observed between the analogous iron arsenide compounds $A_3Sc_2O_5Fe_2As_2$ where *A* = Sr and Ba, reported in the literature.[72,78]

The predicted decrease in copper-sulfur bond length and increase in sulfur-copper-sulfur angle from the strontium to barium analogue, expected to increase conductivity was not observed here. Conversely, a large increase in copper-sulfur bond length was observed in addition to a decrease in sulfur-copper-sulfur angle. The effect of the observed alteration in conductive layer geometry on the conductivity could not be qualitatively determined. An increase in copper-sulfur distance was expected to reduce hybridisation and conductivity at the VBM, whereas a decrease in sulfur-copper-sulfur angle towards ideal tetrahedral geometry may have had a competing effect.

The predicted increase in visible transparency relative to the strontium analogue, as determined by the predicted optical band-gap energy of 3.24 eV, was confirmed by measurement of the band gap for the compound $Ba_3Sc_2O_5Cu_2S_2$ from a linear fit to the Tauc plot shown in *figure 3.8*. The calculated band gap energy of 3.24 eV is in exact agreement with that predicted by Williamson.[76] Despite the observed band gap energy being greater than the 3.1 eV threshold, the sample still showed significant colouration, similar to the 'sandy' beige/ light brown colour observed for the strontium analogue synthesised here and reported in the literature.[48] The close agreement between the predicted and observed band gap energy indicates that the electronic band structure is close to that predicted and that $Ba_3Sc_2O_5Cu_2S_2$ may still be a promising candidate transparent p-type conductor in spite of the deviation in observed crystalline geometry in the conductive layer.

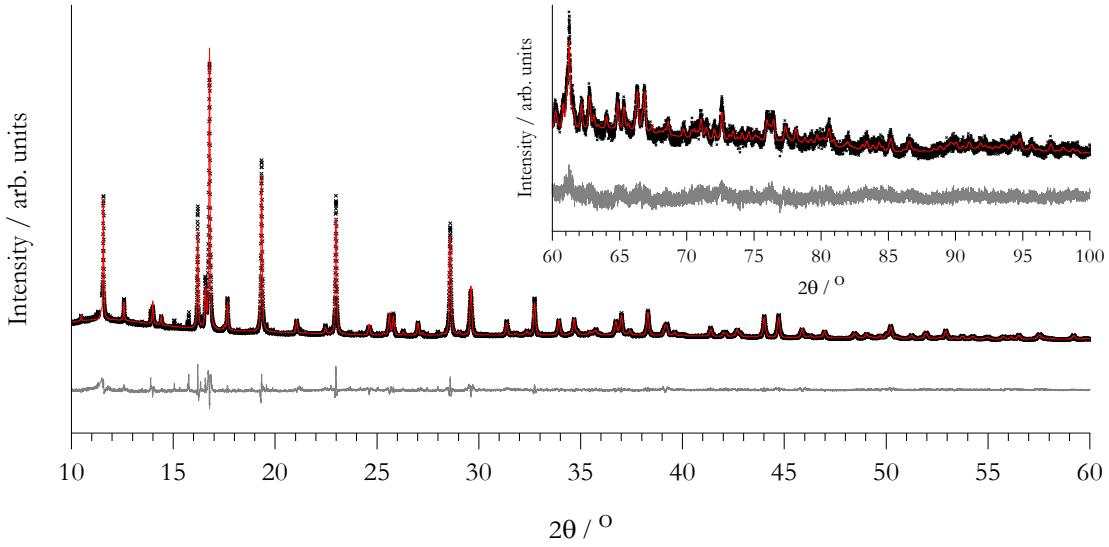

Figure 3.6 *Polycrystalline powder synchrotron x-ray diffraction pattern of the sample with composition $Ba_3Sc_2O_5Cu_2S_2$. Data was collected on the I11 beamline at the Diamond Light Source (λ = 0.826027(10) Å, E = 15 keV and I = 300 mA). Data was collected over a 2θ angular range of 0 - 150 ° at intervals of 0.001 °.The 2θ range 8 - 60 ° and 60 - 100 ° (inset) is shown. The data regions 2θ < 10 ° and 11.35 < 2θ < 11.5 ° were excluded from the refinement. The initial region showed complex background features and the second corresponded to a diffraction peak by the additive used to prevent x-ray absorption. Data was re-binned to 0.003 °. This was deemed suitable to retain peak definition and reduce computation time. The observed data points are represented as black crosses, the calculated profile, the red line and the difference between the two, the grey line. The reflection tick-marks are not shown in the plot as the increased spatial frequency of reflections for the smaller wavelength radiation, rendered many indistinguishable at the current resolution. R_{wp} = 8.85 % and χ^2_{red} = 4.182.*

Table 3.4 *Summary of the lattice parameters and key distances and angles, in terms of the electronic structure, for the prototype and newly synthesised compounds $A_3Sc_2O_5Cu_2S_2$, where A = Sr and Ba, respectively, as determined by various methods (column 1, parentheses).*

Compound (Method)	***a*** **/ Å**	***c*** **/ Å**	**Cu-Cu / Å**	**Cu-S / Å**	**S-Cu-S / °**	**E_g / eV**
$Sr_3Sc_2O_5Cu_2S_2$ (Predicted)[76]	4.08	26.07	2.89	2.45	114.55	3.1
$Sr_3Sc_2O_5Cu_2S_2$ (Literature)[48]	4.08	25.99	2.88	2.49	110.00	3.1
$Ba_3Sc_2O_5Cu_2S_2$ (Predicted)[76]	4.15	27.44	2.94	2.45	115.37	3.24
$Ba_3Sc_2O_5Cu_2S_2$ (Observed here)	4.14462(2)	27.12390(8)	2.92894(9)	2.45532(6)	115.024(3)	3.24

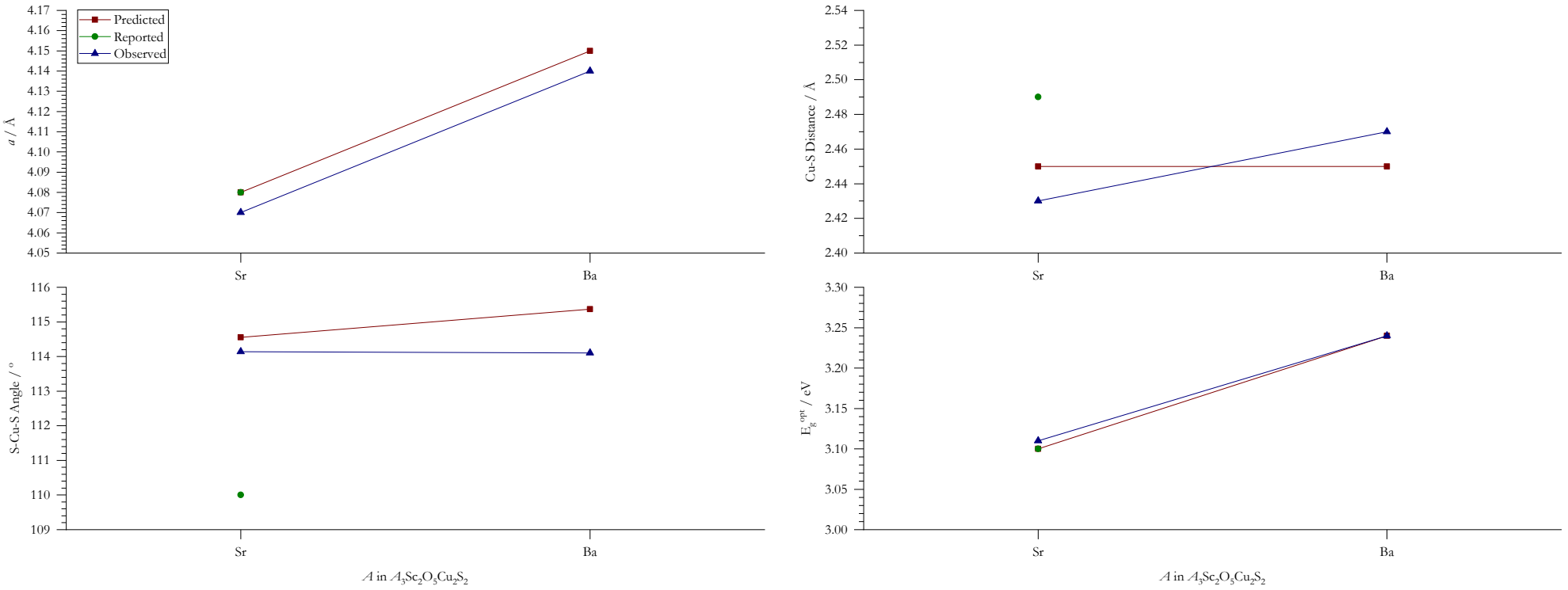

Figure 3.7 *Graphical representation of the data in table 3.4 summarising the lattice parameters and key distances and angles, in terms of the electronic structure; and band-gap energies (see axes titles) for the prototype and newly synthesised compounds $A_3Sc_2O_5Cu_2S_2$, where A = Sr and Ba, respectively, as determined by various methods (see legend).*

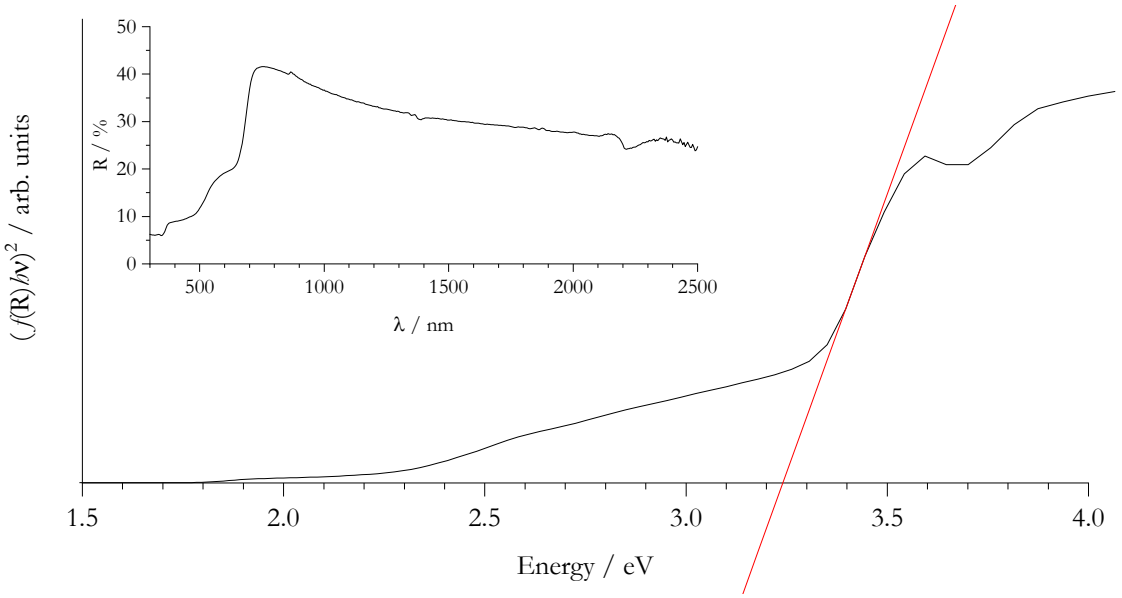

Figure 3.8 *Tauc plot for the compound $Ba_3Sc_2O_5Cu_2S_2$ constructed from the collected raw diffuse reflectance data (inset). The solid red line shows a linear fit to the region of steepest gradient; its x-intercept marking the band gap energy at 3.24 eV.*

3.3.4 $Sr_3Ga_2O_5Cu_2S_2$

When attempting the synthesis of the target compound with the formula $Sr_3Ga_2O_5Cu_2S_2$ at the conventional synthetic conditions of 800 °C for 12 h, it was found that the competing phase, $Sr_4Ga_2O_6Cu_2S_2$, already reported in the literature, was present as the resulting product phase.[79] The resultant x-ray diffraction pattern can be seen in *figure 3.9*. It was expected by Scanlon *et al.* that the 325-type target compound would be the most thermodynamically stable potential component formed from the mixture of elements in the proportions used.

It was proposed that the observed competing phase may have been a meta-stable kinetic product, potentially formed at a faster rate than the target from the precursors used. In order to investigate this, the synthesis of the 325-structured target was attempted at reduced temperature (600 °C) for the same time of 12 h. It can be seen from the resulting diffraction pattern in *figure 3.10 (lower)*, that the competing 426 phase was still present, however, in a lower proportion, compared to the phase $Sr_3Ga_4O_9$ now observed. In order to ensure that the reaction at lower temperature had gone to completion, and in an attempt to observe the predicted thermodynamically stable compound $Sr_3Ga_2O_5Cu_2S_2$ targeted, the sample synthesised at 600 °C for 12 h was recycled for a further 100 h (at 600 °C). The resulting diffraction pattern of the product of the increased-duration synthesis is shown in *figure 3.10 (upper)*. It can be seen that the same mixture of competing phases $Sr_3Ga_4O_9$ and $Sr_4Ga_2O_6Cu_2S_2$ are observed after the much-prolonged synthesis indicating that these are the most thermodynamically stable phases under these conditions.

Despite its synthesis having been previously reported in the literature, the band gap energy of the observed competing layered oxysulfide phase, $Sr_4Ga_2O_6Cu_2S_2$, was not found to have been reported.[79] It was, therefore, decided to attempt the phase-pure synthesis of the 426-type compound to measure its band gap energy and evaluate its potential as a transparent p-type conductor. This is the subject of the following *section 3.3.4.1*.

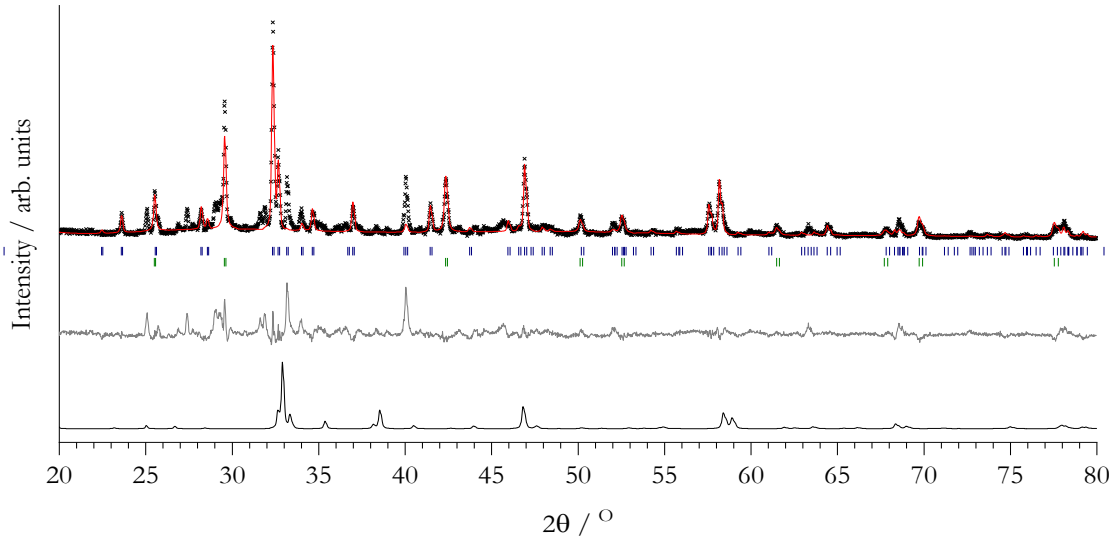

Figure 3.9 *Observed PXRD pattern for products from attempted synthesis of target compound with composition $Sr_3Ga_2O_5Cu_2S_2$. The black crosses illustrate the observed data points, the red line shows the calculated profile from the Rietveld refined model and the grey line is the difference profile between the two. The black profile (lower) shows a predicted pattern calculated from the predicted crystal structure of the target. Observed phases included $Sr_4Ga_2O_6Cu_2S_2$ (blue, 94 wt. %) and SrS (green, 6 wt.%). R_{wp} = 14.82 % and χ^2_{red} = 9.459.*

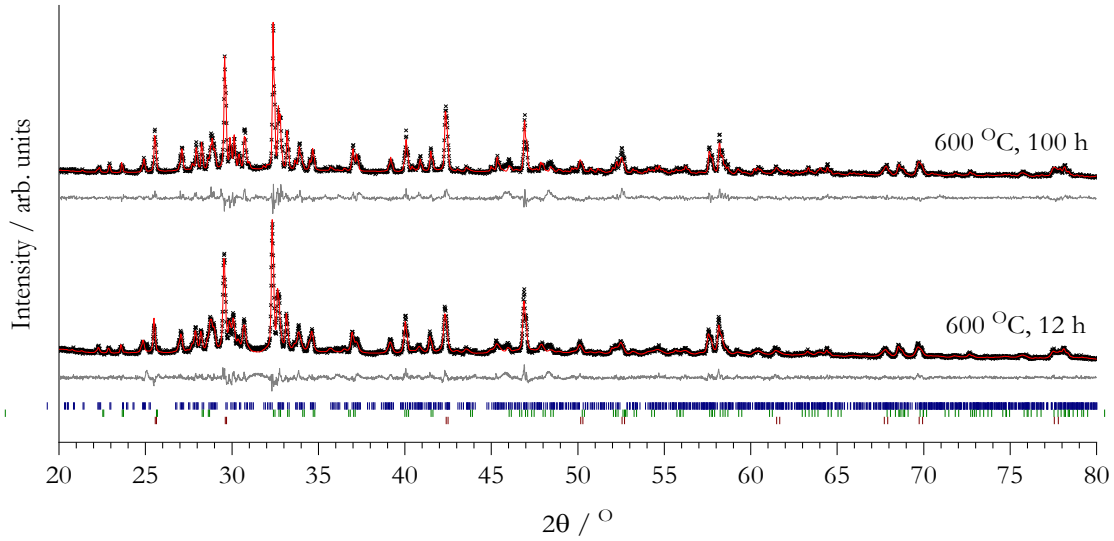

Figure 3.10 *Observed PXRD patterns for products from reduced temperature (600 °C) attempted syntheses of target compound with composition $Sr_3Ga_2O_5Cu_2S_2$ for differing times (12 h, bottom; 100 h, top). The black crosses illustrate the observed data points, the red lines show the calculated profiles from the Rietveld refined models and the grey lines are the differences between the two. Observed phases included $Sr_3Ga_4O_9$ (blue, 53 wt. %), $Sr_4Sc_2O_6Cu_2S_2$ (green, 35 wt. %) and SrS (red, 12 wt.%), after the second cycle at 600 °C (top). R_{wp} = 6.96 % and χ^2_{red} = 2.705.*

3.3.4.1 $Sr_4Ga_2O_6Cu_2S_2$

The compound $Sr_4Ga_2O_6Cu_2S_2$ observed previously as a competing phase in the synthesis of the 325-type analogue, was successfully synthesised as the sole product phase, as determined by PXRD. The same synthetic conditions of 800 °C for 12 h were used, as was the procedure previously described, with the addition of a further stoichiometric equivalent of the SrO precursor. It is noted that this phase-pure synthesis was achieved at a temperature 150 °C lower than that reported in the literature after the same duration of 12 h.[79] The Rietveld refined PXRD pattern for the compound $Sr_4Ga_2O_6Cu_2S_2$ synthesised here is shown in *figure 3.11*.

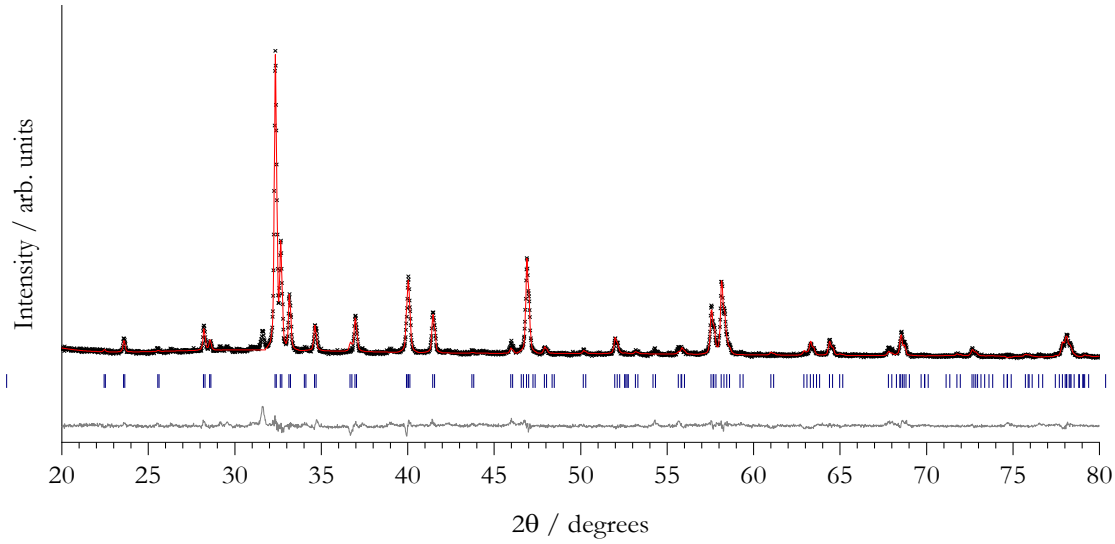

Figure 3.11 *Observed PXRD pattern for products from attempted synthesis of target compound with composition $Sr_4Ga_2O_6Cu_2S_2$ previously reported in the literature The black crosses illustrate the observed data points, the red line shows the calculated profile from the Rietveld refined model and the grey line is the difference between the two. R_{wp} = 9.60 % and χ^2_{red} = 3.561.*

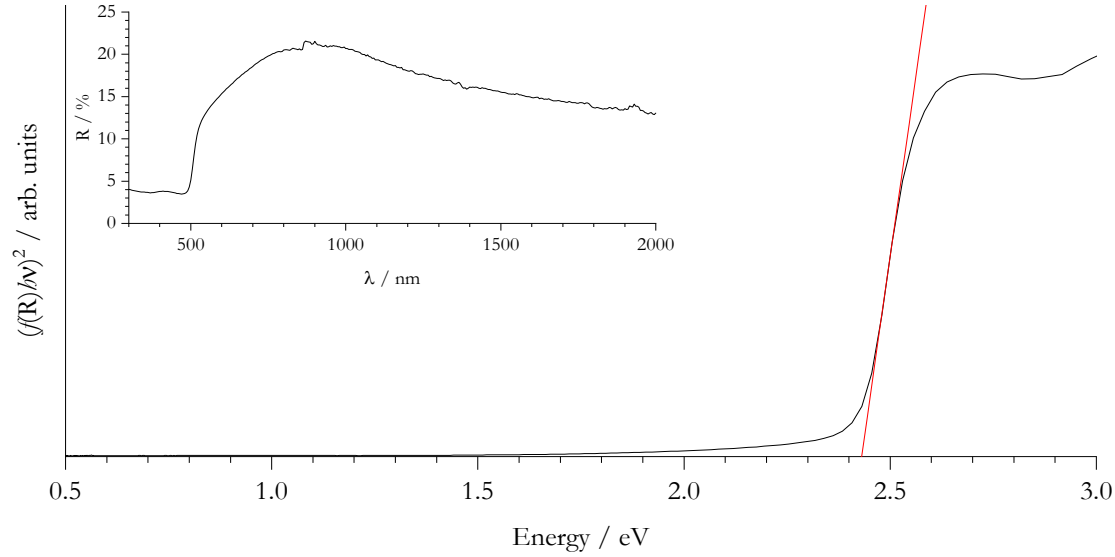

Figure 3.12 *Tauc plot for the literature reported compound with composition $Sr_4Ga_2O_6Cu_2S_2$ constructed from the diffuse reflectance spectrum (inset) indicating the experimentally calculated band gap energy of 2.42 eV, as given by the point at which the linear fit (red) intercepts the abscissa.*

Table 3.5 Comparison of the lattice parameters and key distances and angles, in terms of the electronic structure, for the compounds $Sr_3Sc_2O_5Cu_2S_2$ and $Sr_4Ga_2O_6Cu_2S_2$, respectively.

Compound	a / Å	c / Å	Cu-Cu / Å	Cu-S / Å	S-Cu-S / °	E_g / eV
$Sr_3Sc_2O_5Cu_2S_2$ [48]	4.08	25.99	2.88	2.49	110.00	3.1
$Sr_4Ga_2O_6Cu_2S_2$ [79]	3.86	15.73	2.73	2.43	124.15	2.4*

The sample appeared a light brown/beige colour, similar to that of $Sr_3Sc_2O_5Cu_2S_2$. Its fundamental band gap energy was measured by diffuse reflectance *(figure 3.12)*. The band gap, not found to have been previously reported, was measured here to be 2.42 eV. This may have been due in part, to the reduced copper-copper interatomic distance and copper-sulfur bond length in the crystal structure. (Selected lattice parameters, bond lengths and angles, and band gap energies are provided in *table 3.5*.) The smaller ionic radius gallium (III) ion had the effect of reducing the basal lattice parameter and compressing the flexible conductive layer. Most notably, was the increase in sulfur-copper-sulfur angle away from that of an ideal tetrahedron. While the competing effects of the reduced copper-sulfur distance and the increased sulfur-copper-sulfur angle on the hybridisation and conductivity at the VBM could not be quantitatively determined, the large increase in angle and reduced band gap is likely to preclude the compound $Sr_4Ga_2O_6Cu_2S_2$ from application as a transparent p-type conductor.

3.3.5 Attempted Synthesis of Remaining Analogous Compounds

The syntheses of the remaining members of the shortlist of compounds predicted to be stable with general formulae $A_3M_2O_5Cu_2S_2$, where AM = CaSc, CaGa, SrAl, BaAl and BaGa, were attempted using the experimental process described previously. The heating process was continued in cycles until consistent PXRD patterns were observed. In each case a single cycle was sufficient to observe the phases deemed to be the final stable products for each composition. The observed PXRD patterns *(figures 3.13 to 3.17)* were fitted to known crystallographic phases using the Rigakuu PDXL2 software package and the ICSD. PXRD patterns were phase-matched and refined as far as possible; however, in many cases some peaks remain unattributed to known crystalline phases. In each case, simple (binary or tertiary) apparently competing crystalline phases were observed in place of the intended compound.

* *The band gap energy was not reported in the referenced literature and was determined experimentally here.*

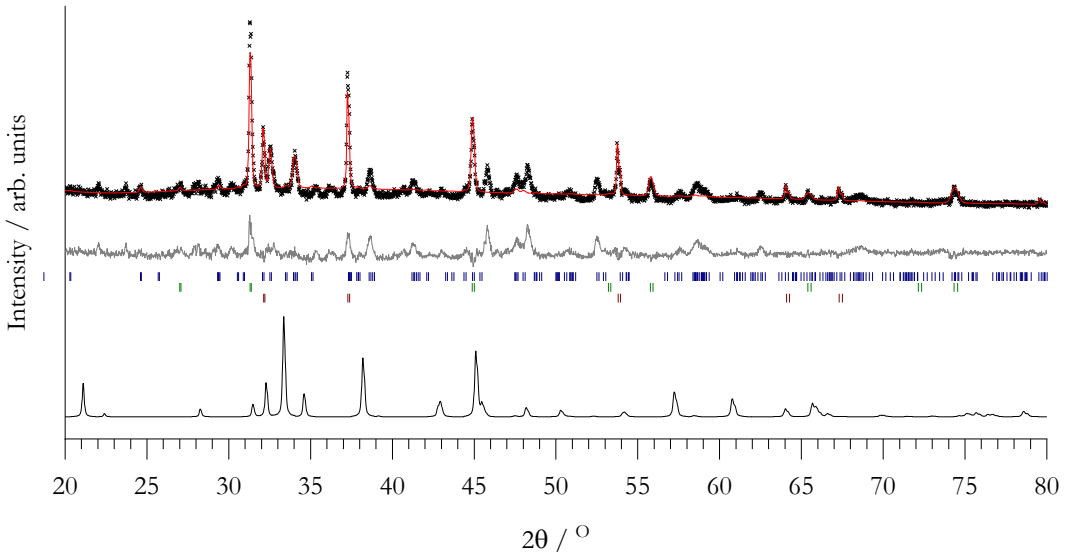

Figure 3.13 *Observed PXRD pattern for products from attempted synthesis of target compound with composition $Ca_3Sc_2O_5Cu_2S_2$. The black crosses illustrate the observed data points, the red line shows the calculated profile from the Rietveld refined model and the grey line is the difference between the two. The black profile (bottom) shows a predicted pattern calculated from the predicted crystal structure of the target. Observed phases included $CaSc_2O_4$ (blue, 70 wt. %), CaS (green, 16 wt.%) and CaO (red, 14 wt.%). R_{wp}= 13.98 % and χ^2_{red} = 5.585.*

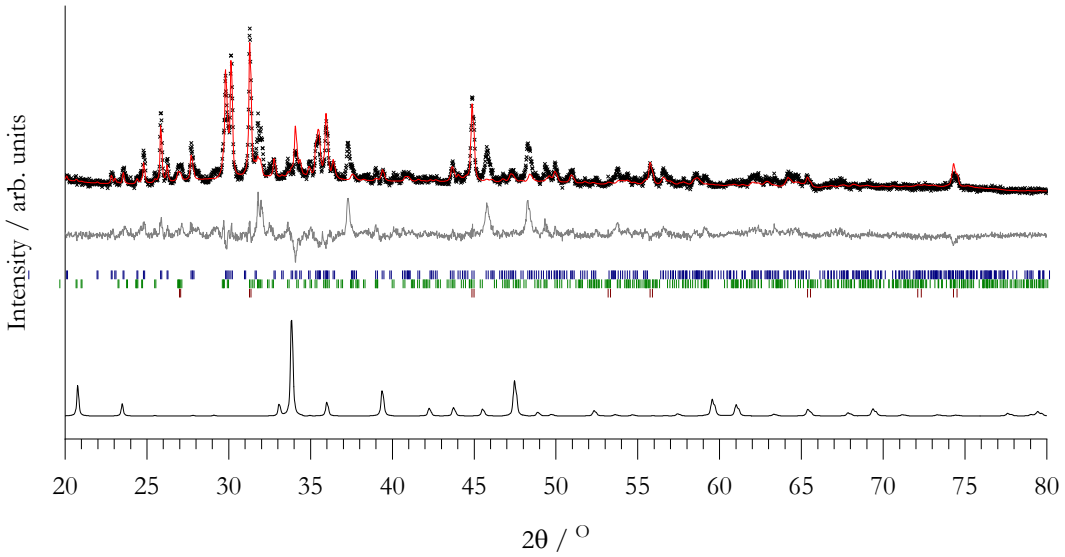

Figure 3.14 *Observed PXRD pattern for products from attempted synthesis of target compound with composition $Ca_3Ga_2O_5Cu_2S_2$. The black crosses illustrate the observed data points, the red line shows the calculated profile from the Rietveld refined model and the grey line is the difference between the two. The black profile (bottom) shows a predicted pattern calculated from the predicted crystal structure of the target. Observed phases included $Ca_3Ga_2O_6$ (blue, 47 wt. %), $Ca_3Ga_4O_9$ (green, 41 wt.%) and CaS (red, 13 wt.%). R_{wp} = 12.75 and χ^2_{red} = 6.221.*

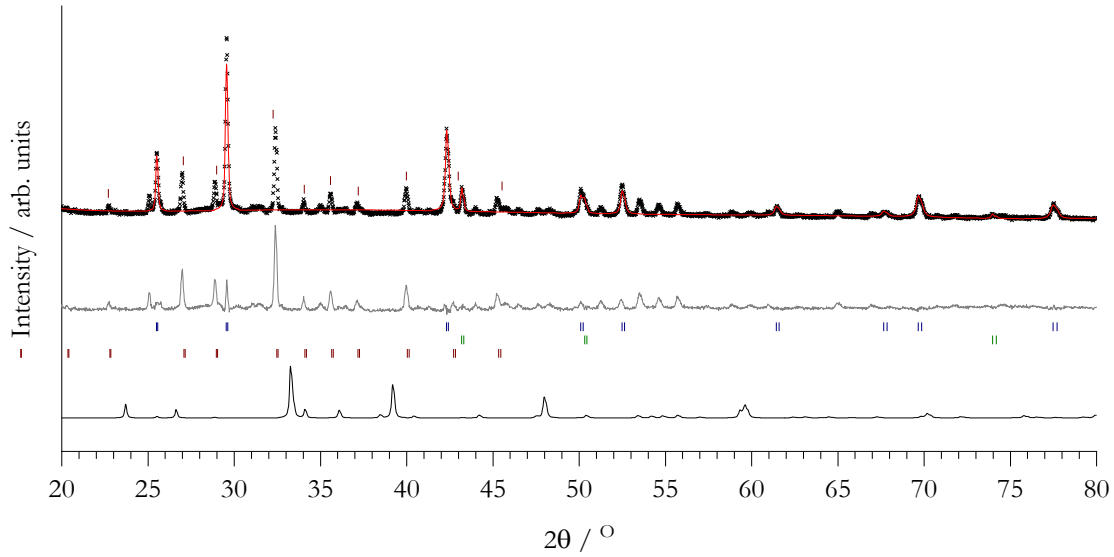

Figure 3.15 *Observed PXRD pattern for products from attempted synthesis of target compound with composition $Sr_3Al_2O_5Cu_2S_2$. The black crosses illustrate the observed data points, the red line shows the calculated profile from the Rietveld refined model and the grey line is the difference between the two. The black profile (bottom) shows a predicted pattern calculated from the predicted crystal structure of the target. Observed phases included SrS (blue, 88 wt. %) and Cu (green, 12 wt.%). R_{wp} = 18.78 and χ^2_{red} = 14.68. The observed diffraction pattern was also matched to the phase $Sr_{12}Al_{14}O_{33}$ (red). The 2θ positions were gathered from analysis conducted by Yamuguchi as no crystallographic information file or crystal structure data suitable for its construction could be found.*[80] *The diffraction data extracted from the reference apparently only covered a 2θ range of around 17 – 46 °.*

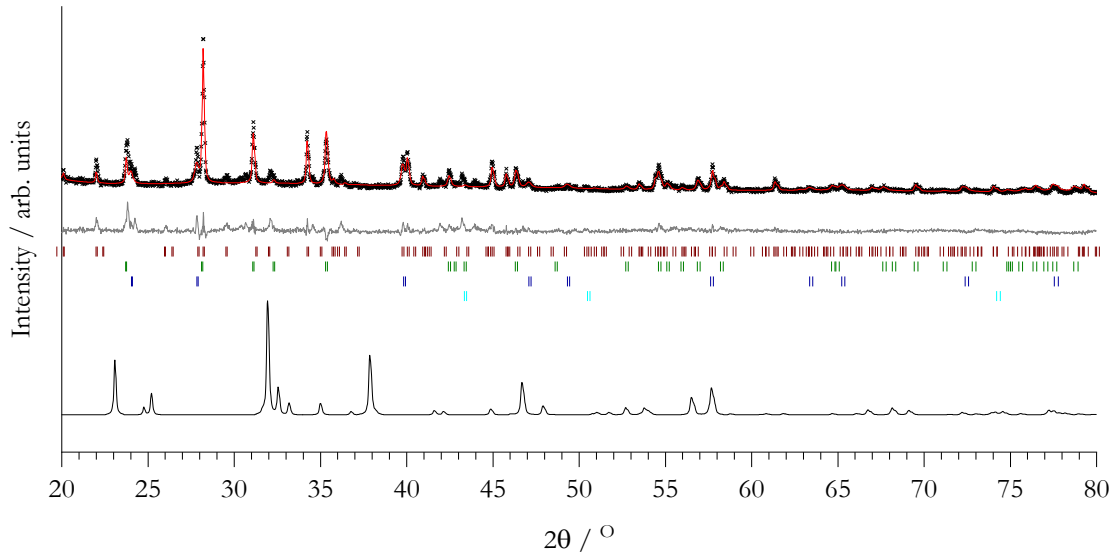

Figure 3.16 *Observed PXRD pattern for products from attempted synthesis of target compound with composition $Ba_3Al_2O_5Cu_2S_2$. The black crosses illustrate the observed data points, the red line shows the calculated profile from the Rietveld refined model and the grey line is the difference between the two. The black profile (bottom) shows a predicted pattern calculated from the predicted crystal structure of the target. Observed phases included Al_2BaO_4 (red, 38 wt. %), $BaCu_2S_2$ (green, 37 wt. %). BaS (blue, 20 wt. %) and Cu (cyan, 4 wt. %). R_{wp} = 13.79 and χ^2_{red} = 4.969.*

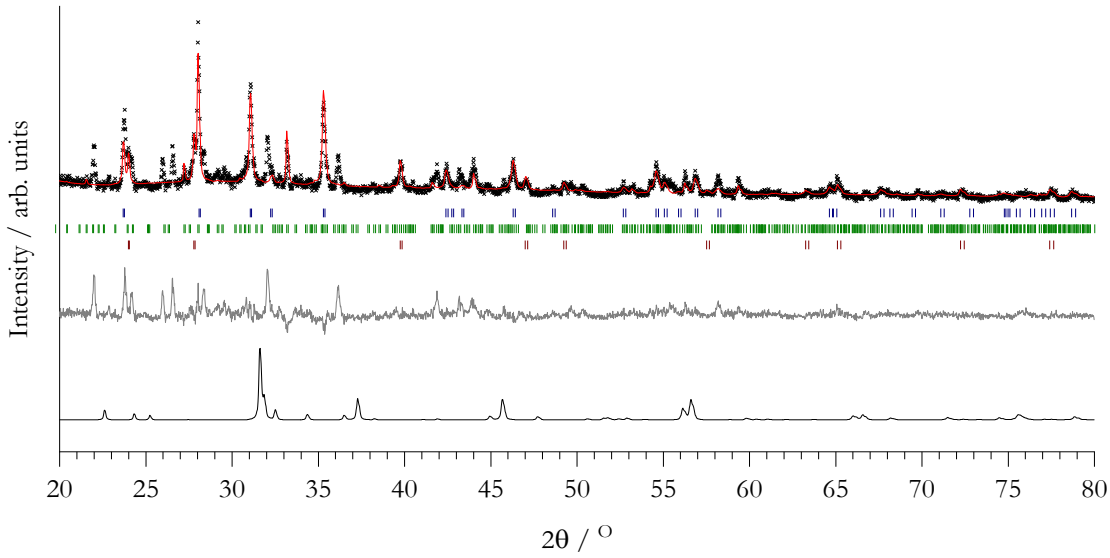

Figure 3.17 Observed PXRD pattern for products from attempted synthesis of target compound with composition $Ba_3Ga_2O_5Cu_2S_2$. The black crosses illustrate the observed data points, the red line shows the calculated profile from the Rietveld refined model and the grey line is the difference between the two. The black profile (bottom) shows a predicted pattern calculated from the predicted crystal structure of the target. Observed phases included $BaCu_2S_2$ (blue, 60 wt. %), $BaGa_2O_4$ (green, 30 wt. %) and BaS (red, 10 wt.%). R_{wp} = 15.34 and χ^2_{red} = 4.210.

3.4 Conclusions and Outlook

The thermodynamic stability of the compounds $A_3M_2O_5Cu_2S_2$ (where A = Mg, Ca, Sr and Ba; and M = Al, Sc, Ga, Y, In and La) were predicted by Williamson and Scanlon. Eight were predicted to be stable in addition to the strontium/scandium prototype already reported in the literature. The synthesis of these nine compounds was attempted. Three of the eight, including the prototype, were expected to possess optical band gap energies above the 3.1 eV visible light threshold. The additional compounds had the formulae $Ca_3Al_2O_5Cu_2S_2$ and $Ba_3Sc_2O_5Cu_2S_2$ and their syntheses were attempted initially.

In order to confirm the effectiveness of the synthetic procedure, the syntheses of the prototype compound $Sr_3Sc_2O_5Cu_2S_2$ already reported in the literature was attempted. It proved successful as monitored by powder x-ray diffraction. The structural geometries conformed to those predicted and previously reported apart from the sulfur-copper-sulfur angle. The value reported in the literature differed by ≈ 4° from that predicted by Williamson and confirmed here. The band gap energy as measured by diffuse reflectance spectrophotometry was in good agreement with that previously reported and predicted.

The compound $Ca_3Al_2O_5Cu_2S_2$ predicted stable and transparent was not realised here. The synthesis resulted in the observation of simple binary oxide and sulfide precursor phases with significant contribution of $Al_{14}Ca_{12}O_{33}$. Iron pnictides sharing the same perovskite-like layer with the target, $[Ca_3Al_2O_5]^{2+}$, were reported in the literature. Their syntheses, however, required high-pressure. The predicted unit cell volume of the target compound was larger than those synthesised under high pressure yet smaller than that of $Sr_3Fe_2O_5Cu_2S_2$, the analogous compound with the smallest unit cell volume reported to have been synthesised under conventional pressure. These findings indicated that the target transparent conductor compound $Ca_3Al_2O_5Cu_2S_2$ may be amenable to high-pressure synthesis.

The attempted synthesis of the compound $Ba_3Sc_2O_5Cu_2S_2$ resulted in the observation of a new candidate transparent conductor as confirmed by synchrotron powder x-ray diffraction. Its band gap energy of 3.24 eV was in exact agreement with that predicted, showing promise towards transparency. This indicated that its predicted band structure and therefore high conductivity, was close to that observed, despite the discrepancy in trend in copper-sulfur bond length and sulfur-copper-sulfur angle between the strontium prototype and barium analogues.

The attempted synthesis of the targeted compound $Sr_3Ga_2O_5Cu_2S_2$ persistently resulted in the observation of the related layered perovskite oxysulfide, $Sr_4Ga_2O_6Cu_2S_2$, previously reported in the literature. The band gap energy of this compound could not be found in the literature. The synthesis of the 426 structure-type analogue was targeted and successfully achieved. The band gap energy of the compound was measured experimentally and reported here to be 2.42 eV, a value undesirable for high visible-light transparency.

The syntheses of the remaining compounds predicted to be stable; $Ca_3Sc_2O_5Cu_2S_2$, $Ca_3Ga_2O_5Cu_2S_2$, $Sr_3Al_2O_5Cu_2S_2$, $Ba_3Al_2O_5Cu_2S_2$ and $Ba_3Ga_2O_5Cu_2S_2$, were attempted without success. The observed crystalline phases identified in the case of each targeted compound are summarised in *table 3.6*.

In the case of the barium aluminium composition, the observed crystalline phases were consistent with those expected by Williamson et al. with the addition of $BaCu_2S_2$. The expected $BaSO_4$ was not observed, however. The phases predicted from the expectedly unstable Ca/Sc compound differed from those found experimentally with the presence of CaS being the only similarity. The other combinations were expected to be the most thermodynamically stable possible phases at the synthetic temperatures used.

Table 3.6 *Summary of the crystalline product phases observed after attempted solid-state synthesis of targeted oxychalcogenides $A_3M_2O_5Cu_2S_2$ where A = Ca, Sr and Ba and M = Al, Sc and Ga. Observed phase compositions are reported in order of decreasing weight fraction as calculated from the Rietveld refined calculated diffraction profile.*

***A* Cation**	***M* Cation**	**Observed Phase(s) Composition**
Ca	Al	Al_2O_3, CaO, $Al_{12}Ca_{14}O_{33}$ and CaS
	Sc	$CaSc_2O_4$, CaS and CaO
	Ga	$Ca_3Ga_2O_6$, $Ca_3Ga_4O_9$ and CaS
Sr	Al	SrS, Cu and $Al_{14}Sr_{12}O_{33}$
	Sc	$Sr_3Sc_2O_5Cu_2S_2$
	Ga	$Sr_4Ga_2O_6Cu_2S_2$ and SrS
Ba	Al	$BaAl_2O_4$, $BaCu_2S_2$, BaS and Cu
	Sc	$Ba_3Sc_2O_5Cu_2S_2$
	Ga	$BaCu_2S_2$, $BaGa_2O_4$ and BaS

Chapter 4 Conductive Layer Geometry Modification by Isovalent Mixing of Perovskite *A* Cations

4.1 Introduction

The perovskite 'building-block' of the layered oxychalcogenides reported here, shows compositional flexibility. The analogous layered oxychalcogenides and oxypnictides with the 325 structure type found to be reported in the literature, contain seven different combinations of perovskite cations, namely: calcium, aluminium[73]; strontium, iron[70]; strontium, scandium[49]; europium, scandium[74]; barium, scandium[72]; barium, lutetium[69]; and barium, yttrium[69]. In addition to the range of elements reported in 'site-pure' 325-type mixed anion oxides, mixing of the pairs of elements aluminium, titanium[81]; magnesium, titanium[82]; and scandium, titanium[72] was reported in the similar layered iron oxyarsenide compounds $Ca_4(Al_{0.67}Ti_{0.33})_2O_6Fe_2As_2$, $Sr_4(Mg_{0.5}Ti_{0.5})_2O_6Fe_2As_2$ and $Sr_4(Sc_xTi_{1-x})_3O_8Fe_2As_2$, where x = 0.4, 0.5 and 0.6. This confirmed that although the substitution was shown to occur on the *M* perovskite cation site and the titanium transition metal exhibited varying oxidation state, the perovskite could support significant mixing, of up to 50 %, of different cations in these layered mixed anion structures.

Isovalent cation mixing on the perovskite *A* site has been previously reported, for example between strontium and barium in the compounds $Sr_{2-x}Ba_xCoO_2Cu_2S_2$ and $Ba_{2.6}Sr_{1.4}Mn_4O_8Cu_2S_2$.[83,84] Complete substitution of strontium for barium in the prototype compound $Sr_3Sc_2O_5Cu_2S_2$ reported by Liu *et al.*, to yield the analogous compound $Ba_3Sc_2O_5Cu_2S_2$, was reported by the current author in the previous chapter. It was shown that the increased radius of $^{XII}Ba^{2+}$ (1.61 Å), *c.f.* $r_{ionic}(^{XII}Sr^{2+})$ = 1.41 Å, had the effect of increasing the basal lattice parameter (from 4.08 to 4.14 Å) and therefore, copper-copper distance required to raise the energy of the CBM, desirable for high visible transparency.[85] An increase in band gap energy from 3.11 to 3.24 eV was observed.

It was decided that the phase space between the prototype and analogous compounds $Sr_3Sc_2O_5Cu_2S_2$ and $Ba_3Sc_2O_5Cu_2S_2$ respectively, would be investigated with a focus on the effect of cation mixing in the perovskite layer on the geometry and therefore optoelectronic properties of the conductive copper sulfide layer. The present chapter reports on the synthesis of two intermediate compounds in the phase space $Ba_xSr_{3-x}Sc_2O_5Cu_2S_2$, where x = 1 and 2.

4.2 Experimental

The syntheses of compounds with compositions $Ba_xSr_{3-x}Sc_2O_5Cu_2S_2$, where x = 1 and 2 were attempted in bulk powder form using the same solid-state synthetic procedure as is described in *section 3.2*. The end-members where x = 0 and 3 had already been synthesised. The powder precursors were combined in the stoichiometric ratios given in *equations 4.1 and 4.2*, mixed and ground into homogeneous powders. They were then pressed into pellets (≈ 0.75 GPa), loaded into oven-dried (70 °C) alumina crucibles, sealed under static vacuum in quartz tubes and subsequently heated in a box furnace at a rate of 10 °C min^{-1} to 800 °C, at which point the temperature was held for 12 h before cooling naturally to room temperature. The preparations were carried out under inert atmosphere owing to the moisture and carbon dioxide sensitivity of the oxide and sulfide precursors. The precursors Sc_2O_3 (99.9 % Sigma-Aldrich) and Cu_2S (99.5 % Alfa Aesar) were purchased and used as supplied. The alkaline earth oxides (BaO and SrO) and sulfides (BaS and SrS) were synthesised from their corresponding carbonates *(appendices D.1 and D.2)*.

x = 1 $$2\,SrO + BaS + Sc_2O_3 + Cu_2S \rightarrow BaSr_2Sc_2O_5Cu_2S_2 \quad (4.1)$$

x = 2 $$2\,BaO + SrS + Sc_2O_3 + Cu_2S \rightarrow Ba_2SrSc_2O_5Cu_2S_2 \quad (4.2)$$

4.3 Results and Discussion

4.3.1 Evidence for the Successful Single-Phase Mixing of Perovskite *A* Site Cations

The synthesis of the compounds $BaSr_2Sc_2O_5Cu_2S_2$ and $Ba_2SrSc_2O_5Cu_2S_2$ (intermediates in the phase space $Ba_xSr_{3-x}Sc_2O_5Cu_2S_2$, where $x = 1$ and 2) after a single heating cycle at 800 °C for 12 h is reported here. Refinement of models, isostructural to the $x = 0$ and 3 strontium and barium end-members, to the intermediates, for which $x = 1$ and 2 respectively, successfully modelled all of the observed diffraction peaks as can be seen in *figure 4.1*. The diffraction patterns for the intermediate compounds were initially modelled by the crystal structures of the end-members closest in composition *i.e.* $BaSr_2Sc_2O_5Cu_2S_2$ ($x = 1$) by $Sr_3Sc_2O_5Cu_2S_2$ ($x = 0$) and $Ba_2SrSc_2O_5Cu_2S_2$ ($x = 2$) by $Ba_3Sc_2O_5Cu_2S_2$ ($x = 3$). Refinement of the unit cell parameters revealed an increase for $x = 1$ relative to the strontium end-member and a decrease for $x = 2$ compared to the barium end-member, indicating successful incorporation of the two perovskite *A* site cations in a single phase for each of the intermediates. The refined unit cell parameters $a=b$, c and the resulting volume, V, are summarised graphically in *figure 4.2* in addition to those of the end-members.

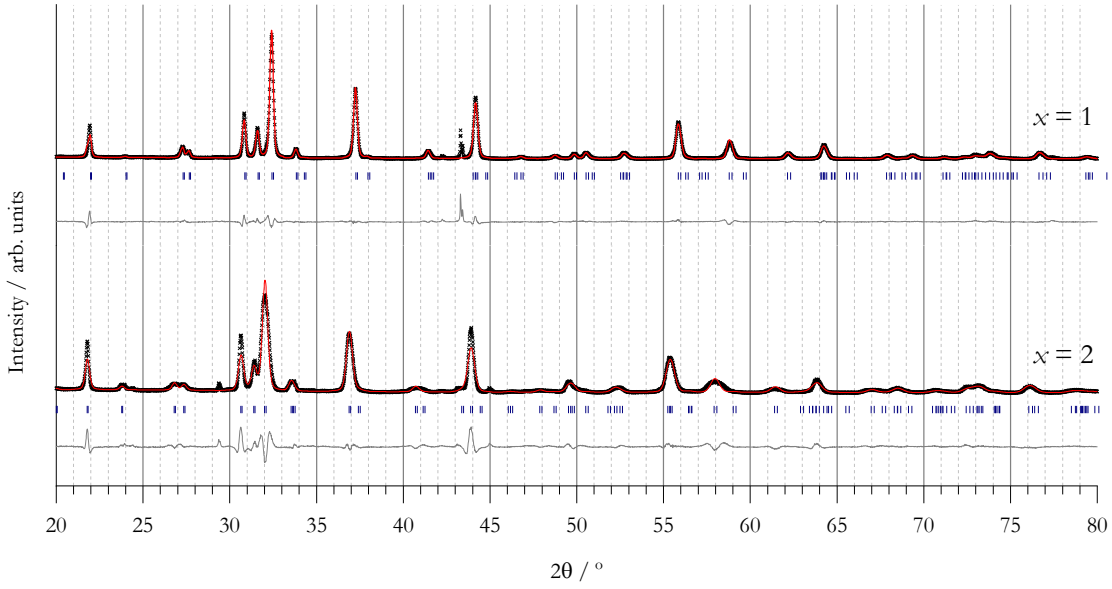

Figure 4.1 *Rietveld refined powder x-ray diffraction patterns for the compounds in the homologous series $Ba_xSr_{3-x}Sc_2O_5Cu_2S_2$, where $x = 1$ and 2. The diffraction measurements were performed on pulverised bulk samples using the higher flux (9 kW) Rigaku SmartLab with observed intensity collected across a 2θ range of 20 – 80 °.*

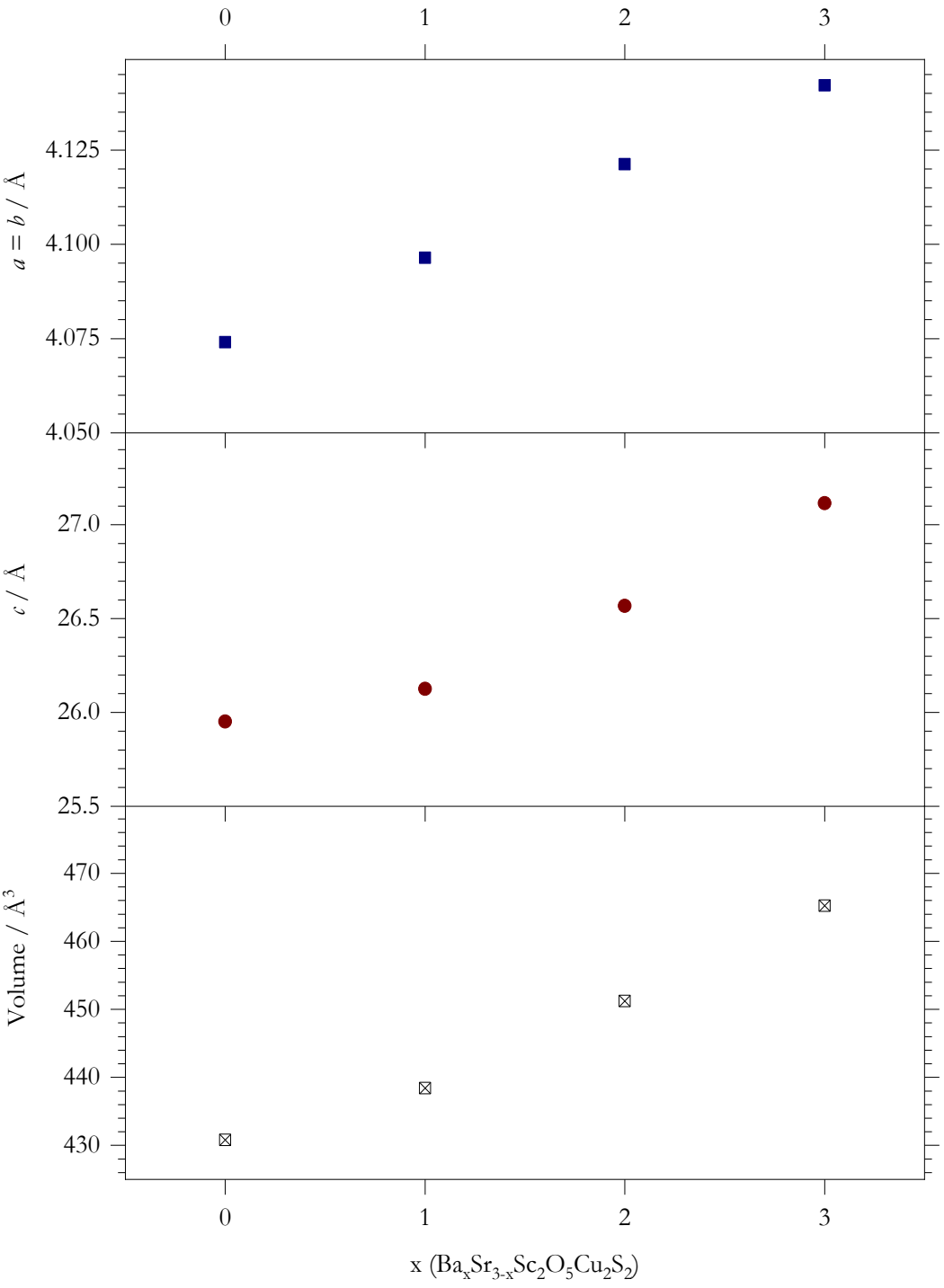

Figure 4.2 *Summary of the trend in unit cell parameters a=b (blue squares; top), c (red circles; middle) and V (crossed squares; bottom), for the series of compounds $Ba_xSr_{3-x}Sc_2O_5Cu_2S_2$, where x = 0, 1, 2 and 3. The raw data used in this plot is provided in appendix F.1.*

The increase in unit cell volume, V, with increasing nominal barium content, x, confirms the successful substitution of the strontium ions by the barium with larger ionic radii, $r_{ionic}(^{XII}Sr^{2+})$ = 1.41 Å *c.f.* $r_{ionic}(^{XII}Ba^{2+})$ = 1.61 Å.[85] The trend in the basal direction was found to be linear, reflecting the rigidity of the perovskite building-block that limited expansion in this dimension.

In order to seek further evidence for the successful incorporation of both strontium and barium of the A cation sites, the fractional occupancies of the A cations in the modified end-member composition models of the intermediate compounds were refined without constraint. The results of these refinements are shown in *table* 4.1, with the refined fractional occupancies in the end-members shown for comparison.

Table 4.1 *Summary of the freely refined fractional occupancies of the A site cations in the series of compounds $Ba_xSr_{3-x}Sc_2O_5Cu_2S_2$, where x = 0, 1, 2 and 3. The fit statistics are also provided. The intermediate compounds where x = 1 and 2 were modelled by the unmixed end-member closest in composition i.e. x = 1 was modelled with a composition equal to x = 0 and x =2 by x = 3.*

Nominal Composition, *x* **($Ba_xSr_{3-x}Sc_2O_5Cu_2S_2$)**	***A*1**	***A*2**	**R_{wp} / %**	**χ^2_{red}**
	***A* = Sr**			
0	1.0061	0.9966	21.31	33.34
1	1.3832	1.0508	14.47	11.43
	***A* = Ba**			
2	1.0044	0.8607	21.97	22.00
3	1.0164	1.008	14.11	9.005

It can be seen from the refined A site fractional occupancies for the intermediate compound where x = 1, that there is an overall tendency of the occupancy to increase relative to the strontium-only end-member, the composition of which is used in the model. The increase in fractional occupancy to values greater than unity is physically unrealistic, however, suggests that a better fit to the observed diffraction data is achieved by increasing the electron density on the A sites. This expected increased electron density on the A sites gives evidence for the incorporation of the higher atomic number barium. The converse is observed for the refined fractional occupancies of barium in the compound where x = 2. A reduction in electron density is observed, indicating substitution in the crystal structure for the relatively lower-Z strontium.

It was noted that the changes in fractional occupancies across the two crystallographically unique *A* cation sites, *A*1 and *A*2, did not change in proportion to one another. This indicated that the mixed *A* cation elements strontium and barium were not evenly distributed across the two sites. To probe this further, both strontium and barium were incorporated into the models for the intermediate compounds for which $x = 1$ and 2. Their occupancies were set to match the nominal composition and were initially set to show an even distribution across the two *A* sites as illustrated in *figure 4.3*. The fractional occupancies were constrained to maintain the overall nominal composition in the compound and the *A* sites assumed fully occupied. The atomic coordinates of the *A* site cations were also constrained to maintain single sites for *A*1 and *A*2. The fractional occupancies and atomic coordinates of the *A* cations were then refined. Those which achieved the best fit, as determined by the fit statistics (provided), are summarised in *figure 4.4* and *table 4.2*.

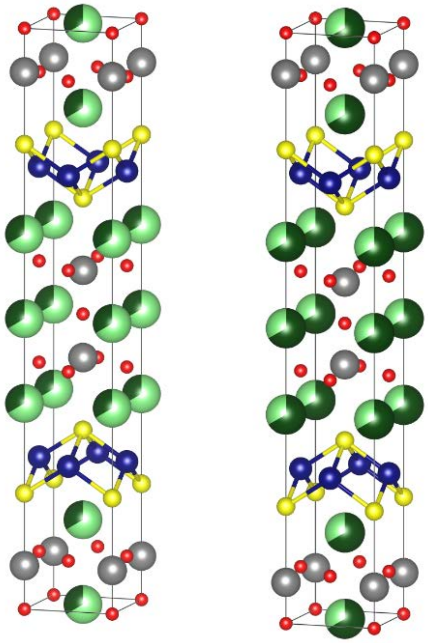

Figure 4.3 *Representation of the initial crystallographic model used in the refinement of the mixed A compounds* $Ba_xSr_{3-x}Sc_2O_5Cu_2S_2$ *where* $x = 1$ *(left) and 2 (right) showing the expected even distribution of strontium (light green) and barium (dark green) across the A perovskite cation sites (green) and constraint of the elements to both occupy crystallographic sites with the same coordinates.*

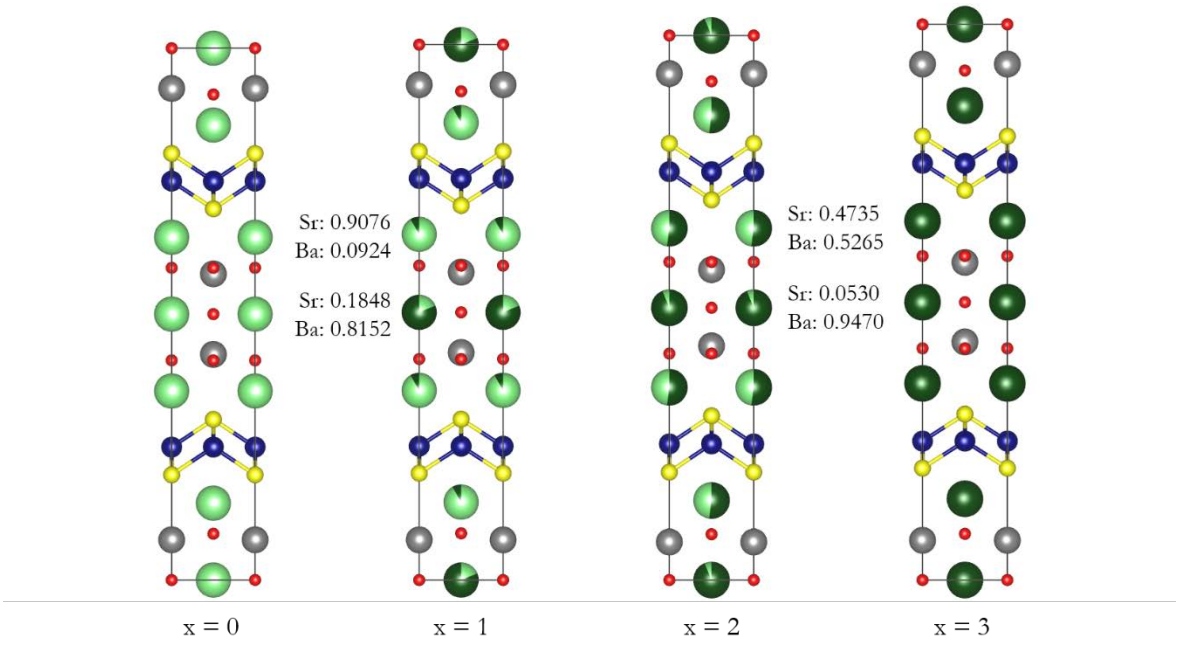

Figure 4.4 *Visual summary of refined fractional occupancies of A site cations barium (dark green) and strontium (light green) in the compounds $Ba_xSr_{3-x}Sc_2O_5Cu_2S_2$, where x = 1 and 2. Those of the end-members are shown for comparison.*

Table 4.2 *Summary of refined fractional occupancies of cations barium and strontium across the A perovskite-like layer crystallographic sites in the compounds $Ba_xSr_{3-x}Sc_2O_5Cu_2S_2$, where x = 1 and 2.*

Nominal Composition, x ($Ba_xSc_{3-x}Sc_2O_5Cu_2S_2$)	Sr1	Sr2	Ba1	Ba2	R_{wp} / %	χ^2_{red}
1	0.1848	0.9076	0.8152	0.0924	12.45	8.90
2	0.0530	0.4735	0.9470	0.5265	30.75	19.64

It can be seen that the fractional occupancy of the *A*1 site remained high while the 'remaining' mixture of *A* elements was spread across the *A*2 sites for both compounds where x = 1 and 2. This was rationalised by invocation of the 'Goldschmidt tolerance factor', described in *appendix G*. This factor semi-empirically describes the expected stability of cubic perovskites comprising given combinations of elements. The factor is calculated using the ionic radii of the given elements and effectively describes their fit with one another in a cubic perovskite lattice. Values closest to unity are expected to most likely yield stable perovskite structures. The Goldschmidt tolerance factors were calculated for the hypothetical perovskite moieties $[SrScO_3]^-$ and $[BaScO_3]^-$ and were found to be 0.94 and 0.99, respectively. This indicates a 'better' fit of the barium cations into a scandium oxide perovskite-like lattice, compared to that of strontium.

Closer inspection of each of the *A* cation sites, reveals that they have different local coordination environments. The *A*1 sites shown in dark green in *figure 4.5,* lie within the perovskite layer and are as such termed 'intra-layer' sites herein. The *A2* sites (light green) lie between the perovskite and litharge-like layers and are, as such, named 'inter-layer' sites. The intra-layer *A* cations exhibit immediate coordination environments identical to those in bulk perovskite lattices, namely $[A_{intra}O_6]$ octahedra, whereas the inter-layer *A* cations border the copper sulfide litharge-like layer and as such are found in $[A_{inter}O_4S_4]$ square anti-prismatic geometry. It was therefore concluded that the mixed *A* element compounds had crystallised in their most stable form which included the 'better' fitting barium cation predominately occupying the more rigid *A* intra-layer sites. The 'poorer' fitting strontium (and any remaining barium) was found to be mainly distributed across the *A* inter-layer sites in coordination with the copper sulfide layer shown to be more flexible and stable in a wider range of geometries.[49] The idealised observed occupancies are represented in *figure 4.6*.

Analysis of the Goldschmidt tolerance factor shed light on the observed trend in *c* unit cell parameter with increasing barium content, *x (figure 4.2)*. It was suggested that a two-gradient function could be fitted to the observed trend in *c*, increasing linearly from x = 0 to 1 where a change in gradient is observed, then continuing to increase linearly from x = 1 to 3 as shown in the plot. This was explained by substitution on the intra-layer site until x = 1, after which substitution occurred at the inter-layer position.

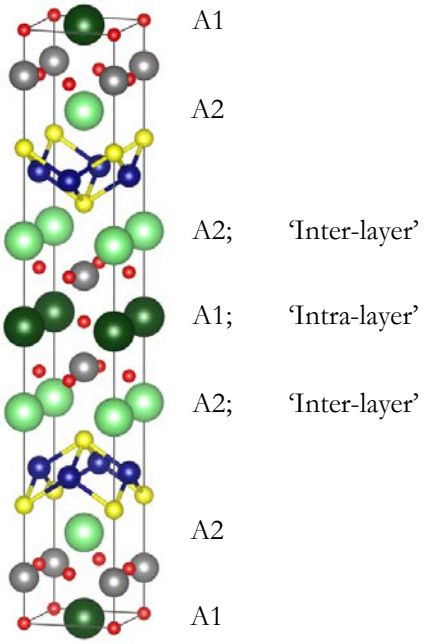

Figure 4.5 *Unit cell representation, shown mainly along 'a', of the crystal structure of the $A_3M_2O_5M'_2Ch_2$ family of quinary oxychalcogenide compounds crystallising into a lattice described by the tetragonal I4/mmm space group. The A cations (green) occupy two crystallographically unique sites: A1 'intra-layer' (dark green) and A2 'inter-layer' (light green).*

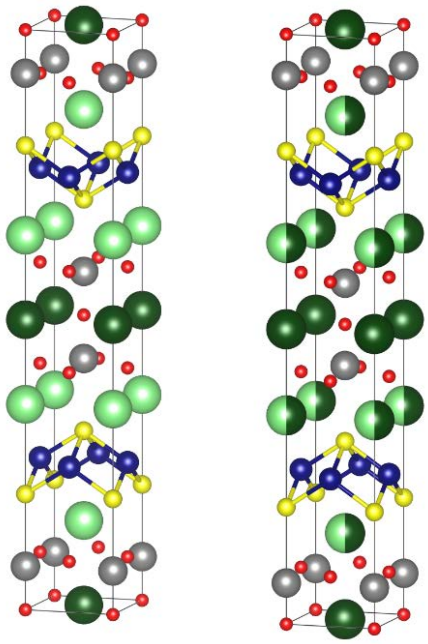

Figure 4.6 *Graphical representation of the unit cell, viewed mainly along 'a', illustrating the idealised most stable distribution of strontium (light green) and barium (dark green) mixing across the A cation sites (green) in the layered oxysulfide compounds $Ba_xSr_{3-x}Sc_2O_5Cu_2S_2$ where $x = 1$ (left) and 2 (right), as predicted by the Goldschmidt tolerance factor.*

4.3.2 Effect of Perovskite *A*-Site Cation Mixing on the Geometry of the Copper Sulfide Layer

In order to investigate the effect of the perovskite *A* cation isovalent mixing on the geometry of the conductive copper sulfide layer and, therefore, the optoelectronic properties of the compound, the refined unit cell parameters and atomic coordinates *(appendices F.1 and F.2)* for the compounds were used to calculate the distances and angles between atoms in the compounds for which x = 0, 1, 2 and 3 *(appendix F.3)*. The values for a selection of the distances and angles pertaining to the geometry of the conductive copper sulfide layer, illustrated in *figure 4.7*, are summarised graphically in *figure 4.8* and provided in *table 4.3*. Those previously reported in the literature for the end-members are also given for comparison.

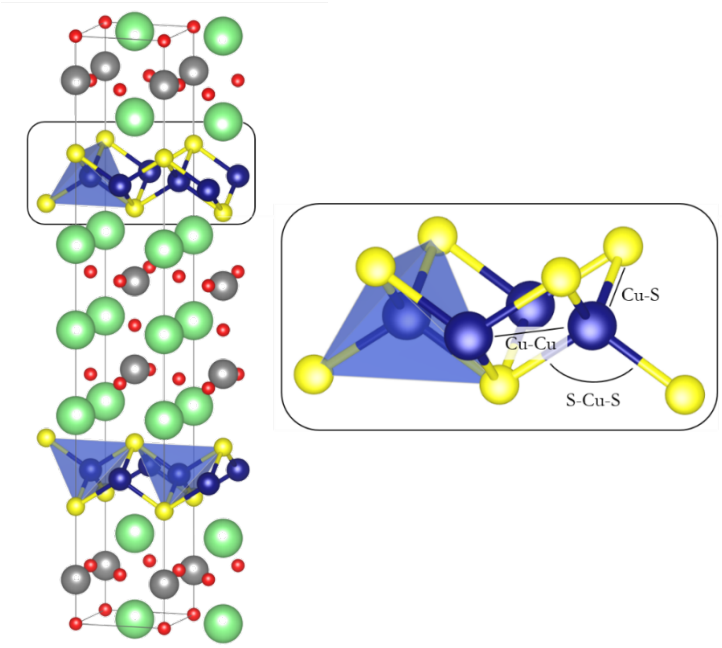

Figure 4.7 Illustration of the geometric parameters (lengths and angles) investigated in the conductive copper sulfide layers in the layered oxysulfide compounds studied here.

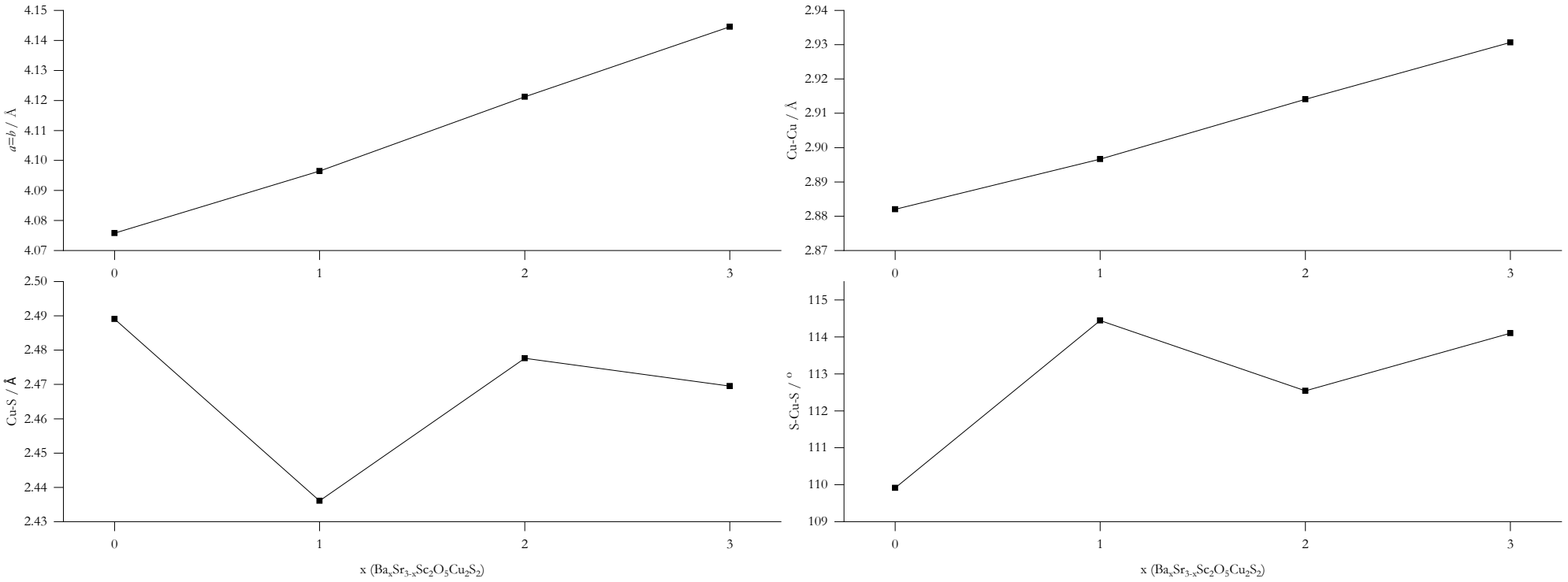

Figure 4.8 Graphical summary of selected interatomic distances and angles describing the geometry of the conductive copper sulfide layer in the mixed perovskite A cation compounds $Ba_xSr_{3-x}Sc_2O_5Cu_2S_2$, where x = 0, 1, 2 and 3. The raw data from which the plot was constructed is provided in table 4.3.

Table 4.3 *Summary of selected interatomic distances and angles describing the geometry of the conductive copper sulfide layer in the mixed perovskite A cation compounds $Ba_xSr_{3-x}Sc_2O_5Cu_2S_2$, where x = 0, 1, 2 and 3.*

		0 [48]	**1**	**2**	**3**
Distance/ Angle	***a=b* / Å**	4.0748(2)	4.09645(7)	4.1212(4)	4.14458(2)
	Cu-Cu / Å	2.88203(9)	2.89663(6)	2.9141(3)	2.93067(1)
	Cu-S / Å	2.48909(4)	2.43606(4)	2.4776(2)	2.46951(6)
	S-Cu-S / °	109.916(2)	114.448(2)	112.543(8)	114.1015(3)

It can be seen by inspection of the plots in *figure 4.8* that, as expected, the basal unit cell parameter increases linearly with increasing content of the larger radius barium ion, providing evidence for the successful single-phase *A* perovskite site cation mixing. The copper-copper distance followed the same trend as *a*, given that the distance is directly related to the basal unit cell parameter by a factor of $(\sqrt{2})/2$. This increase was expected to reduce copper-copper hybridisation, and thus reduce the curvature and raise the energy of the CBM, known to benefit transparency.

The copper-sulfur length was previously shown to decrease between the end-members where x = 0 and 3. The same length in the intermediate compound where x = 2, lay between those in the end-member compounds. However, the copper-sulfur length in the compound where x = 1, exhibited a reduced value below the range spanned by the two end-members. The reverse trend is seen in the sulfur-copper-sulfur angle: an increase is observed from the strontium to barium end-members with that of the x = 2 compound intermediate between the two, with a notable increase beyond the range spanned by the end-members for x = 1. The reason for this was unclear. Nonetheless, it is an interesting observation that the observed site preference within the perovskite layer yielded intermediate compositions with extreme geometries in the conductive copper sulfide layer beyond the range covered by the end-members. The effect of these observed geometries on the electronic properties of the compound was difficult to predict qualitatively, owing to the competing effects of the copper-sulfur length and sulfur-copper-sulfur angle on hybridisation at the VBM. The optical properties, however, were considered and are the subject of the following section.

4.3.3 Effect of Copper Sulfide Layer Geometry on Optical Properties

In order to assess the transparency of the mixed *A* cation compounds discussed here, their band gaps were determined by construction of Tauc plots *(figure 4.9)* from the raw diffuse reflectance data collected and shown inset.

When compared to those of the end-members, the copper-copper distance for the compound $x = 1$ suggested that the energy of the CBM, a result of hybridisation of unoccupied copper states, would be intermediate between the two end-members. The band-gap energy was the measured difference between the energies of the CBM and VBM. The hybridisation of, and therefore energy at, the VBM was determined by the overlap between the copper and sulfur states. The relatively short copper-sulfur distance, if considered alone, would have had the effect of increasing the hybridisation and energy of the VBM, however, this is accompanied by a large increase in the sulfur-copper-sulfur angle. The deviation of this angle away from that of an ideal tetrahedron, contributed to reducing the hybridisation. The net effect of these competing geometric contributions to the curvature of the VB and energy of the VBM, combined with that of the intermediate copper-copper distance on the energy of the CBM, resulted in the observation of a band-gap energy of 3.21 eV, which fell within the range spanned by the end-members, as can be seen in the summary in *figure 4.10*.

The copper-copper and copper-sulfur distances both increased with barium content from the compound where $x = 1$ to 2, as previously discussed. This alone would be expected to result in a relative increase in band-gap energy owing to the loss of hybridisation at both the VBM and CBM. There was, however, an accompanying reduction in sulfur-copper-sulfur angle for the compound $x = 2$ towards that of the ideal tetrahedral angle of 109.5°. The observed reduction in band gap to 3.12 eV was attributed to the increase hybridisation at the VBM by the reduced angle in spite of the increase copper-sulfur length. It is also noted that a large contribution to the absorption was observed in the region prior to the absorption onset for the compound $x = 2$. This has been attributed in the literature to absorption by copper (II) defects in the strontium end-member and was expected to be most significant in this compound with the most disorder in the perovskite layer.[27]

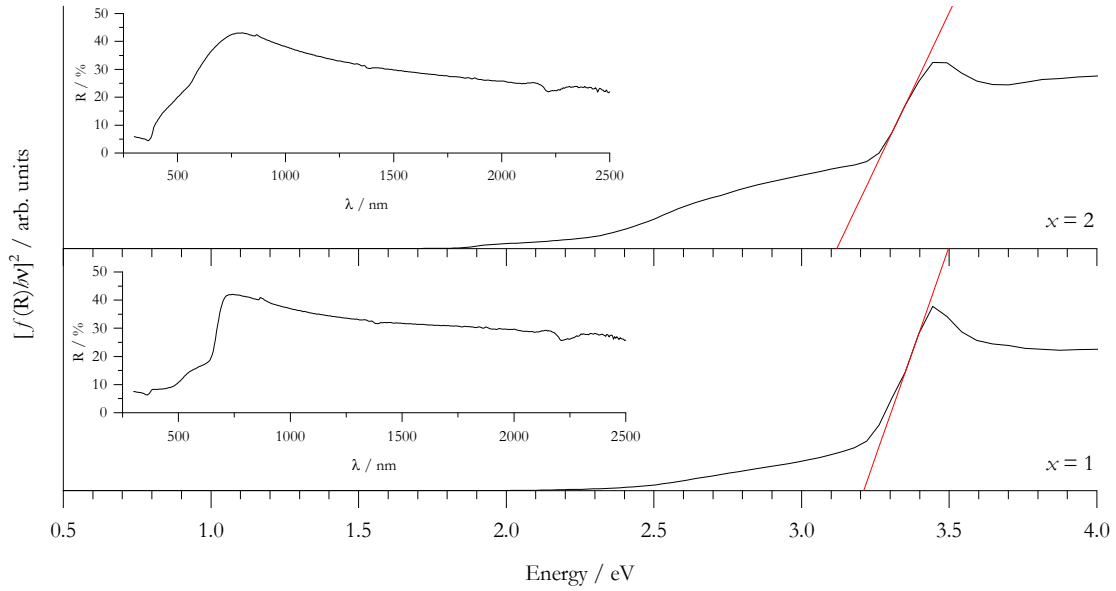

Figure 4.9 *Tauc plots calculated from the diffuse reflectance spectra (inset) for the mixed A homologous series of composition $Ba_xSr_{3-x}Sc_2O_5Cu_2S_2$, where x = 1 and 2. The x-intercepts of the linear fits at the absorption edges (red solid lines) gave band gap energies of 3.21 and 3.12 for x = 1 and 2, respectively.*

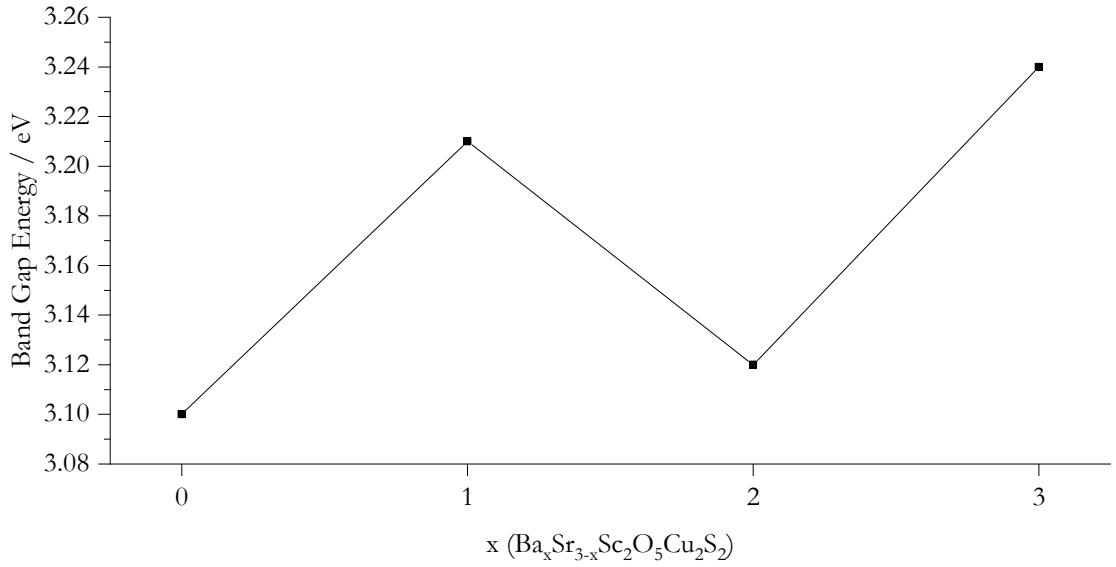

Figure 4.10 *Graphical plot of the observed band gap energies, as calculated from raw diffuse reflectance data via Tauc plots (figure 4.9), for the mixed A cation compounds $Ba_xSr_{3-x}Sc_2O_5Cu_2S_2$, where x = 0, 1, 2 and 3.*

4.3.4 Prediction of the Effect of Copper Sulfide Layer Geometry on Electronic Properties

The intrinsic p-type conductivity in these layered oxysulfide compounds has been shown to arise from migration of positive holes at the VBM which comprises hybridised copper 3*d* and sulfur 3*p* electronic states.[27,48] The conductivity of the compound is in part dependent on the hybridisation of the states as given by the overlap integral, β, in *equation 4.3*. The overlap integral increases with the inverse of the crystallographic distance between the ions, and with proximity of the sulfur-copper-sulfur angle to the ideal tetrahedral angle of 109.45°.

$$\sigma = -\frac{2e^2}{\hbar^2} n \tau \beta a^2 \qquad 4.3$$

σ - conductivity
e - fundamental charge
ħ - reduced Planck constant
n - charge carrier density
τ - mean free time
β - overlap integral
a - lattice parameter

Referring back to *figure 4.8* on *page 69*, it can be seen that the copper-sulfur bonding distance was markedly lower for the compound with composition in which $x = 1$ with the copper-sulfur length in the remaining compounds decreasing with barium content. However, the seemingly desirable, in terms of conductivity, small copper-sulfur distance in the $x = 1$ compound, was found to be accompanied by the largest sulfur-copper-sulfur angle of 114. 448 °, showing the largest deviation from the ideal of 109.5° to which the strontium end-member ($x = 0$) is closest at 109.916°. Quantification of the net expected effects of these contributing factors was not possible and, therefore, a computational model of the band structure for these observed mixed compounds and calculation of the emergent intrinsic conductivity is warranted. Empirical conductivity measurements were seen as desirable, however the effect of the geometry on the band structure and therefore conductivity could not be deconvoluted from the sample parameters affecting the free path of the charge carrier also contributing to the conductivity. This is the subject of the following section.

4.3.5 Williamson-Hall Line Profile Analysis

4.3.5.1 Introduction and Instrumental Correction

The mean free time, τ, on which conductivity depends *(eqn. 4.3)*, is inversely proportional to the frequency of scattering events between the charge carriers and the lattice. The potential effect of crystallite size, and therefore the spatial frequency of scattering grain boundaries, and lattice strain on the conductivity was evaluated by Williamson-Hall line profile analysis of the powder x-ray diffraction pattern. The peaks in observed powder x-ray diffraction profiles result from the observation of x-rays diffracted from particular sets of lattice planes within the diffracting crystalline samples and subsequently amplified by the process of constructive interference. This constructive interference occurs at precise angles and gives rise to sharp peaks. Observed diffraction peaks are never as sharp as would be predicted by scattering from a perfect lattice alone. There are factors relating to both the diffractometer and the diffracting specimen under analysis, that give rise to peak broadening. The total broadening observed in the resultant diffraction pattern is a simple sum of broadening from both of these sources as described in *equation 4.4*.

$$\beta_{Tot} = \beta_{Tot,\,Ins.} + \beta_{Tot,\,Smpl.} \qquad 4.4$$

β_{Tot} - total observed broadening of the diffraction peaks
$\beta_{Tot,\,Ins}$ - the component of the total broadening attributed to the diffractometer used
$\beta_{Tot,\,Smpl}$ - the component of the total broadening attributed to the analysed sample

In order to extract information on sample broadening from the x-ray diffraction profile, the broadening pertaining to only the instrument was calculated. This was determined empirically by measurement of the observed x-ray diffraction peak broadening for a very well defined, large-crystallite-size and strain-free standard sample, lanthanum hexaboride (NIST 660a). By use of the standard, the sample broadening was minimised and the observed broadening when the diffraction pattern of the standard was measured, was attributed directly to the instrument.

The individual peaks of the raw observed diffraction data from the standard were fitted with pseudo-Voigt functions which were used to calculate the full-width at half-maximum intensities, equated to the broadening. The measured broadening was plotted against peak position/diffraction angle as shown in *figure 4.11*. The raw data from which it was constructed is tabulated in *appendix F.4*. The plot was fitted with the Caglioti equation *(eqn. 4.5)*, the refined parameters of which are shown inset in *figure 4.11*.[61,86] The fitted function was then used to perform an interpolation of the $\beta_{Tot,\,Ins}$ versus θ plot to calculate the instrumental broadening contribution to the width of the observed diffraction peaks at the given peak angles for the samples under analysis.

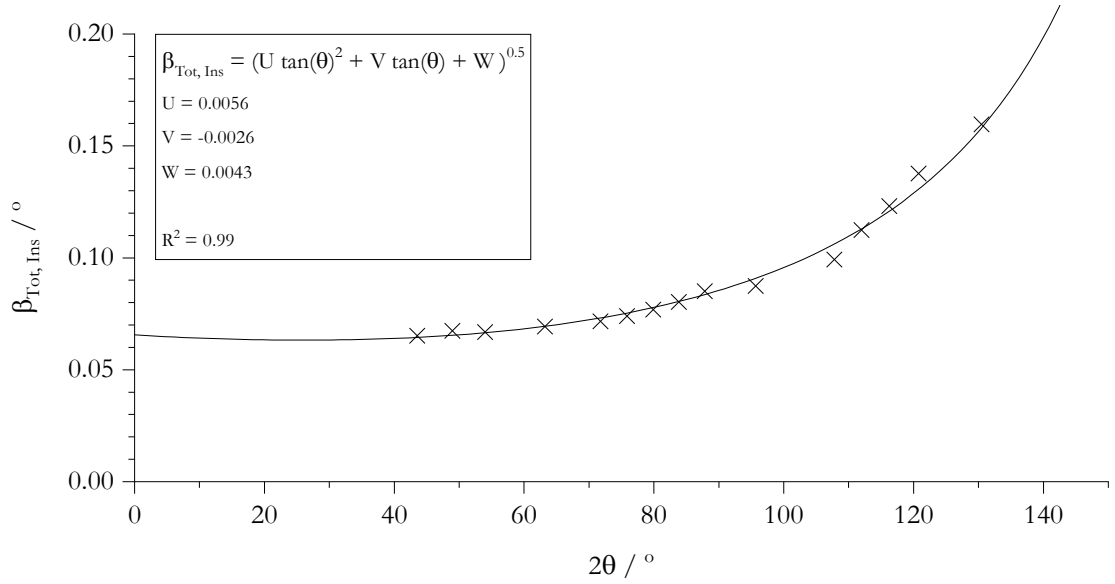

Figure 4.11 Plot of peak width assigned to the instrument ($\beta_{Tot, Ins}$) as a function of detector angle (2θ) for the LaB_6 instrumental broadening standard. The raw data is provided in appendix F.4.

$$\beta_{Tot, Ins} = \sqrt{U \tan^2(\theta) + V \tan(\theta) + W} \qquad 4.5$$

$\beta_{Tot, Ins}$ - observed full-width at half-maximum for peaks in PXRD pattern for the standard
U, V, W - variable 'half-width parameters'
θ - median diffraction angle of peak

Once the instrumental broadening, $\beta_{Tot, Ins.}$, was known by calculation of the total broadening of the diffraction profile peaks for the standard, the broadening due to the sample under analysis was deduced by simple subtraction of the expected instrumental broadening.

The sample broadening, $\beta_{Tot,Smpl.}$, occurs as a result of a sum of contributions from the crystallite domain sizes, $S_{Crys.}$, and lattice strain, $\varepsilon_{Latt.}$, as shown in *equation 4.6*. The smaller the crystallites, the larger the contribution from the surface planes (the spacing of which show deviation from that of those in the bulk), the greater the range of interplanar spacing sampled and the broader the diffraction peaks. Inhomogeneous bulk lattice strain also contributes to diffraction profile peak broadening for the same reason. Both broadening contributions from the crystallite size and lattice strain vary independently with diffraction angle, θ. These relationships are quantified by the Scherrer and Wilson equations given in *equations. 4.7 and 4.8* respectively.[87,88]

$$\beta_{Tot,\ Smpl.} = \beta_{S_{Crys.}} + \beta_{\epsilon_{Latt.}} \quad 4.6$$

$$S_{Crys.} = \frac{K\lambda}{\beta_{S_{Crys.}}\cos(\theta)} \quad 4.7$$

$S_{Crys.}$ - crystallite size
K - shape factor, commonly approximated to 0.9
λ - x-ray wavelength

$$\epsilon_{Latt.} = \frac{\beta_{\epsilon_{Latt.}}}{4\tan(\theta)} \quad 4.8$$

$\epsilon_{Latt.}$ - lattice strain

These can be rearranged to expressions for the contributions to peak broadening, substituted into *equation 4.6* and multiplied by *cos(θ)* to yield the Williamson-Hall equation *(eqn. 4.9)*.[89] The observed sample diffraction peak profile widths, $\beta_{Tot,Smpl}$, and their corresponding diffraction angles, θ, were used to create Williamson-Hall plots of $\beta_{Tot,Smpl}\cos(\theta)$ vs. *sin(θ)* for each sample. Linear fits to the Williamson-Hall plots were made, the gradients and *y*-intercepts of which were related to the lattice strain and crystallite sizes as shown in *equations 4.10* and *4.11*, respectively.

$$\beta_{Tot,Smpl.}\cos(\theta) = 4\,\epsilon_{Latt.}\sin(\theta) + \frac{K\lambda}{S_{Crys.}} \quad 4.9$$

$$\epsilon_{Latt.} = \frac{m}{4} \quad 4.10$$

m – gradient of line of best fit of W-H plot

$$S_{Crys.} = \frac{K\lambda}{c} \quad 4.11$$

c – *y*-intercept of line of best fit of W-H plot

4.3.5.2 Results

The Williamson-Hall plots made from the instrument-corrected pseudo-Voigt modelled diffraction profile peaks for the series of compounds $Ba_xSr_{3-x}Sc_2O_5Cu_2S_2$, where x = 0, 1, 2 and 3, are shown in *figure 4.12*. The raw data from which the plots are constructed is tabulated in *appendix F.5*. The gradient and *y*-intercepts were used to calculate the lattice strain and crystallite sizes. These are represented graphically for each of the compounds in the plots in *figure 4.13* and from the raw data in *table 4.4*.

It can be seen by inspection of the plot in *figure 4.13, lower*, that the calculated inhomogeneous lattice strain was higher in the intermediate compounds (x = 1 and 2) than in the unmixed end-members (x = 0 and 3). The mixing of strontium and barium cations across the *A* sites resulted in regions in the bulk crystal lattice which were occupied by barium and those occupied by strontium. These cations possessed different ionic radii and therefore resulted in differing localised lattice spacing. The increased inhomogeneous strain calculated for the intermediates confirmed the successful mixing of these elements across the *A* sites.

It was also observed that the lattice strain was greatest (0.26 %) for the compound $Ba_2SrScO_5Cu_2S_2$. This confirms the observation made as a result of *A* site occupancy modelling, that the barium ions show a preference for the intra-layer sites with the remaining elemental mixture distributed across the inter-layer sites bordering the more flexible copper sulfide layer. The idealised observed *A* site occupancies for the compounds for which x = 1 and 2 are repeated in *figure 4.14*. It can be seen that for the composition where x = 1, the intra- and inter-layer *A* cation sites are fully occupied by barium and strontium, respectively. The compound x = 2, shows barium wholly occupying the intra-layer site with the remaining mixture of barium and strontium disordered across the inter-layer sites. It was this increased disorder in the compound where x = 2, owing to the relative 'fits' of barium and strontium in the scandium oxide perovskite lattice as calculated by use of the Goldschmidt tolerance factor, that explained the increased inhomogeneous strain calculated for this compound.

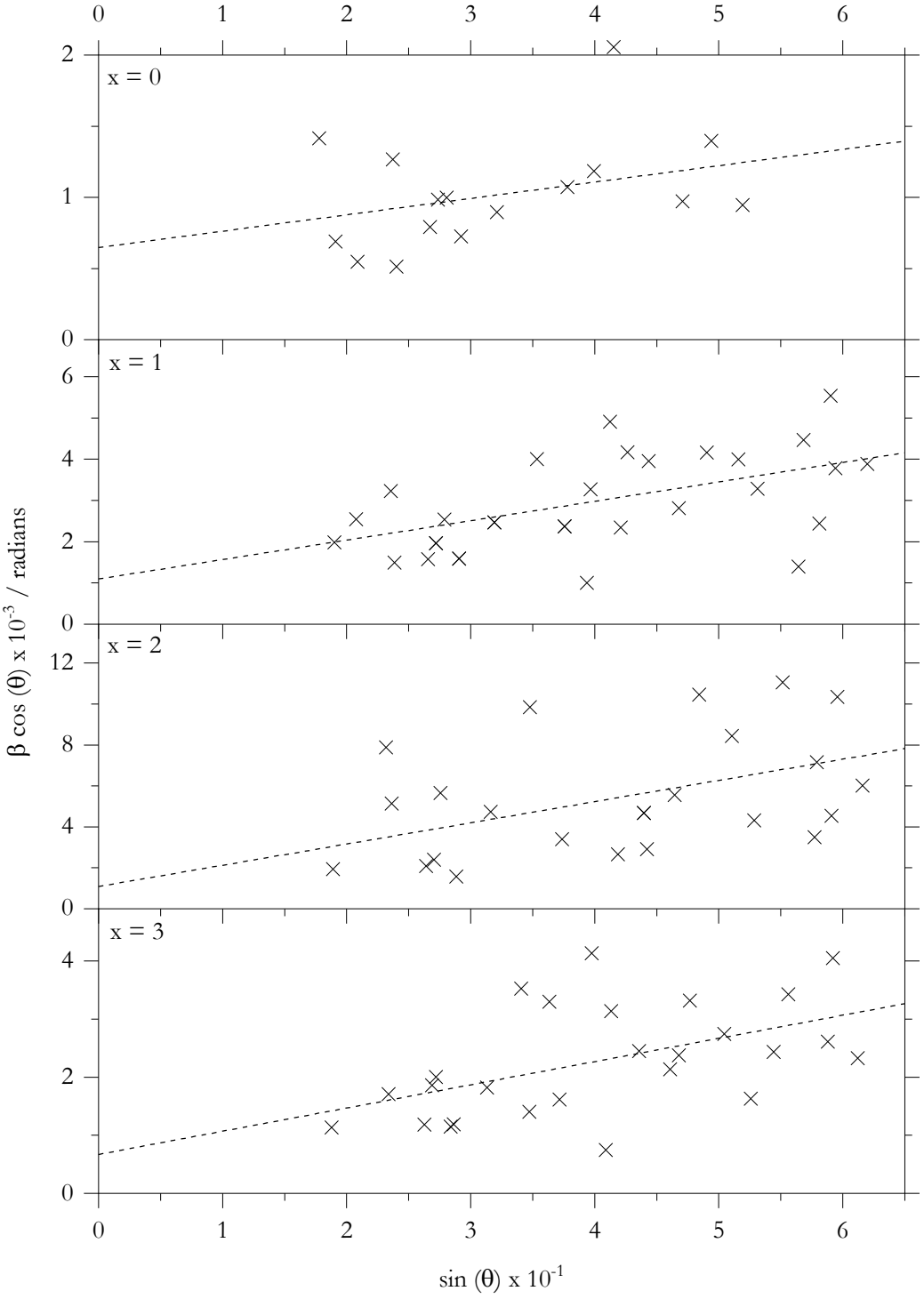

Figure 4.12 Linearly-fitted Williamson-Hall plots made from the instrument-corrected pseudo-Voigt modelled observed diffraction profile peaks for the series of compounds $Ba_xSr_{3-x}Sc_2O_5Cu_2S_2$, where x = 0, 1, 2 and 3. The underlying raw data is provided in appendix F.5.

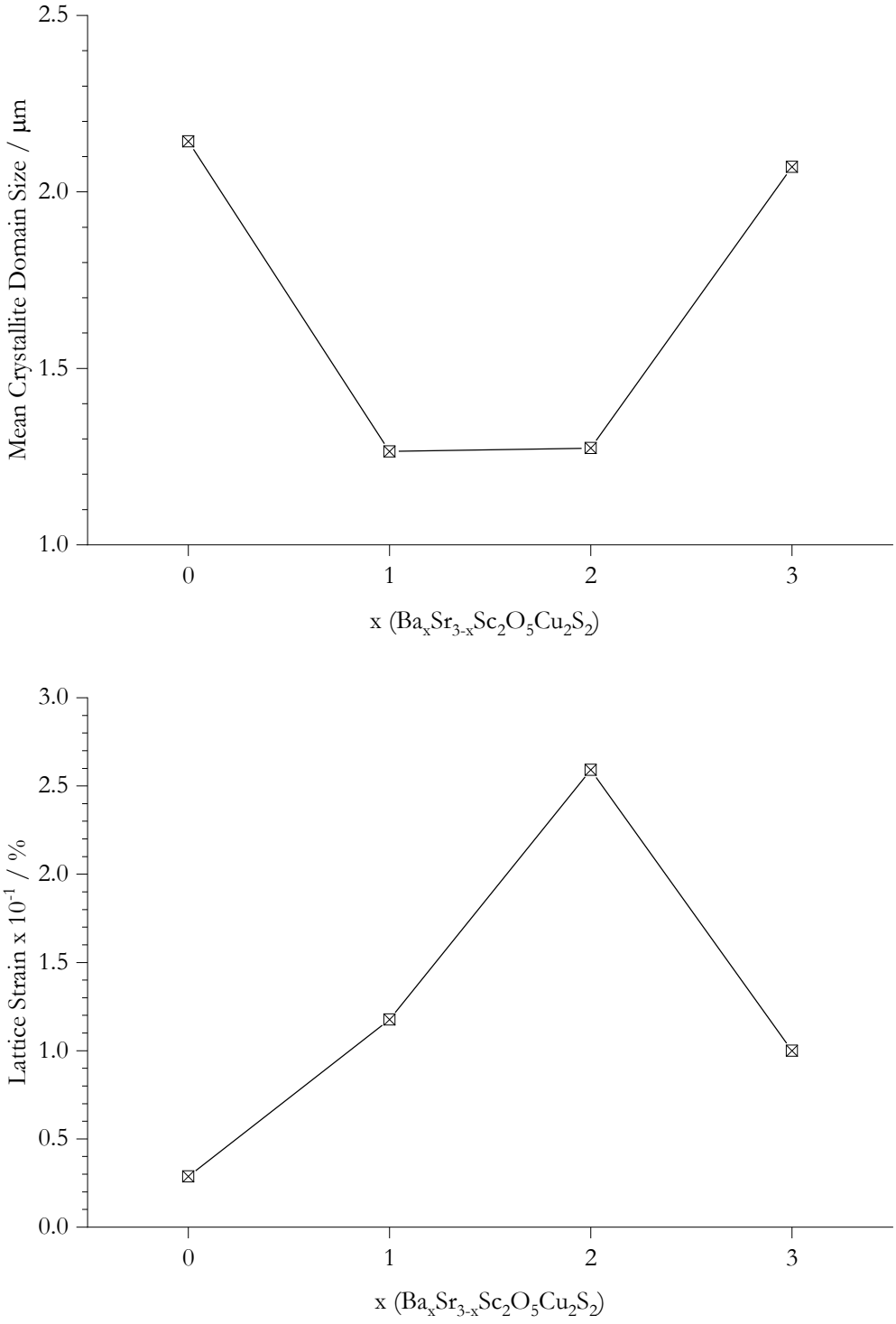

Figure 4.13 Graphical summary of the lattice strain (bottom) and crystallite size (top) values calculated from the gradients and y-intercepts of the linear fits to the data in the Williamson-Hall plots in figure 4.12

Table 4.4 *Summary of the lattice strain and crystallite size values calculated from the gradients and y-intercepts of the linear fits to the data in the Williamson-Hall plots in figure 4.12, from which figure 4.13 was constructed.*

Composition (x)	Ave. Lattice Strain / %	Ave. Crystallite Size / μm
0	0.03	2.14
1	0.12	1.26
2	0.26	1.27
3	0.10	2.07

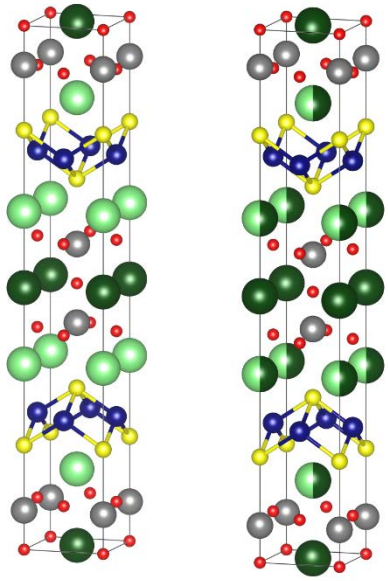

Figure 4.14 *Repeat of the graphical representation of the unit cell viewed mainly along 'a', illustrating the idealised most stable distribution of strontium (light green) and barium (dark green) mixing across the A cation sites in the layered oxysulfide compounds $Ba_xSr_{3-x}Sc_2O_5Cu_2S_2$ where x = 1 (left) and 2 (right), as predicted by the Goldschmidt tolerance factor.*

It was also noted that the calculated crystallite sizes were smaller for the intermediate compounds compared to the end-members. This was rationalised by the previously observed increase in inhomogeneous lattice strain. It was anticipated that the increased strain would retard the rate of crystallite growth, resulting in smaller calculated crystallite sizes for the intermediate compounds.

When labelling the data points in the Williamson-Hall plots with the Miller indices describing the lattice planes represented by each peak, the data points for peaks with corresponding lattice planes primarily stacked in the *c* direction, consistently showed greater $\beta \cos(\theta)$ values. Therefore, the decision was made to divide the data points in the Williamson-Hall plots for each compound, into two sets – those resultant from planes with the majority lattice vector component in the direction parallel to the *c* axis and those with vector mainly oriented in the *ab* direction. These sets (*ab* and *c*), plotted separately in *figure 4.15* were independently fitted with linear functions and their gradients and *y*-intercepts used to calculate the lattice strain and crystallite sizes in those directions. These are shown in the plot in *figure 4.16*. The data represented is given in *table 4.5*.

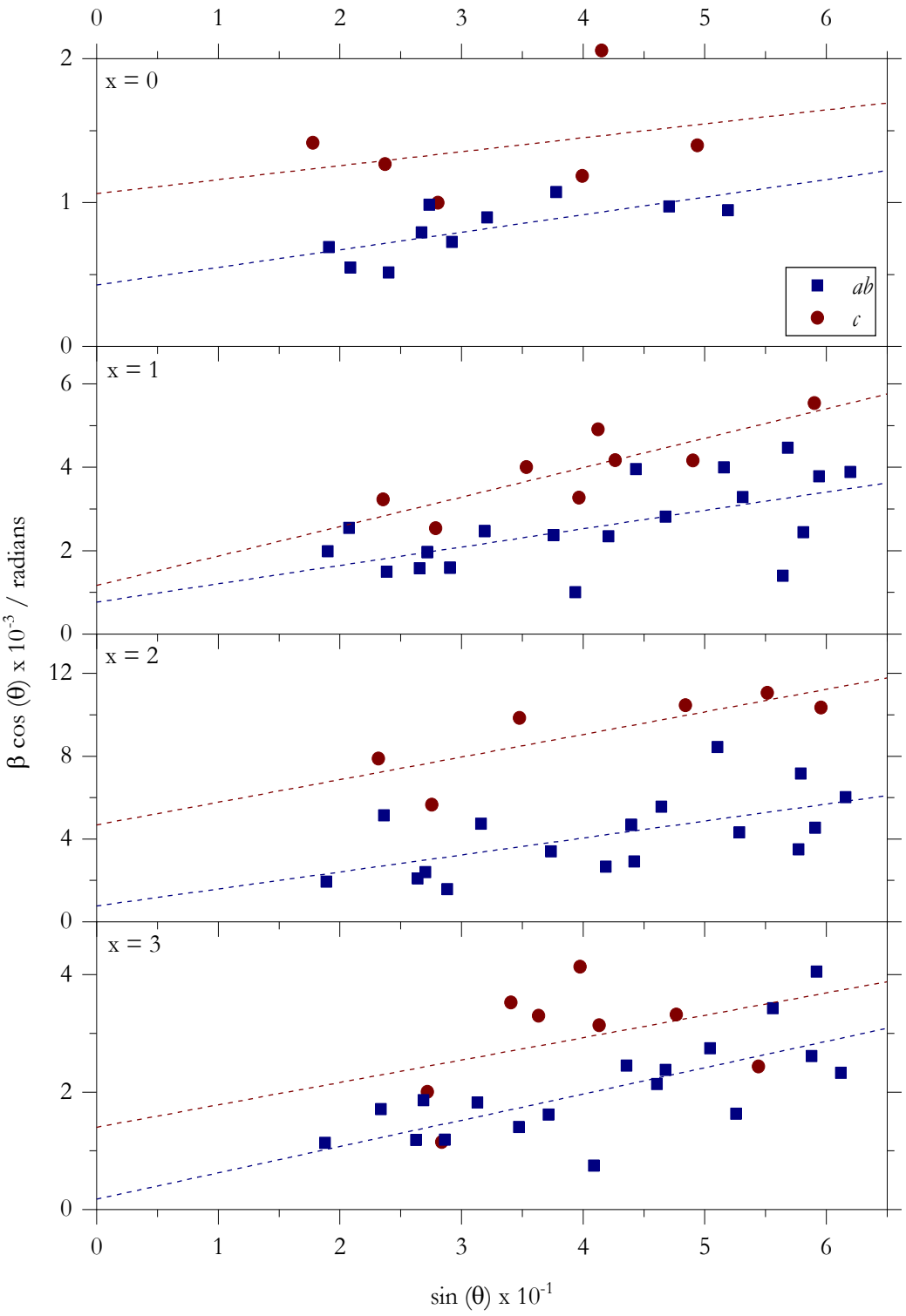

Figure 4.15 *Williamson-Hall plots derived from powder x-ray diffraction profile peak widths of mixed A cation samples $Ba_xSr_{3-x}Sc_2O_5Cu_2S_2$, where x = 0, 1, 2, and 3. The composition for each sample is indicated on the plots. Each data point represents a peak in the diffraction profile described by the Miller indices characterising the lattice plane from which it originates. The data points are divided into two categories: those from planes with lattice vectors with a majority component in the ab plane (blue squares) and those with interplanar spacing primarily occurring along the c axis direction (red circles) as indicated in the key. Linear functions were fitted to the two sets of data points. The gradients of these functions are proportional to the lattice strain and the y-intercepts inversely proportional to the size of the coherently scattering crystal domains (crystallite size).*

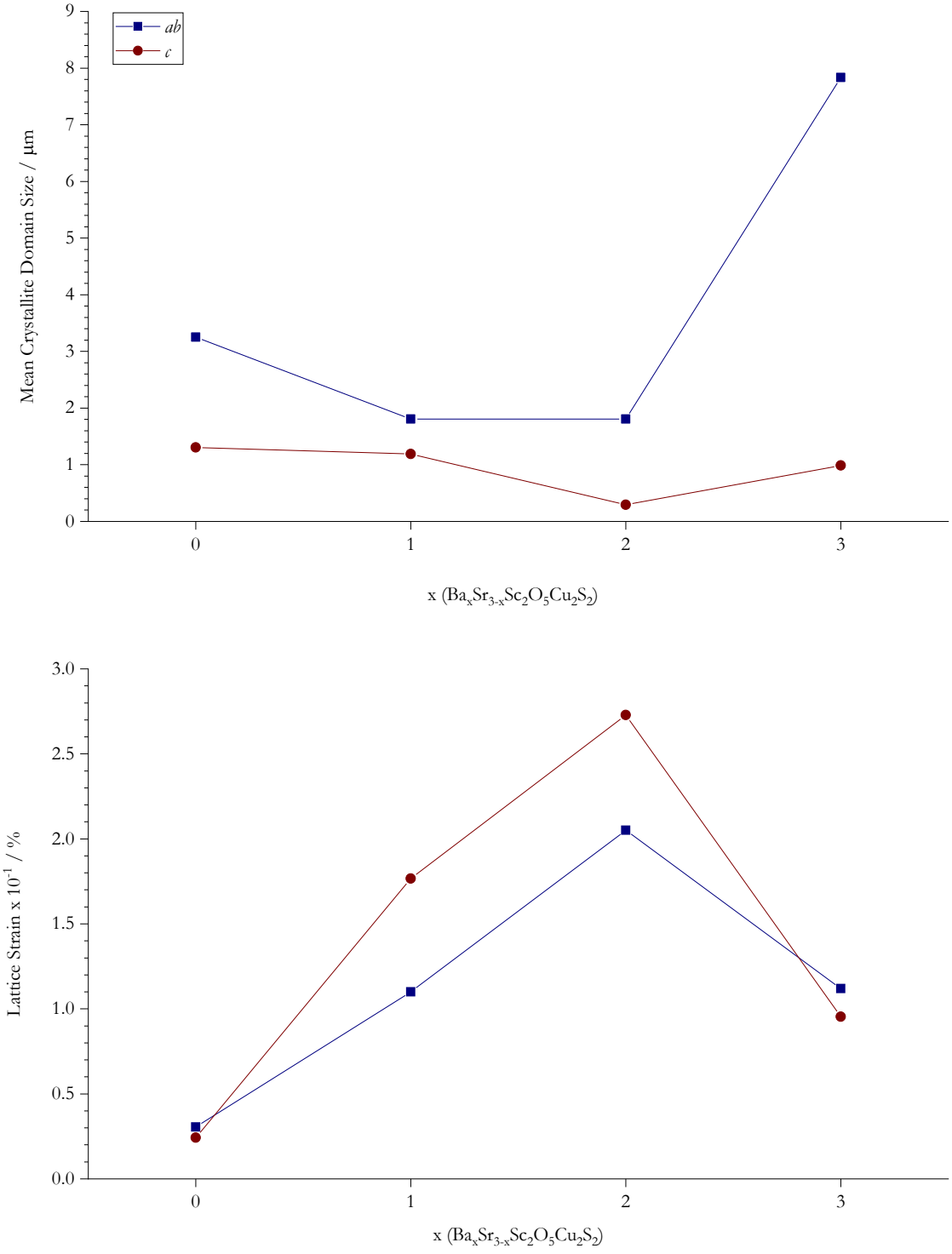

Figure 4.16 *Graphical summary of the inhomogeneous lattice strain and crystallite domain sizes calculated independently for lattice planes with vector oriented primarily in the ab (blue squares) and c (red circles) unit cell directions, by separate linear fits to the corresponding sets in the Williamson-Hall plots in figure 4.15, and derived from the raw data provided in table 4.5.*

Table 4.5 *Summary of the inhomogeneous lattice strain and crystallite domain sizes calculated independently for lattice planes with vector oriented primarily in the ab and c unit cell directions by separate linear fits to the corresponding sets in the Williamson-Hall plots in figure 4.15.*

Composition (x)	Lattice Strain / %			Crystallite Size / μm		
	Ave.	*ab*	c	Ave.	*ab*	*c*
0	0.03	0.03	0.02	2.14	3.25	1.31
1	0.12	0.11	0.18	1.26	1.81	1.19
2	0.26	0.21	0.27	1.27	1.80	0.30
3	0.10	0.11	0.10	2.07	7.83	0.99

It was observed that the lattice strain calculated independently in the two perpendicular lattice directions were very similar and close to the average value for the two end-member compounds. For the intermediate compounds, where $x = 1$ and 2 however, a greater separation in strain was observed. In both cases the lattice strain was greatest in the *c* direction. This was rationalised by the flexibility of the copper sulfide compared to the rigidity of the perovskite building-block.[49] The compound is formed by alteration of these two layers in the *c* lattice direction. The flexibility in that direction, therefore, allows for a greater range of lattice spacing and, therefore, observed strain to accommodate the disorder induced by the elemental mixing of strontium and barium across the *A* perovskite cation sites. Less strain was observed in the basal *ab* direction as this was limited by the dense, highly ionic and rigid perovskite lattice.

Inspection of the calculated crystallite size in the different lattice directions showed that the crystallite domains were consistently larger in *ab* than in *c*. It was suspected that the growth rate in the *ab* direction was greater than in the *c* as the required growth mode would have been 'like-layered' meaning that when growing in the *ab* direction a perovskite-like lattice would have been forming at the perovskite block and the litharge-like layer at the copper sulfide block. Growth in the *c* direction of crystallographic layering, however, required the formation of boundaries between the perovskite and litharge-like units. This was expected to exhibit a higher activation energy owing to the energy required to overcome the lattice mismatch and as a result show a retarded growth rate and smaller size in the *c* dimension.

The largest crystallite domain size was observed in the *ab* dimension of the barium end-member compound, $Ba_3Sc_2O_5Cu_2S_2$. It was proposed that the increased fit of the barium cation into the scandium oxide perovskite-like lattice, increased the rate of like-layer growth of the perovskite layer in the barium end-member compound, resulting in the largest *ab* dimension.

The lattice strain was found to be lowest in the strontium ($x = 3$) end-member in both *ab* and *c* directions. This indicated the potential of this compound as a high-conductivity material, by consideration of lattice strain alone. The observed anisotropic growth rate and, therefore, geometry of the crystallites was expected to benefit the conductivity of the materials. The conduction of positive-hole charge carriers in these compounds was shown to occur only in the copper sulfide layers by Williamson *et al.*[76] The naturally observed preferred growth direction in these compounds was proposed to reduce the spatial frequency of grain boundaries in the *ab* conduction direction, contributing to an increased mean free time between carrier collision events and conductivity. Based solely on the crystallite size measurements, the conductivity was expected to be greatest for the barium end-member. The anisotropy of these compounds was confirmed by imaging with a scanning-electron microscope. This is the subject of the following section.

4.3.6 Scanning-Electron Microscopic Analysis

The anisotropic 'slab-like' structure of the layered oxysulfide compounds investigated here was confirmed by inspection of the images in *figures 4.17* to *4.20* collected on behalf of the author by Dr Alexander Kulak of the University of Leeds, using a Nova Nano scanning-electron microscope (SEM). The images were collected over a range of magnifications of 8000 to 50000 x with the scale displayed inset in each of the images.

The images confirmed the crystallite sizes of the order of 1 μm as calculated by the Williamson-Hall line profile analysis and the slab-like crystallite geometry with higher dimension in the *ab* plane. This is most easily seen in image 'c' in *figures 4.17* and *4.18*; and 'a' in *4.19* and *4.20*. In addition to the expected slab-like crystallites, an additional form is shown in the SEM images wherein crystallites seemingly grew from a central point along an axis increasing in angular span with distance from the central point to form bundles of needle-like crystallites. These can be most easily described as having shapes reminiscent of that of sheaves of wheat, the ends of which are so small that they were poorly resolved at magnification of 50000 x. The structures seemingly grew at the surface of particles comprising the slab-like crystallites as shown in image 'b' in *figures 4.17* to *4.20*. They seemed to be present for each of the compounds and their effect on the calculated crystallite size is unknown.

In addition, single high-aspect-ratio needle-like crystallites were found in the compositions where $x = 2$ and *3* (image 'd' in *figures 4.19* to *4.20*). Without elemental analysis, it is not possible to confirm that these structures are composed of the compounds in question. It is a possibility that these structures could have resulted from sample contamination by PTFE, alumina or quartz used during the synthetic process. The sizes of these needles are between 5 – 10 μm in length and may give rise to the larger crystallite sizes (≈ 8 μm for *ab*) in the compound $Ba_3Sc_2O_5Cu_2S_2$. However, it is highly unlikely that the population of these needle-like structures is enough to significantly contribute to the widths of the peaks in the XRD pattern and therefore the crystallite domain sizes calculated.

It is also likely that the crystallite sizes calculated by Williamson-Hall analysis, while of the same order, were still overestimates of the true domain sizes. It is likely that the instrumental broadening calculated using the lanthanum hexaboride standard was overestimated. While highly crystalline, the standard will have contributed to broadening to some extent, artificially inflating the estimated instrumental broadening. The correction made in construction of the Williamson-Hall plots, whereby the calculated instrumental broadening was subtracted, was too great a correction. The real broadening as a result of the samples under investigation was expected to be slightly higher than that calculated, resulting in a linear fit with a more positive *y*-intercept and, therefore, smaller calculated crystallite sizes.

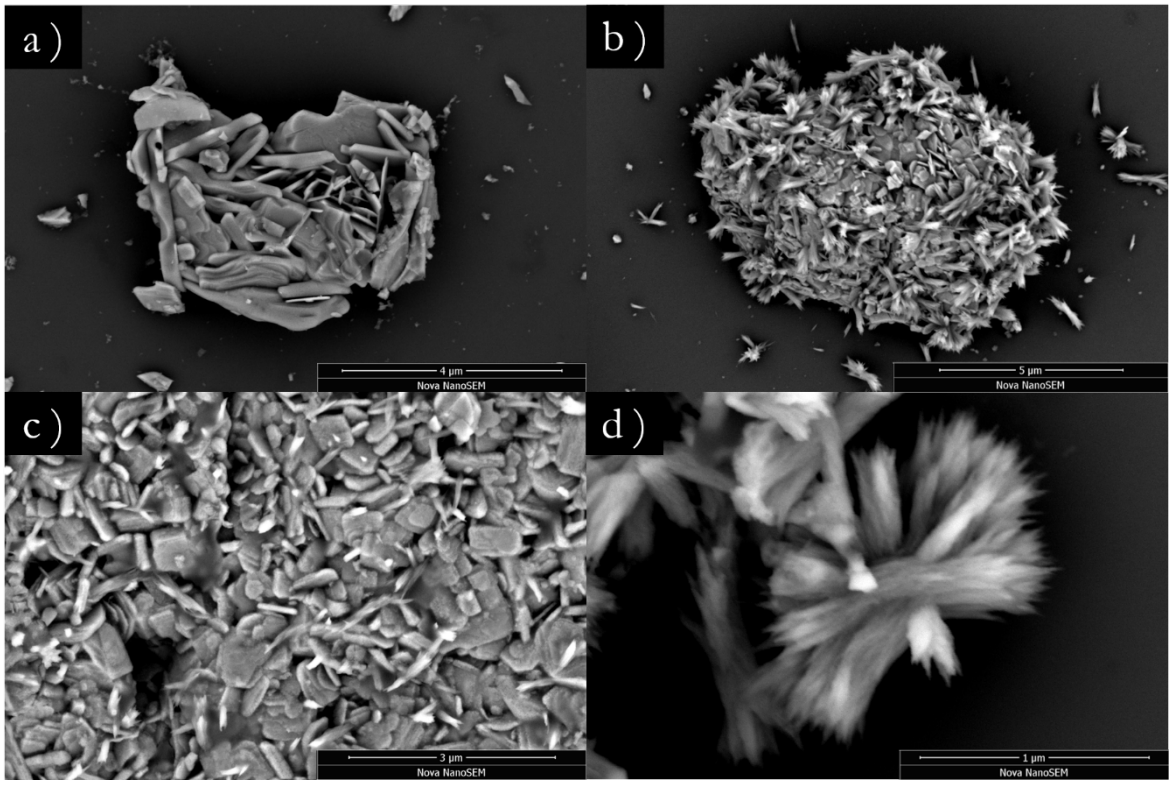

Figure 4.17 Scanning electron microscopy images taken of the compound $Sr_3Sc_2O_5Cu_2S_2$ at magnifications 12000 x *(a), 8000* x *(b), 15000* x *(c) and 50000* x *(d). The reference scales are indicated in the bottom right of each plot and show the distances 4, 5, 3 and 1 µm for images a, b, c and d, respectively.*

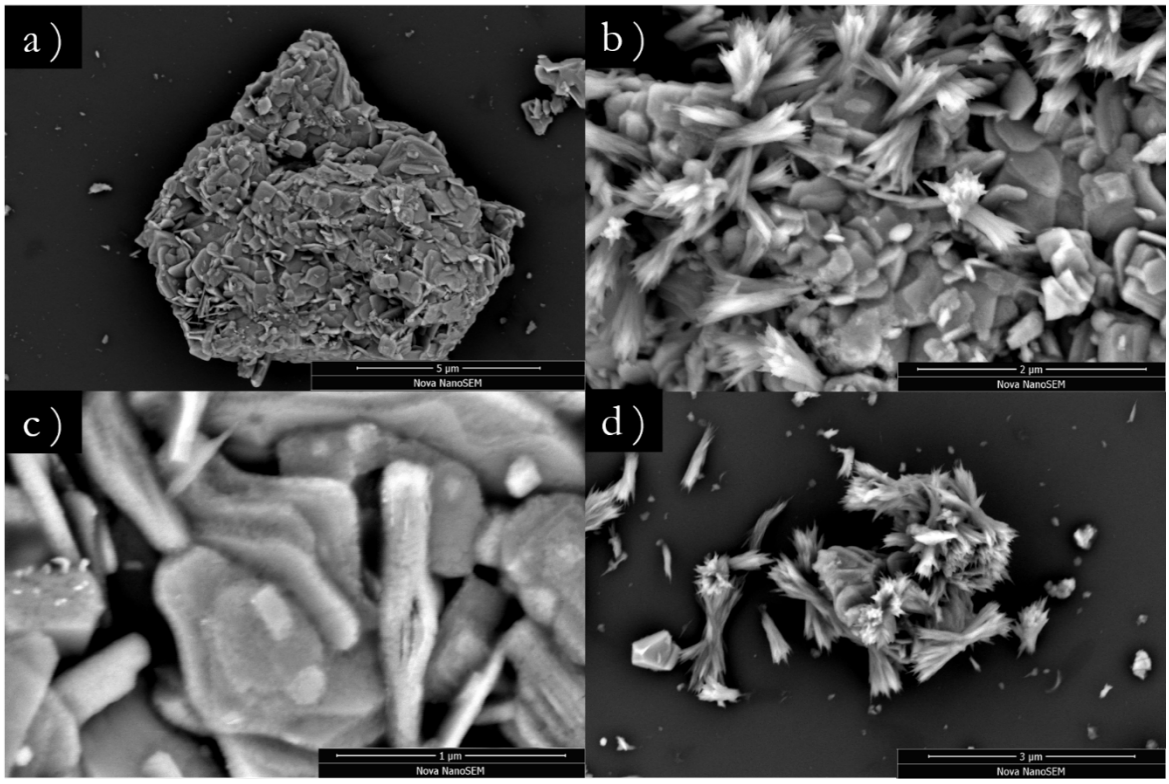

Figure 4.18 Scanning electron microscopy images taken of the compound $BaSr_2Sc_2O_5Cu_2S_2$ at magnifications 8000 x *(a), 25000* x *(b), 50000* x *(c) and 15000* x *(d). The reference scales are indicated in the bottom right of each plot and show the distances 5, 2, 1 and 3 µm for images a, b, c and d, respectively.*

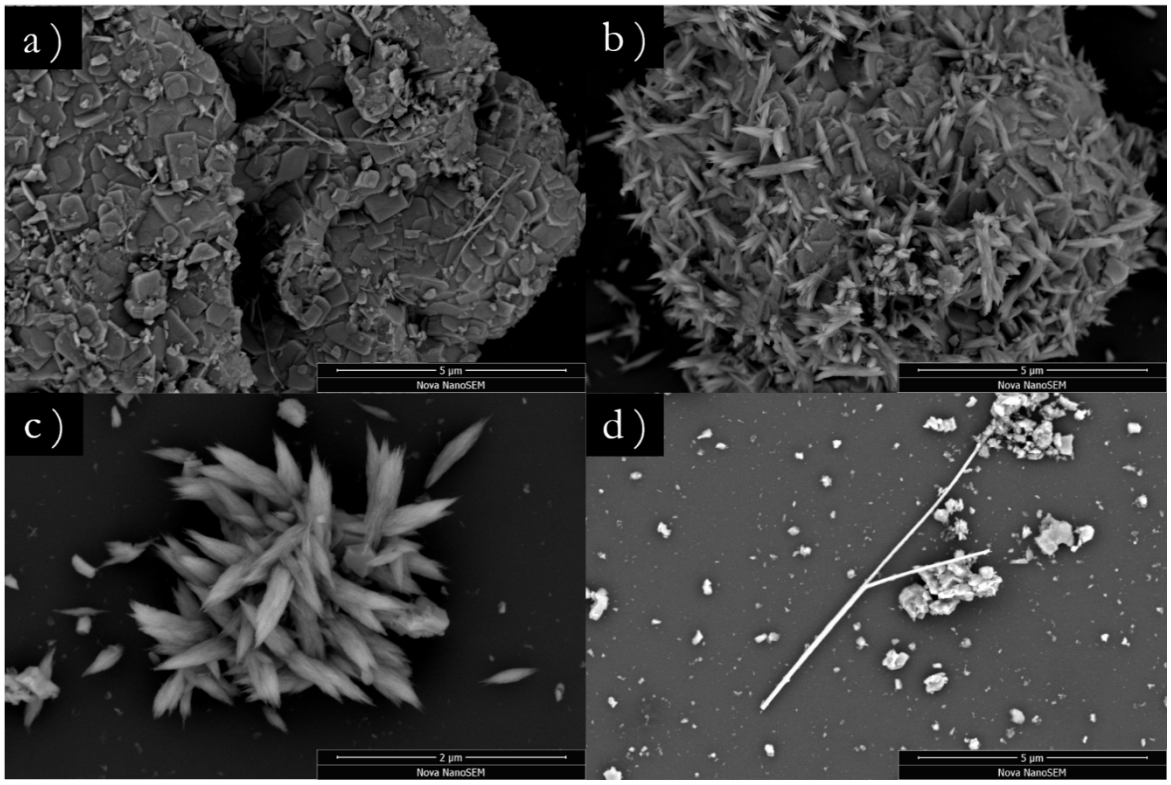

Figure 4.19 Scanning electron microscopy images taken of the compound $Ba_2SrSc_2O_5Cu_2S_2$ at magnifications 10000 x *(a), 10000* x *(b), 25000* x *(c) and 10000* x *(d). The reference scales are indicated in the bottom right of each plot and show the distances 5, 5, 2 and 5 µm for images a, b, c and d, respectively.*

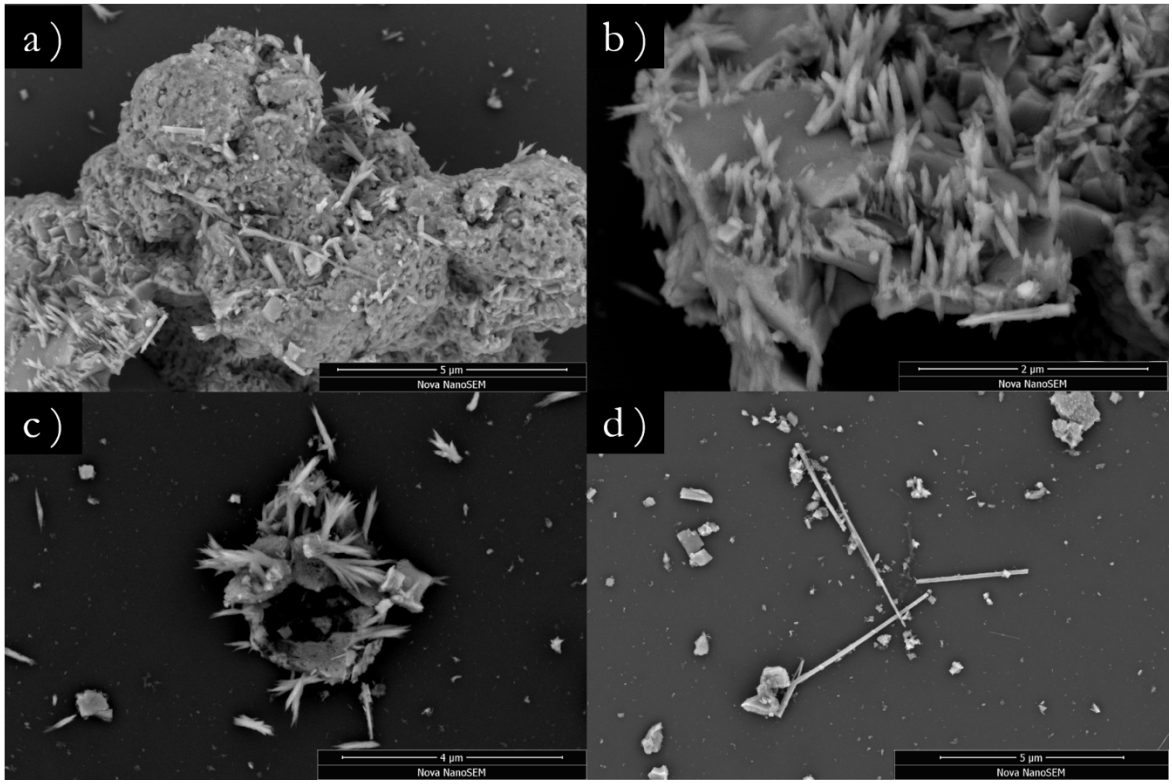

Figure 4.20 Scanning electron microscopy images taken of the compound $Ba_3Sc_2O_5Cu_2S_2$ at magnifications 10000 x *(a), 25000* x *(b), 12000* x *(c) and 8000* x *(d). The reference scales are indicated in the bottom right of each plot and show the distances 5, 2, 4 and 5 µm for images a, b, c and d, respectively.*

4.4 Conclusions and Outlook

Successful mixing of the elements barium and strontium across the *A* perovskite sites in the compounds $Ba_xSr_{3-x}Sc_2O_5Cu_2S_2$ where $x = 1$ and 2, was achieved as confirmed by PXRD. The diffraction peaks observed were matched to those generated from end-member models with refined lattice parameters. The trend in refined lattice parameters increased with increasing barium content, as expected. The refined fractional occupancy of the *A* sites in the end-member models further supported the successful incorporation of the two *A* elements into a single crystallographic phase. Inspection of the refined *A* site occupancies showed preference of barium for the 'intra-layer' perovskite site, as rationalised by the Goldschmidt tolerance factor.

Analysis of the extracted atomic distances and angles revealed extreme copper-sulfur and sulfur-copper-sulfur distances and angles in the compound where $x = 1$, beyond those of the end-members. This demonstrated the benefit of elemental mixing in these compounds to achieve conductive layer geometries not attainable by the end-members. The net effect of the competing extreme geometries on the conductivity could not be qualitatively predicted. Quantitative computational modelling of the band structure would be required to predict the intrinsic conductivity contributions of these compounds. Despite the remarkable distances and angles observed, diffuse reflectance measurements showed that the band gap energies of all compounds in this series remained above the 3.1 eV visible threshold.

Williamson-Hall line-profile analysis revealed the anisotropic growth of the 'slab-like' crystallites in all members in this series. The crystallites show high aspect ratio in the direction of conduction, expected to benefit conductivity. The calculated crystallite sizes were found to be lowest in the intermediate compounds. This was likely a result of the increased lattice strain observed for the intermediates relative to the end-members. These observations provided further evidence for elemental mixing on a single crystallographic site in the intermediates. The highest strain was observed in the compound for which $x = 2$, consistent with the disorder found across the 'inter-layer' sites as determined from refined fractional occupancies.

In summary, perovskite *A* site cation mixing was found to be possible in these compounds to achieve extreme conductive layer geometries and therefore potentially novel optoelectronic properties, with desired maintenance of transparency. Care must be taken to consider the possible detrimental effect of the increased strain and reduced crystallite size observed for the intermediates, on the conductivity.

The barium end-member reported in the previous chapter was shown here to possess the highest crystallite aspect ratio, favouring the *ab* planar direction of conductivity. This furthered its case as a promising high-performance transparent p-type conductor.

Chapter 5 Effect of Isovalent Substitution of Elements on Crystal Structure and Optoelectronic Properties in 325-Type Layered Oxychalcogenides

5.1 Introduction

The layered oxysulfide, $Sr_3Sc_2O_5Cu_2S_2$, investigated with respect to transparent p-type conductivity by Liu *et al.* in 2007, exhibited band gap energies greater than the 3.1 eV visible limit, as did the analogous $Ba_3Sc_2O_5Cu_2S_2$ reported here in *chapter 3*.[48] It was also reported that the strontium compound possessed hole mobility at the VBM of 150 $cm^2\ V^{-1}\ s^{-1}$. Hole mobility is proportional to the extent of hybridisation of its constituent states, namely the copper 3*d* and sulfur 3*p*, in this case. It was shown previously that substitution of strontium with barium at the $^{XII}A^{2+}$ site, had the effect of increasing the basal lattice parameter. This resulted in a corresponding predicted increase in copper-copper distance with observed band gap energy of 3.24 eV.

This chapter reports on the phase-space investigation of candidate transparent p-type conducting materials sharing the 325-type layered structure with the current 'benchmark' compound, $Sr_3Sc_2O_5Cu_2S_2$, of general formula $A_3M_2O_5M'_2Ch_2$. *A* and *M* are perovskite-layer cations; and *M'* is the softer cation, and *Ch*, a group VI/chalcogen anion, in the litharge-like layer. Candidate substitute elements were chosen for each site in terms of their potential effect on the geometry of the conductive metal-chalcogenide tetrahedral layer and therefore the expected resultant optoelectronic properties of the compound.

The complete substitution with the elements indium, yttrium and lanthanum; silver; and selenium on the *M*, *M'* and *Ch* crystallographic sites of the oxychalcogenide $Ba_3M_2O_5M'_2Ch_2$ respectively, was attempted synthetically in various combinations. The compositions of the targeted compounds are listed below and the results of these syntheses are discussed in *section 5.3*: Copper sulfides: $Ba_3In_2O_5Cu_2S_2$, $Ba_3Y_2O_5Cu_2S_2$ and $Ba_3La_2O_5Cu_2S_2$; copper selenides: $Ba_3Sc_2O_5Cu_2Se_2$, $Ba_3In_2O_5Cu_2Se_2$, $Ba_3Y_2O_5Cu_2Se_2$ and $Ba_3La_2O_5Cu_2Se_2$; silver sulfides: $Ba_3Sc_2O_5Ag_2S_2$, $Ba_3In_2O_5Ag_2S_2$, $Ba_3Y_2O_5Ag_2S_2$ and $Ba_3La_2O_5Ag_2S_2$; and silver selenides: $Ba_3Sc_2O_5Ag_2Se_2$, $Ba_3In_2O_5Ag_2Se_2$, $Ba_3Y_2O_5Ag_2Se_2$ and $Ba_3La_2O_5Ag_2Se_2$.

5.2 Experimental

The potential compounds investigated in this chapter were targeted in ≈ 0.5 g batches by the conventional solid-state synthetic route as described previously. The powder precursors in the appropriate stoichiometric ratio (given by *equation 5.1*) were ground, pressed into pellets (≈ 0.75 GPa) and placed into alumina crucibles. The alkali earth oxides, sulfides and, in the case of this chapter, selenides, were synthesised in-house via the procedures described in *appendix D*. (It is noted that it was necessary to fracture the pellet into several pieces in order to fit it into the crucible.) The crucible was placed inside a quartz tube sealed at one end. A quartz spacer, made from a narrower tube, was placed in the bottom of the main tube to avoid the thermal expansion of the alumina crucible from applying pressure on the inner walls of tube at the weaker tapered end. The entire process, as described thus far, was conducted under the inert atmosphere (< 10 ppm O_2) of a nitrogen-filled glovebox. Once the sample-containing crucibles were loaded, the tube was sealed at the open end by use of a Swagelok union, linking the tube to a side arm adapter fitted with a Youngs' tap. The tap was closed and the ensemble removed from the glovebox. The tube was clamped in place and the side-arm adapter connected to a vacuum pump. The tap was opened and the tube kept under dynamic vacuum for > 15 mins. An oxypropane blowtorch [$p(O_2/C_3H_8)$ = 2.5/0.25 bar] was used to seal the quartz tube, creating an ampoule sealed under static vacuum. The ampoule was then heated in a box furnace at a rate of 10 °C min^{-1} typically to 800 °C, at which point the temperature was usually held for 12 h before cooling naturally to room temperature. It is specified in the discussion where these conditions were not used. The ampoules were opened under an inert atmosphere and the contents analysed by air-sensitive powder x-ray diffraction. The samples were subjected to further heating cycles until consistent product(s) were observed by x-ray diffraction.

$$A\mathrm{O} + 2\,ACh + M_2\mathrm{O}_3 + M'_2\mathrm{O} \rightarrow A_3M_2\mathrm{O}_5M'_2Ch_2 \qquad 5.1$$

5.3 Results and Discussion

5.3.1 Isovalent Substitution at the Perovskite Metal, *M*, Site

5.3.1.1 Attempted Syntheses of $Ba_3M_2O_5Cu_2S_2$, where *M* = Y and La

It was previously shown in *chapter 3* and described in the introduction of this chapter that the isovalent substitution of the strontium for barium in the literature compound had the effect of increasing the basal lattice parameter, which had the effect of increasing the band gap energy and predicted conductivity. Further lattice expansion by increased-radius isovalent substitution on the *A* site was precluded by the radioactivity of the larger-radius alkali earth metal, the eponymous radium. The focus was therefore moved to the other perovskite cation site. Here, three alternative *M* site cations were considered which possessed larger $^{VI}M^{3+}$ ionic radii than scandium; namely yttrium, indium and lanthanum. The instability of compounds including these cations predicted by Williamson, was empirically suspected to arise from the size 'mismatch' between the barium *A* cation and the increasing radii of the *M* cations, as indicated by the decrease away from unity in Goldschmidt tolerance factor. These are summarised in *table 5.1* for the candidate *M* site elements when included in a hypothetical bulk barium oxide perovskite lattice, $[BaMO_3]^{2+}$.

Table 5.1 *Summary of the ionic radii and tolerance factors in a barium oxide perovskite lattice, of the candidate replacement M site elements. Those for the current M site element, scandium, are shown for comparison (bottom).*

M^{3+} Cation	$r_{ionic}(^{VI}M^{3+})$ / Å	t ($[BaMO_3]^{2+}$)
La	1.032	0.88
Y	0.9	0.93
In	0.8	0.97
Sc	0.745	0.99

Promising properties were observed upon geometric modification by successful incorporation of barium onto the *A* site. To develop this further, the syntheses of compounds with the larger ionic radii *M* site elements yttrium, indium and lanthanum, were attempted. The largest *A* site cation, barium, was maintained in the targeted compounds to further increase the basal lattice parameter compared to that in $Ba_3Sc_2O_5Cu_2S_2$. The aim was to determine the effects of any successful compositional, and corresponding structural modification, on the predicted optoelectronic properties of these materials.

The yttrium and lanthanum-containing targeted compounds, $Ba_3Y_2O_5Cu_2S_2$ and $Ba_3La_2O_5Cu_2S_2$, were not observed by PXRD after 2 x 12 h heating cycles of the corresponding precursors at 800 ^{o}C. The PXRD patterns for the powders resultant from the attempted syntheses of compounds with intended compositions $Ba_3Y_2O_5Cu_2S_2$ and $Ba_3La_2O_5Cu_2S_2$, refined against the identified impurity phases, are provided in *figures 5.1 and 5.2*. The resultant powders were found to contain mixtures of the crystalline phases of the precursors barium sulfide and the metal oxide, M_2O_3, corresponding to each intended composition, in addition to elemental copper metal. A barium yttrium oxide, BaY_2O_4, phase was also observed as a product in the attempted synthesis of the yttrium-containing analogue.

5.3.1.2 $Ba_3In_2O_5Cu_2S_2$

The phase-pure compound with intended composition of $Ba_3In_2O_5Cu_2S_2$ was successfully synthesised after a single cycle of 800 °C for 12 h. This was confirmed by the Rietveld refinement of a crystallographic model describing the compound isostructural to the prototype, to the x-ray diffraction data collected from the resultant powder shown in *figure 5.3*. The fractional atomic coordinates describing the crystallographic model that were refined to the observed PXRD data, are tabulated in *appendix H.1*. The compound $Ba_3In_2O_5Cu_2S_2$ was observed despite a calculated E above Hull value of 0.34 eV atom^{-1}, as reported by Williamson *et al.*, indicating its thermodynamic instability with respect to its decomposition products.[76]

The observed synthesis of the indium compound and lack of that of the yttrium and lanthanum analogues is consistent with the empirical Goldschmidt tolerance factors for the candidate *M* substitutes in a barium oxide perovskite structure as given previously in *table 5.1*. The calculated tolerance factor is closest to unity for the indium compound and decreases further from a value of one for the yttrium and lanthanum analogues respectively, indicating increasing perovskite cation 'mismatch', strain and decreasing thermodynamic stability, as predicted and supported by the observed synthetic results.

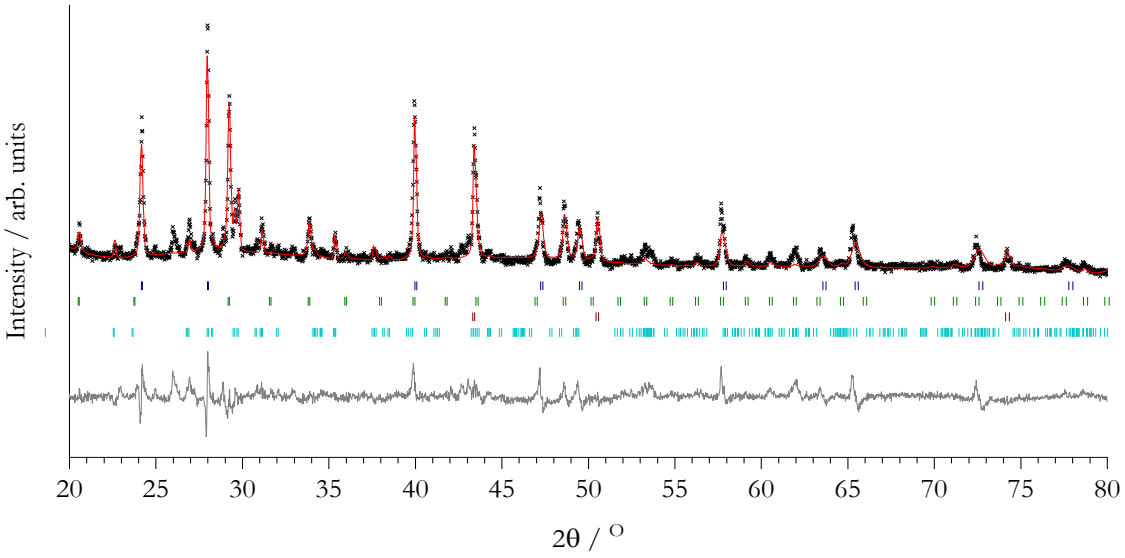

Figure 5.1 *Observed PXRD pattern for products of the attempted synthesis of target compound $Ba_3Y_2O_5Cu_2S_2$. The black crosses illustrate the observed data points, the red line shows the calculated profile from the Rietveld refined model and the grey line is the difference between the two. Observed phases, the diffraction peak positions of which are represented by the tick marks, included BaS (blue), Y_2O_3 (green), Cu (red) and BaY_2O_4 (aqua). R_{wp} = 14.57 % and χ^2_{red} = 4.278.*

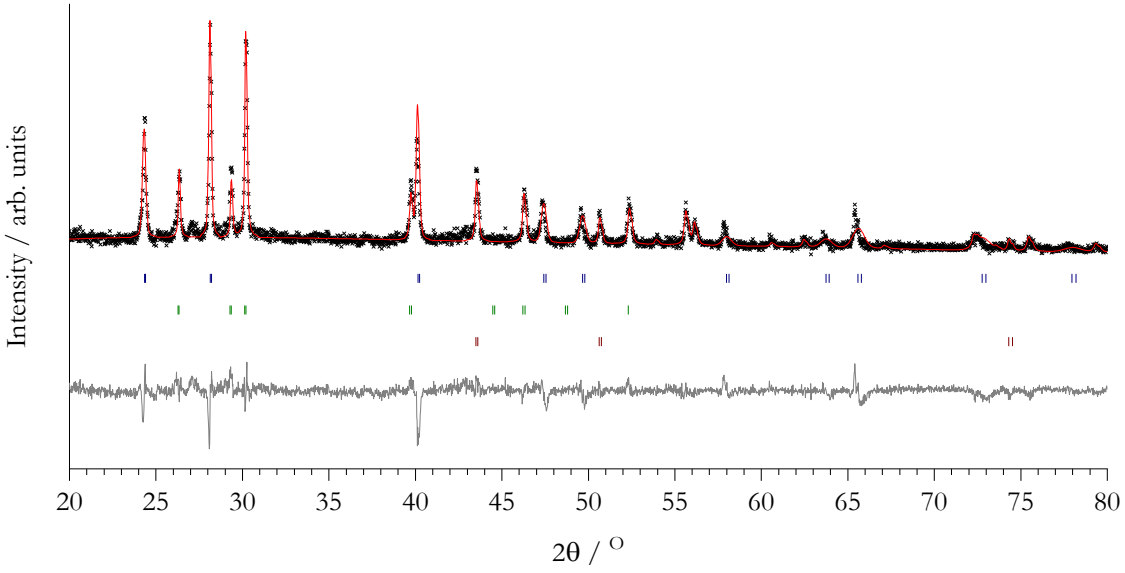

Figure 5.2 *Observed PXRD pattern for products of the attempted synthesis of target compound $Ba_3La_2O_5Cu_2S_2$. The black crosses illustrate the observed data points, the red line shows the calculated profile from the Rietveld refined model and the grey line is the difference between the two. Observed phases, the diffraction peak positions of which are represented by the tick marks, included BaS (blue), La_2O_3 (green), and Cu (red). R_{wp} = 19.85 % and χ^2_{red} = 1.934.*

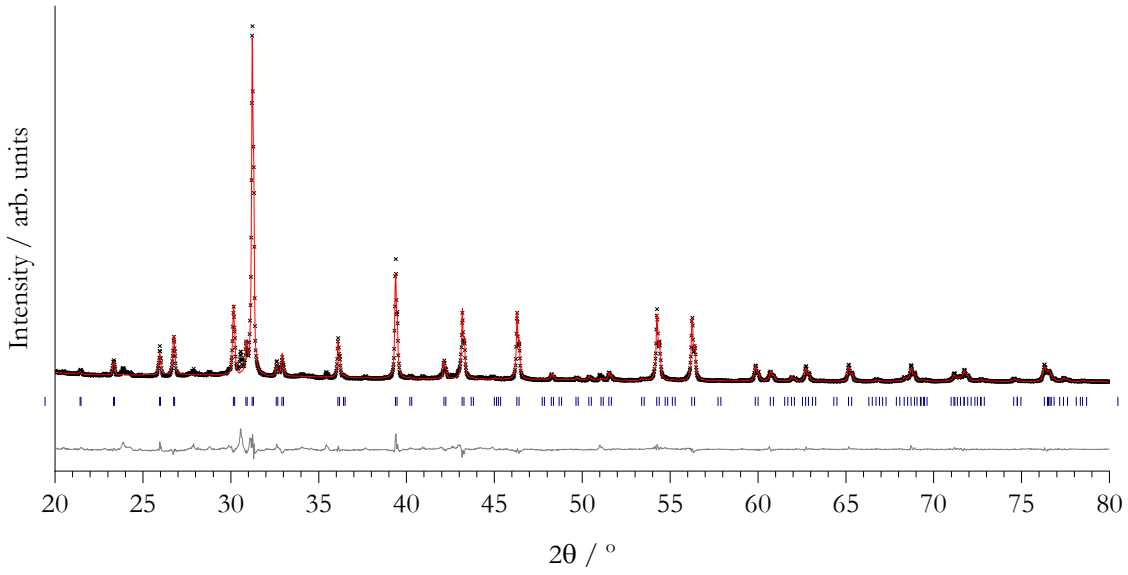

Figure 5.3 *Powder x-ray diffractogram for the observed compound $Ba_3In_2O_5Cu_2S_2$. The observed data is represented by black crosses, the calculated diffraction pattern by a solid red line and the difference profile as a solid grey line below. The blue tick marks show the expected peak positions from the Rietveld refined model. The compound crystallised into a structure with the tetragonal I4/mmm space group. R_{wp} = 9.93 % and χ^2_{red} = 9.260.*

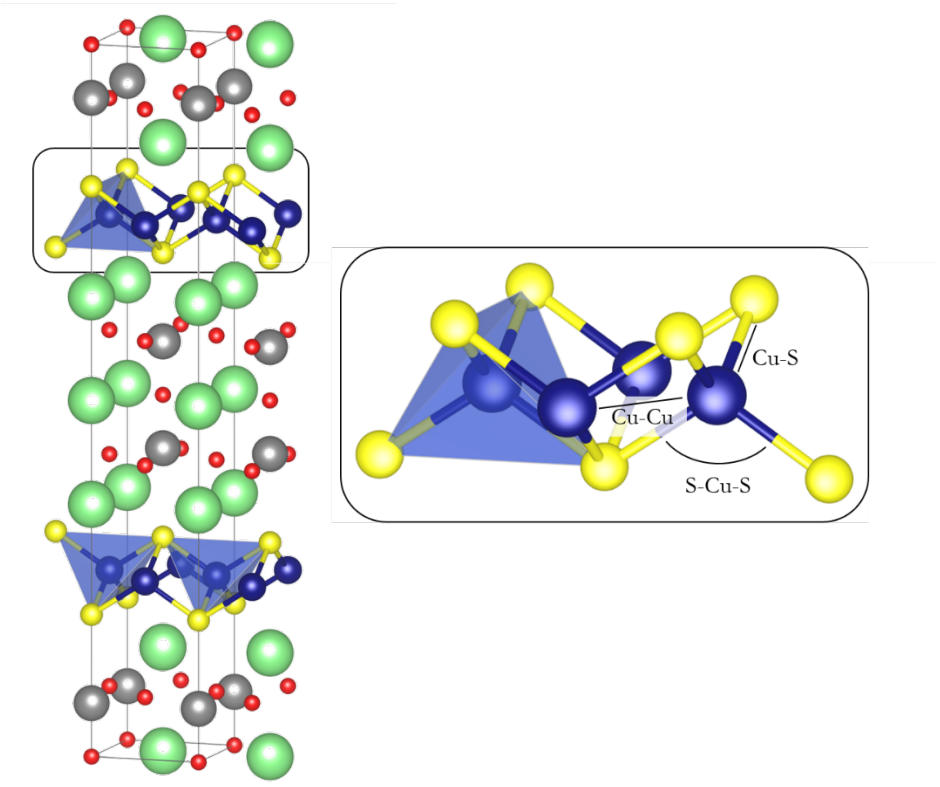

Figure 5.4 *Illustration of the geometric parameters (lengths and angles) investigated in the conductive copper sulfide layers in the 325-type layered oxysulfide compounds studied here.*

Table 5.2 *Summary of the ionic radii of the M cations being substituted and the resultant lattice parameters and interatomic distances/angles of the observed phases. A graphical illustration of the bond lengths, distances and angles is repeated in figure 5.4.*

Compound	$r_{ionic}(^{VI}M^{3+})$ / Å	a=b / Å	Cu-Cu / Å	Cu-S / Å	S-Cu-S / o
$Ba_3Sc_2O_5Cu_2S_2$	0.745	4.14458(4)	2.93067(4)	2.46951(5)	114.1015(9)
$Ba_3In_2O_5Cu_2S_2$	0.8	4.18552(5)	2.95961(4)	2.45024(3)	117.3217(9)

As shown in *table 5.2* the successful substitution of scandium for indium to yield the compound $Ba_3In_2O_5Cu_2S_2$, led to the expected relative increase in basal lattice parameter. The same trend was observed between the two compounds reported in the literature also related by isovalent substitution at the *M* site, $Ba_3M_2O_5Ag_2S_2$ where *M* = Lu and Y.[69] The basal expansion was accompanied by the inevitable increase in copper-copper distance, seen as desirable for the retention of the band gap. The complete substitution of scandium for indium also further decreased the copper-sulfide distance with an observed increase in sulfur-copper-sulfur angle.

The net effect of the reduction in copper-sulfur bond length and increase in sulfur-copper-sulfur angle away from the ideal tetrahedral, on the hybridisation at the VBM and therefore band gap and charge carrier mobility, could not be qualitatively predicted. The effect of the complete indium incorporation on the band gap was determined by linear fitting of a Tauc plot in *figure 5.5* constructed from raw diffuse reflectance data (inset).

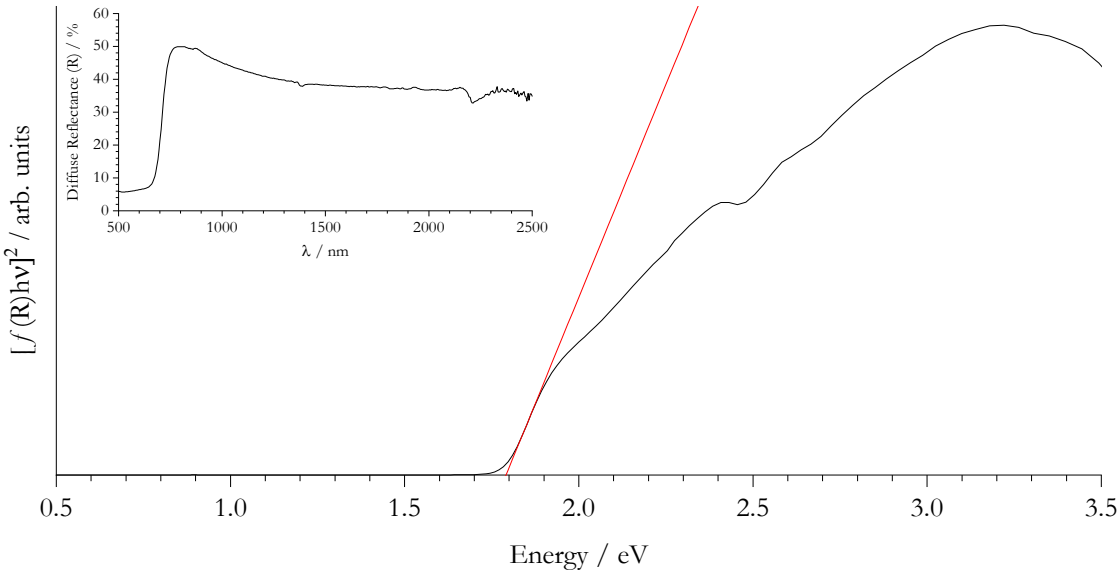

Figure 5.5 *Tauc plot for the compound $Ba_3In_2O_5Cu_2S_2$ constructed from the collected raw diffuse reflectance data (inset). The solid red line shows a linear fit to the region of steepest gradient; its x-intercept marking the band gap energy at 1.8 eV. A change in diffraction grating on the spectrophotometer was responsible for the feature at around 2.5 eV.*

It was found that the band gap of the compound $Ba_3In_2O_5Cu_2S_2$ was appreciably lower than that of the scandium analogue; a band gap of 1.8 eV was observed compared to that of 3.1 eV. It can be seen from inspection of the data provided in *table 5.3* that the electronegativity of indium is higher than that of scandium. Qualitatively, comparable occupied bonding states involving indium were expected to lie lower in energy than those of scandium, precluding the possibility that indium *p*-states were involved in a raised VBM, reducing the band gap. It was realised that the indium atom was the only of the candidates to possess a filled (n-1)*d* sub-shell, namely the $4d^{10}$. It was expected that these *d* electrons occupied non-bonding states within the band gap region, essentially cutting the band gap in two and resulting in the large observed reduction in band gap energy to 1.8 eV.[32] Regardless of the combined effect of the reduced copper-sulfur distance and increased sulfur-copper-sulfur angle, the compound $Ba_3In_2O_5Cu_2S_2$, and most likely many analogous indium-containing compounds, was deemed unsuitable for transparent applications, owing to its band gap energy of 1.8 eV.

While it was not found to be possible in the $Ba_3M_2O_5Cu_2S_2$ prototype compound, the use of perovskite *M* elements yttrium and lanthanum were still thought to have potential for increasing the transparent conductive properties by expansion of the perovskite layer and its effects on the geometry of the conductive layer.

Table 5.3 Extension of table 5.1 including the electronegativity and (n-1)d sub-shell electronic occupany for the candidate replacement M site elements for the discussion of observed band-gap energy. Those for the current M site element, scandium, are shown for comparison (bottom).

M^{3+} Cation	$r_{ionic}(^{VI}M^{3+})$ / Å	t ($[BaMO_3]^{2+}$)	Electronegativity	(n-1)*d* Atomic Sub-shell Occupation
La	1.032	0.88	1.10	Empty
Y	0.9	0.93	1.22	Empty
In	0.8	0.97	1.78	Full
Sc	0.745	0.99	1.36	Empty

5.3.2 Isovalent Substitution at the Chalcogen Site, *Ch*

The perovskite layer had apparently been exhausted of options for suitable isovalent substitutes. At the *A* site, the largest ionic radius A^{2+} cation of the element barium was already employed. Those elements with larger radii are radioactive and therefore undesirable for this application. Scandium at the $^{VI}M^{3+}$ perovskite cation site, seemingly possessed the optimum combination of radius, electronegativity and (n-1)*d* sub-shell occupancy, at least when compared to indium. The use of the elements yttrium and lanthanum may show improvement in optoelectronic properties, however, could not be incorporated into the barium oxide perovskite lattice in combination with the copper sulfide conductive layer. The oxygen was not considered for isovalent substitution for sulfur, as it is the high electronegativity, chemical hardness and radius of the oxygen, compared to that of the sulfur in the conductive layer, that leads to the segregation of these compounds into layered structures, crucial for transparency.

However, isovalent chalcogen substitution is possible in the litharge-like conductive layer. The possibility of substituting sulfur for the heavier chalcogen, selenium, was investigated. Selenium was observed on the conductive-layer chalcogen site of a range of compounds with the same layered 325 structure. For example, in the compounds $Sr_3Fe_2O_5M'_2Se_2$, where *M* = Cu and Ag, and $Ba_3M_2O_5Ag_2Se_2$, where *M* = Y and Lu , reported in the literature.[69,70] The substitution of sulfur for selenium in the prototype compound $Ba_3Sc_2O_5Cu_2S_2$ was expected to increase the mobility at the VBM, owing to the expected increased hybridisation between the copper and chalcogen in the conductive layer.[27] The increase in conductivity in layered mixed anion compounds as a result of a complete substitution of sulfur for selenium on the chalcogen site was reported in the literature for the compounds SrFCu*Ch*, where *Ch* = S and Se.[90]

This increase in hybridisation was also expected to have the effect of increasing the energy of the VBM. The effect of this on the band gap energy was difficult to predict as the increased radius of the selenide compared to the sulfide in the conductive layer was expected to increase the basal lattice parameter and copper-copper distance. This increase was expected to increase the energy at the CBM, the net effect of which in combination with the increased VBM on the band gap energy, was not possible to qualitatively predict. Decreases in band gap energy were reported in the literature when sulfur in the layered oxychalcogenides SrFCu*Ch* and LaOCu*Ch*, for example, was substituted for selenium.[90,91] This indicated that the effect of the reduced copper-chalcogen bonding distance, in addition to the increase in energy of the occupied electronic states owing to reduced electronegativity, had a greater effect on the band gap than the increased copper-copper distance, at least for these '202'-type ($A_2M_0O_2Cu_2Ch_2$ = *A*OCu*Ch*) layered oxychalcogenides.

5.3.2.1 $Ba_3Sc_2O_5Cu_2Se_2$

The synthesis of the compound with the target composition $Ba_3Sc_2O_5Cu_2Se_2$ was attempted using the synthetic conditions of 800 °C for 12 h. It was anticipated that the complete incorporation of selenium would increase the conductivity compared to that of the literature and previously synthesised prototypes, $Sr_3Sc_2O_5Cu_2S_2$ and $Ba_3Sc_2O_5Cu_2S_2$, respectively. A decrease in band gap energy in relation to the sulfur analogue, $Ba_3Sc_2O_5Cu_2S_2$, was also expected. The band gap of the barium sulfur compound was found to be 3.24 eV. It was thought that this increase relative to the 3.11 eV of $Sr_3Sc_2O_5Cu_2S_2$, may have been sufficient to allow increased conductivity by the incorporation of selenium, whilst maintaining the band gap energy, by use of the larger barium perovskite *A* cation, when comparing the compound targeted here, $Ba_3Sc_2O_5Cu_2Se_2$, with the current literature benchmark, $Sr_3Sc_2O_5Cu_2S_2$.

The compound $Ba_3Sc_2O_5Cu_2Se_2$ was observed, albeit impure, by x-ray diffraction after an initial cycle under the standard conditions of 800 °C for 12 h *(figure 5.6, top)*. A significant fraction of the barium selenide precursor (the diffraction peak positions of the crystalline phase of which were highlighted and indicated with the green tick marks) remained after this initial cycle. A second cycle at 800 °C for 12 h was completed on the resultant sample which had been reground and stored under an inert atmosphere. X-ray diffraction analysis of this product found that the fraction of the barium selenide precursor impurity *(green tick marks)* had decreased, yet remained significant as can be seen in *figure 5.6, bottom*. In order to ensure completion of the reaction, the resulting product was reground and subjected to a further heating cycle at the increased temperature of 900 °C, for a prolonged duration of 24 h. X-ray diffraction analysis showed that this third cycle of increased temperature and time was sufficient to ensure complete reaction of the barium selenide precursor, leaving no detectable indication in the diffraction pattern in *figure 5.7*. The phase purity of the observed $Ba_3Sc_2O_5Cu_2Se_2$ was confirmed by Rietveld refinement of a crystallographic model *(appendix H.2)* isostructural to the tetragonal layered 325-type oxychalcogenides to the observed powder diffraction data.

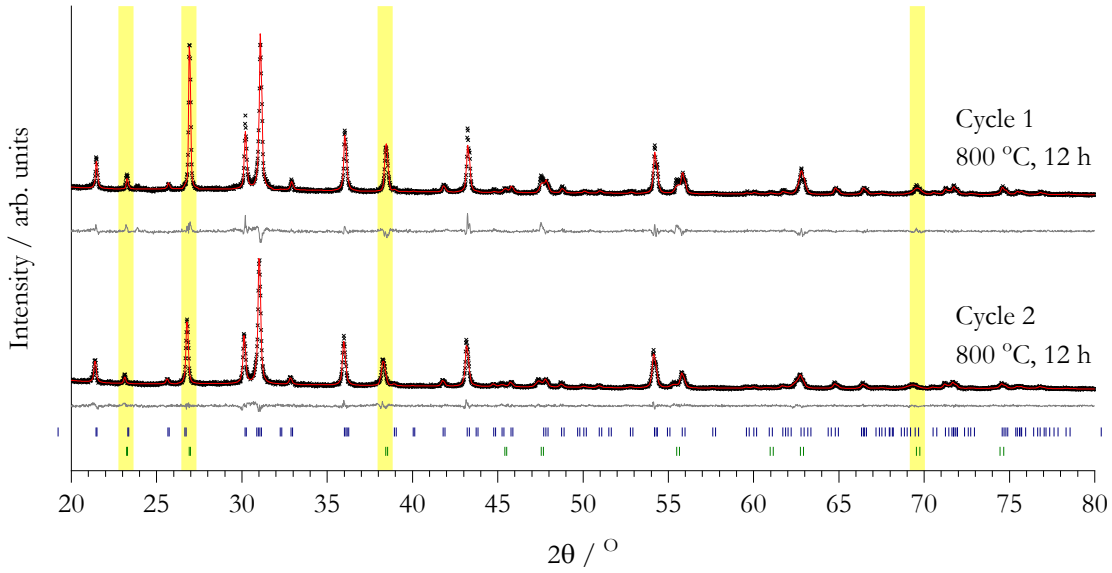

Figure 5.6 *Powder x-ray diffractograms of samples with intended composition $Ba_3Sc_2O_5Cu_2Se_2$. The observed data is represented by black crosses, the calculated diffraction patterns by solid red lines and the difference profiles as solid grey lines below. The blue tick marks show the expected peak positions from the Rietveld refined model of target compound and the green ticks and highlighted peaks indicate the peak positions of the remnant BaSe precursor impurity phase. The synthesis was attempted at 800 °C for cycles of 12 h. The number of cycles completed for each observed phase composition is indicated.*

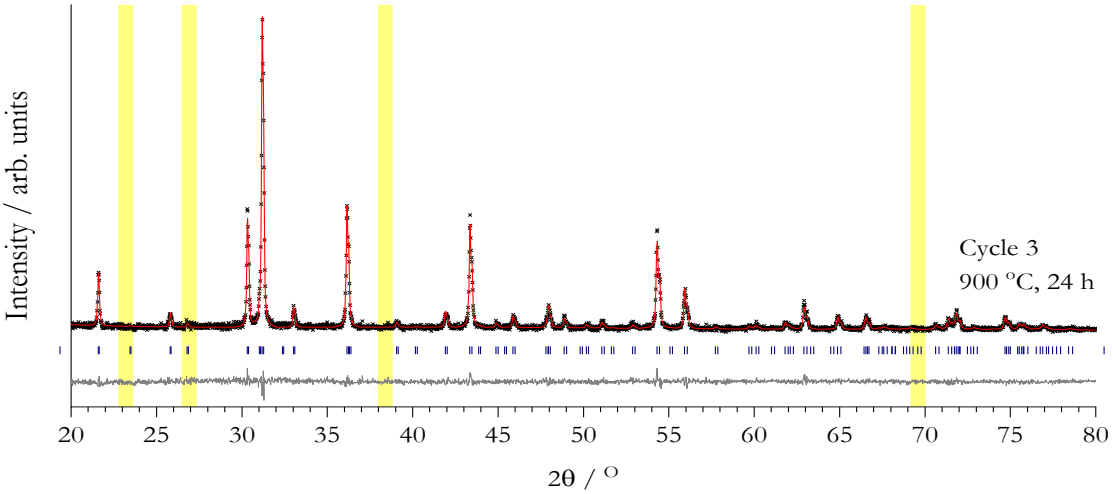

Figure 5.7 *Powder x-ray diffractogram of phase-pure $Ba_3Sc_2O_5Cu_2Se_2$. The observed data is represented by black crosses, the calculated diffraction pattern by a solid red line and the difference profile as a solid grey line below. The blue tick marks show the expected peak positions from the Rietveld refined model and the highlighted regions the peak positions of the barium selenide precursor. The compound crystallised into a structure analogous to the prototype with the tetragonal I4/mmm space group. R_{wp} = 13.05 % and χ^2_{red} = 1.086.*

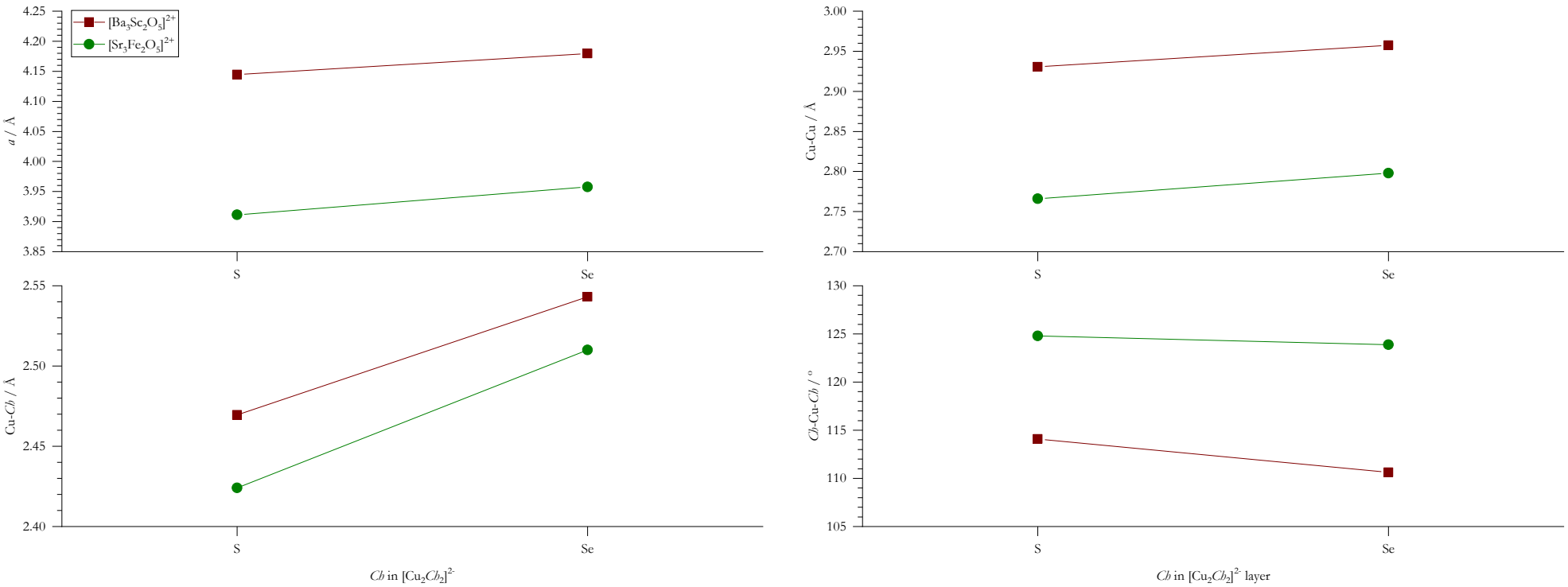

Figure 5.8 Graphical summary of the effect on the lattice parameters and distances and angles, of ionic substitution of sulfur for selenium on the chalcogen (Ch) site, in the two sets of analogous compounds with general formulae $Ba_3Sc_2O_5Cu_2Ch_2$ synthesised here (red squares) and the analogous $Sr_3Fe_2O_5Cu_2Ch_2$ reported in the literature (green circles).

Table 5.4 *Summary of ionic radii of the chalcogen ions being substituted and the lattice parameters of the resultant crystalline phases. Those for the analogous pair of compounds $Sr_3Fe_2O_5Cu_2Ch_2$, where Ch = S and Se, also related by isovalent substitution at the chalcogen site, are shown for comparison (bottom). These data are summarised graphically in figure 5.8.*

Compound	$r_{ionic}(^{IV}Ch^{2-})$ / Å	*a=b* / Å	Cu-Cu / Å	Cu-*Ch* / Å	*Ch*-Cu-*Ch* / o	Ref.
$Ba_3Sc_2O_5Cu_2S_2$	1.84	4.14458(4)	2.93067(4)	2.46951(5)	114.1015(9)	*n/a*
$Ba_3Sc_2O_5Cu_2Se_2$	1.98	4.18227(8)	2.95731(6)	2.54316(5)	110.623(3)	*n/a*
$Sr_3Fe_2O_5Cu_2S_2$	1.84	3.9115	2.766	2.424	124.792	70
\$Sr_3Fe_2O_5Cu_2Se_2$	1.98	3.95770	2.798	2.510	123.875	70

Substitution of sulfur, $r_{ionic}(^{IV}S^{2-})$ = 1.84 Å, for selenium, $r_{ionic}(^{IV}Se^{2-})$ = 1.98 Å, in the structural prototype, yielded an expected increase in basal lattice parameter as can be seen by the summary of crystallographic geometries in *table* 5.4 represented graphically in *figure 5.8*. In terms of the geometry of the conductive layer, the copper-copper distance was found to increase with selenium addition, as was expected owing to its inextricable link to the basal lattice parameter. In contrast to the effect on the conductive layer geometry of lattice expansion by substitution in the perovskite layer, the increase in the radius of the chalcogenide had the effect of, unsurprisingly, increasing the copper-chalcogen bond length. However, the increase in copper-chalcogen distance was not as great as was expected by the sum of the atomic radii alone. The distance calculated by the simple sum of the ionic radii of the copper (I) and sulfur (-II) ions was 2.44 Å and for copper (I) selenium (-II), 2.58 Å. The copper-chalcogen distances calculated from the atomic coordinates in the crystallographic model refined to the collected powder x-ray diffraction data for the compounds $Ba_3Sc_2O_5Cu_2Ch_2$, where *Ch* = S and Se, were found to be 2.46951 and 2.54316 Å, respectively. As the combined ionic radii of the elements in the conductive layer increased by 5.7 %, the observed extension in the distance between them increased by only 3.0 %, indicating a greater degree of overlap between the copper and selenium atoms compared with that of the copper and sulfur.

It was also found that the effect of the substitution of sulfur by the increased-radius selenium was to reduce the chalcogen-copper-chalcogen angle. This is in contrast to the effect on the same angle induced by the substitution of larger radius cations on the *M* site, found previously. The trend in effects on lattice geometry of substitution of sulfur for selenium in this example was found to be the same as that found between the compounds $Sr_3Fe_2O_5Cu_2Ch_2$, where *Ch* = S and Se, as reported in the literature, as illustrated in the plot (*fig. 5.8, bottom right)*.[90,91]

The geometry of the conductive layer in the compound $Ba_3Sc_2O_5Cu_2Se_2$ suggested relatively high intrinsic mobility and therefore potentially increased bulk conductivity. The larger radius of the selenium had the effect of increasing the basal lattice parameter and therefore the copper-copper distance desirable for maintaining transparency at the CBM; increasing the copper-chalcogen distance, but to such an extent that an increase in hybridisation was still anticipated; and reducing the chalcogen-copper-chalcogen bond angle towards the ideal tetrahedral angle, maximising hybridisation. The expected increase in p-type conductivity upon substitution of sulfur for selenium in a layered oxychalcogenide was consistent with empirical conductivity trends observed for the analogous compounds in the literature, as described previously.[90,91]

The effect on the band gap energy of the chalcogen substitution was investigated by diffuse reflectance measurement. The resulting Tauc plot constructed from the raw data shown plotted inset, is shown in *figure 5.9*. It was found that the band gap energy of the compound $Ba_3Sc_2O_5Cu_2Se_2$ was 3.05 eV. This showed a small expected decrease relative to that of $Ba_3Sc_2O_5Cu_2S_2$. However, this is promising as the expected increase in conductivity, relative to the current benchmark candidates, was shown to be coupled with relatively high maintenance of the band separation, and therefore transparency. The measured band gap energy of 3.05 eV lay only 0.05 eV below that of the widely-excepted criteria for visible light transparency. It may be that, given the expected increase in conductivity, the transparency can be sacrificed for some applications. Furthermore, in preparing these materials for high-conductivity, p-type doping is required. The increase in positive hole charge carrier concentration at the VBM that this is intended to cause, may affect the band gap by a Moss-Burstein shift sufficiently that the band gap is increased above the 3.1 eV threshold, once doped.[92] Therefore the compound $Ba_3Sc_2O_5Cu_2Se_2$ is a promising candidate for a high-performance transparent p-type conductor.

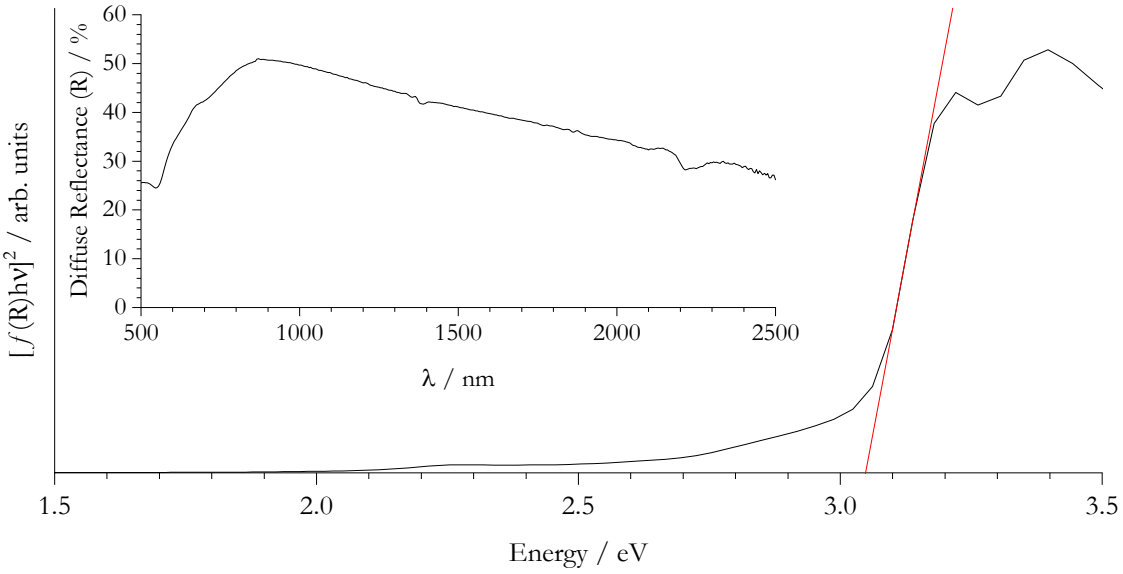

Figure 5.9 *Tauc plot for the compound $Ba_3Sc_2O_5Cu_2Se_2$ constructed from the collected raw diffuse reflectance data (shown plotted inset). The solid red line shows a linear fit to the region of steepest gradient; its x-intercept marking the band gap energy at 3.05 eV.*

5.3.3 Isovalent Substitution at the Perovskite Metal, *M*, Site | Revisited

The potential towards improved transparent conductivity of substitution of scandium by yttrium or lanthanum on the *M* perovskite cation site was identified previously in *section 5.3.1*. The yttrium and lanthanum were expected to increase the basal perovskite lattice parameter owing to their increased ionic radii compared to that of scandium. The increase in basal lattice parameter by cationic substitution in the perovskite layer was previously shown to potentially benefit transparent conductivity by alteration of geometry in the conductive copper sulfide layer. This was observed for indium, however, as discussed previously, the filled (n-1)*d* states of the indium led to the formation of 'interband' states, consistent with those indicated by Hosono, and a corresponding large reduction in band gap energy from 3.24 to 1.8 eV.[32] Despite its calculated tolerance factor which deviates from unity (0.93) and the previous failure to synthesise the compound $Ba_3Y_2O_5Cu_2S_2$, the perovskite oxide block containing barium and yttrium cations, $[Ba_3Y_2O_5]^{2+}$, was reported in the literature in the analogous compound, $Ba_3Y_2O_5Ag_2Se_2$.[69] It was proposed that the larger silver and selenium ions, compared to those of copper and sulfur, accommodated the mismatch in the perovskite lattice between the barium and yttrium cations. In light of the observed synthesis of the compound $Ba_3Sc_2O_5Cu_2Se_2$, the possibility of using a larger chalcogenide, selenium in this case, to stabilise the incorporation of the larger yttrium and lanthanum cations in the perovskite layer was investigated. The syntheses of the compounds with target compositions $Ba_3M_2O_5Cu_2Se_2$, where *M* = Y, La and In, were attempted at 900 °C for durations of 24 h.

5.3.3.1 $Ba_3Y_2O_5Cu_2Se_2$

The compound $Ba_3Y_2O_5Cu_2Se_2$ was successfully synthesised, apparently for the first time, as confirmed by Rietveld refinement of a representative crystallographic model to the collected powder x-ray diffraction data shown in *figure 5.10*. The refined atomic coordinates of the model are provided in *appendix H.3* and were used to calculate the geometries of the conductive layer. These are summarised in *table 5.5* with those for the analogous compound $Ba_3Sc_2O_5Cu_2Se_2$ for comparison.

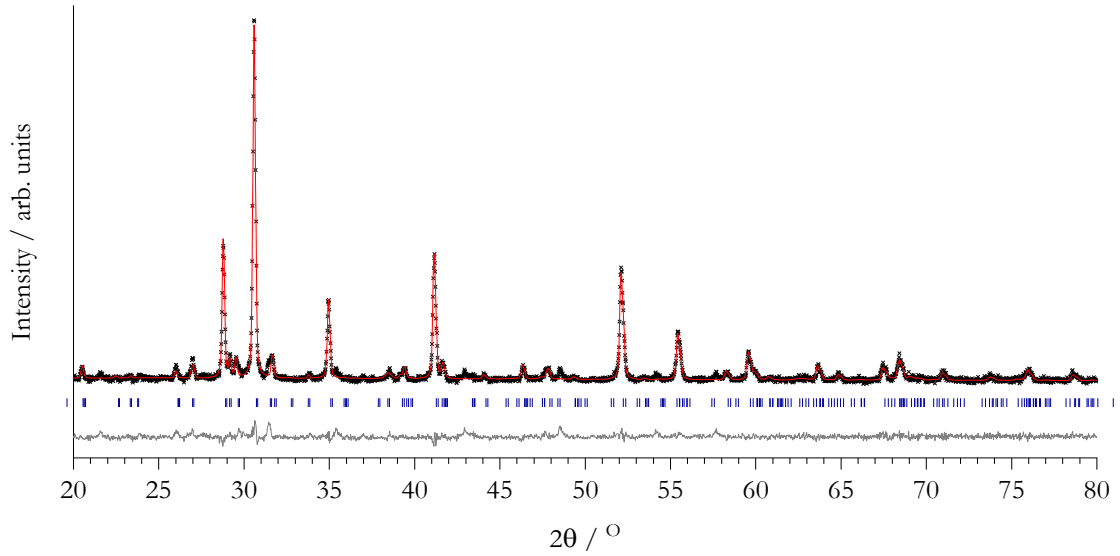

Figure 5.10 *Powder x-ray diffractogram of $Ba_3Y_2O_5Cu_2Se_2$. The observed data is represented by black crosses, the calculated diffraction pattern by a solid red line and the difference profile as a solid grey line below. The blue tick marks show the expected peak positions from the Rietveld refined model. The compound crystallised into a structure with the tetragonal I4/mmm space group. R_{wp} = 11.77 % and χ^2_{red} = 1.095.*

Table 5.5 *Summary of ionic radii of the M site cations being substituted in $Ba_3M_2O_5Cu_2Se_2$ and the corresponding lattice parameters describing the crystalline phases formed.*

Compound	$r_{ionic}(^{VI}M^{3+})$ / Å	*a=b* / Å	Cu-Cu / Å	Cu-Se / Å	Se-Cu-Se / °
$Ba_3Sc_2O_5Cu_2Se_2$	0.745	4.18227(8)	2.95731(6)	2.54316(5)	110.623(3)
$Ba_3Y_2O_5Cu_2Se_2$	0.9	4.3912(1)	3.10505(7)	2.57504(5)	117.002(3)

The complete substitution of scandium for the larger ionic radius yttrium observed in the compound $Ba_3Y_2O_5Cu_2Se_2$ had the expected effect of increasing the basal lattice parameter and copper-copper distance. The copper-selenium distance increased in this case, which opposed the trend observed by the substitution of scandium for the larger indium in the $Ba_3M'_2O_5Cu_2S_2$ reported previously. The combined increases of the copper-selenium length and selenium-copper-selenium angle were expected to be detrimental to conductivity. The effect of the yttrium on the band gap energy was investigated by calculation of the band gap from the Tauc plot shown in *figure 5.11*, derived from the collected raw diffuse reflectance data shown inset.

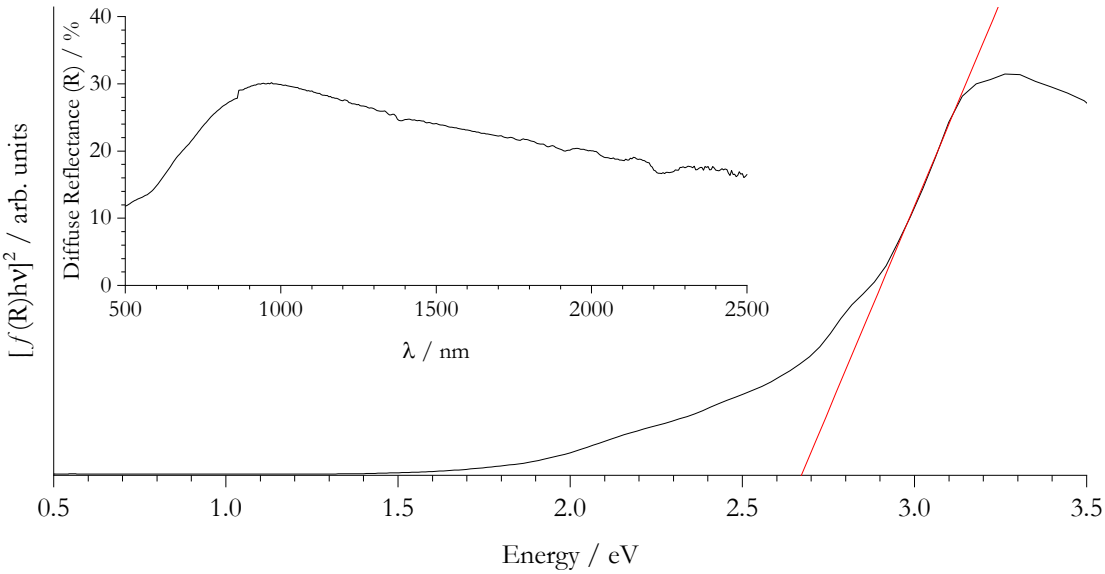

Figure 5.11 Tauc plot constructed from raw diffuse reflectance data (inset) for the compound $Ba_3Y_2O_5Cu_2Se_2$, the solid red line shows a linear fit to the region of steepest gradient – its x-intercept marking the band gap energy at 2.67 eV.

The band gap energy of $Ba_3Y_2O_5Cu_2Se_2$ of 2.67 eV showed a reduction compared to the 3.05 eV of the scandium analogue. The increased ionic radius of the yttrium compared to that of the scandium had the anticipated effect of expanding the basal lattice parameter and the copper-copper distance. This was expected to have the effect of reducing hybridisation of the copper states and raising the energy at the CBM. Therefore, the reduction in band gap must have arisen from a change in average energy of the band edges or presence of additional states between the copper-copper and copper-selenium bands. The increased copper-selenium bond length (contrary to that observed for increased radius *M* ion substitution in the copper sulfides) and increased angle away from the ideal tetrahedral, was expected to also reduce hybridisation at the VBM. Seen as detrimental to the p-type mobility, this would, however, have been expected to increase the band gap energy. Therefore, the observed reduction is likely to be a result of the incorporation of yttrium states into either the CBM or VBM, or both, as a result of its lower electronegativity compared to that of scandium, causing their energies to converge and the band gap to decrease. A small decrease in electronegativity from 1.36 for scandium to 1.22 for yttrium resulted in the *M* states likely hybridising with the copper-copper and copper-selenium states typically occupying the band edges in the scandium analogous and encroaching on the band gap. This indicated that the scandium states lay close to, but crucially beyond those of the band edges, resulting in the consideration of electronegativity, in addition to the (n-1)*d* state occupancy previously discussed with regard to indium, when seeking to expand the lattice by isovalent substitution at the *M* perovskite lattice site.

5.3.3.2 $Ba_3La_2O_5Cu_2Se_2$

To further investigate this trend, the synthesis was attempted of the compound $Ba_3La_2O_5Cu_2Se_2$ containing the larger, and less electronegative still, lanthanum ion on the *M* site. The powder resulting from the attempted synthesis was analysed by powder x-ray diffraction and the precursor phases barium sulfide, lanthanum oxide and elemental copper were identified as being present. A model containing the crystal structures of the identified precursors was fitted against the observed diffraction pattern as shown in *figure 5.12*.

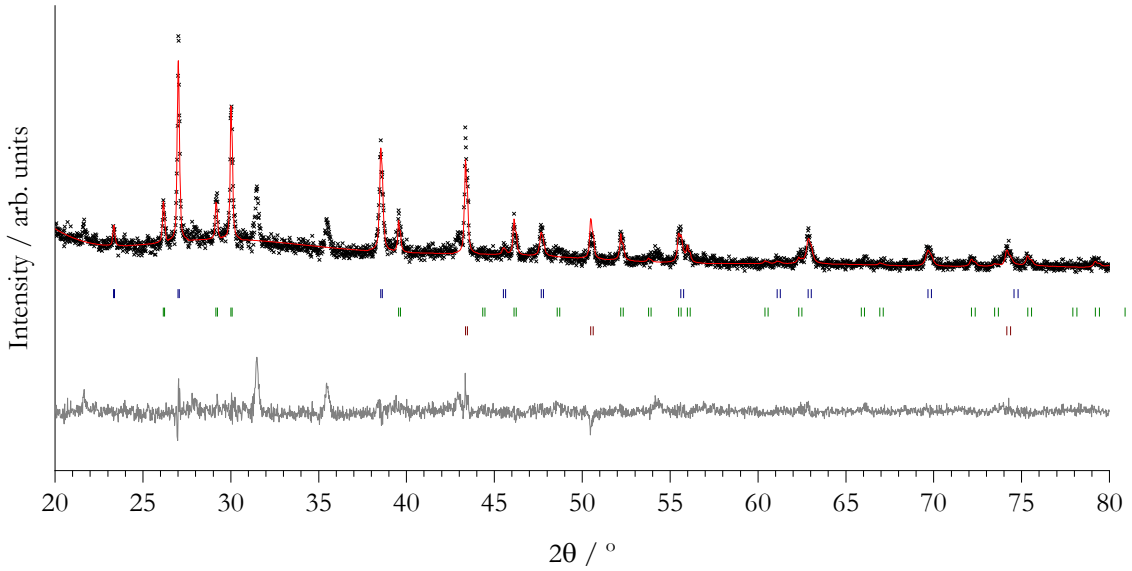

Figure 5.12 Observed PXRD pattern for products of the attempted synthesis of target compound $Ba_3La_2O_5Cu_2Se_2$. The black crosses illustrate the observed data points, the red line shows the calculated profile from the Rietveld refined model and the grey line is the difference between the two. Observed phases, the diffraction peak positions of which are represented by the tick marks, included BaS (blue), La_2O_3 (green), and Cu (red). R_{wp} = 13.63 % and χ^2_{red} = 1.671.

The reason for the unsuccessful attempted synthesis of this compound was expected to be illustrated by its tolerance factor describing the mismatch in ionic radius between the barium and lanthanum in a perovskite lattice. Neither the yttrium nor the lanthanum compounds $Ba_3M_2O_5Cu_2S_2$ were reported to have been synthesised, both possessing tolerance factors further from unity than that of the scandium analogue which was found to exist. The yttrium-containing perovskite block, $[Ba_3Y_2O_5]^{2+}$ was found to exist within the analogous compound $Ba_3Y_2O_5Ag_2Se_2$ reported in the literature and was observed here in the successful synthesis of the targeted compound $Ba_3Y_2O_5Cu_2Se_2$. The increased mismatch compared to that of the barium/scandium perovskite oxide was expected to have been stabilised by the increased lattice parameter as a result of the selenium ion on the chalcogen site of the conductive layer. The mismatch between barium and lanthanum was deemed to be too large to have been supported even by the copper selenide layer. In fact, to the author's knowledge, there has been no barium/lanthanum containing perovskite building-blocks in the layered oxychalcogenides or pnictides reported in the literature. The only example of lanthanum incorporation onto the *M* site in these compounds is in conjunction with bismuth, in the compound $Bi_2LaO_4Cu_2Se_2$, with which it has a tolerance factor of 0.81 in a bulk oxide perovskite.[93]

5.3.3.3 $Ba_3In_2O_5Cu_2Se_2$

In addition to that of yttrium and lanthanum, the substitution of scandium for indium to yield the compound $Ba_3In_2O_5Cu_2Se_2$, was attempted to further evaluate the relationship between ionic radius and conductive layer geometry. This was despite the fact that the indium *M* site element had been concluded to be detrimental to transparency by virtue of the position of its occupied (n-1)*d* states between the valence and conduction band edges. The indium compound $Ba_3In_2O_5Cu_2Se_2$, was successfully synthesised and its structure verified by Rietveld refinement to the observed PXRD data as shown in *figure 5.13* overleaf. The atomic coordinates describing the positions of atoms in this refined model are given in *appendix H.4*, from which the distances and angles are calculated which are tabulated in *table 5.6* and summarised graphically in *figure 5.15*. The band gap energy of this compound was calculated by analysis of the Tauc plot shown in *figure 5.14* which was constructed using the raw diffuse reflectance data collected shown inset.

Table 5.6 *Summary of ionic radii of the M site cations being substituted in $Ba_3M_2O_5Cu_2Se_2$ and the corresponding lattice parameters describing the crystalline phases formed. The analogous yttrium-containing compound previously discussed which completes this homologous set is also repeated for comparison.*

Compound	$r_{ionic}(^{VI}M^{3+})$ / Å	$a=b$ / Å	Cu-Cu / Å	Cu-S / Å	S-Cu-S / °
$Ba_3Sc_2O_5Cu_2Se_2$	0.745	4.18227(8)	2.95731(6)	2.54316(5)	110.623(3)
$Ba_3In_2O_5Cu_2Se_2$	0.8	4.2220(1)	2.98542(9)	2.54431(6)	112.136(3)
$Ba_3Y_2O_5Cu_2Se_2$	0.9	4.3912(1)	3.10505(7)	2.57504(5)	117.002(3)

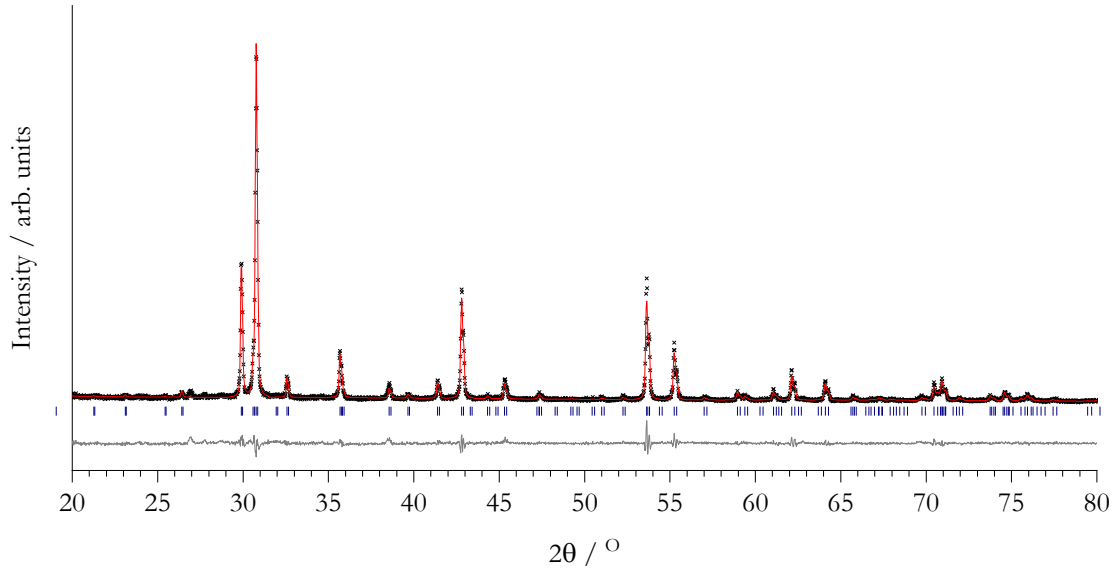

Figure 5.13 *Powder x-ray diffractogram of $Ba_3In_2O_5Cu_2Se_2$. The observed data is represented by black crosses, the calculated diffraction pattern by a solid red line and the difference profile as a solid grey line below. The blue tick marks show the expected peak positions from the Rietveld refined model. The compound crystallised into a structure with the tetragonal I4/mmm space group. R_{wp} = 10.33 % and χ^2_{red} = 1.838.*

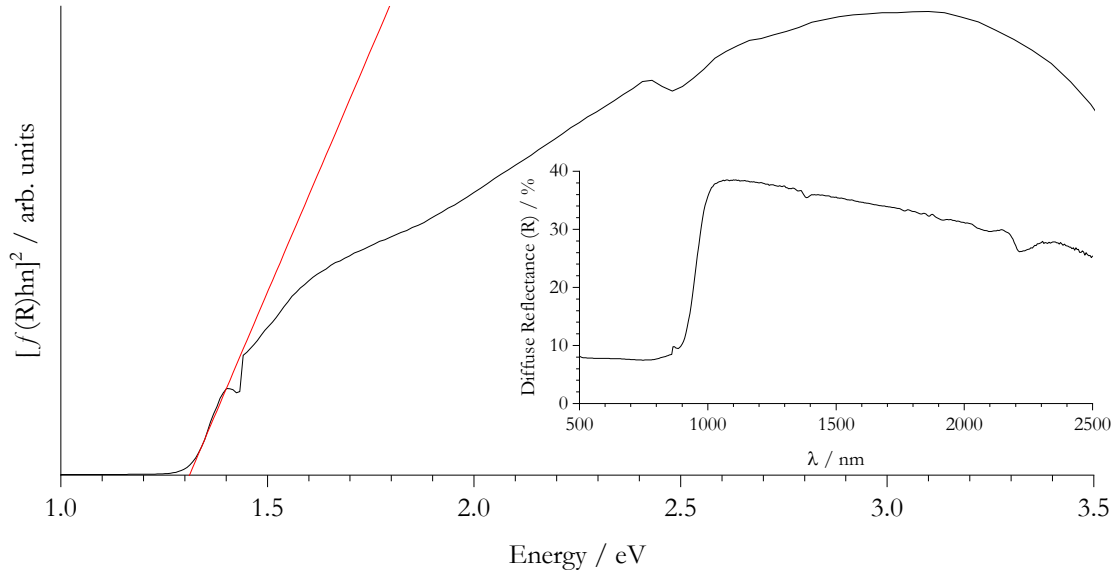

Figure 5.14 *Tauc plot of the compound $Ba_3In_2O_5Cu_2Se_2$ constructed from the raw diffuse reflectance spectrum (inset) collected from the sample. The solid red line shows a linear fit to the region of steepest gradient – its x-intercept marking the band gap energy at 1.31 eV.*

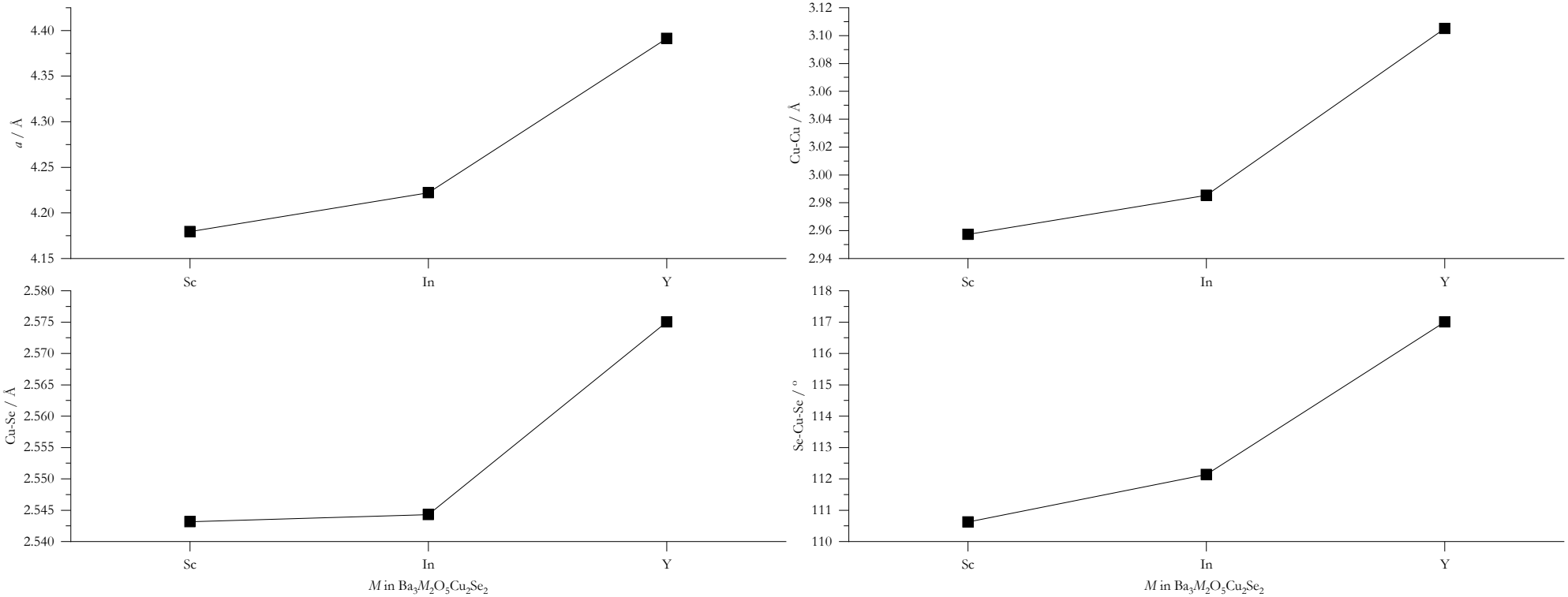

Figure 5.15 Graphical summary of the lattice parameters and key distances and angles, in terms of the electronic structure, for the compounds $Ba_3M_2O_5Cu_2Se_2$, where M = Sc, In and Y.

As can be seen in *figure 5.15*, the effect on the lattice parameters of substitution of scandium for the larger ionic radius indium in the compound $Ba_3M_2O_5Cu_2Se_2$, conformed to the same trend as was observed for the previous substitution of the yet larger yttrium. Namely, the expansion in the lattice parameter and increase in the copper-copper, copper-selenium distances and selenium-copper-selenium angle, away from the ideal tetrahedral.

Indium obeyed the same trend as yttrium, albeit it to not such an extent, owing to its ionic radius which is intermediate between that of scandium and yttrium. The use of larger *M* site cations in the homologous series $Ba_3M_2O_5Cu_2Se_2$ was expected to show reduced mobility at the VBM owing to the increased copper-selenium distance and angle. In the case of indium and yttrium, reduced transparency was observed, as measured by the band gap energy. This was expected to be a result of the occupied (n-1)*d* states and reduced electronegativity, respectively.

5.3.4 Isovalent Substitution at the Coinage Metal, *M'*, Site

5.3.4.1 … in the Silver Sulfides, $Ba_3M_2O_5Ag_2S_2$

After the successful substitution of the sulfur for selenium in the conductive layer and the observed resultant crystallographic geometry apparently beneficial for high p-type mobility with reasonably high maintenance of the wide band gap, attention was shifted towards the cationic site in the conductive layer, *M'* in $A_3M_2O_5M'_2Ch_2$, currently occupied by copper (I) ions. The pairs of analogous 325-type layered oxychalcogenide compounds $Sr_3Fe_2O_5M'_2S_2$ and $Sr_3Fe_2O_5M'_2Se_2$, where *M'* = Cu and Ag, related by the substitution of copper for silver, were reported in the literature to have been observed.[70,71]

To investigate the effect of the substitution at the cationic site in the conductive layer on its geometry and therefore optoelectronic properties, the synthesis of the compound $Ba_3Sc_2O_5Ag_2S_2$ was attempted, along with that of the set of analogous silver sulfide compounds with general formulae, $Ba_3M_2O_5Ag_2S_2$, where *M* = Y, In and La. The results of the syntheses were monitored by x-ray diffraction of the powders resultant after a single synthetic cycle at 800 °C for a duration of 12 h. It was found for the compounds attempted here that in each case, the crystalline phases identified in the powder x-ray diffraction patterns *(figures 5.16 to 5.19; top, overleaf)* corresponded to the precursor compounds, indicating a lack of reaction in each case.

It is noted that Bragg peaks were observed in the diffractograms which could not be confidently assigned to those of any known, anticipated phases. Of these unaccounted peaks, that with the highest intensity in each case lies around $2\theta = 30$ °. This is also the case with the predicted diffraction patterns of the three target compounds, admittedly along with the patterns of crystalline phases of many other compounds. It may have been the case, particularly as many of the observed phases were precursors, that the reactions had not gone to completion and, given longer time duration and/or higher temperature, conversion of the precursors to the potential target phase may have been observed.

It is worth noting here that Cario *et al.* reported the necessity for a temperature 100 °C higher (900 versus 800 °C) than that for the other copper sulfide, copper selenide and silver selenide analogues in the synthesis of the silver sulfide analogues of the isostructural layered compounds $Sr_3Fe_2O_5M'_2Ch_2$, where *M'* = Cu and Ag and *Ch* = S and Se.[70] A time of "3 days" was also used. The synthetic conditions of 900 °C and an assumed 72 h found to be required for the synthesis of the compound $Sr_3Fe_2O_5Ag_2S_2$, were then used in a second attempt of the syntheses of the compounds $Ba_3M_2O_5Ag_2S_2$, where *M* = Sc, Y, In and La.

The resultant powder samples were again analysed by PXRD and crystalline phases were assigned to their resultant patterns. The patterns can be seen for each cycle and for each compound in the *figures 5.16 to 5.19 (bottom)*. In the cases of the compounds where *M* = Sc, In and La, the phases assigned to the x-ray diffraction pattern of the sample treated at 900 °C for cycles of 72 h were the same precursor phases as were identified after the attempted synthesis at 800 °C for 12 h. In the case of *M* = Y, the yttrium oxide precursor phase was seemingly no longer present. The impurity precursor phases present in the resultant powder samples for each attempted composition are summarised in *table 5.7*.

The peaks at angles of around thirty degrees found after the first cycle were shown to decrease in relative intensity for the compound where *M* = Y and remained for *M* = Sc and In, indicating that, for these compounds, while the peaks were not able to be assigned, it is suspected that the samples contained a minor undesirable phase comprising at least the *M* site cation. It can be seen in the diffraction patterns for the compounds where *M* = Sc and In, that between each cycle, the relative intensity of the unassigned peaks change. While this may be due to preferred orientation, which was confirmed to occur in these compounds (as was previously reported on in *chapter 4*), it is more likely that the peaks are a result of at least two different minor impurity phases and are not indicative of the presence of a single target phase. The compounds $Ba_3M_2O_5Ag_2S_2$, where *M* = Sc, Y, In and La, were not observed after the syntheses at 800 °C for 12 h nor 900 °C for 72 h, attempted in this project.

Table 5.7 Summary of the composition of crystalline phases identified by PXRD for the attempted syntheses at 900 °C for 72 h of the family of compounds $Ba_3M_2O_5Ag_2S_2$, where M = Sc, Y, In and La.

Attempted Composition $Ba_3M_2O_5Ag_2S_2$, *M*	**Identified Post-Synthesis Crystalline Phases Present**
Sc	BaS, Ag
Y	Y_2O_3, BaS, Ag
In	In_2O_3, BaS, Ag
La	La_2O_3, BaS, Ag

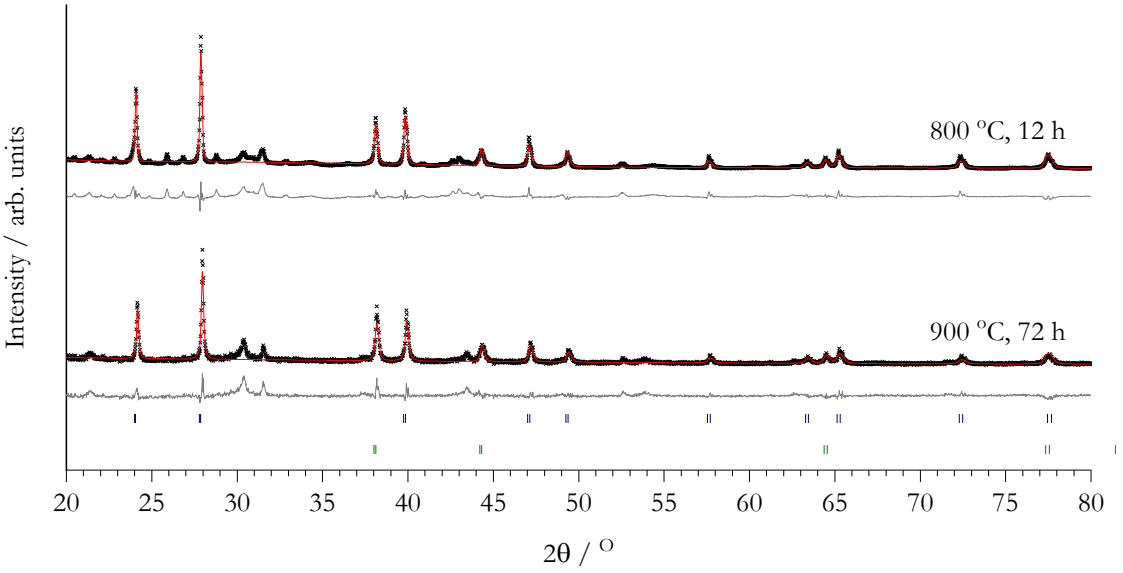

Figure 5.16 *Observed PXRD patterns for products from attempted syntheses at 800 °C for 12 h (top) and 900 °C for 72 h (bottom) of the target compound with composition $Ba_3Sc_2O_5Ag_2S_2$. The black crosses illustrate the observed data points, the red lines show the calculated profile from the Rietveld refined model and the grey lines are the difference between the two. Observed phases, the diffraction peak positions of which are represented by the tick marks, included BaS (blue) and Ag (green). R_{wp} = 19.21 % and χ^2_{red} = 24.71 and 21.84 and 3.215 for the plots top and bottom, respectively.*

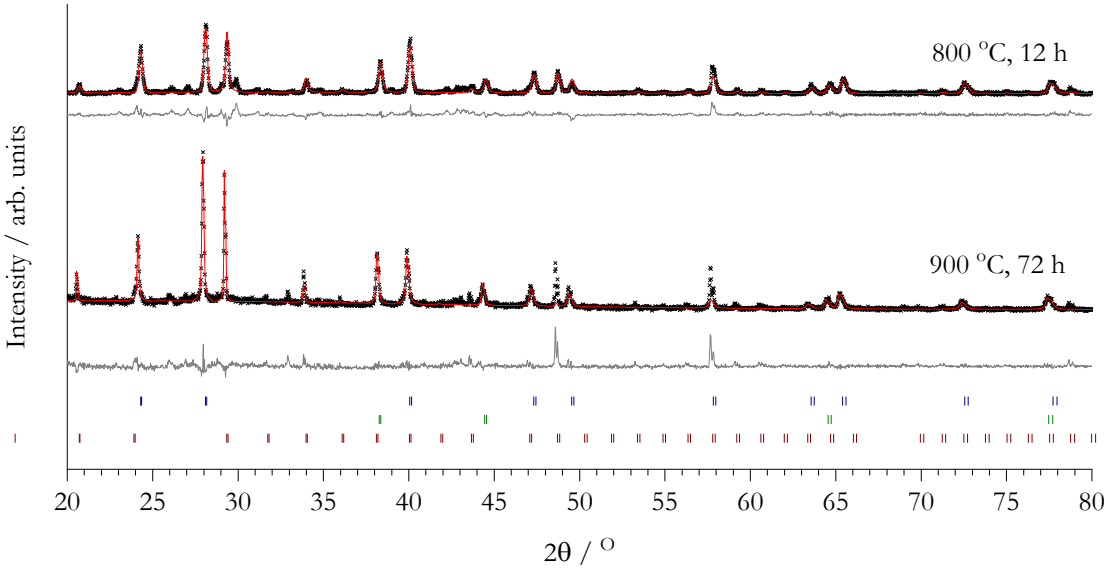

Figure 5.17 *Observed PXRD patterns for products from attempted synthesis at 800 °C for 12 h (top) and 900 °C for 72 h (bottom) of target compound with composition $Ba_3Y_2O_5Ag_2S_2$. The black crosses illustrate the observed data points, the red lines show the calculated profile from the Rietveld refined model and the grey lines are the difference between the two. Observed phases, the diffraction peak positions of which are represented by the tick marks, included BaS (blue), Y_2O_3 (green) and Ag (red). R_{wp} = 18.55 % and χ^2_{red} = 1.869 and 17.26 and 2.657 for the plots top and bottom, respectively.*

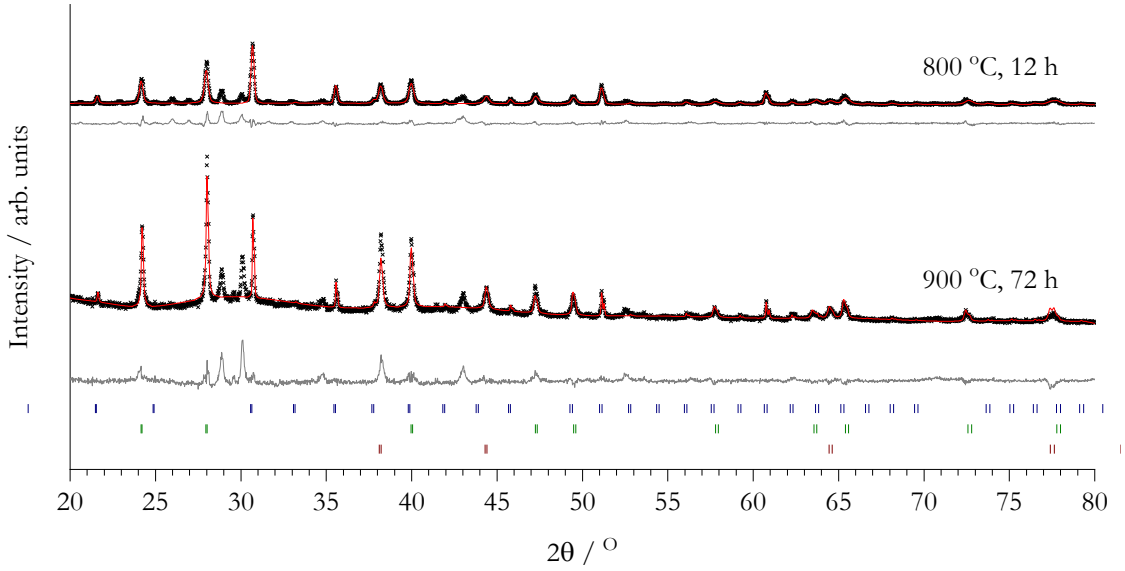

Figure 5.18 *Observed PXRD patterns for products from attempted synthesis at 800 °C for 12 h (top) and 900 °C for 72 h (bottom) of target compound with composition $Ba_3In_2O_5Ag_2S_2$. The black crosses illustrate the observed data points, the red lines show the calculated profile from the Rietveld refined model and the grey lines are the difference between the two. Observed phases, the diffraction peak positions of which are represented by the tick marks, included In_2O_3 (blue), BaS (green) and Ag (red). R_{wp} = 26.73 % and χ^2_{red} = 3.094 and 14.49 and 4.679, for the plots top and bottom, respectively.*

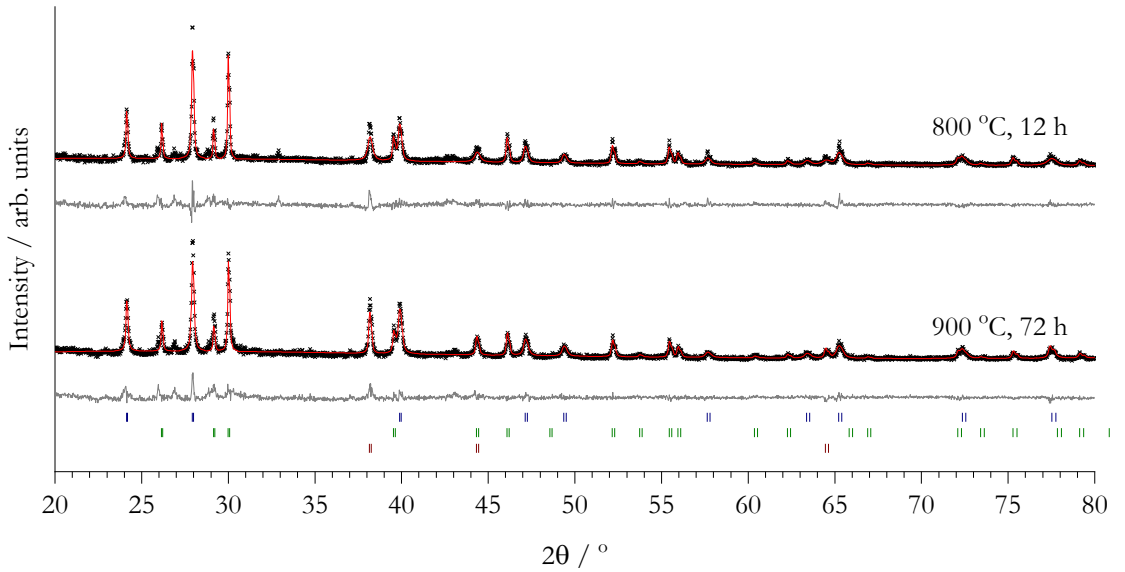

Figure 5.19 *Observed PXRD patterns for products from attempted synthesis at 800 °C for 12 h (top) and 900 °C for 72 h (bottom) of target compound with composition $Ba_3La_2O_5Ag_2S_2$. The black crosses illustrate the observed data points, the red lines show the calculated profile from the Rietveld refined model and the grey lines are the difference between the two. Observed phases, the diffraction peak positions of which are represented by the tick marks, included BaS (blue), La_2O_3 (green) and Ag (red). R_{wp} = 16.56 % and χ^2_{red} = 1.770 and 17.77 and 2.088, for the plots top and bottom, respectively.*

5.3.4.2 … in the Silver Selenides, $Ba_3M_2O_5Ag_2Se_2$

In a continued search for novel conductive layer geometry, the isovalent substitution of the conductive layer cation, *M'*, in the 325-type layered oxychalcogenide compounds, $Ba_3M_2O_5Cu_2Se_2$ previously discussed was investigated. It was anticipated that the increased radius selenium (-II) ions would contribute to a lattice expansion with the potential of incorporating the larger radius silver ions. This was not found to be possible in the set of silver sulfide compounds $Ba_3M_2O_5Ag_2S_2$, discussed in the previous section. The effect of substitution on this site could not be evaluated from the literature as, although the analogous pair of compounds $Sr_3Fe_2O_5Cu_2S_2$ and $Sr_3Fe_2O_5Ag_2S_2$ related by the isovalent substitution of copper for silver at the conductive cationic site, was found to have been reported in the literature, neither the interatomic distance and angles, nor the refined atomic coordinates, from which they could have been calculated, were found to be available for the silver analogue.[70,71]

Here, the synthesis of the homologous series of compounds with formulae $Ba_3M_2O_5Ag_2Se_2$ where M = Sc, In and La, were attempted. The compound for which M = Y was already found to have been reported in the literature by Ogino *et al.*[69] It was found that the resultant powder x-ray diffractograms, shown subsequently in *figures 5.20 and 5.21*, could be modelled by the refined crystal structures of the intended layered oxyselenides after a single cycle at 800 °C for 12 h for the compounds where M = Sc and In. The lanthanum analogue was not observed after the attempted synthesis under the same conditions *(figure 5.22)*. The identified crystalline phases present in the resultant sample were found to be the precursors barium selenide, lanthanum oxide and silver, the predicted diffraction peak positions of which are shown relative to the observed diffraction data.

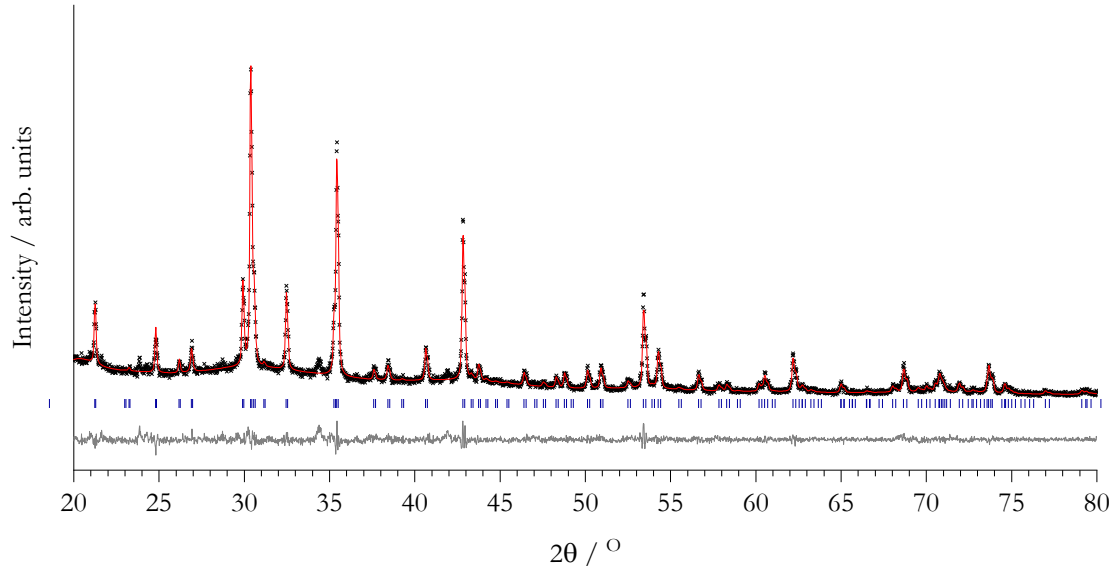

Figure 5.20 Powder x-ray diffractogram of the compound $Ba_3Sc_2O_5Ag_2Se_2$ which crystallised into a structure with the tetragonal I4/mmm space group. The observed data is represented by black crosses, the calculated diffraction pattern by a solid red line and the difference profile as a solid grey line below. The blue tick marks show the expected peak positions from the Rietveld refined model. R_{wp} = 8.42 % and χ^2_{red} = 1.431.

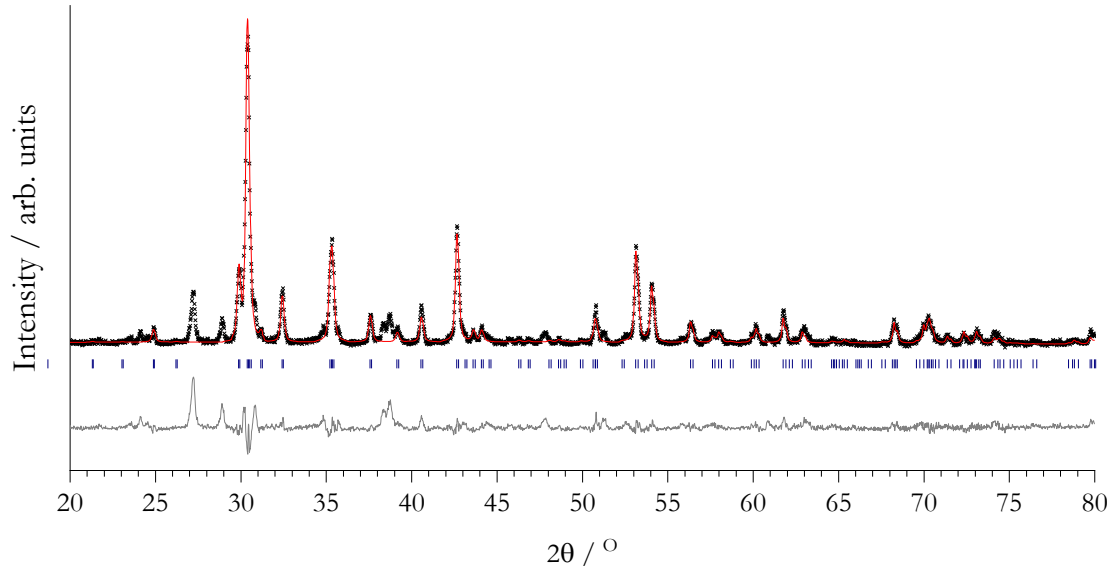

Figure 5.21 *Powder x-ray diffractogram of the compound $Ba_3In_2O_5Ag_2Se_2$ which crystallised into a structure with the tetragonal I4/mmm space group. The observed data is represented by black crosses, the calculated diffraction pattern by a solid red line and the difference profile as a solid grey line below. The blue tick marks show the expected peak positions from the Rietveld refined model. The peaks at 2θ ≈ 27 and 29° could not be assigned to a phase. R_{wp} = 22.74 % and χ^2_{red} = 2.979.*

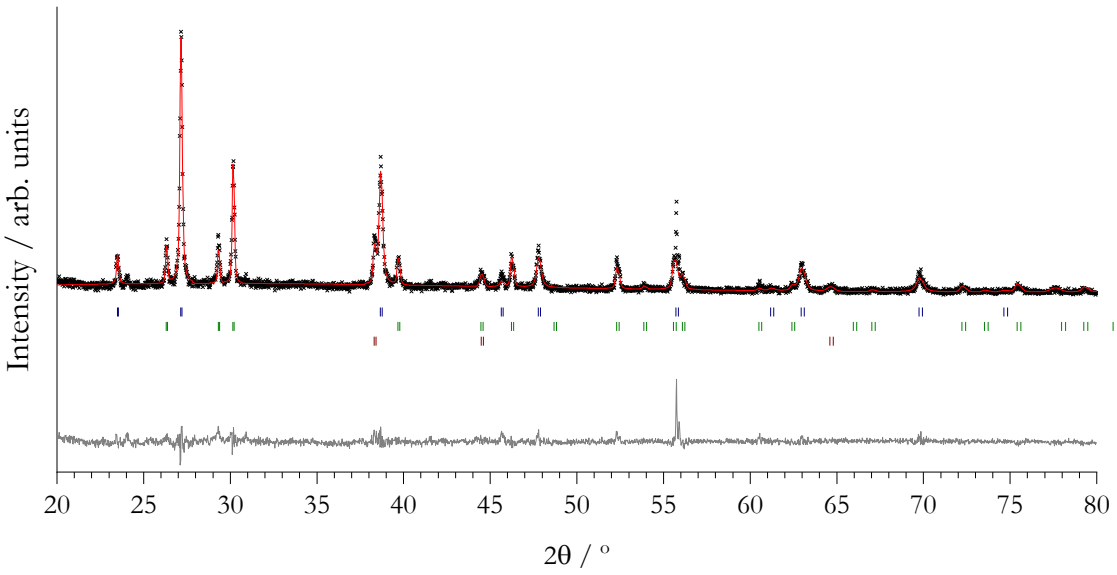

Figure 5.22 *Observed PXRD pattern for products from attempted synthesis of the target compound with composition $Ba_3La_2O_5Ag_2Se_2$. The black crosses illustrate the observed data points, the red line shows the calculated profile from the Rietveld refined model and the grey line is the difference between the two. Observed phases, the diffraction peak positions of which are represented by the tick marks, included BaSe (blue) La_2O_3 (red) and Ag (green). R_{wp} = 18.82 % and χ^2_{red} = 1.686.*

The lattice parameters and interatomic distances and angles calculated from the refined fractional atomic coordinates of the compounds for which *M* = Sc and In *(appendices H.5 and H.6),* are summarised in *table 5.8* and represented graphically in *figure 5.23*. It can be seen that the substitution of copper with silver, the ionic radii of which is considerably larger than that of copper (0.6 compared to 1.0 Å for the tetrahedrally coordinated (I) ions), had the expected effect of expanding the lattice parameter and therefore also the metal-metal distance in the conductive layer of the compounds $Ba_3Sc_2O_5M'_2Se_2$ and $Ba_3In_2O_5M'_2Se_2$, where *M'* = Cu and Ag. This was expected to have the desirable effect of reducing hybridisation at the CBM, contributing to maintenance of high transparency.

As was observed when substituting sulfur for the larger selenium ion on the chalcogen site, the increased radius introduced into the conductive layer had the expected effect of increasing the coinage metal-chalcogen distance. As was also the case with the chalcogen site substitution, the incorporation of the silver in place of copper had the effect of increasing the metal-chalcogen interatomic distance but not to such an extent as was predicted by consideration of the ionic radii alone, an 8 versus 16 % increase respectively. A decrease in chalcogen-coinage metal-chalcogen angle was again observed. However, in this case, the angle was decreased to values further beyond that of an ideal tetrahedron.

While the increase in basal lattice parameter and coinage metal-metal distance was seen as beneficial for transparency, the net effect of the competing increase in coinage metal/ selenium hybridisation and decrease in angle on the conductivity, could not be predicted. The effect on the band gap energy of the successful substitution of *M'* = Cu for Ag in the compounds $Ba_3M_2O_5M'_2Se_2$ where *M* = Sc and In, was investigated by calculating the band gap energy from the diffuse reflectance spectra measured from the samples. These plots are shown in *figures 5.24 and 5.25*.

Table 5.8 *Summary of ionic radii of the M' site cations, Cu and Ag, being substituted in the compounds $Ba_3M_2O_5M'_2Se_2$ where M = Sc and In, and the corresponding lattice parameters describing the crystalline phases formed.*

Compound	$r_{ionic}(^{IV}M'^{3+})$ **/ Å**	***a=b*** **/ Å**	***M'-M'*** **/ Å**	***M'*-Se** **/ Å**	**Se-*M'*-Se** **/ °**
$Ba_3Sc_2O_5Cu_2Se_2$	0.6	4.18227(8)	2.95731(6)	2.54316(5)	110.623(3)
$Ba_3Sc_2O_5Ag_2Se_2$	1	4.2168(2)	2.9818(1)	2.74680(9)	100.277(4)
$Ba_3In_2O_5Cu_2Se_2$	0.6	4.2220(1)	2.98542(9)	2.54431(6)	112.136(3)
$Ba_3In_2O_5Ag_2Se_2$	1	4.2601(4)	3.0123(3)	2.7822(2)	95.406(4)

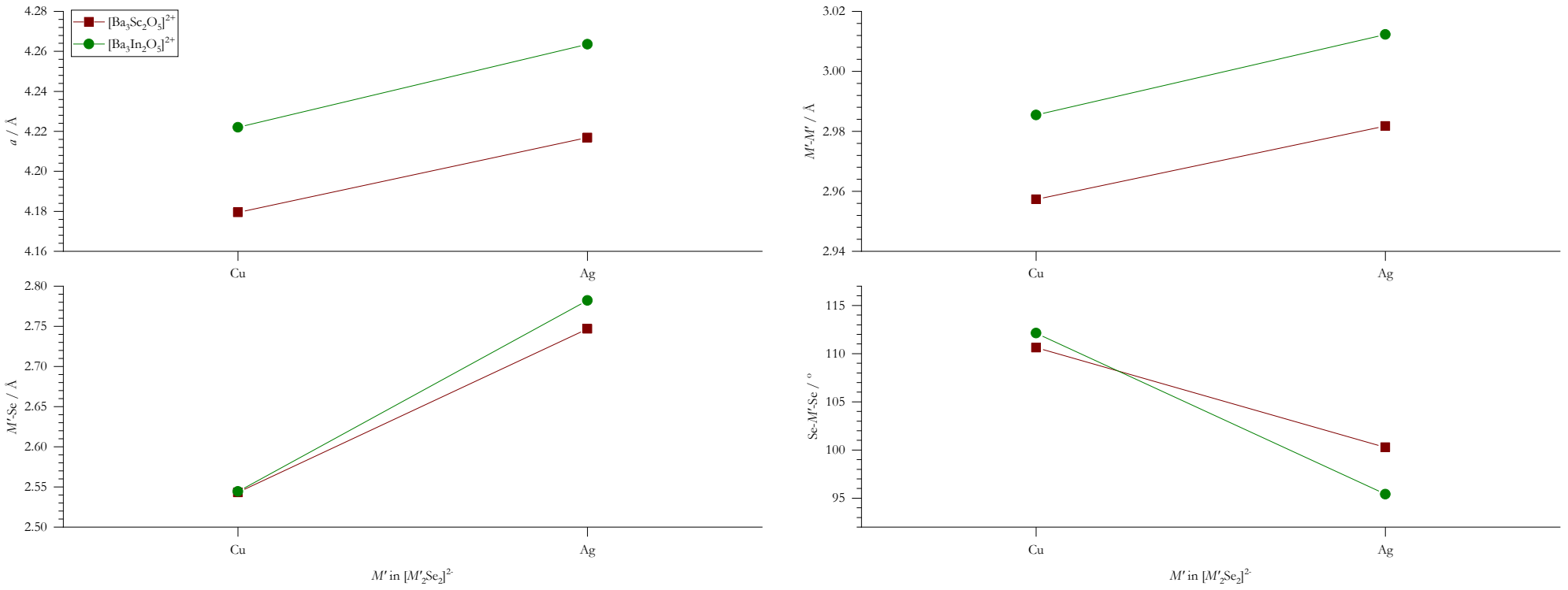

Figure 5.23 Graphical summary of the effect on the lattice parameters and distances and angles, of ionic substitution of copper for silver on the coinage metal (M') site, in the two sets of analogous compounds with general formulae $Ba_3Sc_2O_5M'_2Se_2$ (red squares) and $Ba_3In_2O_5M'_2Se_2$ (green circles), where M' = Cu and Ag synthesised here.

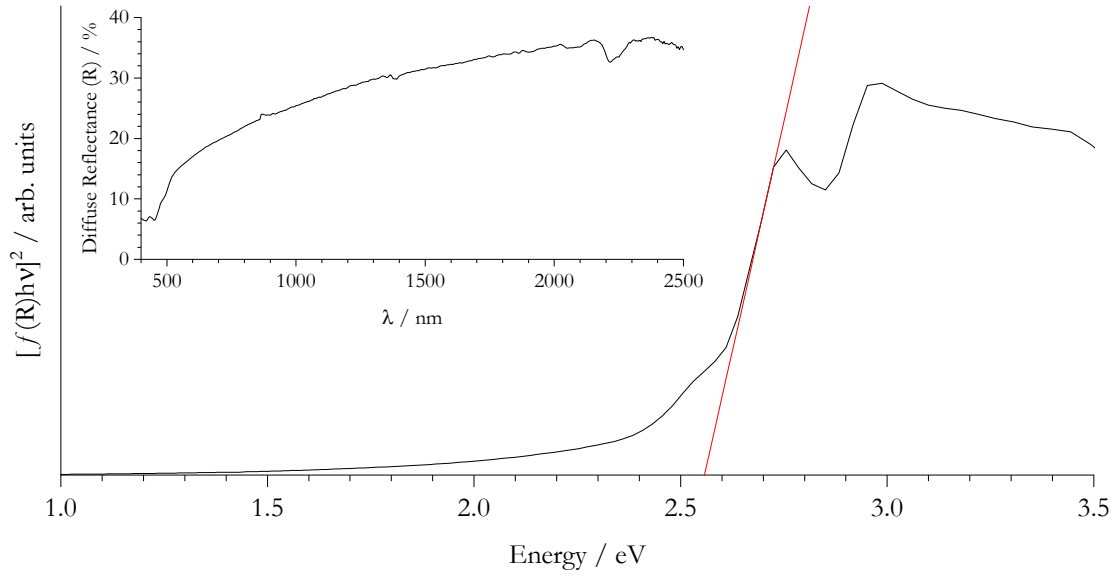

Figure 5.24 *Tauc plot constructed from the raw diffuse reflectance data (inset) of the compound $Ba_3Sc_2O_5Ag_2Se_2$. The solid red line shows a linear fit to the region of steepest gradient – its x-intercept marking the band gap energy at 2.56 eV.*

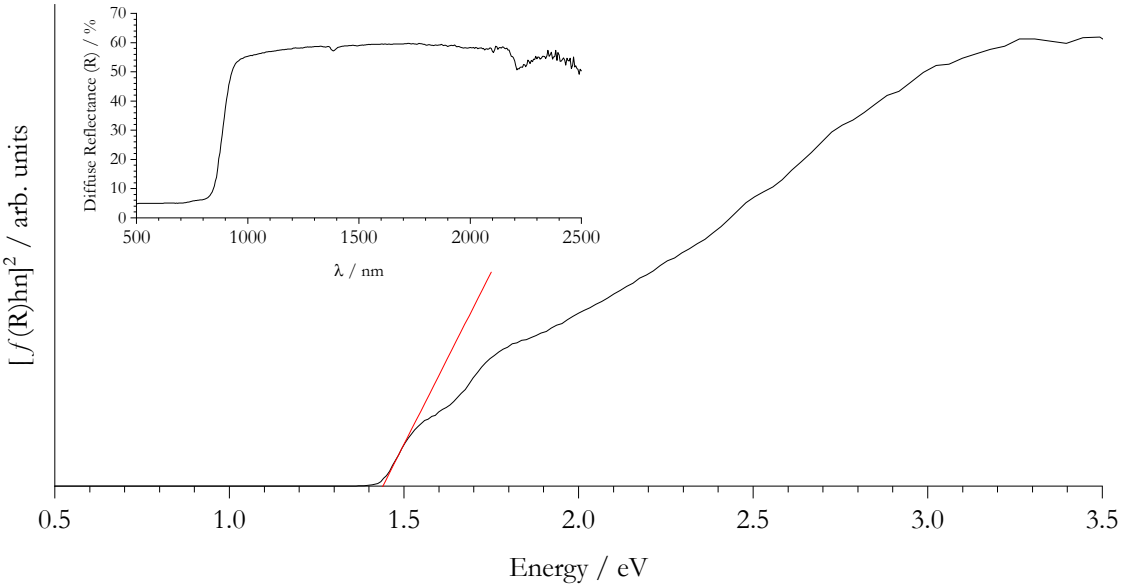

Figure 5.25 *Tauc plot constructed from the raw diffuse reflectance data (inset) of the compound $Ba_3In_2O_5Ag_2Se_2$. The solid red line shows a linear fit to the region of steepest gradient – its x-intercept marking the band gap energy at 1.44 eV.*

The observed band gap energies were found to equal 2.56 and 1.44 eV for the compounds $Ba_3Sc_2O_5Ag_2Se_2$ and $Ba_3In_2O_5Ag_2Se_2$ respectively. Comparison of the band gap energies for the indium analogues $Ba_3In_2O_5M'_2Se_2$ where *M'* = Cu and Ag, showed a small observed increase from 1.31 to 1.44 eV upon substitution of copper for silver. A contrary decrease in band gap energy from 3.05 to 2.56 eV was found between the scandium analogues, $Ba_3Sc_2O_5M'_2Se_2$.

The reason for the increase in band gap energy observed between the indium analogues was attributed to the position of the filled (n-1)d^{10} sub-shell in the indium (III) ion between the metal-chalcogen and metal-metal states, typically comprising the VBM and CBM respectively. The band gap in these compounds either exists between the VBM and indium inter-band states or indium states and the CBM. It may have been the case that the net effect of the increased hybridisation of the coinage metal and selenium, and the decreased angle was to reduce the energy of the VBM, increasing the band gap. This would have indicated loss of hybridisation at the VBM and reduced p-type mobility. Conversely, it was known that the CBM comprised the coinage metal states in these compounds. Substitution of copper for silver had the effect of reducing the hybridisation and raising the energy of the CBM. This would have been countered by the use of the less electronegative silver. It may have been that the increase in *M'-M'* length outweighed this and the band gap, possibly between the indium states and the CBM, increased as observed.

It was expected that the increased basal lattice parameter and coinage metal-metal distance in $Ba_3Sc_2O_5M'_2Se_2$, where *M'* = Cu is substituted for Ag, reduced the energy of the CBM, contributing to a wide band gap. Therefore, the observed decrease in band gap energy suggested that hybridisation at the VBM increased as the net result of the increased hybridisation and reduced angle between the coinage metal and selenium. The band gap of 2.56 eV of the compound $Ba_3Sc_2O_5Ag_2Se_2$ lay below that of the 3.1 eV benchmark. However, given the possible increase in mobility compared to the high-transparency candidates discussed so far, the reduction in transparency may be acceptable for applications where conductivity is of primary importance.

5.4 Conclusions

This chapter focussed on the effect of compositional modification in the layered perovskite oxychalcogenides on the geometry of the tetrahedral layer shown to have the greatest influence over the optoelectronic properties in these materials.[27] Barium substitution of strontium on the perovskite *A* site in the literature benchmark compound $Sr_3Sc_2O_5Cu_2S_2$, led to the discovery of the isostructural compound with composition $Ba_3Sc_2O_5Cu_2S_2$, apparently previously unreported.

The substitution for the larger radius $^{XII}Ba^{2+}$ ion was found to expand the basal lattice parameter which had the effect of increasing the copper-copper distance and reducing hybridisation at the CBM, useful for maintaining a wide band gap. An increase in the copper-sulfur distance and angle was also reported. The net effect of these observed alterations in geometry did not look promising for hybridisation at the VBM. However, the recorded band gap was in good agreement with that calculated from the predicted band structure, indicating that $Ba_3Sc_2O_5Cu_2S_2$ may well be a promising candidate transparent p-type conductor as expected.

This result suggested that simple isostructural compositional modification at different crystallographic sites in the initial compound could lead to alterations in conductive layer geometry measurable by PXRD and possibly qualitatively predictable effects on the predicted optoelectronic properties of these compounds.

5.4.1 Perovskite Metal Site *(M)*

Systematic substitution of scandium on the ***M*** perovskite cation site by the candidate elements indium, yttrium and lanthanum was attempted. The series of compounds $Ba_3\mathbf{Sc}_2O_5Cu_2S_2$ and $Ba_3\mathbf{In}_2O_5Cu_2S_2$; $Ba_3\mathbf{Sc}_2O_5Cu_2Se_2$, $Ba_3\mathbf{In}_2O_5Cu_2Se_2$ and $Ba_3\mathbf{Y}_2O_5Cu_2Se_2$; and $Ba_3\mathbf{Sc}_2O_5Ag_2Se_2$ and $Ba_3\mathbf{In}_2O_5Ag_2Se_2$* were discovered apparently for the first time. The effect of substitution at the *M* site on selected optoelectronic properties is summarised for each series in *figure 5.26*, the members within each sharing the common conductive layers $[Cu_2S_2]^{2-}$, $[Cu_2Se_2]^{2-}$ and $[Ag_2Se_2]^{2-}$. The perovskite layer within which the substitution occurred in each case had the general formula $[Ba_3M_2O_5]^{2+}$, where *M* = Sc, In and/or Y.

It can be seen that the increased radius of the $^{VI}M^{3+}$ site cation scandium, indium and yttrium in each series, increased the basal lattice parameter in proportion to the radius. The coinage metal-metal distance in the conductive layer is not shown as it is proportional to the basal lattice parameter and therefore exhibited the same increasing trend.

* *The yttrium member of this series $Ba_3Y_2O_5Ag_2Se_2$ was found to have already been reported in the literature.*[69]

The effect of the substitution of a larger radius *M* site cation on the metal-chalcogen distance in the conductive layer, seemingly depended on the combined radii of the conductive-layer metal and chalcogen atoms. In the case of the largest combined conductive-layer radii, the silver selenide series, the trend in metal-chalcogen distance showed a clear increase with increasing perovskite metal ionic radius. In the copper selenide series, for which the combined ionic radii in the conductive layer was intermediately smaller, the trend of increased conductive metal-chalcogen bond length was less pronounced. In the case of the copper sulfides, with the smallest combination of ionic radii in the conductive layer, the increase in perovskite metal cationic radii had the opposite effect of decreasing the conductive metal-chalcogen length.

A trend contrary to that observed in the metal-chalcogen bond length, was found for the chalcogen-metal-chalcogen bond angle in the conductive layer. The greatest increase in angle was observed in the series possessing, in this case, the smallest combined conductive metal chalcogen ionic radii, the copper sulfides. A less obvious increase was observed in the copper selenides and a very small decrease found for the largest combined conductive layer ionic radii series, the silver selenides. In each case the substitution of larger radius cations had the effect of distorting the chalcogen-metal-chalcogen angle away from the ideal tetrahedral, one way or the other, compared to that of the scandium analogues.

In all series the calculated band gap energy decreased for the indium substitution and increased again for yttrium, although not to the values observed for scandium. The occupied (n-1)*d* states in the indium resided between the usual band edges, effectively halving the band gap. The yttrium, whilst possessing unoccupied (n-1)*d* orbitals, had lower electronegativity and therefore higher energy states contributing to the VBM, raising its energy and reducing the band gap energy into that of the visible light region. It was concluded that the performance of these compounds could not be improved by isovalent substitution of scandium and that it was therefore the (III) ion found to occupy the *M* site, that showed most promise for improved transparent conductive properties in this family of compounds.

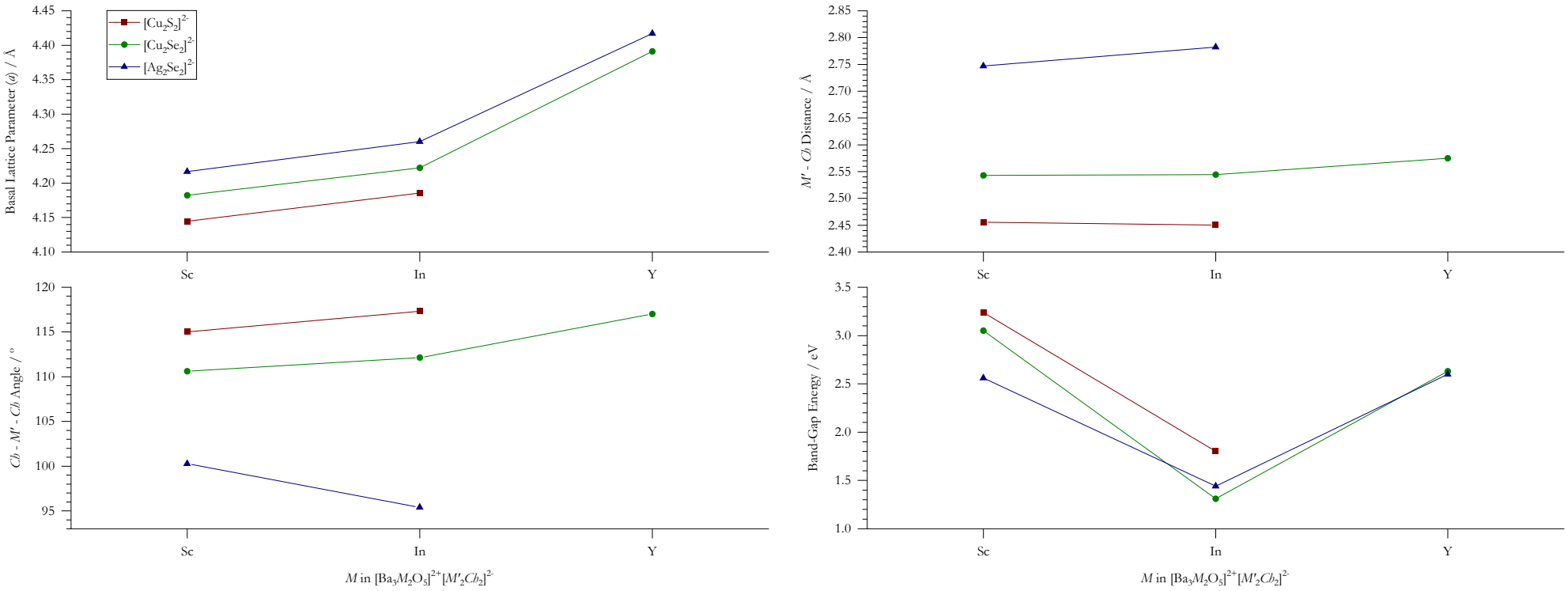

Figure 5.26 *Summary of the geometric properties of the crystalline lattice and band gap energy for the compounds where M = Sc, In and Y in the perovskite layer $[Ba_3M_2O_5]^{2+}$ within series of compounds $Ba_3M_2O_5M'_2Ch_2$ each with a different conductive layer in common for each member, namely $[Cu_2S_2]^{2-}$ (red squares), $[Cu_2Se_2]^{2-}$ (green circles) and $[Ag_2Se_2]^{2-}$(blue triangles). The values corresponding to the compound $Ba_3Y_2O_5Sg_2Se_2$ are taken from the literature and are indicated by unfilled blue triangles.*

5.4.2 Conductive Chalcogen Site *(Ch)*

When comparing the sets of compounds $Ba_3Sc_2O_5Cu_2Ch_2$ *(red squares, figure 5.27)* and $Ba_3In_2O_5Cu_2Ch_2$ *(green circles)*, where *Ch* = S and Se in each case, it can be seen that, as expected and as is the case in the perovskite layer, the incorporation of the larger ion, selenium, has the effect of expanding the basal lattice parameter and therefore also the copper-copper distance, desirable for the maintenance of a wide band gap.

The copper-chalcogen bond length was shown to increase upon substitution of sulfur for selenium in both cases, as would have been expected. However, the increase was not as great as was anticipated from the sum of the increased radii alone, indicating increased overlap. It was found that the chalcogen-copper-chalcogen angle decreased for the selenide relative to the analogous sulfide closer to the 109.5 ° of an ideal tetrahedron in both cases. In fact, the angle in the compound $Ba_3Sc_2O_5Cu_2Se_2$ is the closest of any compound synthesised in this project. The reduced orbital distance and optimised angle indicated increased hybridisation between the copper and chalcogen, the electronic states of which constitute the VBM. It was anticipated that this compound would exhibit the highest mobility of the compounds investigated here, higher than the current literature benchmark, $Sr_3Sc_2O_5Cu_2S_2$. The compound was calculated to possess a band gap energy of 3.05 eV, close to the 3.1 eV requirement. This may be suitable for some applications if the conductivity was proven to show a marked increase from that of the literature analogue. It was also posited that successful p-type doping would yield an increase in band gap energy owing to a Moss-Burstein shift in energy of the VBM, possibly raising it above the visible threshold.

The isovalent substitution of *M* = *S* for Se at the chalcogen site of $Ba_3M_2O_5Cu_2Ch_2$, where *M* = Sc and In, was shown to increase hybridisation at the VBM, potentially increasing mobility while increasing the energy of the CBM sufficiently to maintain a wide band gap energy of 3.05 eV for the scandium/selenium analogue.

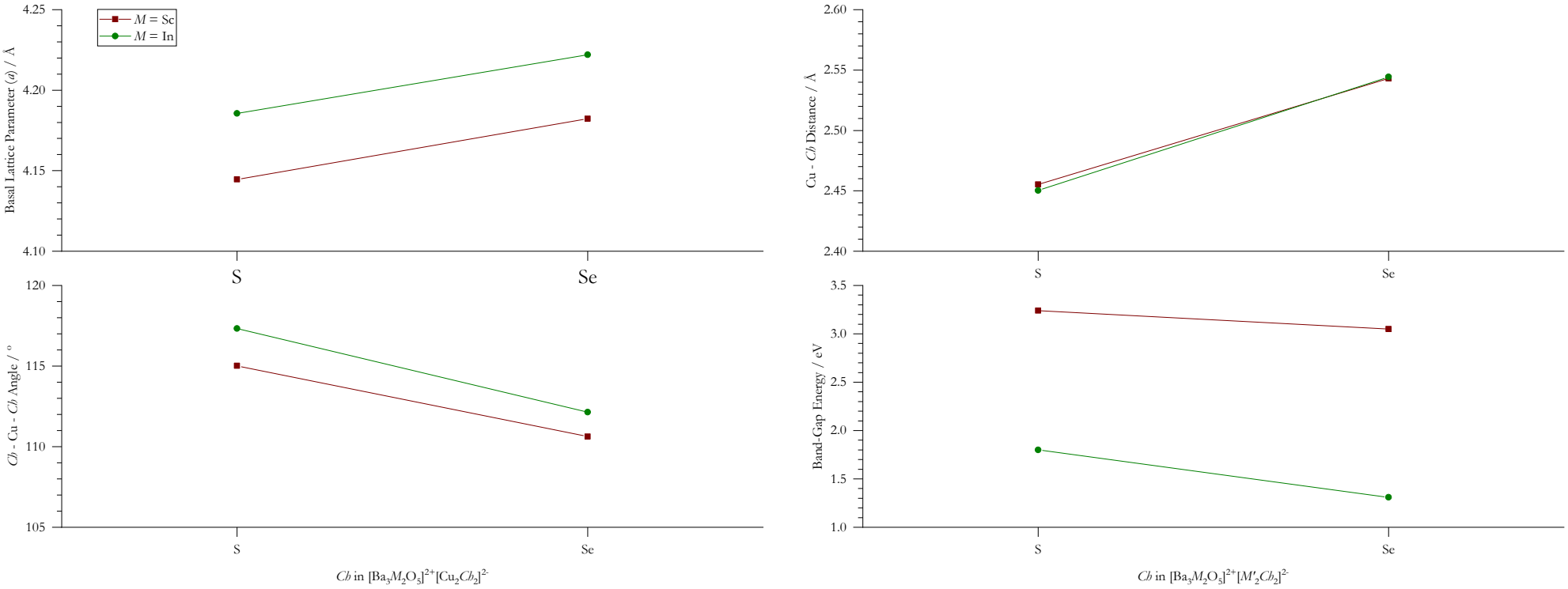

Figure 5.27 Summary of the geometric properties of the crystalline lattice and band gap energy for the compounds where Ch = S and Se in the conductive layer $[Cu_2Ch_2]^{2-}$ within the series of compounds $Ba_3M_2O_5Cu_2Ch_2$ each with a different perovskite layer in common, namely $[Ba_3Sc_2O_5]^{2+}$(red squares) and $[Ba_3In_2O_5]^{2+}$(green circles).

5.4.3 Coinage Metal Site *(M')*

As shown in *figure 5.28*, substitution of copper for silver on the conductive layer metal site had the effect of expanding the basal lattice parameter and metal-metal distance in the conductive layer, as is the case on each site investigated here. The metal-selenide bond length was shown to increase, but again as with substitution on the chalcogen site, not to such an extent as would have been expected by the sum of the increased radii. The full incorporation of silver ions into the structure had the effect of reducing the selenium-metal-selenium angle to further below that of an ideal tetrahedron. The combined competing effects of the relatively reduced metal-selenium bond length and the reduced angle on the mobility within the VBM was not possible to predict qualitatively. It was calculated that the band gap energy decreased for the scandium set $Ba_3Sc_2O_5M'_2Se_2$ upon substitution of M' = Cu for Ag. The CBM was expected to exhibit a reduction in curvature as a result of the increased metal-metal distance. At the VBM, a competition of distance and angle affecting the hybridisation and electronegativity controlling the average energy were expected to contribute to an overall change the energy of the CBM. The observed reduction in band gap energy from 3.05 to 2.56 eV for the $Ba_3Sc_2O_5M'_2Se_2$ copper to silver substitution, suggested that the hybridisation of the CBM had increased, beneficial for p-type conductivity.

An increase in band gap energy was observed for the same substitution between the compounds of the analogous indium containing set, $Ba_3In_2O_5M'_2Se_2$. As previously discussed, it was determined that the occupied *d* states lie between the bands at a fixed energy. The band gap was then proposed to be the difference between these occupied indium states and the CBM. As this was observed to increase for $Ba_3In_2O_5M'_2Se_2$, it was concluded that the energy of the CBM must have increased as a result of the increased metal-metal distance, again beneficial for p-type conductivity.

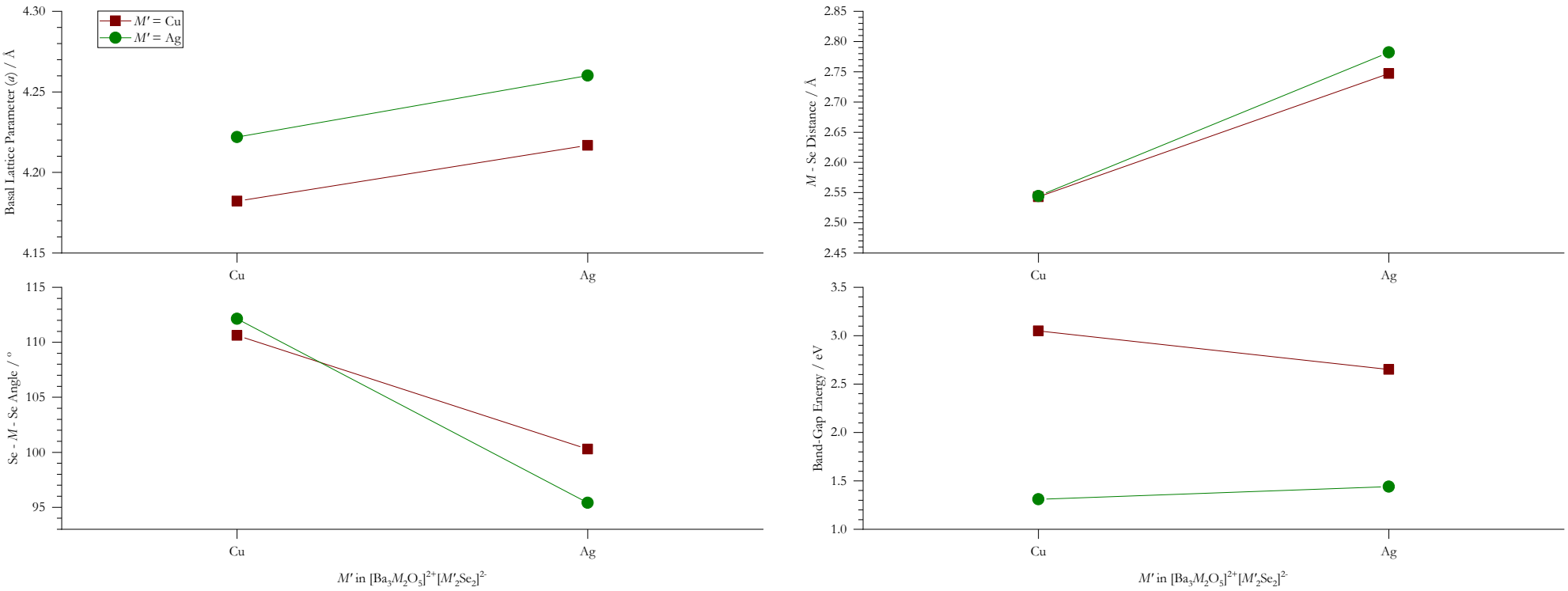

Figure 5.28 *Summary of the geometric properties of the crystalline lattice and band gap energy for the compounds where M' = Cu and Ag in the conductive layer $[M'_2Se_2]^{2-}$ within the series of compounds $Ba_3M_2O_5M'_2Se_2$ with a different perovskite layer in common, namely $[Ba_3Sc_2O_5]^{2+}$ (red squares) and $[Ba_3In_2O_5]^{2+}$ (green circles).*

5.4.4 Summary

In summary, the isovalent substitution of elements with larger ionic radii exhibited an expected expansion of the basal lattice parameter and associated increase in metal-metal distance in the conductive layer, beneficial for retention of a wide band gap. Substitution of scandium with yttrium, indium and lanthanum at the *M* site in the series $Ba_3M_2O_5M'_2Ch_2$, where $M'_2Ch_2 = Cu_2S_2$, Cu_2Se_2 and Ag_2Se_2, highlighted the dependence of the trend in conductive layer geometry with the *M* ionic radius, on the combined ionic radii in the conductive layer. Increased combined atomic radii in the conductive layer caused an increase in *M'-Ch* and reduction in *Ch-M'-Ch* angle. However, the use of indium or yttrium to do this was detrimental to transparency, owing to their (n-1)*d* states and reduced electronegativity respectively. In all series, the bond angle in the conductive layer deviated from the ideal tetrahedral angle with increasing radius of perovskite *M*'-site cation. It was, therefore, deemed that scandium was the most promising of the suitable elements for transparent p-type conductivity in these compounds.

Substitution of sulfur for selenium on the chalcogen site, in addition to expanding the basal parameter and metal-metal distance, increased the metal-chalcogen length. The increase, however, was less than the relative increase in ionic radii. The chalcogen-copper-chalcogen angle was reduced towards that of an ideal tetrahedron with sulfur to selenium substitution in both sets of compounds, $Ba_3Sc_2O_5Cu_2Ch_2$ and $Ba_3In_2O_5Cu_2Ch_2$. These effects were predicted to increase hybridisation and mobility at the VBM. The use of indium in these compounds for transparent conductivity was ruled out owing to the reduced band gaps of its compounds. The chalcogen substitution in the scandium analogues showed a small reduction in band gap energy to 3.05 eV. Coupled with the expected increase in hybridisation and possibility of increasing the band gap energy by acceptor doping, the here newly synthesised compound $Ba_3Sc_2O_5Cu_2Se_2$ was expected to be a promising candidate for a high-performance transparent p-type conductor.

Substitution of *M'* = Cu for Ag in the conductive layer in the compounds $Ba_3\mathbf{Sc}_2O_5M'_2Se_2$ and $Ba_3\mathbf{In}_2O_5M'_2Se_2$ caused an increase in metal-selenium distance, yet expected increase in hybridisation, and reduction of the selenium-metal-selenium angle beyond that of the ideal tetrahedral angle. The effect of this on mobility at the VBM was not possible to qualitatively elucidate. The net effect of the change in geometry was proposed to be an increase in mobility at the VBM, as supported by the measured band gap energy of 2.56 eV. Given the expected increase in conductivity, the band gap energy within the energy range of visible light photons, may be tolerated in some applications.

As a result of the investigation of compositional variation on optoelectronic properties via geometric modification, the syntheses of the following analogous 325-type layered oxychalcogenide compounds was achieved and reported here apparently for the first time: $Ba_3In_2O_5Cu_2S_2$, $Ba_3Sc_2O_5Cu_2Se_2$, $Ba_3In_2O_5Cu_2Se_2$, $Ba_3Y_2O_5Cu_2Se_2$, $Ba_3Sc_2O_5Ag_2Se_2$ and $Ba_3In_2O_5Ag_2Se_2$.

Chapter 6 Final Conclusions and Outlook

6.1 Conclusions

The aim of this project was to use the compound $Sr_3Sc_2O_5Cu_2S_2$ reported by Liu *et al.* to possess a band gap energy of 3.1 eV and notably high p-type charge carrier mobility of 150 $cm^2\ V^{-1}\ s^{-1}$, as a structural prototype to investigate the transparent p-type conductive potential of related 325-type layered perovskite oxychalcogenides.

Initial collaboration with the Scanlon Materials Theory Group, UCL afforded a list of eight structural analogues of the prototype compounds of general formula $A_3M_2O_5Cu_2S_2$ proposed to be thermodynamically stable by computational prediction. Two of these, $Ca_3Al_2O_5Cu_2S_2$ and $Ba_3Sc_2O_5Cu_2S_2$ were expected to exhibit band gap energies greater than the 3.1 eV required for visible-light transparency.

The syntheses of the eight compounds in addition to the strontium scandium prototype were attempted here. The syntheses of the compounds $Sr_3Sc_2O_5Cu_2S_2$ and $Ba_3Sc_2O_5Cu_2S_2$ were confirmed successful by polycrystalline x-ray diffraction, that of the barium analogue apparently for the first time. Its band gap energy as measured by diffuse reflectance was confirmed to be in exact agreement with the 3.24 eV predicted, desirable for visible-light transparency. $Ba_3Sc_2O_5Cu_2S_2$ was predicted to increase p-type conductivity compared to that of the analogous strontium prototype. The synthesis of the compound $Ca_3Al_2O_5Cu_2S_2$, the conductivity of which is also expected to exceed that of the prototype, is proposed to be achievable by use of high-pressure synthesis. The related compound $Sr_4Ga_2O_6Cu_2S_2$ already reported in the literature was synthesised and its band gap energy of 2.42 eV, not found in the literature, is reported here.

The realisation of a second compound, $Ba_3Sc_2O_5Cu_2S_2$, isostructural to the strontium prototype, with desirable transparency and p-type conductivity, allowed for investigation of the effect of *A* site elemental mixing in the perovskite-like layer, on the optoelectronic properties in these layered perovskite oxychalcogenides.

The intermediate compounds $Ba_xSr_{3-x}Sc_2O_5Cu_2S_2$ where $x = 1$ and 2, were successfully synthesised in single phases showing lattice parameters intermediate between the two end-members. Refinement of the fractional occupancy of the elements across the perovskite *A*-sites revealed a preference of the barium for the intra-layer site within the perovskite block, with any remaining *A* atoms distributed across the more flexible inter-layer sites at the boundary between the building-block layers. This observed preference was found to be rationalised by evaluation of the respective Goldschmidt tolerance factors. This preference and disorder induced in the x = 2 analogue, was found to affect the geometry in the conductive layer to such an extent that the copper-sulfur distance was reduced and the sulfur-copper-sulfur angle increased to values outside of the range spanned by the end-members. The unique preference observed upon single-site elemental mixing in the perovskite layer and the extreme geometries achieved in the conductive layer, confirmed the promise of these layered perovskite compounds for transparency and p-type conductivity.

Williamson-Hall line profile analysis was performed on the observed diffraction patterns of this series of compounds to investigate the effect of the site mixing on the lattice strain and crystallite sizes. Increased strain and reduced crystallite size in the intermediate compounds further evidenced the successful single-phase elemental mixing achieved. Further analysis of the anisotropy of the crystallite sizes in these compounds revealed preferential growth in the *ab* lattice direction, confirmed by the slab-like crystallites observed in the scanning-electron microscope images. The conductivity in the compounds was reported by Scanlon and Williamson to occur in the two-dimensional copper sulfide planes. This was found to be largest in the barium end-member, contributing to increased predicted conductivity compared to the strontium prototype.

The successful substitution of strontium for barium to yield the compound $Ba_3Sc_2O_5Cu_2S_2$ with increased predicted conductivity resulted in the observation of a band gap of 3.24 eV. In attempts to further increase the conductivity, the sulfur was successfully substituted with selenium to yield the compound $Ba_3Sc_2O_5Cu_2Se_2$, which, to the author's knowledge was also synthesised here for the first time. It possessed a measured band gap energy of 3.05 eV. Considering its increased conductivity, this may be suitable for some applications. Furthermore, it is anticipated that, should the compound be successfully doped, it will exhibit an increased band gap energy as a result of a Moss-Burstein shift.

To realise a compound with increased conductivity and band gap energy above 3.1 eV, the synthesis of the analogous compound $Ba_3Sc_2O_5Ag_2S_2$ was attempted. This synthesis, along with that of all silver sulfides attempted here, proved unsuccessful. However, the silver selenide $Ba_3Sc_2O_5Ag_2Se_2$, with predicted increased conductivity yet reduced band gap energy of 2.56 eV, was successfully realised, apparently for the first time.

The possibility of realising a compound with increased band gap energy was investigated by attempted substitution of scandium for the cations with larger ionic radii: indium, yttrium and lanthanum. The seemingly novel compounds $Ba_3In_2O_5Cu_2Se_2$, $Ba_3Y_2O_5Cu_2Se_2$ and $Ba_3In_2O_5Ag_2Se_2$ were synthesised with band gaps of 1.31, 2.67 and 1.44 eV, respectively. These results highlighted the benefit of scandium as the perovskite-like layer *M* site cation. The general decrease in band gap energies observed in these compounds from scandium to yttrium was attributed to its reduced electronegativity and the more profound drop with inclusion of indium a result of interband states formed from its occupied (n-1)*d* states.

The remaining combinations of substitute elements in this structural prototype were investigated to ascertain relationships between the *M* site cation size and geometry of the various conductive layers. As a result of this, the compound $Ba_3In_2O_5Cu_2S_2$ was realised. It was found that, as expected, the increased radius *M* site cations had the effect of increasing the basal lattice parameter in all cases. As a result of the aforementioned competing effects of the substitute elements, the band gap energies actually decreased, despite this expansion. Both the conductive layer metal-chalcogen bond length and angle, increased with increased ionic radius at the perovskite *M* site, for both copper sulfides and copper selenides, and decreased for the silver selenides. In all cases, the band gap increased and the angle in the conductive layer deviated from the ideal tetrahedral.

6.2 Outlook

6.2.1 Conductivity and Hall Effect Measurements

Difficulty arose in the synthesis of sintered whole-pellet samples suitable for conductivity measurements. As a result, such measurements were not performed in the timescale of the project. The conductivities of the original group of analogues investigated in *chapter 3* were predicted at a given charge carrier concentration from the calculated band structure via the charge carrier mobility. The microstructural effects of defects and crystallite geometry in physical samples was not, therefore, taken into account.

Conductivity can be inferred from the directly measured sheet resistance by the four-probe method and knowledge of the sample geometry.[94,95] Hall effect measurements are required to deconvolute the observed conductivity into charge carrier concentration and mobility contributions.[96] These involve the measurement of the induced Hall voltage across a sample through which a current and magnetic field is applied in mutually orthogonal directions. The charge carrier concentration can be inferred from the calculated Hall coefficient, and this then combined with the previously measured resistivity, to yield the mobility of the charge carriers.[97]

6.2.2 Extrinsic p-Type Acceptor Doping

A charge carrier concentration of ≈ 1 x10^{17} cm^{-3} was reported for the $Sr_3Sc_2O_5Cu_2S_2$ benchmark compound.[48] In the calculations of Williamson and Scanlon, however, an arbitrary charge carrier concentration of 1 x10^{21} cm^{-3} was employed to achieve predicted conductivities within an order of magnitude of those observed for the current commercialised n-types.[76] In order to realise these concentrations in physical samples, extrinsic p-type carrier doping of the samples was required.

In a preliminary investigation into the p-type dopability of these compounds, the synthesis of 5 at. % Na:$Sr_3Sc_2O_5Cu_2S_2$ was attempted. The *A* cation site in the perovskite-like layers of the 325-type compounds studied here, were chosen for doping. This process had been accomplished and reported in the literature, for example in the compound $Sr_xLa_{1-x}CuOS$.[98] There are relatively few reports on compounds with these structure types and investigations of these materials with the aim of transparent p-type conductivity rarer still. The call for further research into the doping of the compound $Sr_3Sc_2O_5Cu_2S_2$ was exemplified by the following quotations:

"Further investigation of aliovalent and isovalent doping of [$Sr_3Sc_2O_5Cu_2S_2$] is thus warranted."
Liu 2007 [27]

"We suggest that doped, transparent p-type [$Sr_3Sc_2O_5Cu_2S_2$] thin film devices could be a very promising candidate for optoelectronic applications."
Scanlon 2009 [48]

"It is undoubtedly of significant interest to […] dope [$Sr_3Sc_2O_5Cu_2S_2$] with monovalent cations (K^+) at Sr sites or divalent (Mg^{2+}) at Sc sites to improve the conductivity in this material"
Zhang 2016 [99]

In this project, the subvalent alkali metal sodium was chosen as a dopant as its monovalent ions possessed ionic radii closest to those of the $^{XII}Sr^{2+}$ used currently and was therefore expected to reduce any strain induced. In order to introduce the Na^+ dopant in place of Sr^{2+}, the SrS precursor was partially substituted by Na_2S and the Cu_2S partially replaced with the more sulfur rich CuS, to compensate for the accompanying sulfur deficiency. The ratio of precursors used to synthesise the compound $Na_xSr_{3-x}Sc_2O_5Cu_2S_2$ where x = 0.15 or 5 at. % is summarised in *equation 6.1*. The Na_2S was synthesised from its elements in a liquid ammonia solvent under an inert atmosphere as described in *appendix D.4*.

$$0.075\ Na_2S + SrO + 0.85\ SrS + Sc_2O_3 + 0.925\ Cu_2S + 0.15\ CuS \rightarrow Na_{0.15}Sr_{2.85}Sc_2O_5Cu_2S_2 \qquad 6.1$$

The refined diffraction pattern of the powder sample resulting from a single heat treatment cycle of 800°C for 12 h, is shown in *figure 6.1* along with its Tauc plot (inset). The observed pattern closely matched that of the undoped compound $Sr_3Sc_2O_5Cu_2S_2$. It was observed that the refined occupancy of the strontium inter-layer site was 0.9685, tending towards that expected for the 5 at. % sodium-doped sample. Sodium was introduced onto the *A* sites in the model which was then refined with constraints such that an increase in sodium on the *A* site would be countered by a corresponding decrease in strontium, to represent the physically realistic situation of site competition. The refinement yielded a modified model with seemingly identical fit statistics of R_{wp} = 6.68 % and χ^2_{red} = 1.722. However, the *A* site occupancy gave an indication of successful sodium incorporation onto the *A* sites. The average strontium occupancy of the *A* sites fell to 0.9479 from 0.9771 in the undoped model. A corresponding average sodium occupancy of 0.0522 was also observed. These values are close to the intended concentrations of 0.95 and 0.05 respectively, confirming successful doping.

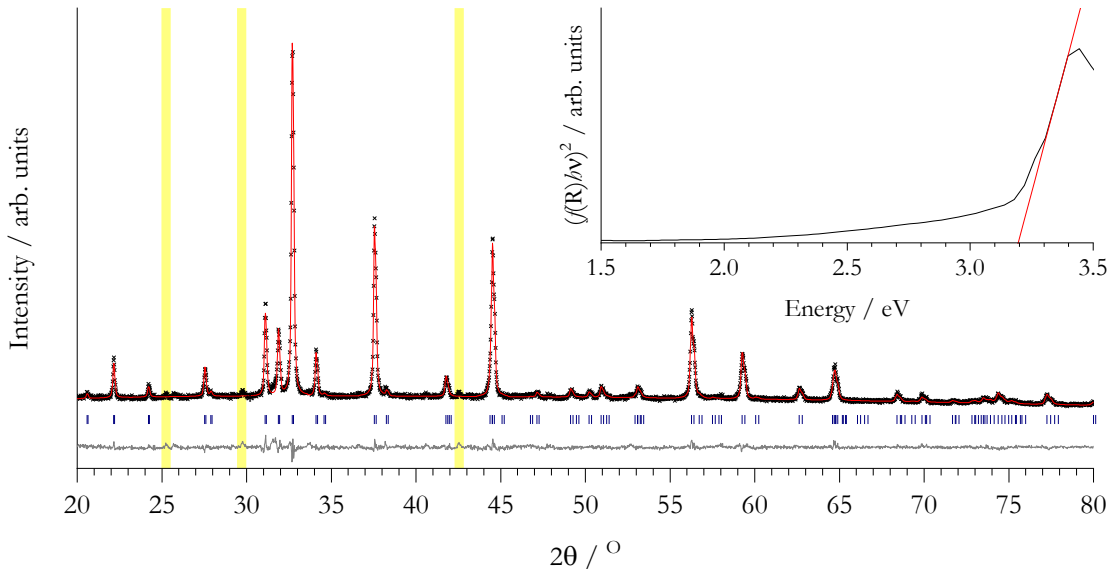

Figure 6.1 *Powder x-ray diffractogram and Tauc plot (inset) of the newly observed doped compound $Na_{0.15}Sr_{2.85}Sc_2O_5Cu_2S_2$. The observed data is represented as black crosses, the calculated diffraction pattern as a solid red line and the difference profile as a solid grey line below. R_{wp} = 6.68 % and χ^2_{red} = 1.722. Peaks highlighted in yellow are currently unassigned. It has been ruled out as far as possible that they correspond to a sodium containing impurity phase and the shoulder peak at 2θ = 31.55 ° is also present in the undoped sample $Sr_3Sc_2O_5Cu_2S_2$, ruling out a sodium containing phase as its origin. In the Tauc plot, the solid red line shows a linear fit to the region of steepest gradient; its x-intercept marking the band gap energy at approximately 3.2 eV.*

The individual site occupancies were also monitored. It was seen that sodium dominated the the inter-layer site, adjacent to the more flexible copper sulfide layers, and strontium the intra-layer sites at the centre of the perovskite layer. (Occupancy A_{inter}: Na = 0.0652 and Sr = 0.9348; A_{intra}: Na = 0.0391 and Sr = 0.9609) These were rationalised by consideration of the tolerance factor. The strontium showed the higher tolerance factor of 0.94, compared with the 0.92 for sodium and hence had a better fit in a scandium oxide perovskite structure. Therefore, the strontium preferentially occupied the intra-layer sites and the 'poorer-fitting' sodium distributed across the inter-layer sites in which its smaller size could be accommodated by the more flexible tetrahedral layer. This result was consistent with that observed in the isovalent mixing of *A* site cations within the same structure reported in *chapter 4*.

Further evidence for successful doping was gleaned from the band gap analysis. The calculated band gap of the doped sample increased by 0.09 eV, from 3.11 to 3.20 eV, compared to the undoped equivalent. This can be explained in terms of a Moss-Burstein shift *i.e.* the reduction in energy of the VBM as holes are introduced and the electron occupation decreased.[92] Synthesis of this compound as a sintered pellet and conductivity/Hall measurements are recommended, in addition to the attempted doping of the analogous compounds $Ba_3Sc_2O_5Cu_2S_2$ and $Ba_3Sc_2O_5Cu_2Se_2$ with higher predicted undoped conductivity.

6.2.3 Further Layered Perovskite Mixed-Anion Oxide Structure Types

Continued investigation into layered perovskite mixed-anion oxides for application as transparent p-type conductors may benefit from consideration of the range of structure types other than the 325 investigated here.

Some of the earliest work on these compounds was that of Zhu and Hor who reported on their observations of four of the "rare" and "unusual" structure types described here as xyz = 212, 426 and 438 in the general formula $A_xM_yO_zM'_2Ch_2$.[71,79,100,101] A '214' structure type was also reported by Evans *et al.* in a brief Chemical Communications paper.[102] These have the general formulae $Bi_2LnO_4Cu_2Se_2$ wherein *Ln* = Y, Gd, Sm, Nd and La. Interestingly, these are the only known examples in which a post-transition metal resides on the *A* cation site. The only other structure type known for these quinary oxychalcogenides has the xyz ratio 448, or 224 when simplified. This was reported in 2008 by Hyett *et al.* and possessed the formula $Ba_4Mn_4O_8Cu_{2-\delta}S_2$.[84] In the two decades following the early work of Zhu and Hor, thirty-five related oxychalcogenide compounds have been found to be reported and are summarised in *appendix C*. Representations of the crystal structures of these quinary oxychalcogenides, including the 325-type investigated here, are depicted in *figure 6.2*.

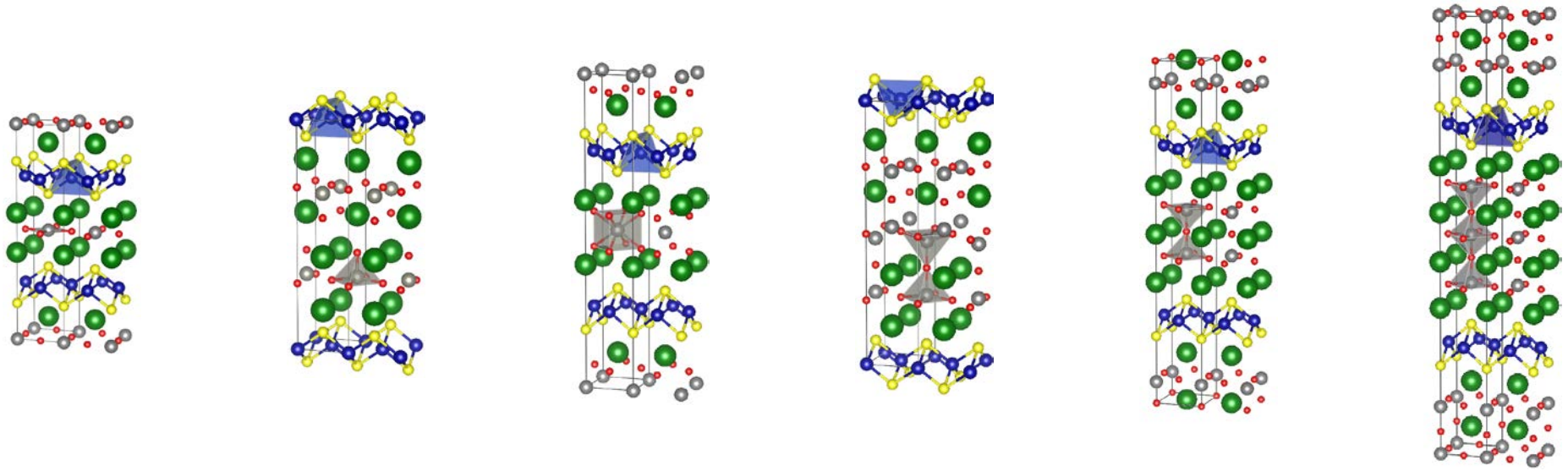

212	426 (213)	214	448 (224)	325	438
$\{Sr_2Mn_2Sb_2O_2\}$	$\{Sr_2CuGaO_3S\}$	$\{U_2Cu_4As_5\}$	$\{Ba_2Mn_2O_4CuS\}$	$\{Ni_3SmGe_3\}$	{n/a}
I4/mmm [139]	*P4/nmm* [129]	*I4/mmm* [139]	*P4/nmm* [129]	*I4/mmm* [139]	*I4/mmm* [139]
$A_2MO_2M'_2Ch_2$	$A_4M_2O_6M'_2Ch_2$	$A_2MO_4M'_2Ch_2$	$A_4M_4O_8M'_2Ch_2$	$A_3M_2O_5M'_2Ch_2$	$A_4M_3O_8M'_2Cu_2$

Figure 6.2 *Summary of the crystal structures of quinary layered perovskite oxychalcogenides. The unit cells are shown and expanded by a multiple of b in the b direction to clarify the layered structure. Structure types are given showing the simplified ratio in parentheses ( ) where applicable. The text in braces { } refers to the structure type as assigned by the ICSD, the space group is provided below with its assigned number in square brackets [ ] and the italicised text gives the general formula for each structure type. Colour key: green - A, grey - M, red - O, blue - M', yellow – Ch.*

The expansion of the range of prototype structures considered may well enable the possibility of the incorporation of elements or the synthesis of compositions not attainable for the 325s, for example the silver sulfides, proposed to show increased conductivity. These other structures may also yield novel conductivity layer geometries and therefore optoelectronic properties which may not vary with ionic substitution in the perovskite-like layer in a way consistent with that for the 325s studied here.

Interesting series of compounds have also been reported, in which extreme layer thickness had been observed in both the intervening perovskite-like and tetrahedral conductive layers. Ogino *et al.* reported on an interesting modification of the existing 426 structure type.[103] This oxypnictide exhibited magnesium (II) and titanium (IV) cations sharing the *M* site in a compound with the formula $Sr_4(Mg,Ti)O_6Fe_2As_2$. The parentheses indicated that the two elements were found to share the same crystallographic site in single-phase solid solution.

This technique based on the site sharing of aliovalent cations permitted the realisation of a new homologous series of layered perovskite oxypnictides with expanded perovskite layers and hence new structure types. The aluminium analogue of this new mixed 426 structure, $Ca_4(Al,Ti)O_6Fe_2As_2$, proved to be the first in a three-membered series with general formulae $Ca_{n+2}(Al,Ti)_nO_{3n}Fe_2As_2$ where n = 2, 3 and 4.[81] The nominal ratios between the *M* site ions were reported as 2:1, 1:1 and 1:2 respectively. This resulted in the expansion of the set of known structure types to include those with idealised structures termed here as 539 and 64$\underline{12}$. The n = 2 structure (426) was already known.

A report on a second series was published in which the same idea was employed to substitute aluminium for scandium.[104] This was found to enable the synthesis of an oxygen deficient variant on the known 438 structure using the mixed *M* cations: $Ca_4(Sc_2Ti)O_{7.5}Fe_2As_2$. This was again the first in a new homologous series including the new structure types 5$\underline{411}$ and 6$\underline{514}$. A year later, an analogue of the 5$\underline{411}$ was reported by the same group, this time including the original combination of magnesium and titanium as the *M* site cations.[105]

Gál *et al.* under the supervision of Clarke, the same group behind Hyett's report of the 448 structure, published on a homologous series of compounds based on the $Sr_2MnO_2Cu_2S_2$ compound, with 212 structure.[106] This series possessed the general formula $Sr_2MnO_2Cu_{2m-\delta}S_{m+1}$, where m = 1, 2 and 3, and δ represents the observed varying copper deficiency, and exhibited the expanded litharge layers $[Cu_4S_3]^{2-}$ and $[Cu_6S_4]^{2-}$. The novel and rare layering observed in these examples may yield unique optoelectronic properties and further investigation of their structure/property relationships is therefore worthwhile.

6.3 Summary

The successful synthesis of the compound $Ba_3Sc_2O_5Cu_2S_2$ was achieved. It possessed a larger band gap and increased predicted conductivity compared to the current literature benchmark, $Sr_3Sc_2O_5Cu_2S_2$. The intermediates $Ba_xSr_{3-x}Sc_2O_5Cu_2S_2$ where $x = 1$ and 2 were successfully synthesised by elemental mixing on the perovskite *A* site. An interesting preference for the intra-layer site of the barium led to increased observed disorder in the compound $x = 2$ and extreme geometry in the conductive layer beyond the range spanned by the end-members. Williamson-Hall PXRD line-profile analysis of lattice strain and crystallite size proved that the strain was increased as expected in the mixed samples and that the crystallite growth mode in all cases was anisotropic, resulting in slab-like structures elongated in the *ab* plane. It was found that this dimension was largest in the compound $Ba_3Sc_2O_5Cu_2S_2$ and was predicted to further contribute to high experimental conductivity.

Phase space investigation by isovalent elemental substitution yielded the compound $Ba_3Sc_2O_5Cu_2Se_2$, with a band gap of 3.05 eV and a predicted increase in conductivity compared to the prototype and its barium analogue. The analogous compounds $Ba_3Sc_2O_5Ag_2Se_2$, $Ba_3Y_2O_5Cu_2Se_2$, $Ba_3In_2O_5Cu_2S_2$, $Ba_3In_2O_5Cu_2Se_2$ and $Ba_3In_2O_5Ag_2Se_2$ were also successfully synthesised apparently for the first time.

Investigation of the crystal structure of these compounds revealed that increasing cationic radius on the *M* perovskite site had the effect of increasing the conductive coinage metal-metal *(M'-M')* distance and decreasing coinage metal chalcogen *(M'-Ch)* distance for the copper sulfides and selenides, seen as desirable for conductivity and transparency. Scandium, however, was found to be the optimum cation in terms of transparency with the less electronegative yttrium and (n-1)*d*-filled indium exhibiting undesirably low band gaps in all cases.

Looking forward, it is recommended that the conductivity of the samples (and its mobility and charge carrier concentration contributions) is investigated experimentally by four-probe van der Pauw and Hall effect measurements. In order to achieve high p-type conductivity in these compounds, acceptor doping is still required. To this end, the p-type carrier doped literature prototype compound, $Na_{0.15}Sr_{2.85}Sc_2O_5Cu_2S_2$, was successfully realised in a preliminary investigation and confirmed by refinement of PXRD data and observation of a Moss-Burstein shift resulting in a band gap energy of 3.2 eV.

The full range of structure types reported for other layered perovskite mixed-anion oxides is yet to be investigated for transparency and p-type conductivity. These structures may exhibit novel conductive layer geometry. The extreme examples of compounds showing increased layer thickness in both the perovskite-like and conductive layers invoke intrigue with regard to novel optoelectronic properties and their investigation to this end, is suggested.

Appendices

A Derivation of the Plasma Frequency

The plasma frequency is a characteristic of the conduction electrons in an electrically conductive sample.[107] These electrons are modelled most simply as a 'cold' electron gas or plasma. The 'cold' indicating that the thermal motion of the electrons is ignored. It is assumed that the equilibrium charge distribution in the sample is constant throughout. Upon interaction with the electric field of an incident electromagnetic wave, the conduction electrons are displaced relative to the stationary (again, neglecting thermal motion) cationic lattice.

The electrons displaced by the electric field of the incident radiation, experience a restoring force, as a result of their mutual Coulombic repulsion, proportional to and opposing the electric field, E, created by the displacement, as in *equation A 1,* overleaf. The electric field density at the surface of the sample (given by the surface integral of the electric field) is related to the displacement of the oscillation as shown in *equation A 2*. Differentiating gives an expression for the magnitude of the electric field in the direction of the displacement, as in *equation A 3*. This can be substituted into *equation A 1* and rearranged to give *equation A 4*, which has the second-order differential equation form of a harmonic oscillator, shown generally in *equation A 5*, with solution as given by *equation A 6*. An expression for the plasma frequency *(eqn. A 9)* is obtained by substitution of the expression for the spring constant, k *(eqn. A 8)*, into an equation for the frequency *(eqn. A 7)* from the general solution of the harmonic oscillator partial differential *equation A 6*.

$$\mathbf{F} = m \frac{d^2\mathbf{x}}{dt^2} = -q\,\mathbf{E} \qquad \text{A 1}$$

F – force
m – mass
x – displacement
t – time
q – charge
E – electric field

$$\oint \mathbf{E}\, d\mathbf{S} = \frac{Q}{\varepsilon_0} = \left(\frac{S\, n_e\, e}{\varepsilon_0}\right) x \qquad \text{A 2}$$

d**S** – infinitesimal surface element vector
Q – charge
ε_0 - vacuum permittivity
n_e – electron number density
e – fundamental charge on electron

$$E_x = \left(\frac{n_e\, e}{\varepsilon_0}\right) x \qquad \text{A 3}$$

$$\frac{d^2x}{dt^2} + \left(\frac{n_e\, e^2}{\varepsilon_0\, m_e}\right) x = 0 \qquad \text{A 4}$$

m_e – electron rest mass

$$\frac{d^2x}{dt^2} + \frac{k}{m}\, x = 0 \qquad \text{A 5}$$

k – spring constant

$$x = A\cos(\omega\, t) \qquad \text{A 6}$$

ω – angular frequency

$$\omega = \sqrt{\frac{k}{m}} \qquad \text{A 7}$$

$$k = \frac{n_e\, e^2}{\varepsilon_0} \qquad \text{A 8}$$

$$\omega_p = \sqrt{\frac{n_e\, e^2}{\varepsilon_0\, m_e}} \qquad \text{A 9}$$

B Derivation of the Conductivity Equation

The current density, as previously expressed in *equation 1.3* (repeated here in *equation A 10*), can also be written in terms of the volumetric number density, charge and velocity of the charge carriers *(eqn. A 11)*. This expression can then be substituted into *equation A 10* and rearranged to yield an expression for conductivity as given by *equation A 12*. This can be simplified by use of the mobility. This is the proportionality constant, relating the charge carrier velocity to the applied electric field strength *(eqn. A* 13*)*. Rearranging *equation A 13* and substituting into *equation A 12*, gives the simplified equation for conductivity in *equation A 14*. The mobility can also be expressed in terms of the mean free time between scattering events, and the mass, of the charge carriers *(eqn. A 15)*. This can be substituted into *equation A 14* to yield *equation A 16*, as in *equation 1.4*.

$$j = \sigma E \qquad \text{A 10}$$

j – current density
σ – conductivity
E – electric field strength

$$j = n e \nu \qquad \text{A 11}$$

n – volumetric number density of charge carriers
e – fundamental charge
ν – charge carrier velocity

$$\sigma = \frac{n e \nu}{E} \qquad \text{A 12}$$

$$\nu = \mu E \qquad \text{A 13}$$

μ - charge carrier mobility

$$\sigma = n e \mu \qquad \text{A 14}$$

$$\mu = \frac{e \tau}{m} \qquad \text{A 15}$$

τ - mean free time
m – charge carrier mass

$$\sigma = \frac{n e^2 \tau}{m} \qquad \text{A 16}$$

C Selected Lattice Parameters for Quinary Layered Mixed Anion Oxides

Table A 1 Selected lattice parameters of analogous quinary layered mixed-anion oxides extracted from the literature.

Compound $A_xM_yO_zM'_2(Ch/Pn)_2$					Selected Lattice Parameters				
Structure Type *xyz*	*A*	*M*	*M'*	*Ch/Pn*	**a**	**M'-Ch**	**Ch-M'-Ch** *cis*	**Ch-M'-Ch** *trans*	**Ref.**
2 1 2	Ba	Co	Ag	Se	4.22323	2.7440	100.62	114.07	[108]
2 1 2	Ba	Co	Cu	S	4.06420	2.4395	107.824	112.82	[83]
2 1 2	Ba	Mn	Ag	Se	4.26514	2.7576	113.70	101.31	[108]
2 1 2	Sr	Co	Ag	Se	4.0980	2.7647	116.77	95.69	[109]
2 1 2	Sr	Co	Cu	S	3.99129	2.4356	109.185	110.04	[83]
2 1 2	Sr	Co	Cu	Se	4.0488	2.5235	110.88	106.69	[109]
2 1 2	Sr	Mn	Cu	S	4.0018	2.446	109.31	109.79	[100]
2 1 2	Sr	Ni	Cu	S	3.9248	2.440	110.7	107.1	[49]
2 1 2	Sr	Zn	Cu	S	4.0079	2.450	109.31	109.79	[100]
4 2 6 (2 1 3)	Ba	Sc	Fe	As	4.1266	2.441	160.6	115.39	[110]
4 2 6 (2 1 3)	Ca	Fe	Cu	S	3.8271	2.411	111.72	105.07	[111]
4 2 6 (2 1 3)	Ca	Fe	Cu	Se	3.8605	2.505	113.99	100.78	[111]
4 2 6 (2 1 3)	Sr	Cr	Cu	S	3.9000	2.449	111.46	105.56	[71]
4 2 6 (2 1 3)	Sr	Cr	Fe	As	3.918	2.413	109.921	108.575	[112]
4 2 6 (2 1 3)	Sr	Fe	Cu	S	3.9115	2.424	111.8	104.9	[71]
4 2 6 (2 1 3)	Sr	Fe	Cu	Se	3.9367	2.515	112.79	103.02	[113]
4 2 6 (2 1 3)	Sr	Ga	Cu	S	3.8606	2.432	111.70	105.10	[79]
4 2 6 (2 1 3)	Sr	Sc	Fe	As	4.05	2.434	107.9219	112.6164	[114]
4 2 6 (2 1 3)	Sr	V	Fe	As	2.9296	2.427	110.1573	108.1076	[115]

Compound $A_xM_yO_zM'_2(Ch/Pn)_2$					Selected Lattice Parameters				
Structure Type *xyz*	*A*	*M*	*M'*	*Ch/Pn*	**a**	**M'-Ch**	**Ch-M'-Ch** *cis*	**Ch-M'-Ch** *trans*	**Ref.**
3 2 5	Sr	Fe	Ag	Se	3.94505	2.65	116.43	96.30	[70]
3 2 5	Sr	Fe	Cu	Se	3.95770	2.51	112.2	104.8	[70]
3 2 5	Sr	Fe	Cu	S	3.9115	2.424	110.42	107.60	[71]
3 2 5	Sr	Sc	Cu	S	4.0758	2.489	109.2	110	[49]
3 2 5	Sr	Sc	Fe	As	4.0781	2.447	107.37	113.76	[75]
4 3 8	Sr	Mn	Cu	Se	3.888	2.506	113.46	101.76	[101]
4 3 8	Sr	Mn	Cu	S	3.890	2.430	111.05	106.4	[101]

D Precursor Syntheses

D.1 Alkali Earth Oxides

The alkali earth oxides, with general formulae *A*O, used in this project were synthesised by the thermal decomposition of the corresponding carbonate, ACO_3, under dynamic vacuum according to the *equation A 17*.

$$ACO_3 \rightarrow AO + CO_2 \qquad \text{A 17}$$

The carbonate was loaded into an alumina boat that was placed at the end of a quartz tube sealed at one end. The open end was capped with a quartz head fitted with a Young's tap adaptor, which was then attached to a vacuum pump by rubber tubing. The sample was placed under dynamic vacuum, allowed to purge and heated to 1000 °C at a rate of 10 °C min^{-1}. Once heated, the temperature was held for 12 and 14 h for calcium and strontium, and barium respectively, before being allowed to cool naturally to room temperature. After the synthesis, the Young's tap was closed, vacuum line removed and the quartz tube assembly taken into a glovebox and the alkali-earth oxide removed and stored within. Storage in an inert gas-filled glovebox was necessary as the oxides have a thermodynamic tendency to revert to the carbonate under atmospheric carbon dioxide concentrations. The phase purity of the synthesised precursors was verified by PXRD and the refined resulting patterns shown in *figure A 1*.

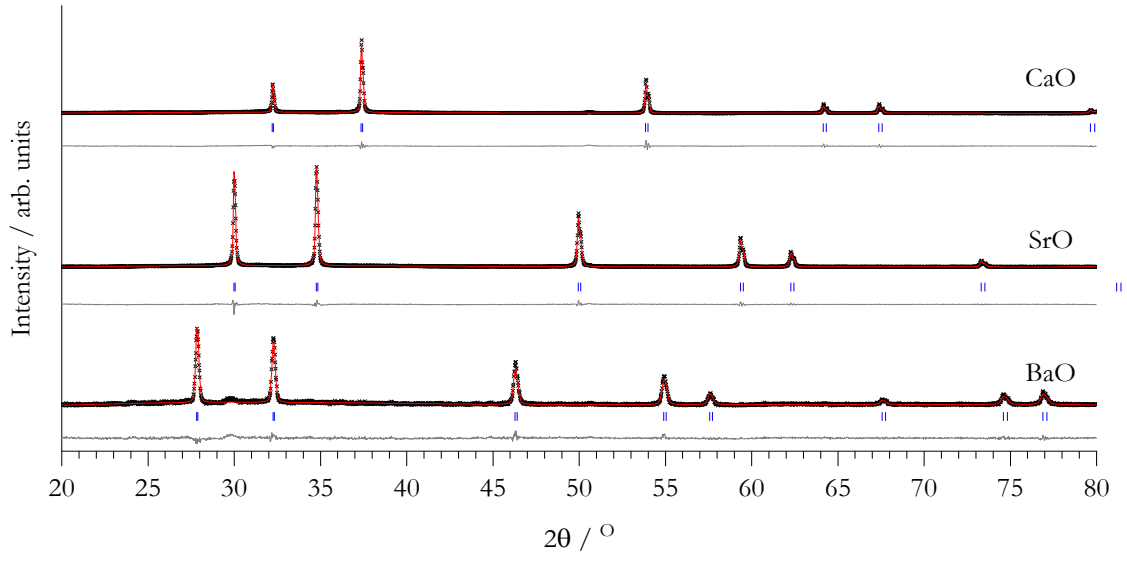

Figure A 1 *Powder x-ray diffraction patterns indicating the successful syntheses of the phase-pure alkali earth oxide precursors CaO (top), SrO (centre) and BaO (bottom). The black crosses represent the intensity and angle of the observed diffracted x-rays, the red line the calculated profile from the Rietveld refined model, the grey line the difference between these two profiles and the blue tick marks show the expected 2θ peak positions for the corresponding rock-salt structure (Fm-3m). CaO: R_{wp} = 15.63 % and χ^2_{red} = 3.309. SrO: R_{wp} = 8.25 % and χ^2_{red} = 2.209. BaO: R_{wp} = 18.58 % and χ^2_{red} = 1.505.*

D.2 Alkali Earth Sulfides

Alkali earth metal sulfides (*A*S, where *A* = Sr and Ba) used as precursors for the solid-state synthesis of target compounds in this project were synthesised in-house via the sulfurization of the corresponding carbonates (ACO_3). The carbonates were heated in the presence of carbon disulfide vapour according to the *equation A 18*.

$$2\,ACO_{3\,(s)} + CS_{2\,(g)} \rightarrow 2\,AS_{\,(s)} + 3\,CO_{2\,(g)} \qquad \text{A 18}$$

In practice, this was achieved by placing the carbonate powder inside an alumina boat, which was then positioned centrally inside a quartz tube closed at one end, passing through a tube furnace. The tube head contained both an inlet and outlet such that the whole tube could be removed from the furnace, evacuated and transferred to a glove box without opening. The inlet gas consisted of the inert nitrogen carrier that had passed through a sequence of two bubblers. The first was empty to prevent back-fill in the event of a negative pressure difference and the second was filled with carbon disulfide liquid to generate a reactant CS_2 vapour. The exhaust gasses were worked up by passing them through two hydroxide/bleach bubblers. This would have neutralised the unreacted CS_2 and any hydrogen sulfide inadvertently produced before releasing the gas into the ventilation system of the fumehood. The quartz tube was purged with reaction gas before heating at a rate of 10 °C min^{-1} to 900 °C. This temperature was held for 4 and 8 h for SrS and BaS respectively, prior to cooling naturally to room temperature under continued inert gas flow. The purity of the resultant sulfides were monitored by PXRD and the corresponding refined patterns are shown in *figure A 2*.

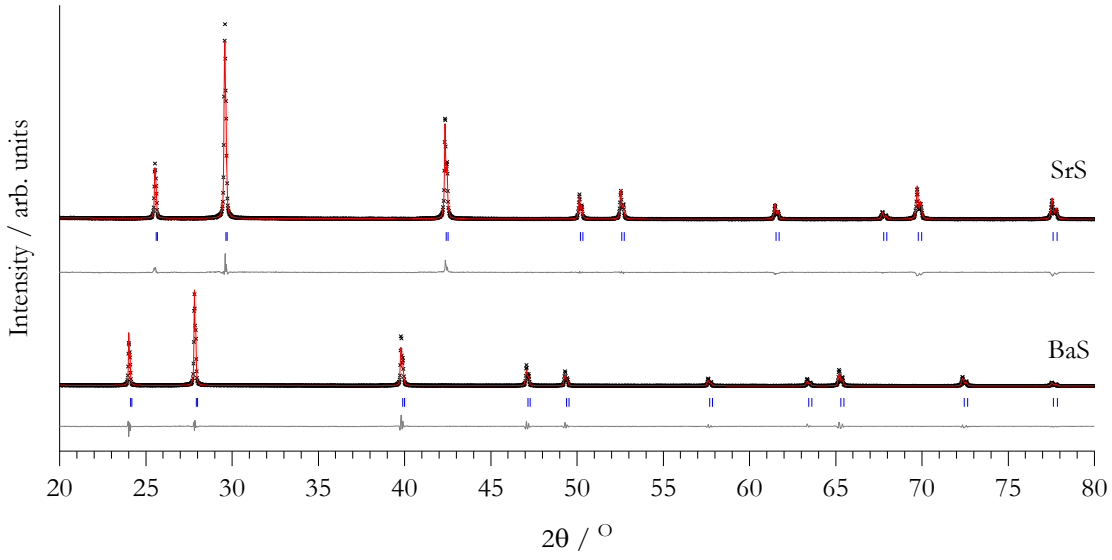

Figure A 2 *Powder x-ray diffraction patterns indicating the successful syntheses of the phase-pure alkali earth sulfide precursors SrS (top) and BaS (bottom). The black crosses represent the intensity and angle of the observed diffracted x-rays, the red line the calculated profile from the Rietveld refined model, the grey line the difference between these two profiles and the blue tick marks show the expected 2θ peak positions for the rock-salt structure (Fm-3m). SrS: R_{wp} = 9.33 % and χ^2_{red} = 3.049. BaS: R_{wp} = 14.76 % and χ^2_{red} = 3.59.*

D.3 Barium Selenide by Selenate Reduction

Barium selenide was made by the reduction of barium selenate. The water-insoluble barium selenate was prepared by precipitation upon mixing two aqueous solutions over ice; one of sodium selenate and the other of barium nitrate, as described by *equation A 19*. The barium selenate precipitate was removed by filtration and dried in an oven at approximately 70 °C in air. The resulting barium selenate powder was then reduced under 5 % hydrogen, as per *equation A 20*.

$$Na_2SeO_{4\,(aq)} + Ba(NO_3)_{2\,(aq)} \rightarrow BaSeO_{4\,(s)} + 2\,NaNO_{3\,(aq)} \qquad \text{A 19}$$

$$BaSeO_{4\,(s)} + 8\,H_{2\,(g)} \rightarrow BaSe_{\,(s)} + 4\,H_2O_{\,(g)} \qquad \text{A 20}$$

The powder was placed in an alumina boat slid to the end of a quartz tube sealed at one end. The open end was sealed with a quartz cap containing Young's tap adaptors for inlet and outlet. The inlet was attached to a 5 % H_2/N_2 cylinder gas supply with which the tube was purged before heating to 500 °C at a rate of 10 °C min^{-1}. The maximum temperature was held for 4 h before cooling naturally to room temperature. During the reaction, the exhaust gases were passed through a fan-cooled coil of tube before exiting the reactor system through a silicone oil bubbler to prevent back diffusion of air. After the reaction was completed the reactor tube was sealed, evacuated, removed from the furnace and transported to an inert-atmosphere glovebox in which the sample was removed from the reactor tube and stored. PXRD analysis confirmed the phase purity of these compounds *(figure A 3)*.

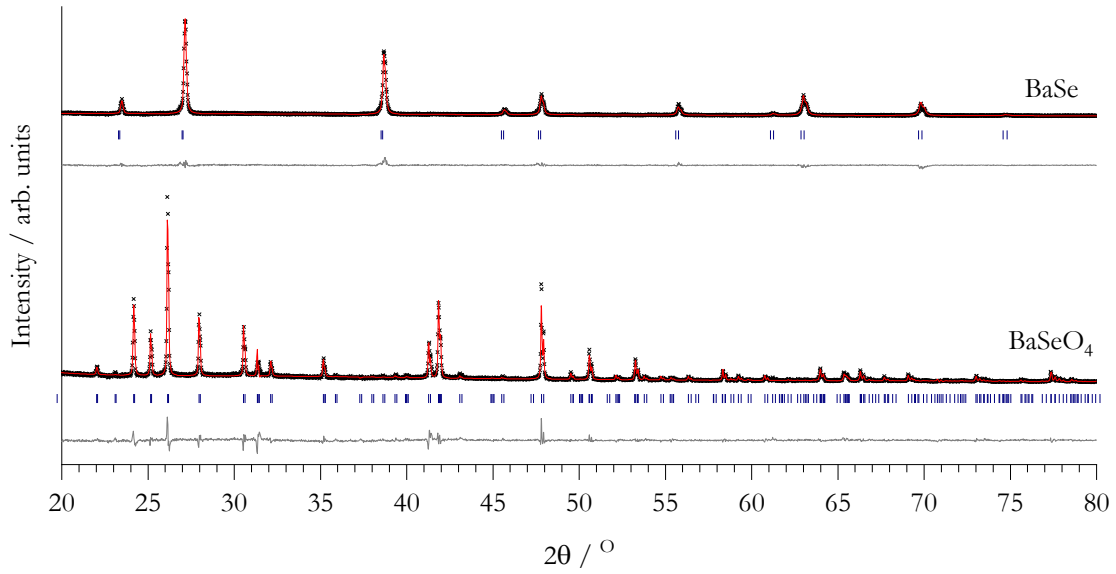

Figure A 3 *Powder x-ray diffraction patterns indicating the successful synthesis of the phase-pure precursor BaSe (top) and $BaSeO_4$ (bottom) from which it was synthesised. The black crosses represent the intensity and angle of the observed diffracted x-rays, the red line, the calculated profile from the Rietveld refined model, the grey line, the difference between these two profiles and the blue tick marks show the expected 2θ peak positions for the rock-salt (Fm-3m) BaSe and orthorhombic (Pnma) $BaSeO_4$ structures. BaSe: R_{wp} = 14.00 % and χ^2_{red} = 1.621. $BaSeO_4$: R_{wp} = 11.59 % and χ^2_{red} = 3.016. The pattern for the $BaSeO_4$ was collected on behalf of the author by undergraduate student, Mathew Stephens.*

D.4 Sodium Sulfide

Sodium sulfide was synthesised by direct reaction between the elemental sodium and sulfur dissolved in liquid ammonia. Stoichiometric quantities of each were weighed out in an inert-atmosphere glovebox, placed together in a borosilicate glass ampoule sealed with a Young's tap, and stoppered at the ground glass joint. The ampoule was removed from the glovebox and kept under inert gas on a Schlenk line. A second ampoule was placed under inert gas on the Schlenk line and cooled with a bath of solid carbon dioxide in isopropyl alcohol. Ammonia from a cylinder supply was condensed into this via a sidearm joint and dried by addition of a sodium flake, taking care to maintain the gas seal for as long as possible. Once a suitable volume of ammonia had condensed (~ 30 cm^3), the sidearm was removed and re-stoppered. To prevent explosion, care was taken to maintain an open path through the Schlenk line from the liquid ammonia and bubbler outlet at all times. A cannula was placed through the Suba-Seals of the drying flask, in which the ammonia was condensed, and the reaction flask, in which the reactants were placed, connecting the two. The drying flask was closed to the Schlenk line and the 'dry ice' bath removed. The pressure of the evaporating ammonia induced a flow of the gas into the reaction flask under which the dry ice bath was then placed. The ammonia condensed onto the reactants that were agitated by stirring with a glass-coated magnetic stirrer. Once all of the ammonia had transferred, the stirring and cooling was maintained until the sulfur had fully dissolved. The metal dissolved immediately within a suitable volume of ammonia, its solvated electrons yielding a dark red when concentrated and then blue solution as it became more dilute. Stirring and manual agitation was required to ensure that all sulfur had visibly reacted. After being allowed to warm naturally overnight, the off-white/pale yellow sample was transferred to a glovebox where it was stored and its identity verified by powder x-ray diffraction *(fig. A 4)*.

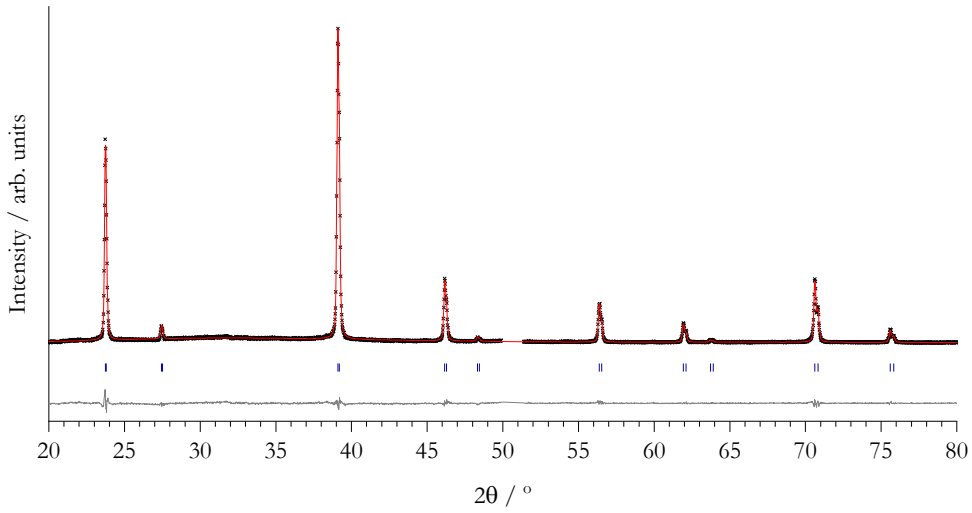

Figure A 4 *Powder x-ray diffraction pattern indicating the successful synthesis of the phase-pure precursor Na_2S. The black crosses represent the intensity and angle of the observed diffracted x-rays, the red line, the calculated profile from the Rietveld refined model, the grey line, the difference between these two profiles and the blue tick marks show the expected 2θ peak positions for the Na_2S of rock salt structure (Fm-3m). R_{wp} = 9.54 % and χ^2_{red} = 1.947. A diffraction peak at 2θ ≈ 50° was identified and attributed to the metal beam knife in the custom air-sensitive x-ray diffraction holder. The data points corresponding to the peak were excluded from the refinement process and the plot shown.*

E $Ba_3Sc_2O_5Cu_2S_2$ Refined Crystal Structure Parameters

Table A 2 Summary of the Rietveld refined crystal structure parameters of the compound with composition $Ba_3Sc_2O_5Cu_2S_2$.

Atom	Fractional Coordinates			Fractional Occupancy	Isotropic Thermal Parameter / Å^2
	x	y	z		
Ba1	-0.5	0.5	0	0.9573	0.01309
Ba2	0	0	-0.353818	0.9265	0.01454
Cu1	0	0.5	-0.25	0.8791	0.01892
O1	-0.5	0	-0.081964	0.9469	0.01654
O2	0	0	0	0.8604	0.02021
S1	0	0	-0.200477	1.0000	0.00504
Sc1	0	0	-0.072790	0.8573	0.00108

F Chapter 4 Supplementary Data

F.1 Refined Unit Cell Parameters

Table A 3 Summary of lattice parameters, as determined by refined powder x-ray diffraction data, of the intermediate mixed A perovskite cation compounds $Ba_xSr_{3-x}Sc_2O_5Cu_2S_2$, where x = 1 and 2.

x $Ba_xSr_{3-x}Sc_2O_5Cu_2S_2$	a=b / Å	c / Å	Vol / Å^3
1	4.09645(7)	26.1258(8)	438.41(2)
2	4.1212(4)	26.568(3)	451.2(1)

F.2 Refined Fractional Atomic Coordinates

Table A 4 Fractional atomic coordinates extracted from the Rietveld refined model describing the crystal structures of mixed A site compounds of composition $Ba_xSr_{3-x}Sc_2O_2Cu_2S_2$, where x = 1 and 2.

	Fractional Atomic Coordinates					
Composition (x)	1			2		
Atom	x	y	z	x	y	z
*A*1	0.5	0.5	0	0.5	0.5	0
*A*2	0.5	0.5	0.1457(1)	0.5	0.5	0.1461(2)
Sc1	0	0	0.0750(2)	0	0	0.0699(4)
O1	0.5	0	0.0872(4)	0.5	0	0.0844(7)
O2	0	0	0	0	0	0
Cu1	0.5	0	0.25	0.5	0	0.25
S1	0	0	0.1995(3)	0	0	0.1986(5)

F.3 Crystal Structure Geometry (Distances and Angles)

Table A 5 Summary of distances, bond lengths and angles calculated from the Rietveld refined model for the crystal structures of the mixed A compounds with compositions $Ba_xSr_{3-x}Sc_2O_5Cu_2S_2$.

	0	1	2	3
Parameter	**Length / Å**			
Perovskite Thickness	7.501(3)	7.6125(3)	7.7630(9)	7.9296(3)
Sc-O_{Eq}	2.0581(9)	2.07272(4)	2.0954(2)	2.09468(7)
Sc-O_{Ax}	1.9643(8)	1.96061(7)	1.8560(3)	1.93964(8)
A_{Intra}-O_{Ax}	2.881(1)	2.89663(6)	2.9141(3)	2.92894(9)
A_{Intra}-O_{Eq}	3.0408(9)	3.06368(6)	3.0409(3)	3.06044(8)
A_{Inter}-O_{Eq}	2.5256(8)	2.55534(5)	2.6368(2)	2.68681(7)
A_{Inter}-S	3.197(1)	3.22000(6)	3.2266(3)	3.28852(9)
Cu-S	2.4446(8)	2.43606(4)	2.4776(2)	2.45532(6)
Cu-Cu	2.881(1)	2.89663(6)	2.9141(3)	2.92894(9)
	Angle / º			
O_{Eq}-Sc-O_{Eq}	88.836(1)	88.6534(1)	88.1123(6)	88.7160(1)
O_{Eq}-Sc-O_{Ax}	98.193(5)	98.8180(4)	100.457(2)	98.6092(5)
A_{Inter}-O_{Eq}-A_{Inter}	107.52(4)	106.556(3)	102.791(8)	100.857(3)
A_{Inter}-O_{Eq}-A_{Intra}	84.18(4)	84.766(3)	85.946(9)	86.983(3)
A_{Inter}-S-A_{Inter} (*ab*)	128.62(3)	128.204(2)	129.149(7)	125.911(3)
S-Cu-S	112.88(3)	114.448(2)	112.543(8)	115.024(3)

F.4 Instrumental Broadening Calibration Data

Table A 6 Summary of peak parameters in collected powder x-ray diffraction profile for the LaB_6 instrumental broadening standard.

Position (2θ) / o	Full-Width at Half-Maximum (FWHM) / o
43.5143	0.0652219
48.9663	0.0674172
53.9988	0.0669132
63.2305	0.0693324
71.7597	0.0716105
75.8594	0.0739486
79.8863	0.0768121
83.8632	0.0802645
87.8106	0.0850684
95.693	0.0873722
107.776	0.0992633
111.963	0.112414
116.276	0.123103
120.757	0.13774
130.451	0.159683

F.5 Williamson-Hall Analysis Raw Data

Table A 7 Raw data used in the construction of the Williamson-Hall plots.

Composition (x)	Orientation	h k l	2θ / °	β Tot. / °	β Tot., Ins. / °	β Tot., Smpl. / °	sin (θ)	β cos (θ) / c
0	ab	1 0 1	22.0365	0.103515	0.063293449	0.040221551	0.1911217	0.000689058
0	ab	1 0 3	24.096	0.0952713	0.063246935	0.032024365	0.2087311	0.000546619
0	ab	1 0 5	27.7862	0.093544	0.06324167	0.03030233	0.2401111	0.000513403
0	ab	1 1 0	30.9886	0.110348	0.063321338	0.047026662	0.2671425	0.000790941
0	ab	1 1 2	31.7637	0.121952	0.063352776	0.058599224	0.2736545	0.000983709
0	ab	1 1 4	33.9944	0.106896	0.063470428	0.043425572	0.292325	0.000724813
0	ab	1 1 6	37.4517	0.117874	0.06373491	0.05413909	0.3210403	0.000894887
0	ab	2 0 0	44.4111	0.130944	0.064589498	0.066354502	0.3779305	0.001072213
0	ab	2 1 7	56.1848	0.130219	0.067139627	0.063079373	0.4708949	0.00097124
0	ab	2 0 12	62.5736	0.13258	0.069195599	0.063384401	0.5193222	0.000945392
0	c	0 0 6	20.4865	0.145717	0.063348476	0.082368524	0.1778276	0.001414689

Composition (x)	Orientation	h k l	2θ / °	β Tot. / °	β Tot., Ins. / °	β Tot., Smpl. / °	sin (θ)	β cos (θ) / c
0	c	0 0 8	27.4437	0.137885	0.063237848	0.074647152	0.2372086	0.001265654
0	c	0 0 14	49.0838	0.194912	0.065424555	0.129487445	0.4153586	0.00205581
0	c	1 0 7	32.6023	0.122964	0.063392239	0.059571761	0.280686	0.000997926
0	c	1 1 10	47.0685	0.139108	0.065037302	0.074070698	0.3992972	0.001185246
0	c	1 1 14	59.2048	0.160053	0.068047045	0.092005955	0.4939783	0.001396208
1	ab	1 0 1	21.9193	0.179028	0.063297014	0.115730986	0.1901176	0.001983047
1	ab	1 0 3	23.9592	0.212263	0.063249071	0.149013929	0.2075634	0.002544143
1	ab	1 0 5	27.6149	0.151294	0.063239647	0.088054353	0.2386597	0.001492429
1	ab	1 1 0	30.8079	0.156946	0.063314699	0.093631301	0.2656226	0.00157547
1	ab	1 1 2	31.5754	0.180305	0.063344696	0.116960304	0.2720737	0.001964336
1	ab	1 1 4	33.7842	0.158625	0.063457598	0.095167402	0.2905703	0.001589319

Composition (x)	Orientation	h k l	2θ / °	β Tot. / °	β Tot., Ins. / °	β Tot., Smpl. / °	sin (θ)	β cos (θ) / c
1	ab	1 1 6	37.2077	0.212873	0.063712884	0.149160116	0.319023	0.002467303
1	ab	2 0 0	44.1286	0.211325	0.064545983	0.146779017	0.3756469	0.00237416
1	ab	1 1 2	31.5754	0.180305	0.063344696	0.116960304	0.2720737	0.001964336
1	ab	1 1 4	33.7842	0.158625	0.063457598	0.095167402	0.2905703	0.001589319
1	ab	1 1 6	37.2077	0.212873	0.063712884	0.149160116	0.319023	0.002467303
1	ab	2 0 0	44.1286	0.211325	0.064545983	0.146779017	0.3756469	0.00237416
1	ab	2 1 7	55.7895	0.249496	0.067029039	0.182466961	0.4678488	0.00281462
1	ab	2 0 4	46.3677	0.12757	0.064912374	0.062657626	0.3936828	0.001005271
1	ab	2 1 1	49.7976	0.213626	0.065571876	0.148054124	0.4210168	0.002343853
1	ab	2 0 8	52.6434	0.318972	0.066213772	0.252758228	0.4434107	0.003954076
1	ab	2 0 12	62.0944	0.336067	0.069023108	0.267043892	0.515744	0.003993102

Composition (x)	Orientation	h k l	2θ / °	β Tot. / °	β Tot., Ins. / °	β Tot., Smpl. / °	sin (θ)	β cos (θ) / c
1	ab	2 2 0	64.1792	0.291783	0.069796314	0.221986686	0.5312448	0.003282462
1	ab	2 1 13	69.2618	0.382961	0.071940919	0.311020081	0.5682876	0.004466588
1	ab	3 0 1	68.6989	0.168657	0.07168442	0.09697258	0.5642388	0.00139734
1	ab	3 1 6	76.5847	0.359208	0.075749983	0.283458017	0.6196742	0.003882914
1	ab	2 2 8	71.0615	0.244598	0.072794328	0.171803672	0.5811398	0.002440223
1	ab	3 1 0	72.8756	0.342887	0.073707577	0.269179423	0.5939498	0.003779605
1	c	0 0 8	27.2529	0.253492	0.063236106	0.190255894	0.2355908	0.003227125
1	c	1 0 7	32.3863	0.214608	0.063381529	0.151226471	0.2788763	0.002534687
1	c	0 0 12	41.3891	0.309519	0.064163528	0.245355472	0.3533859	0.004005959
1	c	1 1 10	46.7296	0.268978	0.064976269	0.204001731	0.396584	0.003268535
1	c	0 0 14	48.6967	0.374199	0.065346905	0.308852095	0.4122833	0.004911033

Composition (x)	Orientation	h k l	2θ / °	β Tot. / °	β Tot., Ins. / °	β Tot., Smpl. / °	sin (θ)	β cos (θ) / c
1	c	1 0 13	50.4821	0.329845	0.065718239	0.264126761	0.4264275	0.004169738
1	c	1 1 14	58.7392	0.341424	0.067899798	0.273524202	0.4904414	0.004160329
1	c	1 0 19	72.3439	0.466525	0.073434268	0.393090732	0.5902105	0.005538318
2	ab	1 0 1	21.7788	0.176505	0.063301417	0.113203583	0.1889138	0.001940199
2	ab	1 0 5	27.3374	0.366184	0.063236843	0.302947157	0.2363074	0.005137677
2	ab	1 1 0	30.6278	0.187368	0.063308341	0.124059659	0.264107	0.002088369
2	ab	1 1 2	31.3753	0.205821	0.063336421	0.142484579	0.2703929	0.002394191
2	ab	1 1 4	33.5279	0.15756	0.063442449	0.094117551	0.2884294	0.00157285
2	ab	1 1 6	36.8684	0.349812	0.063683115	0.286128885	0.3162154	0.004737642
2	ab	2 0 0	43.8769	0.273997	0.064507862	0.209489138	0.3736104	0.003391509
2	ab	2 1 1	49.5108	0.23336	0.065512036	0.167847964	0.4187453	0.002660289

Composition (x)	Orientation	h k l	2θ / °	β Tot. / °	β Tot., Ins. / °	β Tot., Smpl. / °	sin (θ)	β cos (θ) / c
2	ab	2 0 8	52.1729	0.364607	0.066101518	0.298505482	0.4397268	0.004679179
2	ab	2 1 5	52.4848	0.251993	0.066175657	0.185817343	0.4421697	0.00290886
2	ab	2 0 8	52.1729	0.364607	0.066101518	0.298505482	0.4397268	0.004679179
2	ab	2 1 7	55.3448	0.426355	0.066906842	0.359448158	0.4644155	0.005555969
2	ab	2 0 12	61.3912	0.631602	0.068775538	0.562826462	0.5104769	0.008446864
2	ab	2 2 8	70.4977	0.318088	0.072521442	0.245566558	0.5771288	0.00350013
2	ab	2 2 0	63.8054	0.361144	0.069653293	0.291490707	0.5284783	0.004318993
2	ab	3 0 5	70.7594	0.575416	0.072647473	0.502768527	0.5789923	0.007154519
2	ab	3 1 0	72.4407	0.396196	0.073483674	0.322712326	0.5908922	0.004543936
2	ab	3 1 6	76.0439	0.513004	0.075436964	0.437567036	0.6159633	0.006016225
2	c	0 0 8	26.7952	0.527799	0.063233053	0.464565947	0.2317072	0.007887545

Composition (x)	Orientation	h k l	2θ / °	β Tot. / °	β Tot., Ins. / °	β Tot., Smpl. / °	sin (θ)	β cos (θ) / c
2	c	1 0 7	32.0048	0.400273	0.063363539	0.336909461	0.2756776	0.005652323
2	c	0 0 12	40.692	0.665491	0.064077425	0.601413575	0.3476885	0.009841762
2	c	1 1 14	57.9172	0.752818	0.06764645	0.68517155	0.4841775	0.010463326
2	c	2 0 14	66.9568	0.830222	0.070921142	0.759300858	0.5516226	0.011053662
2	c	2 0 16	73.1079	0.812075	0.073828477	0.738246523	0.5955794	0.01035034
3	ab	1 0 1	21.6618	0.129534	0.06330519	0.06622881	0.187911	0.001135319
3	ab	1 0 5	27.0411	0.163963	0.063234496	0.100728504	0.2337941	0.001709322
3	ab	1 1 0	30.4709	0.133505	0.063303011	0.070201989	0.2627862	0.001182193
3	ab	1 1 2	31.1921	0.173991	0.063329127	0.110661873	0.2688534	0.001860302
3	ab	1 1 4	33.2714	0.134619	0.063427831	0.071191169	0.2862854	0.001190514
3	ab	1 1 6	36.5034	0.173559	0.063652203	0.109906797	0.313192	0.001821729

Composition (x)	Orientation	h k l	2θ / °	β Tot. / °	β Tot., Ins. / °	β Tot., Smpl. / °	sin (θ)	β cos (θ) / c
3	ab	1 1 8	40.6542	0.149864	0.064072884	0.085791116	0.3473792	0.00140409
3	ab	2 0 0	43.6446	0.164084	0.064473221	0.099610779	0.3717292	0.001613955
3	ab	2 0 6	48.275	0.112118	0.065264093	0.046853907	0.4089278	0.000746256
3	ab	2 0 8	51.656	0.222009	0.065981023	0.156027977	0.435671	0.00245117
3	ab	2 1 7	54.8695	0.204758	0.066778804	0.137979196	0.4607382	0.002137357
3	ab	2 0 10	55.7852	0.221107	0.067027846	0.154079154	0.4678157	0.002376775
3	ab	2 0 12	60.5739	0.250503	0.068495986	0.182007014	0.504331	0.002743046
3	ab	2 2 0	63.4446	0.179331	0.06951708	0.10981392	0.5258028	0.001630285
3	ab	2 1 13	67.5542	0.307545	0.071177745	0.236367255	0.5559634	0.003429049
3	ab	3 1 0	72.0157	0.258264	0.073267916	0.184996084	0.5878961	0.002611887
3	ab	3 0 7	72.6121	0.361619	0.073571539	0.288047461	0.5920983	0.004051391

Composition (x)	Orientation	h k l	2θ / °	β Tot. / °	β Tot., Ins. / °	β Tot., Smpl. / °	sin (θ)	β cos (θ) / c
3	ab	3 1 6	75.4834	0.243752	0.075118143	0.168633857	0.6121027	0.002327431
3	c	1 0 7	31.5729	0.182583	0.06334459	0.11923841	0.2720527	0.002002609
3	c	0 0 10	32.9826	0.131936	0.063412019	0.068523981	0.2838698	0.00114677
3	c	0 0 12	39.8376	0.278764	0.063977962	0.214786038	0.3406881	0.003524461
3	c	1 0 11	42.6222	0.267269	0.064326892	0.202942108	0.3634317	0.003299808
3	c	0 0 14	46.845	0.323201	0.064996921	0.258204079	0.3975083	0.004135168
3	c	1 0 13	48.8223	0.262853	0.065371927	0.197481073	0.4132816	0.003138572
3	c	1 1 14	56.9281	0.283805	0.06735263	0.21645237	0.4766073	0.003321131
3	c	2 0 14	65.9588	0.236809	0.070504203	0.166304797	0.5443375	0.002434865

G Derivation of the Goldschmidt Tolerance Factor

The Goldschmidt tolerance factor is a measure of stability of a cubic perovskite. It is defined as the ratio between the *a* lattice parameter calculated in terms of the different metal cationic radii, r_A and r_M.[116–118] The expression for *a* in terms of the ionic radius of cation *A* is derived by inspection of the right-angled triangle across the unit cell face as in *figure A 5 (III)*. The lattice parameter is equal to the short sides of the triangle and Pythagoras' theorem was used to relate the lattice parameter, *a*, to the known radii, r_A and r_O as in *equation A 21* overleaf. This can be rearranged to yield the expression for the lattice parameter as in *equation A 22*. An alternative expression for *a* in terms r_M (*eqn. A 23)* can be easily obtained by inspection of the line bisecting the unit cell central plane in *figure A 5 (IV)*. The tolerance factor, *t*, is then given by the simplified ratio between the lattice parameter, *a* and *a'*, calculated in the two different terms as provided in *equation A 24*.

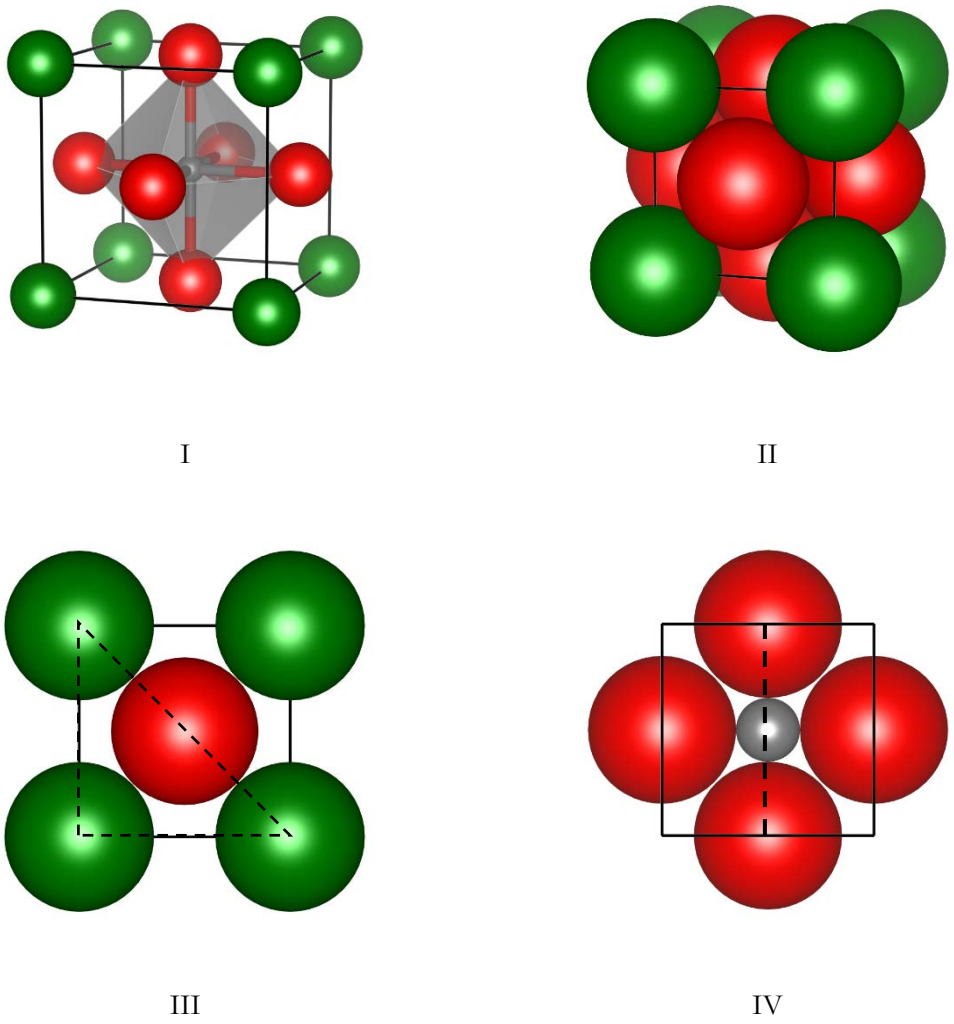

Figure A 5 *'Ball-and-stick' (I) and 'space-filling' (II) representations of the generic perovskite, AMO_3, unit cell and the $[A_4O]$ square plane on the unit cell face (III) and the $[MO_4]$ plane at 0.5a (IV), as viewed along the cubic crystallographic axis. Colour key: green - A, grey - M and red - O.*

$$a^2 + a^2 = (2\,r_A + 2\,r_O)^2 \qquad \text{A 21}$$

a – lattice parameter calculated in terms of r_A and r_O
r_A – ionic radius of generic A site ion

$$a = \frac{2\,(r_A + r_O)}{\sqrt{2}} \qquad \text{A 22}$$

$$a' = 2\,r_M + 2\,r_O \qquad \text{A 23}$$

a' - lattice parameter a calculated in terms of r_M and r_O

$$t = \frac{a}{a'} = \frac{(r_A + r_O)}{\sqrt{2}\,(r_M + r_O)} \qquad \text{A 24}$$

H Chapter 5 Fractional Atomic Coordinates of Rietveld Refined Crystallographic Models

H.1 $Ba_3In_2O_5Cu_2S_2$

Table A 8 Summary of the fractional atomic coordinates of the atomic sites within the $Ba_3In_2O_5Cu_2S_2$ I4/mmm crystal structure. a = b = 4.18552(5) and c = 27.4242(3) Å.

Atom	x	y	z
Ba1	-0.5	0.5	0
Ba2	0	0	-0.35248(9)
In	0	0	-0.763(1)
O1	-0.5	0	-0.0858(5)
O2	0	0	0
Cu	0	0.5	-0.25
S	0	0	-0.2035(3)

H.2 $Ba_3Sc_2O_5Cu_2Se_2$

Table A 9 Summary of the fractional atomic coordinates of the atomic sites within the $Ba_3Sc_2O_5Cu_2Se_2$ I4/mmm crystal structure. a = b = 4.18227(8) and c = 27.7381(9) Å.

Atom	x	y	z
Ba1	-0.5	0.5	0
Ba2	0	0	-0.3578(2)
Sc	0	0	-0.0718(5)
O1	-0.5	0	-0.0824(9)
O2	0	0	0
Cu	0	0.5	-0.25
Se	0	0	-0.1978(2)

H.3 $Ba_3Y_2O_5Cu_2Se_2$

Table A 10 Summary of the fractional atomic coordinates of the atomic sites within the $Ba_3Y_2O_5Cu_2Se_2$ I4/mmm crystal structure. a = b = 4.3912(1) and c = 27.460(1) Å.

Atom	x	y	z
Ba1	-0.5	0.5	0
Ba2	0	0	-0.3537(2)
Y	0	0	-0.0758(4)
O1	-0.5	0	-0.088(1)
O2	0	0	0
Cu	0	0.5	-0.25
Se	0	0	-0.2010(3)

H.4 $Ba_3In_2O_5Cu_2Se_2$

Table A 11 Summary of the fractional atomic coordinates of the atomic sites within the $Ba_3In_2O_5Cu_2Se_2$ I4/mmm crystal structure. a = b = 4.2220(1) and c = 27.992(1) Å.

Atom	x	y	z
Ba1	-0.5	0.5	0
Ba2	0	0	-0.356307(2)
In	0	0	-0.073883(1)
O1	-0.5	0	-0.082920(4)
O2	0	0	0
Cu	0	0.5	-0.25
Se	0	0	-0.199332(3)

H.5 $Ba_3Sc_2O_5Ag_2Se_2$

Table A 12 Summary of the fractional atomic coordinates of the atomic sites within the $Ba_3Sc_2O_5Ag_2Se_2$ I4/mmm crystal structure. a = b = 4.2168(2) and c = 28.657(1) Å.

Atom	x	y	z
Ba1	-0.5	0.5	0
Ba2	0	0	-0.3634(1)
Sc	0	0	-0.0684(4)
O1	-0.5	0	-0.0802(8)
O2	0	0	0
Ag	0	0.5	-0.25
Se	0	0	-0.1885(2)

H.6 $Ba_3In_2O_5Ag_2Se_2$

Table A 13 Summary of the fractional atomic coordinates of the atomic sites within the $Ba_3In_2O_5Ag_2Se_2$ I4/mmm crystal structure. a = b = 4.2601(4) and c = 28.885(3) Å.

Atom	x	y	z
Ba1	-0.5	0.5	0
Ba2	0	0	-0.3617(2)
In	0	0	-0.0711(2)
O1	-0.5	0	-0.081(1)
O2	0	0	0
Ag	0	0.5	-0.25
Se	0	0	-0.1880(4)

I Summary of Distances and Angles

Table A 14 Summary of interatomic distances and angles for compounds successfully synthesised and reported in Chapter 5.

Parameter	Distance / Å					
	$Ba_3In_2O_5Cu_2S_2$	**$Ba_3Sc_2O_5Cu_2Se_2$**	**$Ba_3Y_2O_5Cu_2Se_2$**	**$Ba_3In_2O_5Cu_2Se_2$**	**$Ba_3Sc_2O_5Ag_2Se_2$**	**$Ba_3In_2O_5Ag_2Se_2$**
M'-Ch	2.45024(3)	2.54316(5)	2.57504(5)	2.54431(6)	2.74680(9)	2.7822(2)
M'-M'	2.95961(4)	2.95731(6)	3.10505(7)	2.98542(9)	2.9818(1)	3.0123(3)
	Angle / °					
Ch-M'-Ch	117.3217(9)	110.623(3)	117.002(3)	112.136(3)	100.277(4)	95.406(4)

List of References

1 G. Haacke, *Annu. Rev. Mater. Sci.*, 1977, **7**, 73–93.

2 R. R. Mehta and S. F. Vogel, *J. Electrochem. Soc.*, 1972, **119**, 752.

3 R. G. Gordon, *MRS Bull.*, 2000, **25**, 52–57.

4 K. C. Sanal and M. K. Jayaraj, *Mater. Sci. Eng. B*, 2013, **178**, 816–821.

5 J. C. Manifacier, M. De Murcia, J. P. Fillard and E. Vicario, *Thin Solid Films*, 1977, **41**, 127–135.

6 United States Patent Office, 2429420, 1947.

7 United States Patent Office, 2,566,346, 1951.

8 W. R. Sinclair, F. G. Peters, D. W. Stillinger and S. E. Koonce, *J. Electrochem. Soc.*, 1965, **112**, 1096–1100.

9 J. a. Aboaf, V. C. Marcotte and N. J. Chou, *J. Electrochem. Soc.*, 1973, **120**, 701.

10 United States Patent Office, 2,516,663, 1950.

11 D. B. Fraser, H. D. Cook, D. B. Fraser and H. D. Cook, *J Electrochem Soc. Solid-State Sci. Technol.*, 1972, **119**, 1368.

12 Y. Shigesato, S. Takaki and T. Haranoh, *J. Appl. Phys.*, 1992, **71**, 3356–3364.

13 R. K. Gupta, K. Ghosh, S. R. Mishra and P. K. Kahol, *Appl. Surf. Sci.*, 2008, **254**, 4018–4023.

14 R. A. Afre, N. Sharma, M. Sharon and M. Sharon, *Rev. Adv. Mater. Sci*, 2018, **53**, 79–89.

15 D. S. (David S. . Ginley, H. Hosono and D. C. Paine, *Handbook of transparent conductors*, Springer, 2010.

16 K. Ellmer, *Nat. Photonics*, 2012, **6**, 809–817.

17 Y. R. Ryu, W. J. Kim and H. W. White, *J. Cryst. Growth*, 2000, **219**, 419–422.

18 US Patent Office, US5756192A, 1996.

19 S. Calnan and A. N. Tiwari, *Thin Solid Films*, 2010, 518, 1839–1849.

20 W. Cao, J. Li, H. Chen and J. Xue, *J. Photonics Energy*, 2014, **4**, 040990.

21 H. U. Yang, J. D'Archangel, M. L. Sundheimer, E. Tucker, G. D. Boreman and M. B. Raschke, *Phys. Rev. B*, 2015, **91**, 235137.

22 P. . Cox, *The Electronic Structure and Chemistry of Solids*, Oxford University Press, New York, 1987.

23 M. H. Li, P. S. Shen, K. C. Wang, T. F. Guo and P. Chen, *J. Mater. Chem. A*, 2015, **3**, 9011–9019.

24 J. R. Manders, S.-W. Tsang, M. J. Hartel, T.-H. Lai, S. Chen, C. M. Amb, J. R. Reynolds and F. So, *Adv. Funct. Mater.*, 2013, **23**, 2993–3001.

25 D. Shin, S.-H. Choi, D. H. Shin and S.-H. Choi, *Coatings*, 2018, **8**, 329.

26 K. K. Chattopadhyay and A. N. Banerjee, *Prog. Cryst. Growth Charact. Mater.*, 2005, **50**, 52–105.

27 D. O. Scanlon and G. W. Watson, *Chem. Mater.*, 2009, **21**, 5435–5442.

28 K. Minegishi, Y. Koiwai, Y. Kikuchi, K. Yano, M. Kasuga and A. Shimizu, *Jpn. J. Appl. Phys.*, 1997, **36**, L1453–L1455.

29 S. J. Pearton, D. P. Norton, K. Ip, Y. W. Heo and T. Steiner, *Prog. Mater. Sci.*, 2005, 50, 293–340.

30 R. Swapna and M. C. S. Kumar, *Mater. Res. Bull.*, 2014, **49**, 44–49.

31 D. Kyu, K. · Kyeong, M. Kim, · Choon, B. Park, D. K. Kim, K. M. Kim and C. B. Park, *Appl. Phys. A*, 2010, 98, 913–917.

32 H. Hosono and K. Ueda, in *Electronic and Photonic Materials*, Springer International Publishing AG 2017, 2nd edn., 2017, pp. 1391–1404.

33 H. Kawazoe, M. Yasukawa, H. Hyodo, M. Kurita, H. Yanagi and H. Hosono, 1997, **389**, 939–942.

34 C. Friedel and Daubree, *Comptes rendus Acad. Sci.*, 1873, **77**, 211.

35 J. M. Crafts, *J. Chem. Soc. Trans.*, 1900, **77**, 993–1019.

36 K. Momma and F. Izumi, *J. Appl. Crystallogr.*, 2011, **44**, 1272–1276.

37 R. Nagarajan, A. D. Draeseke, A. W. Sleight and J. Tate, *J. Appl. Phys.*, 2001, **89**, 8022.

38 N. Duan, A. W. Sleight, M. K. Jayaraj and J. Tate, *Appl. Phys. Lett.*, 2000, **77**, 1325.

39 M. Snure, A. Tiwari, M. Snure and A. Tiwari, *Appl. Phys. Lett.*, 2009, **092123**, 20–23.

40 M. K. Jayaraj, A. D. Draeseke, J. Tate and A. W. Sleight, *Thin Solid Films*, 2001, **397**, 244–248.

41 K. Ueda, S. Inoue, S. Hirose, H. Kawazoe and H. Hosono, *Appl. Phys. Lett.*, 2000, **77**, 2701.

42 S. ichiro Inoue, K. Ueda, H. Hosono and N. Hamada, *Phys. Rev. B - Condens. Matter Mater. Phys.*, 2001, **64**, 2452111–2452115.

43 H. Hiramatsu, K. Ueda, H. Ohta, M. Orita, M. Hirano and H. Hosono, *Thin Solid Films*, 2002, **411**, 125–128.

44 H. Hiramatsu, K. Ueda, H. Ohta, M. Hirano, M. Kikuchi, H. Yanagi, T. Kamiya and H. Hosono, *Appl. Phys. Lett.*, 2007, **91**, 2701.

45 H. Hiramatsu, K. Ueda, H. Ohta, M. Hirano, T. Kamiya and H. Hosono, *Appl. Phys. Lett.*, 2003, **82**, 1048–1050.

46 H. Hiramatsu, M. Orita, M. Hirano, K. Ueda and H. Hosono, *J. Appl. Phys.*, 2002, **91**, 9177.

47 M. L. Liu, L. Bin Wu, F. Q. Huang, L. D. Chen and J. A. Ibers, *J. Solid State Chem.*, 2007, **180**, 62–69.

48 M.-L. Liu, L.-B. Wu, F.-Q. Huang, L.-D. Chen and I.-W. Chen, *J. Appl. Phys.*, 2007, **102**, 116108.

49 K. Otzschi, H. Ogino, J. Shimoyama and K. Kishio, *J. Low Temp. Phys.*, 1999, **117**, 729–733.

50 D. N. Stavropoulos and G. N. Stavropoulos, *Oxford Greek-English learner's dictionary*, Oxford University Press, 2008.

51 G. R. Levi, *Nuovo Cim.*, 1924, **1**, 335–344.

52 R. G. Pearson, *J. Am. Chem. Soc.*, 1963, **85**, 3533–3539.

53 M. L. Liu, F. Q. Huang and L. D. Chen, *Scr. Mater.*, 2008, **58**, 1002–1005.

54 M. L. Liu, I. W. Chen, F. Q. Huang and L. D. Chen, *Adv. Mater.*, 2009, **21**, 3808–3812.

55 NobelPrize.org, Wilhelm Conrad Rontgen - Biographical, https://www.nobelprize.org/prizes/physics/1901/rontgen/biographical.

56 E. A. Underwood, *Proc. R. Soc. Med.*, 1945, **38**, 697–706.

57 NobelPrize.org, The Nobel Prize in Physics 1915, https://www.nobelprize.org/prizes/physics/1915/summary.

58 W. H. Bragg and W. L. Bragg, *Proc. R. Soc. A Math. Phys. Eng. Sci.*, 1913, **88**, 428–438.

59 W. Clegg, *Crystal structure determination*, Oxford University Press, 1998.

60 A. Hewat, W. I. F. David and L. van Eijck, *J. Appl. Crystallogr.*, 2016, **49**, 1394–1395.

61 H. M. Rietveld, *J. Appl. Crystallogr.*, 1969, **2**, 65–71.

62 J. Tauc; R. Grigorovici; A. Vancu, *Phys. stat. sol.*, 1966, 15, 627–637.

63 J. Tauc, *Mater. Res. Bull.*, 1968, **3**, 37–46.

64 V. M. Huxter, University of Toronto, 2009.

65 P. Kubelka, *Zeitschrift fur Tech. Phys.*, 1931, **12**, 539–601.

66 P. Kubelka and F. Munk, *Z. Tech. Phys*, 1931, **12**, 593–601.

67 V. Džimbeg-malčić, Ž. Barbarić-mikočević and K. Itrić, *Tech. Gaz.*, 2011, **18**, 117–124.

68 G. Kortüm, W. Braun and G. Herzog, *Angew. ChemieZeitschrift Tech. Phys. Int. Ed. English*, 1963, **2**, 333–341.

69 H. Ogino, Y. Katagi, J. I. Shimoyama, K. Yamanoi, M. Tsuboi, T. Shimizu, N. Sarukura and K. Kishio, in *Optical Materials*, North-Holland, 2014, vol. 36, pp. 1978–1981.

70 L. Cario, A. Lafond, T. Morvan, H. Kabbour, G. André and P. Palvadeau, *Solid State Sci.*, 2005, **7**, 936–944.

71 W. J. Zhu and P. H. Hor, *J. Solid State Chem.*, 1997, **134**, 128–131.

72 N. Kawaguchi, H. Ogino, Y. Shimizu, K. Kishio and J. I. Shimoyama, *Appl. Phys. Express*, 2010, **3**, 063102.

73 P. M. Shirage, K. Kihou, C. H. Lee, H. Kito, H. Eisaki and A. Iyo, *J. Am. Chem. Soc.*, 2011, **133**, 9630–9633.

74 F. Hummel, M. Tegel, B. Gerke, R. Pöttgen and D. Johrendt, *Zeitschrift für Naturforsch. B*, 2015, **70**, 671–676.

75 M. Tegel, I. Schellenberg, F. Hummel, R. Poettgen and D. Johrendt, *ZEITSCHRIFT FUR Naturforsch. Sect. B-A J. Chem. Sci.*, 2009, **64**, 815–820.

76 B. A. D. Williamson, G. J. Limburn, G. W. Watson, G. Hyett and D. O. Scanlon, *ChemRXiv*.

77 W. Sun, S. T. Dacek, S. P. Ong, G. Hautier, A. Jain, W. D. Richards, A. C. Gamst, K. A. Persson and G. Ceder, *Sci. Adv.*, 2016, **2**, e1600225.

78 X. Zhu, F. Han, G. Mu, B. Zeng, P. Cheng, B. Shen and H. H. Wen, *Phys. Rev. B - Condens. Matter Mater. Phys.*, , DOI:10.1103/PhysRevB.79.024516.

79 W. J. Zhu and P. H. Hor, *Inorg. Chem.*, 1997, **36**, 3576–3577.

80 O. Yamaguchi, A. Narai and K. Shimizu, *J. Am. Ceram. Soc.*, 1986, **69**, C36–C37.

81 H. Ogino, K. Machida, A. Yamamoto, K. Kishio, J. Shimoyama, T. Tohei and Y. Ikuhara, *Supercond. Sci. Technol.*, 2010, **23**, 115005.

82 S. Sato, H. Ogino, N. Kawaguchi, Y. Katsura, K. Kishio, J. I. Shimoyama, H. Kotegawa and H. Tou, *Supercond. Sci. Technol.*, 2010, **23**, 045001.

83 C. F. Smura, D. R. Parker, M. Zbiri, M. R. Johnson, Z. A. Gál and S. J. Clarke, *J. Am. Chem. Soc.*, 2011, **133**, 2691–2705.

84 G. Hyett, Z. A. Gál, C. F. Smura and S. J. Clarke, *Chem. Mater.*, 2008, **20**, 559–566.

85 R. D. Shannon and C. T. Prewitt, *Acta Crystallogr. Sect. B Struct. Crystallogr. Cryst. Chem.*, 1969, **25**, 925–946.

86 G. Caglioti, A. Paoletti and F. P. Ricci, *Nucl. Instruments*, 1958, **3**, 223–228.

87 P. Scherrer, *Nachrichten von der K. Gesellschaft der Wissenschaften zu Gottingen*, 1918, 98–100.

88 A. R. Stokes and A. J. C. Wilson, *Proc. Phys. Soc. Lond.*, 1944, **56**, 174.

89 G. K. Williamson and W. H. Hall, *Acta Metall.*, 1953, **1**, 22–31.

90 E. Motomitsu, H. Yanagi, T. Kamiya, M. Hirano and H. Hosono, *J. Solid State Chem.*, 2006, **179**, 1668–1673.

91 S. J. Clarke, P. Adamson, S. J. C. Herkelrath, O. J. Rutt, D. R. Parker, M. J. Pitcher and C. F. Smura, *Inorg. Chem.*, 2008, 47, 8473–8486.

92 E. Burstein, *Phys. Rev.*, 1954, 93, 632–633.

93 J. S. O. Evans, E. B. Brogden, A. L. Thompson and R. L. Cordiner, *Chem. Commun. (Camb).*, 2002, **39**, 912–3.

94 L. J. van der Pauw, *Philips Tech. Rev.*, 1958, 20, 220–224.

95 L. J. van der Pauw, *Philips Res. Reports*, 1958, **13**, 1–9.

96 P. W. Bridgman, *NATIONAL ACADEMY OF SCIENCES OF THE UNITED STATES OF AMERICA BIOGRAPHICAL MEMOIRS VOLUME XXI SECOND MEMOIR BIOGRAPHICAL MEMOIR OF EDWIN HERBERT HALL 1855-1938*, .

97 E. H. Hall, *Am. J. Math.*, 1879, **2**, 287.

98 H. Hiramatsu, K. Ueda, H. Ohta, M. Hirano, T. Kamiya and H. Hosono, *Thin Solid Films*, 2003, **445**, 304–308.

99 K. H. L. Zhang, K. Xi, M. G. Blamire and R. G. Egdell, *J. Phys. Condens. Matter.*

100 W. J. Zhu and P. H. Hor, *J. Solid State Chem.*, 1997, **130**, 319–321.

101 W. J. Zhu and P. H. Hor, *J. Solid State Chem.*, 2000, **153**, 26–29.

102 J. S. O. Evans, E. B. Brogden, A. L. Thompson and R. L. Cordiner, *Chem. Commun. (Camb).*, 2002, **39**, 912–3.

103 S. Sato, H. Ogino, N. Kawaguchi, Y. Katsura, K. Kishio, J. I. Shimoyama, H. Kotegawa and H. Tou, *Supercond. Sci. Technol.*, 2010, **23**, 045001.

104 H. Ogino, S. Sato, K. Kishio, J.-I. Shimoyama, T. Tohei and Y. Ikuhara, *Appl. Phys. Lett.*, 2010, **97**, 072506–172506.

105 H. Ogino, Y. Shimizu, N. Kawaguchi, K. Kishio, J. I. Shimoyama, T. Tohei and Y. Ikuhara, *Supercond. Sci. Technol.*, 2011, **24**, 085020.

106 Z. A. Gál, O. J. Rutt, C. F. Smura, T. P. Overton, N. Barrier, S. J. Clarke and J. Hadermann, *J. Am. Chem. Soc.*, 2006, **128**, 8530–8540.

107 L. Tonks and I. Langmuir, *Phys. Rev.*, 1929, **33**, 195–211.

108 T. Zhou, Y. Wang, S. Jin, D. Li, X. Lai, T. Ying, H. Zhang, S. Shen, W. Wang and X. Chen, *Inorg. Chem.*, 2014, **53**, 4154–4160.

109 S. Jin, X. Chen, J. Guo, M. Lei, J. Lin, J. Xi, W. Wang and W. Wang, *Inorg. Chem.*, 2012, **51**, 10185–10192.

110 H. Ogino, Y. Shimizu, K. Ushiyama, N. Kawaguchi, K. Kishio and J. I. Shimoyama, *Appl. Phys. Express*, 2010, **3**, 063103.

111 D. O. Charkin, A. V. Sadakov, O. E. Omel'yanovskii and S. M. Kazakov, *Mater. Res. Bull.*, 2010, 45, 2012–2016.

112 M. Tegel, F. Hummel, S. Lackner, I. Schellenberg, A. Pöttgen and D. Johrendt, *Zeitschrift fur Anorg. und Allg. Chemie*, 2009, **635**, 2242–2248.

113 D. Berthebaud, O. I. Lebedev, D. Pelloquin and A. Maignan, *Solid State Sci.*, 2014, **36**, 94–100.

114 H. Ogino, Y. Katsura, S. Horii, K. Kishio and J. Shimoyama, *Supercond. Sci. Technol.*, 2009, **22**, 085001.

115 X. Zhu, F. Han, G. Mu, P. Cheng, B. Shen, B. Zeng and H.-H. Wen, *Phys. Rev. B*, 2009, **79**, 220512.

116 V. M. Goldschmidt, *Naturwissenschaften*, 1926, **14**, 477–485.

117 Q. Sun and W.-J. Yin, *J. Am. Chem. Soc.*, 2017, **139**, 14905–14908.

118 X. Zhao and N.-G. Park, *Photonics*, 2015, **2**, 1139–1151.